DOLOMITIZATION IN THE UTELAND BUTTE MEMBER OF THE EOCENE GREEN RIVER FORMATION, UINTA BASIN, UTAH

by Federico Rueda Chaparro, Hans G. Machel, and Michael D. Vanden Berg

OPEN-FILE REPORT 700
UTAH GEOLOGICAL SURVEY
a division of
UTAH DEPARTMENT OF NATURAL RESOURCES
2019

DOLOMITIZATION IN THE UTELAND BUTTE MEMBER OF THE EOCENE GREEN RIVER FORMATION, UINTA BASIN, UTAH

by

Federico Rueda Chaparro[1], Hans G. Machel[1], and Michael D. Vanden Berg[2]

[1]Department of Earth and Atmospheric Sciences, University of Alberta
[2]Utah Geological Survey

This manuscript is F. Rueda Chaparro's M.S. thesis, written as a condition of graudation from the University of Alberta. H.G. Machel acted as primary advisor and M.D. Vanden Berg was a committee member and research advisor.

Cover photo: *Uteland Butte outcrops in Nine Mile Canyon, Utah.*

Suggested citation:

Rueda Chaparro, F., Machel, H.G., and Vanden Berg, M.D., 2019, Dolomitization in the Uteland Butte Member of the Eocene Green River Formation, Uinta Basin, Utah: Utah Geological Survey Open-File Report 700, 136 p., 8 appendices, https://doi.org/10.34191/OFR-700.

OPEN-FILE REPORT 700
UTAH GEOLOGICAL SURVEY
a division of
UTAH DEPARTMENT OF NATURAL RESOURCES
2019

Blank pages are intentional for printing purposes.

CONTENTS

ABSTRACT

The lacustrine Eocene Green River Formation (GRF) is an important oil-producing formation in the Uinta Basin, Utah (USA). In recent years, the unconventional carbonate reservoirs in the Uteland Butte member (UBm), base of the GRF, have been targeted because of their significant oil and gas resources. The stratigraphic interval of interest lies between the informally named D and C shales, in which there are three dolomite layers named PZ2, PZ1′, and PZ1 that vary from 1.5 to 8 feet in thickness and have up to 30% porosity but only a maximum of 0.1 mD permeability.

The objectives for this study are to characterize the depositional facies types and determine how they are related to dolomitization, to elucidate the dolomitization and how porosity and permeability are related to this process, and to delineate the regional geometry of the dolomite layers. This study employed several methods: outcrop and core descriptions; petrographic analysis (transmitted light, cathodoluminescence, and scanning electron microscopy); mineralogical identification and ordering of dolomites (XRD); elemental composition of dolomite crystals (EDS and EMPA); major and trace element analysis (ICP-MS); and conventional and clumped oxygen and carbon stable isotope analyses.

Deposition of the UBm took place during transgressive-regressive cycles that were likely driven by Eocene climate variations. The carbonate intervals were deposited in a shallow littoral environment as intraclastic grainstone and ooid ostracod grainstone-packstone, and in the sublittoral environments as mudstone, peloidal bioturbated mudstone, and ostracod wackestone. After deposition, these carbonate facies were dolomitized to variable degrees and are characterized by selective dolomitization of matrix, peloids, ooids, and intraclast with variable preservation of the precursor textures. However, bioclasts are partially or not dolomitized. The dolomitization processes crosscut all facies boundaries from the distal sublittoral setting toward the littoral nearshore area.

The dolomite intervals are characterized by %Ca that ranges from 49% to 59% with a strong mode in 52 to 55%, and low cation ordering that ranges from 0.2 to 0.5. $\delta^{13}C$ values for the dolomite range from 6‰ to -5.4‰ (VPDB) suggesting high organic activity and/or organic matter decay, coupled with organic matter oxidation by sulfate reducing bacteria. The $\delta^{18}O$ values for the dolomite range from 0.9 to -7.3‰ (VPDB) and are interpreted as a gradual increase in lake water temperature. Based on $\delta^{18}O$ values for the dolomite, the calculated dolomitizing fluid temperature is between 14° and 36°C.

Dolomitization in the UBm is thus interpreted as the result of two different and superimposed processes—density-driven reflux and evaporative pumping—which were driven by climate changes. During the warmer climate periods, evaporation and reduced river inflow resulted in increased salinity that created density-driven reflux of lake water in the subaqueous parts of the lake, which promoted dolomitization. At the same time, the landward parts of the lake fell dry to form a playa, where dolomite formed from evaporative pumping groundwater. This process overprinted the areas previously dolomitized by reflux.

Increased fresh water input during more humid climate periods caused dolomitization to cease and promoted deposition of lime mud. $\delta^{13}C$ for calcite ranges from 1‰ to -1‰ (VPDB), and the $\delta^{18}O$ ranges from -5.8 to -10.1‰ (VPDB), with a calculated temperature for calcite precipitation of around 3° and 12°C.

The dolomite crystal sizes range from 0.25 to 6 μm and porosity is mainly intercrystal. Dolomite layers PZ2, PZ1′, and PZ1 display four dolomite textures: planar-e, planar-s, nonplanar-a, and planar-c. Dolomitization contributed to the lithification of the lime mud sediments and preserved primary intergranular porosity inherited from the parental lime mud sediments. Moreover, the mole-per-mole dolomite-calcite replacement likely enhanced the porosity of the PZ layers. Dolomite crystals planar-e, planar-s and nonplanar-a textures are weakly correlated with porosity and permeability. Planar textures (planar-e and planar-s) are associated with the highest values of porosity and permeability. However, dolomite textures, crystal size, and shapes are highly variable throughout the PZ layers. In general, the variations in porosity and permeability within each PZ layer and across the entire study area are too small to influence exploration or development strategies.

CHAPTER 1 INTRODUCTION

Lacustrine basins around the world host significant accumulations of hydrocarbons. For example, the fluvial-lacustrine Bohay Bay Basin in China is responsible for about one third of the country's total petroleum production (Hao and others, 2009). In Brazil, roughly 85% of oil produced from continental margin fields is sourced from lacustrine rocks (Mello and Maxwell, 1990). In the United States, the lacustrine Green River Formation (GRF) in the Uinta Basin, Utah, hosts a very large accumulation of conventional oil and gas, as well as one of the largest immature oil shale resources, having an estimated 1.32 trillion barrels of initial oil in place (Johnson and others, 2010). While most drilling efforts in the Uinta Basin target more conventional

sandstone reservoirs, the thin carbonates in the informally named Uteland Butte member (UBm) at the base of the GRF have gained interest in recent years as an unconventional reservoir targeted with horizontal drilling. Recently, Johnson and others (2015) estimated a mean undiscovered resource of 177 million barrels of oil and 218 billion cubic feet of gas for the unconventional reservoirs in the UBm.

The Uinta Basin is part of a series of foreland lake basins located near the junction of Utah, Wyoming, and Colorado (figure 1.1). The geological evolution of these lake basins started with the Sevier orogeny during Jurassic through early Cenozoic time (Johnson, 1985), which defined the western margin of North America by uplift along the Sevier thrust belt. Once the Sevier orogeny stopped, the Laramide orogeny deformed the ancient foreland basin into smaller sedimentary basins during mid Cretaceous to early Paleogene, thus creating the lacustrine basins (Johnson, 1985) at the central area of the ancient Rocky Mountains foreland basin. The Laramide orogeny created the physiographic boundaries of the lake basins as we know them today, including those of the Uinta Basin. The east-west-trending Uinta uplift likely rose prior to the end of the Cretaceous (Hansen, 1965) and was a source of sediments for Paleocene formations (Johnson, 1985). The northwest-southeast-trending Uncompahgre Uplift and the northeast-southwest-trending San Rafael Swell started in the Maastrichtian (Fouch, 1976; Johnson, 1985). The Douglas Creek Arch is a north-south-trending anticline that likely started to rise at the end of the Cretaceous (Tweto, 1975). The two lakes developed in the Laramide foreland basin and created up to several thousand meters of deposits during the early Tertiary.

The GRF was deposited in the Eocene epoch between 53 and 45 Ma (Smith, 2007; Smith and others, 2008). The basal parts of the GRF are thought to have been deposited in fresh water environments, as evidenced by an abundance of fresh water molluscs (Johnson, 1985; Smith, 2007; Smith and others, 2008), and it is represented by the UBm (Johnson and others, 2010). The middle intervals of the GRF contain layers of 'oil shale' that were likely deposited in a brackish lake water environment generated by regression of lake water (Johnson and others, 2010). The upper section of the GRF was deposited in much shallower water and in hypersaline environments, as evidenced by halite and sodium carbonate evaporite beds that have thickness reaching up to 19 feet (Dyni and others, 1985; Johnson, 1985; Long, 2006; Smith and others, 2008; Johnson and others, 2010).

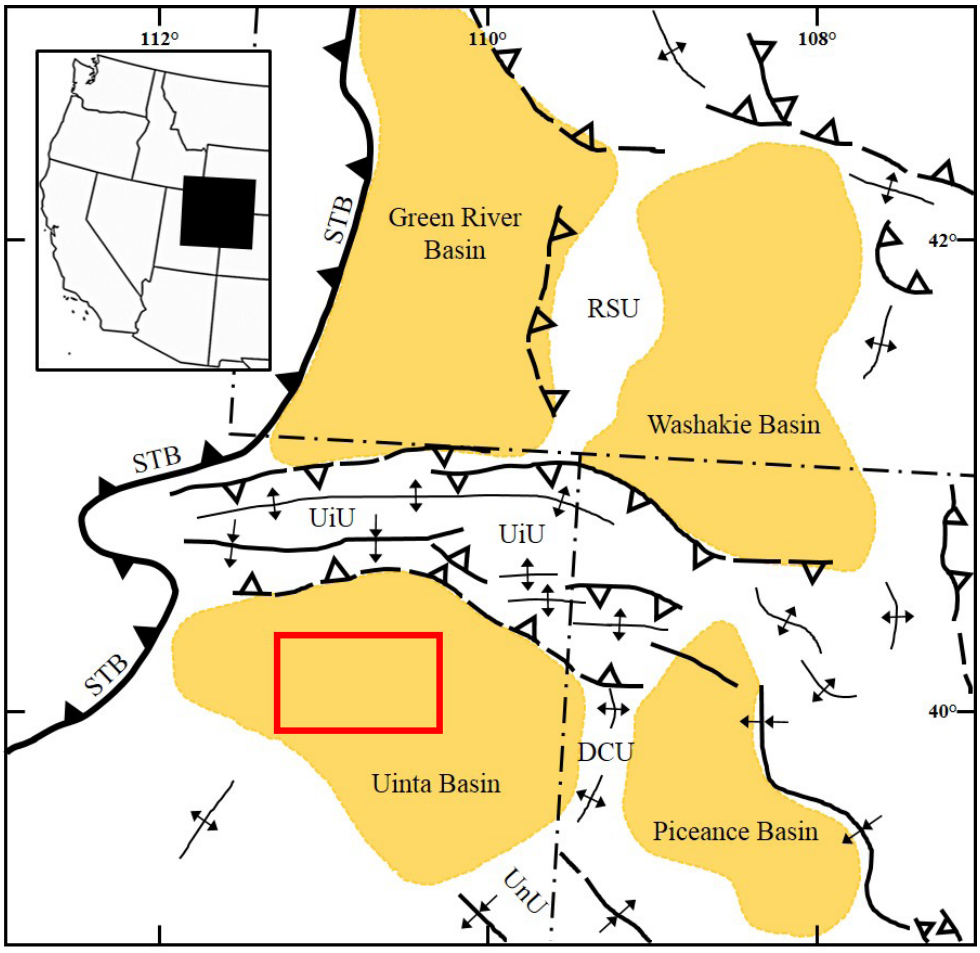

Figure 1.1. *Eocene intermountain lake basins and associated uplifts. Modified from Dickinson and others (1988). Study area highlighted by red rectangle. DCU: Douglas Creek Uplift, RSU: Rock Springs Uplift, STB: Sevier Thrust Belt, UiU: Uinta Uplift, UnU: Uncompahgre Uplift.*

The UBm ranges in thickness from about 49 to 395 feet and is thickest near the depositional center of the Uinta Basin to the north and west (Vanden Berg and others, 2014; Johnson and others, 2016). This member represents the first 'transgression' of ancient Lake Uinta (Vanden Berg and others, 2013; Johnson and others, 2016) and is composed of a succession of interbedded limestone, dolostone, organic-rich calcareous mudstone, siltstone, and some sandstone (Bereskin and others, 2004; Vanden Berg and others, 2014; Johnson and others, 2016).

Pusca (2003) defined the depositional environments for the UBm as shallow lake to playa environments for the carbonate intervals, and as deeper distal lakes for laterally extensive shale units. In the most comprehensive study on facies and depositional environments of the UBm, Logan and others (2016) identified depositional environments ranging from littoral, sublittoral, to profundal, based on outcrops and core descriptions located at the far eastern boundary of the Uinta Basin.

In contrast, this study focuses on the distal UBm facies in the deeper portion of the basin mostly in Duchesne County (Utah) to the west, with a focus to understand the origin of thin dolomite beds (1.5 to 8.2 ft) that exhibit very high porosity, but low permeability, and act as significant hydrocarbon reservoir targets for horizontal drilling and hydraulic fracturing.

1.1 Research Objectives

This project pursues solutions to several questions related to the dolomitization process(es) within the UBm and its relationship for the producibility of hydrocarbon. The specific objectives of this study include:

1) characterization and analysis of facies types for the UBm as they relate to dolomitization;
2) determination of the process(es) of dolomitization;
3) investigation of how porosity and permeability are related to dolomitization;
4) characterization of the geometry (lateral and vertical extent) of the dolomite layers in the study area; and
5) possible implications for reservoir quality and petroleum development.

1.2 Previous Work

There is a substantial body of literature on the Uinta Basin and the GRF (e.g., Picard, 1955; Johnson, 1985; Remy, 1992; Smith, 2007; Johnson and others, 2016; Tänavsuu-Milkeviciene and others, 2017), all of which cover a large range of topics including tectonic evolution, sedimentology, and paleoclimate among others. However, only a few studies have dealt with dolomitization in the GRF.

The first notable attempt to explain dolomitization in the GRF was by Eugster and Surdam (1973), who invoked evaporation in playa flats as the chief cause and location of dolomitization. Implicit to their "playa model" is that the lake margin was very shallow and even drying up during times of prolonged evaporation. In their own words (Eugster and Surdam, 1973):

> In these playa flats alkaline brines evolved through evaporation and precipitation of calcium carbonate and protodolomite in the capillary zone near the ground-water table. Dolomitic mudstones, marlstones, and calcareous and siliciclastic sandstones were the products of occasional floods on the playa.

Williamson and Picard (1974) identified dolomite as a replacement of the microcrystalline and fine-crystalline calcite matrix (micrite and sparite) of certain layers and concluded that dolomitization took place very early in the diagenetic history, prior to lithification. These authors did not identify any specific relationship between facies and dolomitization but nevertheless concluded that dolomitization was promoted by episodic evaporation coupled with high Mg/Ca ratios in the lake water. In addition, they argued that the Mg^{2+} necessary for dolomitization was likely flushed in by river drainage in the form of admixed clay minerals. However, they did not find a correlation between acid-insoluble residues and dolomite contents (Williamson and Picard, 1974).

Ryder and others (1976) differentiated two genetic types of dolomite associated with depositional environments: (i) an open lacustrine (profundal) environment in which dolomite formed from Mg^{2+} that was released from interbedded algae-rich laminites, and (ii) near shore (littoral) environments where the fine-grained carbonate sediments were dolomitized as a result of pumping of brines enriched in Mg^{2+} by evaporation. The latter conforms to the "playa-lake" by Eugster and Surdam (1973).

Desborough (1978) proposed that dolomitization took place in organic-rich (oil shale to-be) layers when the lake was chemically stratified. While much of his work focused on the Parachute Creek Member of the GRF, Piceance Basin, CO (figure 1.1),

he also applied this 'model' to the Uinta Basin. Accordingly, blue-green algae concentrate Mg^{2+} in the chlorophyll molecules through photosynthesis, which was released during post-mortem decay near the water-sediment interface, thereby promoting dolomitization (Desborough, 1978).

More detailed mineralogical work by Cole and Picard (1978) indicated dolomite is most prevalent in Parachute Creek Member on the eastern side of the Uinta Basin and in the neighboring Piceance Basin. They reported a high propensity of dolomite occurs is in the oil shale lithofacies. In the Uinta Basin, other dominant carbonate minerals include ankerite and calcite, and the silicate minerals analcime, potassium feldspar, quartz, and albite in nearshore facies. Cole and Picard (1978) suggested that the dolomite formed as result of biological and chemical conditions of the lake water.

Pitman (1996) was the first researcher to systematically apply stable isotope geochemistry to the dolomite problem in the GRF for both the Douglas Creek and Parachute Creek Members. Based on carbon isotope data, Pitman (1996) identified two types of dolomite: primary and diagenetic. The primary dolomites have $\delta^{13}C$ values ranging from about -2 to +2 ‰ PDB (Pee Dee Belemnite), whereas the diagenetic dolomites have $\delta^{13}C$ values ranging from about +2 to +4 ‰ PDB. According to Pitman (1996), the primary dolomite was formed by gradual increases in the dissolved bicarbonate concentration when the lake evolved from hydrologically open to hydrologically closed, catalyzed by increased photosynthetic activity. On the other hand, Pitman (1996) interpreted the origin of the diagenetic dolomite as mediated by bacterial sulfate reduction. Pitman (1996) did not differentiate between direct formation of dolomite from aqueous solution and replacement of carbonate mud.

Long (2006) investigated dolomitization in several intervals of the GRF and identified two different dolomite crystals based on their lithologic occurrence. The first dolomite is related to the oil shale layers. Long (2006) interpreted this dolomite to have formed as a by-product of bacterial methanogenesis processes that promoted dolomite precipitation. The second dolomite is related to micrite layers in the "Tgl member", the base of which in the Uinta Basin correlates with UBm. Long (2006) interpreted that this dolomite formed as replacement under evaporitic conditions.

Logan and others (2016) completed a comprehensive facies analysis of the UBm from the eastern side of the Uinta Basin. The UBm in this area contains more proximal facies (e.g., grainstones, deltaic, and mouth-bar sand units, etc.) and minor dolomite, compared to the more distal UBm on the west side of the basin (the focus of this study).

In summary, previous studies agree on one point: the dolomite in the GRF, and more specifically in the UBm, formed syndepositionally and/or very early diagenetically. However, these studies offered several possibilities for the source of Mg^{2+}, the driving mechanism for dolomitization (hydrologically and/or geochemically), with some disagreement as to the dolomite(s) being primary or a replacement product of lime mud.

1.3 Study Area and Stratigraphic Interval of Interest

The study area covers the central to southwestern part of the Uinta Basin, mostly in Duchesne County, Utah (figure 1.2). The stratigraphic interval of interest is within the middle part of the UBm, defined at the bottom and top by the informally named D Shale and C Shale, respectively. Within this interval are three prominent and regionally extensive dolomite layers named PZ2, PZ1′, and PZ1 (operator designations). These specific dolomite beds, as well as numerous other thin dolomite beds throughout the UBm, have significant reservoir potential due to their high porosity and lateral extent (figure 1.3).

1.4 Dolomite Theoretical Framework

Dolomite, $CaMg(CO_3)_2$, is a rhombohedral carbonate mineral of Mg and Ca, commonly found in sedimentary rocks. When a rock consists of more than 90% dolomite, it is commonly referred to as dolostone, although many authors use the mineral name dolomite.

The origin of the mineral dolomite has been a focus of a large number of investigations for more than 200 years. Dolomite is important for several reasons including: (1) dolomite is a common carbonate mineral in ancient carbonate successions yet rare in recent carbonate sediments; (2) dolomite has not been synthetized in laboratories at low-diagenetic temperatures (less than about 30°C) inorganically or organically; and (3) most natural dolomites formed via replacement of pre-existing limestone, and many dolomitized carbonates form prolific reservoir rocks for hydrocarbons (Tucker and Wright, 1990; McKenzie, 1991; Purser and others, 1994; Warren, 2000; Machel, 2004; Gregg and others 2015).

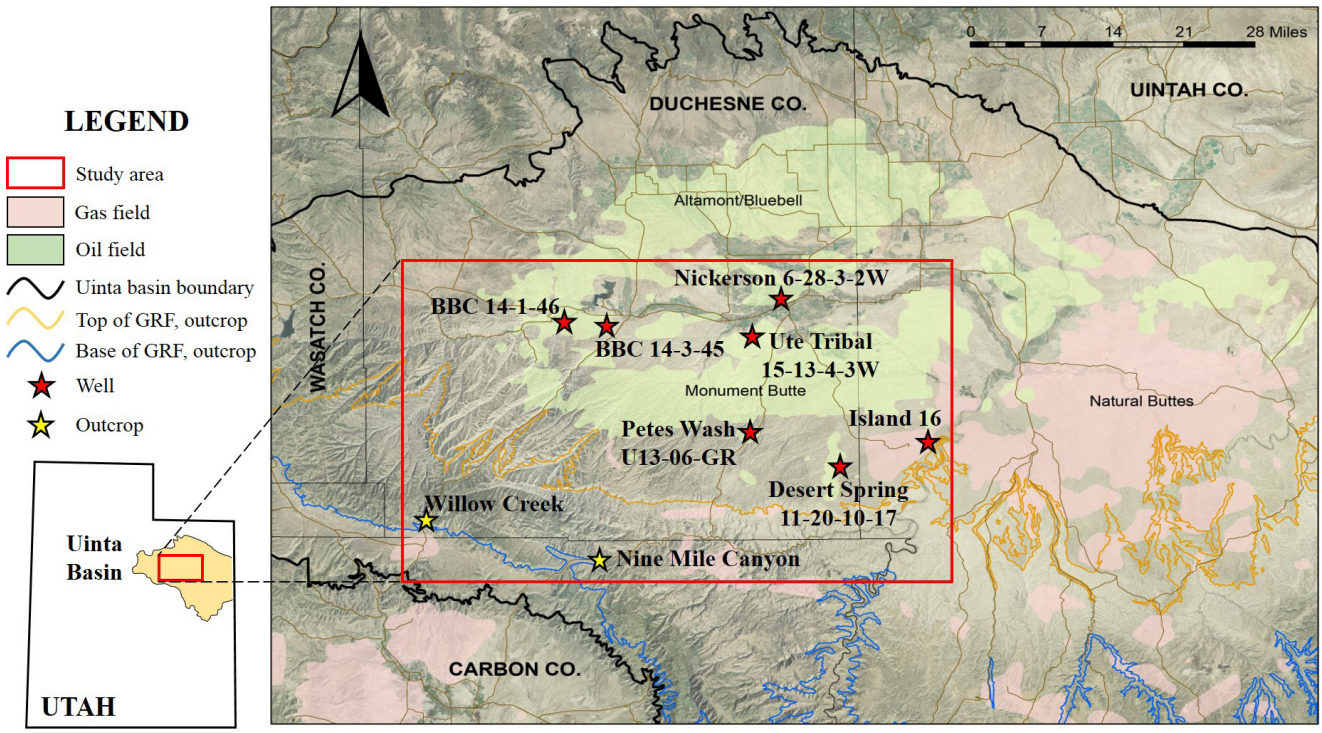

Figure 1.2. *Location of study area (red outline), wells, and outcrops. Modified from Vanden Berg and others (2014).*

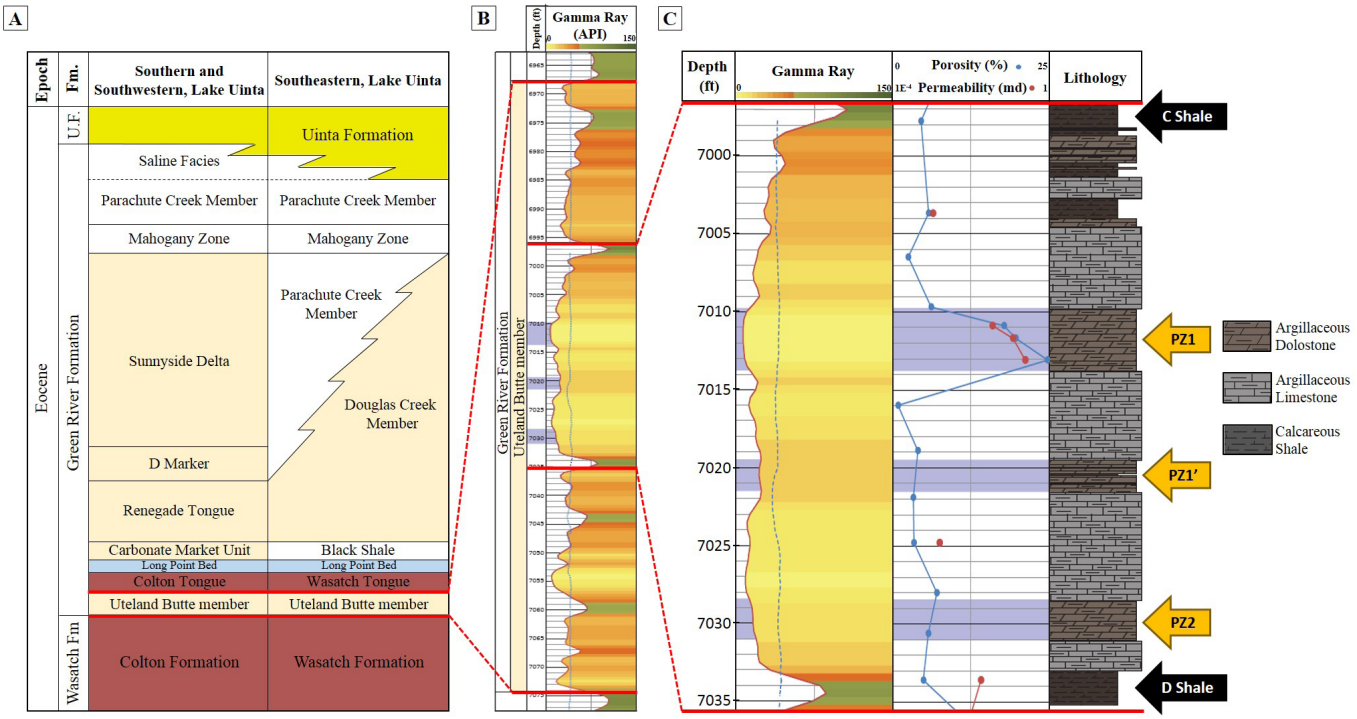

Figure 1.3. A. *Stratigraphic chart of the GRF modified from Logan and others (2016).* ***B.*** *Gamma ray and porosity logs of the entire UBm highlighting the interval of interest, which is located at central section of the UBm (well: UT 15-30).* ***C.*** *Composite of gamma ray, porosity, permeability, and lithology logs of the interval of interest.*

In natural diagenetic environments, dolomite most commonly forms via dolomitization, which is the replacement of calcite by dolomite, or subordinately via direct precipitation from aqueous solution in the form of cements (e.g., Machel, 2004). In addition, dolomite can also form at the sediment-water interface as mud. The latter type is also known as penecontemporaneous dolomite (Budd, 1997).

Over the years many models of dolomitization have been proposed, most of them with the aim to explain the genesis of reservoir-sized geobodies of dolostones, among them the microbial model, the mixing zone model, the related reflux and sabkha models, several seawater models, the compaction model, two thermal convection models, a topography driven model, a tectonic model, and the hydrothermal model (Machel, 2004). In addition, there are viable models for dolomitization that do not form reservoir-sized dolomite/dolostone geobodies, such as the Coorong and playa models (Eugster and Surdam, 1973; Warren, 2000). This study attempts to explain dolomitization of the GRF UBm within the framework of these models.

CHAPTER 2 GEOLOGICAL FRAMEWORK

2.1 Basin and Lake Evolution

The formation of the Uinta Basin began in the Jurassic and continued to the early Cenozoic by the development of the Sevier orogenic belt that resulted from the collision of the Farallon and the North American plate (Johnson, 1985). The uplifted Sevier orogenic belt became the western boundary of Lake Uinta.

Later, during late Cretaceous to early Paleocene, the Laramide Orogeny caused retreat of the Rocky Mountains foreland basin and formed a series of regional uplifts (Johnson, 1985; Johnson and others, 2016) that transformed the epicontinental foreland basin into several smaller basins that filled with lakes in the early Eocene (Dickinson and others, 1988) (figure 2.1).

In the early Eocene, tectonic and climatic conditions allowed the development of several lacustrine basins: the Uinta and Piceance Basins in the NW of Utah and NW of Colorado, respectively, and the Greater Green River Basin to the north in what is now southwest Wyoming (figure 2.1).

The Uinta Basin is a structural and asymmetric basin bounded to the north by the Uinta Mountains, to the east by the Douglas Creek Arch, to the south by the San Rafael Swell and the Uncompahgre Uplift, and to the west by the Wasatch Range.

2.2 Paleohydrology

The tectonic events of the late Paleocene to early Eocene controlled the extent of drainage within the catchment area, and thereby sizes and connections of Lake Uinta and Lake Gosiute.

Ancient Lake Uinta was fed by streams from the surrounding paleo-highlands. The basin received water from the Uinta Mountains to the north and thereby sediments from the erosion of Precambrian to Cretaceous bedrock, including large deposits of Paleozoic carbonates (Hansen, 1965; Pusca, 2003; Smith and others, 2008). From the west, sediment was supplied by the Wasatch Range (Sevier thrust belt) from erosion of Paleozoic and Mesozoic carbonates (Davis, 2008; Gierlowski-Kordesch and others, 2008).

The drainage from the south came from the San Rafael Swell, eroding mostly Paleozoic sedimentary rocks that range from marine shales of the Mancos Shale Formation to alluvial plains and fluvial clastics of the Morrison Formation (Doelling, 2002), and from the Mojave region transported by the California paleoriver (Dickinson and others, 2012). Drainage and sediments were also derived from the Uncompahgre Uplift in the southeast (Cashion, 1967; Dickinson and others, 1988; Davis and others, 2009; Johnson and others, 2010; Smith and others, 2008), mostly composed of Proterozoic metamorphic rocks (Case, 1991) (figure 2.2).

2.3 Sedimentology

The sedimentological evolution of these lakes was governed by climatic and tectonic factors that defined depositional settings and facies associations. Carroll and Bohacs (1999) established a lake classification based on facies associations: overfilled, balanced, and underfilled (figure 2.3). According to Carroll and Bohacs (1999), the most common associations are fluvial-lacustrine, fluctuating profundal, and evaporite facies, which are the result of fluctuations in climate (sediment supply) and tectonism (accommodation rate).

The overfilled lakes are characterized by marlstone and fresh water coquinas interbedded with thin coal seams. Balanced-fill lakes record the flooding and desiccation phases of organic-rich, calcareous mudstone and dolomitic grainstone with evidence of subaerial exposure. The underfilled lake types display a wide variety of facies association from alluvial-fan, laminated oil shale, and evaporite minerals such trona and halite (Carroll and Bohacs, 1999).

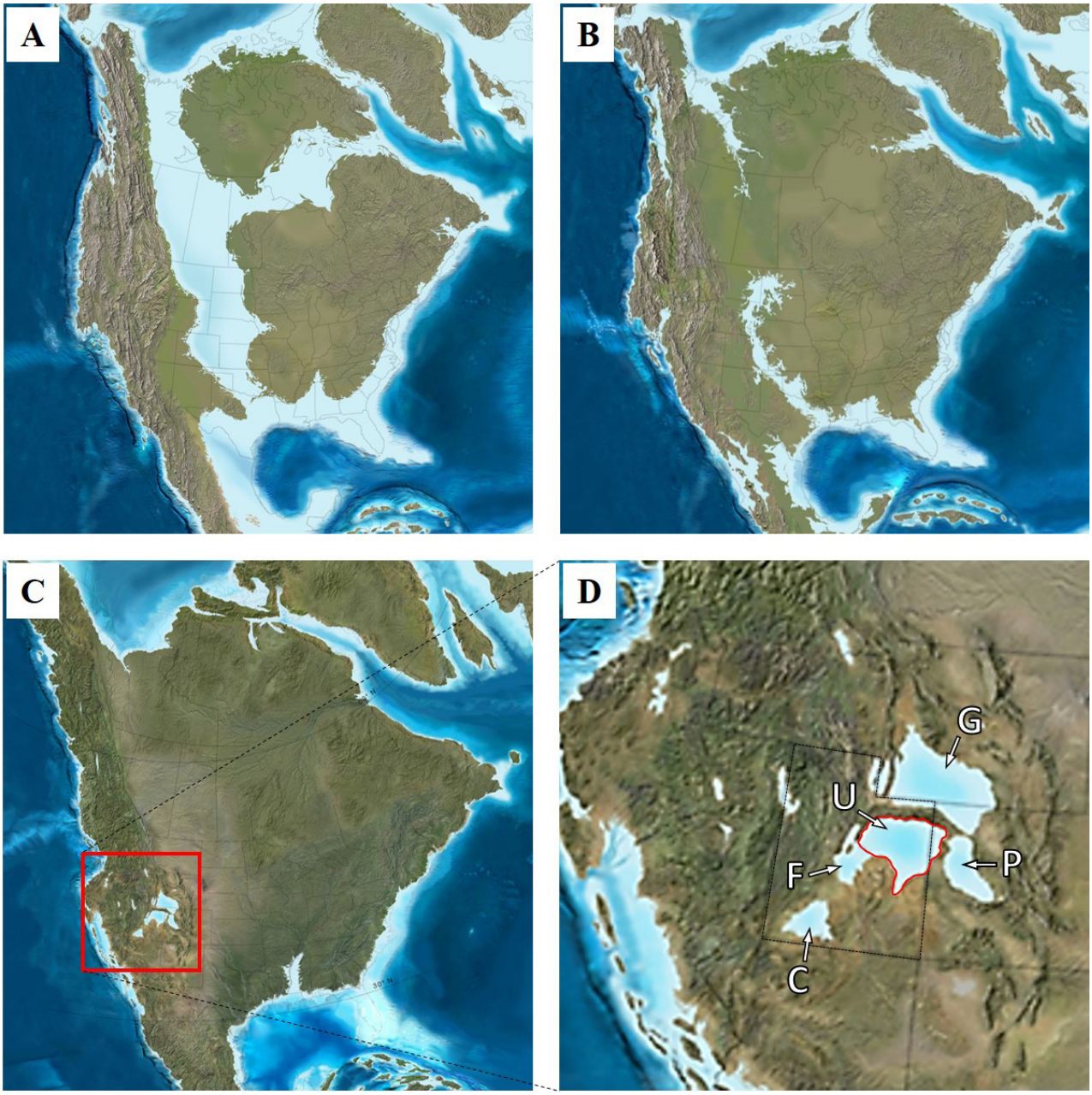

Figure 2.1. *Paleogeographic evolution of North America during the Laramide Orogeny.* ***A.*** *Late Cretaceous.* ***B.*** *Early Paleocene.* ***C.*** *and* ***D.*** *Early Eocene: Intermountain and coexisting lacustrine basins. (D) Enlargement of (C) showing the Greater Green River Basin (Lake Gosiute) (G), Uinta Basin (Lake Uinta, outlined in red) (U), and Piceance Basin (Lake Uinta) (P). Images retrieved from R. Blakey website: http://deeptimemaps.com/north-american-key-time-slices-series/.*

Based on the lithologic characteristics and facies associations, sedimentation in Lake Uinta during deposition of the UBm was controlled mainly by periodic fluctuations of the lake water level and a balance between accommodation space and sediment infill. The UBm is characterized by shallowing upward sequences defined by organic-rich shale, molluscan limestone and coquina, and dolomudstone to ooidal dolograinstone, which likely represent deposition in high-frequency flooding and dry cycles. Therefore, as defined by Carroll and Bohacs' (1999) lakes classification, deposition of the UBm most likely took place in the overfilled or balanced-fill lake types.

2.4 Stratigraphy

The GRF is conformably bounded at the base by the late Paleocene to early Eocene fluvial Wasatch/Colton Formation (Roehler, 1991) and is overlain by the Uinta Formation, which represents the fluvial-volcaniclastic sediments that eventually filled Lake

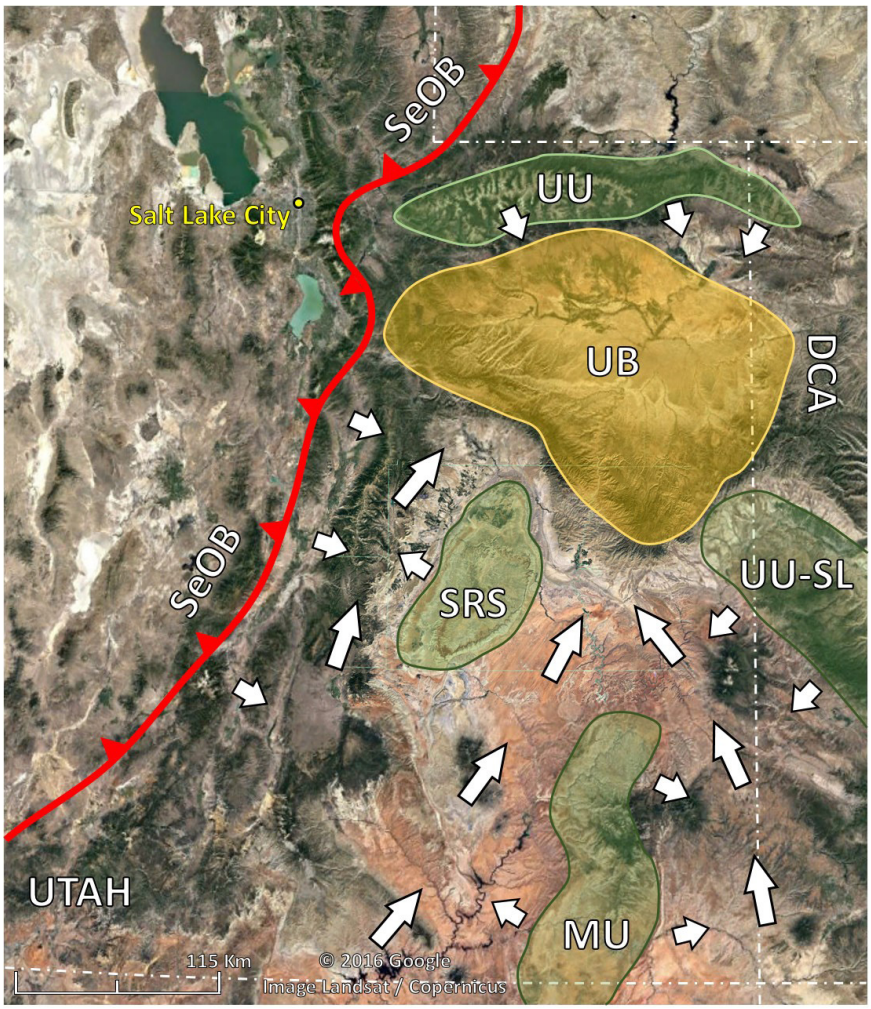

Figure 2.2. *Paleogeographic location of the Uinta Basin and surrounding uplifts. Arrows represent potential paleocurrents that likely fed Lake Uinta. UB - Uinta Basin (Foreman and others, 2012; Vanden Berg and others, 2014), UP - Uinta Uplift (Baars and Stevenson, 1981; Foreman and others, 2012), UU–SL - Uncompahgre Uplift (Sweet and Soreghan, 2012) – San Luis Mountains (Kluth, 1986), MU - Monument Upwarp (Hintze and others, 2000), SRS - San Rafael Swell (Doelling, 2002), SeOB - Sevier Orogenic Belt (Hintze and others, 2000).*

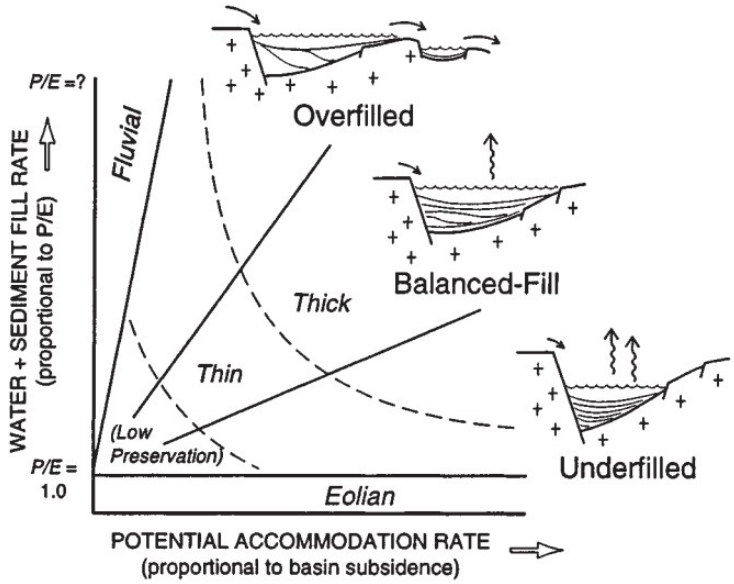

Figure 2.3. *Schematic representation of lake types according to sediment and water supply (controlled by climate) versus accommodation rate (controlled by tectonism) (Carroll and Bohacs, 1999).*

Uinta. The age of deposition is ca. 54 to 45 Ma (Smith, 2007) corresponding to the early and middle Eocene epoch (Eugster and Surdam, 1973; Ryder and others, 1976; Johnson, 1985). The GRF varies in thickness from about 7200 ft in the central to northwestern area of the Uinta Basin to about 1950 ft in the southeastern area (Schamel, 2015).

The Uteland Butte is the basal member of the GRF in the Uinta Basin (Cashion, 1967; Davis and others, 2009; Johnson and others, 2016). Its thickness varies according to its location within the Uinta Basin—it is about 390 ft thickest at the lake's paleodepocenter in the north, close to the Uinta Uplift, and thins to about 49 ft in the southeast (Johnson and others, 2016). The age of deposition for the UBm is estimated as 54 to 52 Ma based on paleontological evidence (Remy, 1992). Moreover, using $^{40}Ar/^{39}Ar$ radiometric dating of sanidine and biotite crystals deposited within the Leavitt Creek and Tabernacle Butte tuffs (Parachute Member), Smith (2007) arrived at 53 to 52 Ma for the UBm.

The GRF was first divided into four members (from top to base) by Bradley (1931) as follows: (1) Douglas Creek, (2) Garden Gulch, (3) Parachute Creek, and (4) Evacuation Creek. Since then, several other authors have provided different andoverlapping subdivisions for the GRF. Morgan and Bereskin (2003) define the UBm at the base of the GRF. Logan and others (2016) summarized the stratigraphic nomenclature of the GRF based on previous studies. In this project, the stratigraphic nomenclature of Logan and others (2016) will be used, as shown in figure 1.3.

2.5 Facies and Depositional Environments

The lithofacies of the UBm generally consists of interbedded limestone, dolostone, calcareous mudstone, siltstone, and some sandstone. The main allochem particles in the limestone are ostracods, ooids, fresh water molluscs (disarticulated pelecypods or tubiform gastropods), algae, fish fragments, peloids, and intraclasts (Morgan and Bereskin, 2003; Bereskin and others, 2004). Bereskin and others (2004) interpreted the GRF as deposits from two main environments: (1) marginal lacustrine carbonate mudflat, deltaic, and inter-deltaic environments; and (2) open, deeper lacustrine facies. Similarly, Ryder and others (1976) identified three main environments: (1) open lacustrine; (2) marginal lacustrine deltaic and inter-deltaic mudflats and paludal; and (3) alluvial deltaic plain, high mudflat, and alluvial fan, based on outcrop observations and well logs from the lower section of the GRF. In outcrops located in the southern margin of the Uinta Basin, Long (2006) identified cyclic intercalations of massive biomicrites with ostracods, gastropods, bivalves, and charophytes at the base, dark organic-rich micrites with nodules in the middle, then grading into shale toward the top. Most recently, based on outcrops and cores located on the far east side of the basin, Logan and others (2016) described the UBm as intercalations of grey to green siltstone, dolomudstone to dolograinstone with abundant peloids, ostracods, and rock fragments, molluscan lime wackestone to mudstone, sandstone, coal seams, and oil shale. Logan and others (2016) interpreted the depositional environments of the UBm as a fresh water ramp margin with minor influence of fluvial systems, based on the absence of stromatolites, lack of evaporite minerals, and abundance of bivalves, gastropods, and ostracods within the limestone beds.

CHAPTER 3 METHODOLOGY

This study investigates the depositional, diagenetic, and geochemical characteristics of the dolomite layers of the UBm to better understand the overall dolomitization processes. This study employed a wide variety of investigative methods including: 1) outcrop and core descriptions; 2) petrographic analysis by means of transmitted light and cathodoluminescence microscopy; 3) scanning electron microscopy (SEM); 4) mineralogical identification via semi-quantitative major element analysis and ordering of dolomites through X-ray diffractometry (XRD); 5) elemental composition by X-ray spectrometry (EDS coupled with SEM); 6) electron microprobe analysis (EPMA); 7) trace element analysis using inductively coupled plasma mass spectrometry (ICP-MS); and 8) conventional and clumped oxygen and carbon stable isotope analysis. In addition, a few extant data (such as ROCK-EVAL and porosity/permeability core plug data) were incorporated in the discussion and interpretation. The methodology of acquisition and reliability of this data is not further discussed here but can be found in the respective cited sources.

3.1 Field Work: Outcrops

Two UBm outcrops were studied in the spring of 2015 and are located in the southwestern part of the Uinta Basin: Nine Mile Canyon and Willow Creek Canyon (figure 1.2). A stratigraphic column was drafted for each outcrop area based on centimetre-scale descriptions of lithology, fossils, sedimentary structures, and contact types. The Willow Creek Canyon section covers a thickness of 175.7 ft and contains the entire UBm. The Nine Mile Canyon section covers a thickness of 34.6 ft and includes only the upper portion of the UBm (appendix A). Table 3.1 contains detailed location information for each outcrop section.

Table 3.1. *Detailed location, operator, and core location of selected wells and outcrops used in this research.*

Code	Operator at time of drilling	Well/Outcrop name	Well/Outcrop location	Current location of core
BBC 14-1	Bill Barrett Corp.	14-1-46	N 40° 9' 26.5" W 110° 30' 48.1"	Utah Core Research Center, Salt Lake City
BBC 14-3	Bill Barrett Corp.	14-3-45	N 40° 9' 23.7" W 110° 26' 17.4"	Utah Core Research Center, Salt Lake City
N 6-28	Newfield	Nickerson 6-28-3-2W	N 40° 11' 40.8" W 110° 7' 1.6"	Newfield facility in Houston
UT 15-13	Newfield	Ute Tribal 15-13-4-3W	N 40° 7' 45.5" W 110° 10' 7.9"	Newfield facility in Houston
PW 13-06	EOG Resources	Petes Wash 13-06 GR	N 39° 58' 44.1" W 110° 10' 7.2"	Utah Core Research Center, Salt Lake City
DS 11-20	Chandler	West Desert Spring 11-20-10-17	N 39° 55' 39.0" W 110° 1' 54.2"	Utah Core Research Center, Salt Lake City
IU 16	Wexpro	Island Unit 16	N 39° 57' 24.2" W 109° 51' 49.8"	Utah Core Research Center, Salt Lake City
WCC		Willow Creek Canyon	N 39° 50' 17.2" W 110° 47' 3.3"	
NMC		Nine Mile Canyon	N 39° 46' 35.5" W 110° 28' 58.5"	

3.2 Core Description and Sampling

Core selection was based on three main features: well location, recovery of the UBm, and core accessibility. The selected cores were those that cover the interval of interest (excluding the BBC 14-3-45 well that only captured the PZ1 dolomite layer) and located in the west-central area of the Uinta Basin. These cores vary from proximal (south) to distal (north) depositional environments and incorporate geologic characteristics of the basin center not exposed in outcrop.

The cores, housed at the Utah Geological Survey (UGS) in Salt Lake City (UT), were first logged at centimetre-scale and sampled from November 11th to 14th, 2014. The remainder of the cores were in a private storage facility in Denver, CO, and were logged from February 15th to 20th, 2015.

The fundamental criteria for sampling was the ability to cover all of the dolomite layers PZ2, PZ1′, and PZ1 from base to top. In addition, interbedded layers of limestone and dolostone below, between, and above the three layers of interest were also sampled, but with less coverage. A total of 167 samples were taken from the cores for further analysis. Stratigraphic columns were made for each studied core (appendix B) and described according to previous criteria.

In addition to the outcrops and core information, extant data were used in this research, such as porosity and permeability values measured from core plugs by Core Laboratories Company (USA). The data is described in Chapter 5, Sections 5.3 and 5.4.

3.3 Petrography

3.3.1 Transmitted Light Microscopy

A total of 140 polished thin sections were investigated using a Zeiss Jenapol Polarizing Microscope under 3.2X, 10X, and 20X magnifications. All thin sections were partially stained, for easier determination of calcite versus dolomite mineralogy, by dipping them halfway into a solution of 1.5% HCl acid plus 0.2 grams (g) of Alizarin red solution plus 2.0 g of potassium ferricyanide, following a procedure proposed by Dickson (1965). Detailed descriptions were generated for each thin section using rock classifications of Dunham (1962), with modifications by Embry and Klovan (1971), and focused on mineralogi-

cal composition as well as identification of bioclasts, coated grains, sedimentary structures, and bioturbation (appendix C). In addition, the carbonate grains were classified according to Flügel (2010) and semi-quantitative estimates of matrix, carbonate grains, and siliciclastic material were made using charts by Baccelle and Bosellini (1965).

3.3.2 Cathodoluminescence Microscopy

Cathodoluminescence microscopy was performed using an Olympus BH-2 microscope coupled with a cold cathode Premier American Technologies Luminoscope Model ELM-3R. Each thin section was placed in the sample vacuum chamber with an appoximate pressure of 0.07 Torr, and subsequently irradiated by an electron beam with a voltage of 10-15 kV and a current of about 0.5 mA. Luminescent images were recorded using a digital camera Pentax K-5.

Twenty-one thin sections from the PZ2, PZ1′, PZ1 dolomite layers were selected from four wells: N 6-28, UT15-13, PW 13-06 GR, and IU 16, which are located along a traverse that encompasses distal (north) to proximal (south) portions of ancient Lake Uinta (figure 1.2).

3.3.3 Scanning Electron Microscopy (SEM)

A total of ten polished thin sections were selected for SEM petrography and energy dispersive X-ray spectroscopy (EDS) analysis (appendix D). All samples were coated with a carbon film to improve conductivity and thus image resolution. A Zeiss EVO LS15 EP equipped with a 25.0 kV electron beam was used in the SEM laboratory at the Department of Earth and Atmospheric Sciences (EAS Department), University of Alberta.

3.4 X-Ray Diffractometry

A total of 76 powder samples were analyzed in the X-ray diffractometry laboratory, EAS Department, University of Alberta. Samples were powdered using a low speed micro-drill with tungsten carbide and diamond bits. Approximately 1 g of each sample was mixed with an internal quartz standard, then mounted on a zero-background plate. The equipment used was an Ultima IV Rigaku X-ray Diffractometer, which uses a cobalt tube with a radiation wavelength (λ) value of 1.78899Å, run at 40 kV and 35 mA. All scans were run from 2° to 100° 2θ, using a 0.02° 2θ step size with a scan speed of 2° 2θ per minute. The resulting peaks were then corrected with the quartz internal standard *d*101 peak (31.035° 2θ). Identification of minerals was done by Jade 9 software. The results are tabulated in appendix E.

As part of collaborative work, a total of 21 powdered samples were analyzed at the X-ray diffractometry laboratory in the EAS Department at Indiana University Bloomington (USA), and a total of 47 powdered samples were analyzed at the X-ray diffractometry laboratory in the Department of Geosciences at Western Michigan University (USA). All powders were acquired using a low speed micro-drill with tungsten carbide and diamond bits. The equipment used at the Indiana University laboratory was a Bruker D8 X-ray Diffractometer, which uses a copper tube with a radiation wavelength (λ) value of 1.540562 Å, run at 45 kV and 35 mA. All scans were run from 2° to 70° 2θ, using a 0.02° 2θ step size with a step time of 0.6° 2θ per minute. The equipment used at the Western Michigan University laboratory was a second-generation Bruker D2 Phaser X-ray Diffractometer, which uses a copper tube with a radiation wavelength (λ) value of 1.54 Å. All scans were run from 20° to 60° 2θ, using a 0.008° 2θ step size with a step time of 0.48°2θ per minute. Results are presented in appendix E.

3.5 Major and Trace Elements Analysis

3.5.1 Electron Microprobe Analysis (EMPA)

Given the aphanocrystalline size of dolomite crystals identified with SEM (see detailed explanation in Chapter 5, Section 5.2.1.1), electron microprobe analysis was selected to obtain quantitative dolomite chemical values.

A total of four highly polished thin sections of PZ2, PZ1′, and PZ1 were analysed using the Electron Micro Probe Cameca SX100 equipped with a five wavelength-dispersive spectrometer (WDS) of the Electron Microprobe Laboratory, EAS Department, University of Alberta. Operating conditions were: 40° takeoff angle; beam energy of 15 keV; 20 nA beam current; and 3 μm beam diameter. Prior to analysis, each thin section was coated with carbon film to enhance conductivity over the polished thin section surface. For data corrections, a series of standard measurements (dolomite, siderite, strontianite, and K-253 NIST RM glass) were conducted before the analysis. The results are summarized in appendix F.

3.5.2 Inductively Coupled Plasma Mass Spectrometry (ICP-MS) Analysis

A total of 50 samples from the PZ2, PZ1′, and PZ1 dolostones and interbedded limestones were analyzed for major and trace element concentrations in the Canadian Centre for Isotopic Microanalysis laboratory at the University of Alberta. The measurements were carried out using a Perkin-Elmer Elan 6000 Inductively Coupled Plasma–Mass Spectrometer (ICP-MS) with a cross-flow nebulizer, a 40 MHz RF-generator, with a working power between 600 and 1600 W.

Powdered samples of 200 mg were digested overnight in 10 ml of nitric acid 8N. After digestion, solid and liquid phases were separated by centrifuge. Concentrations were determined for 10 elements: Mg, Ca, Al, Si, Fe, Mn, Na, Zn, Sr, and Pb. The results are presented in appendix G.

3.6 Stable Isotope Analysis

3.6.1 Conventional Carbon and Oxygen Stable Isotope Analysis

A total of 74 samples were selected for conventional carbon and oxygen stable isotope analysis, including 12 samples from PZ2, 9 from PZ1′, and 18 from PZ1. The rest of the samples are from interbedded layers of limestone and dolostones below, between, and above the three layers of interest. All samples were analyzed in the Isotope Science Laboratory at the University of Calgary. Calcite and dolomite were analyzed by a continuous flow isotope ratio mass spectrometry (CF-IRMS) using a Thermo Finnigan GasBench coupled to a DeltaV^{Plus}. The samples were acquired using a low speed micro-drill with tungsten carbide and diamond bits. A powdered sample of approximately 300 µg was then weighted into a vial and approximately 200 µl of anhydrous phosphoric acid was added for digestion at 25°C for a specific time. The evolved CO_2 was then sampled automatically by the Gas Bench and introduced into the DeltaV^{Plus} stable isotope ratio mass spectrometer for analysis of $\delta^{13}C$ and $\delta^{18}O$ ratios (Applied Geochemistry Group, 2014).

Since previous XRD analyses revealed that many samples contain variable mixtures of calcite and dolomite (with generally very minor contributions of quartz and silicates), the bimineralic carbonate samples were subjected to a selective chemical separation as follows: first, an aliquot of CO_2 was sampled at variable times of about 2–8 hours and deemed to represent calcite only; a second aliquot of CO_2 was retrieved after about 72 hours, at which time all carbonates had been digested, and deemed to represent dolomite. Unexpectedly, and unfortunately, it turned out that the first aliquot also contained some CO_2 from dolomite (further discussed below). Internal lab reference materials were run at the beginning and the end of each set of samples (nine samples per set) and were used to normalize the data and to correct any equipment deviation. All results are reported in the per mill notation (‰) relative to the international VPDB scale for $\delta^{13}C$ and $\delta^{18}O$ (Applied Geochemistry Group, 2014).

While it is common practice in stable isotope research to separate calcite and dolomite through differential phosphoric acid digestion, commonly 1 to 2 hours for calcite and >8 to 12 hours for dolomite (McCrea, 1950; Degens and Epstein, 1964; Walters and others, 1972; Al-Aasm and others, 1990; Swart and others, 1991; Ray and Ramesh, 1998), these acid digestion times could not be used in our work due to the automated system in operation at the University of Calgary. Therefore, the maximum acid digestion time (hours) was exceeded, which resulted in a variable amount of dolomite dissolved along with the calcite (to produce the first aliquot of CO_2, as described previously). Therefore, many isotopic values from bimineralic carbonate samples, and initially deemed to be valid for calcite, are not trustworthy.

The problem was identified by comparing the calcite/dolomite ratios determined by XRD with the calcite/dolomite ratios determined by the amounts of CO_2 of the first and second aliquots. Once this problem was identified many of the samples previously deemed to represent calcite were excluded from the data analysis and/or flagged as calcite-dolomite mixtures. The only values deemed to reliably represent calcite are those that fulfill the following requirements: (1) monomineralic calcite samples (100% calcite), and (2) samples with calcite/dolomite ratios less than 5% (maximum error allowed) based on XRD data. Moreover, samples with >5% dolomite also contain a minor amount of quartz, illite, albite, and/or muscovite. Therefore, dolomite contamination is considered negligible. The results are presented in appendix H.

3.6.2 Clumped Isotopes

The clumped isotope technique was applied to a small subset of samples because it allows for estimation of the temperature of carbonate mineral formation regardless of fluid chemical composition (Ghosh and others, 2006; Eiler, 2007). The relation between ^{13}C and ^{18}O in dolomite crystals is totally independent of the isotopic composition from dolomite precursor fluid (Ghosh and others, 2006; Millán and others, 2016).

A total of 26 samples from the PZ2, PZ1′, and PZ1 dolostones, as well as the interbedded limestones (splits of the powdered samples previously drilled for XRD and conventional isotope analysis), were selected to be run on a collaborative basis at the Department of Earth Sciences at Swiss Federal Institute of Technology (Switzerland). The analytical procedure is described in Millán and others (2016). At the time of this writing, only a small subset of these 26 samples had been run with an insufficient number of duplicate and re-runs. Hence, the data presented in this research are considered preliminary and not sufficiently verified.

CHAPTER 4 FACIES

The facies deposited in lake basins are controlled by a number of independent and partially interdependent external factors such as drainage area, type of surrounding rock outcrop, topography, tectonism, and climate, as well as internal agents such as oxygen availability, nutrients, water chemistry, etc. (Barron, 1990; Gierlowski-Kordesch, 2010). In some cases, even small changes in these factors can impact depositional environments creating disproportionate variations in lateral and vertical facies architecture. Conversely, changes in facies allow, within limits, conclusions about the internal and external agents.

Facies types were identified and characterized using outcrop, core, and thin section descriptions from the stratigraphic interval between the D and C shales, located in the middle section of the UBm at the base of the GRF. These facies types were identified based on detailed and systematic descriptions of: (1) depositional rock textures: rock type, grain size, sorting, and packing; (2) bioclasts; (3) other carbonate grains: coated grains, peloids, and intraclasts; (4) sedimentary structures: stratification, bedding, laminations, and bioturbation; and (5) siliciclastic material. The facies were numbered from 1 to 10 in the order of overall shallowing depositional environments (table 4.1).

Logan and others (2016) defined a total of 18 lithofacies types, which are based on outcrops near the eastern margin of the Uinta Basin complemented by core from central Uintah County (central-east side of basin). Table 4.2 provides a correlation of facies types from Logan and others (2016) with those established in this study. Several facies types defined by Logan and others (2016) are not found in the central-west part of the basin because the east part of the basin contains more proximal facies, and because the stratigraphic interval of interest for this project is only a section of the entire UBm.

4.1 Lithofacies

This section provides descriptions and images of the most distinctive facies types encountered in the study area. Furthermore, this section offers an interpretation of the depositional environments based on described features. Diagenetic features are mostly excluded and were not considered in the interpretations of the depositional environments, unless these features appear to be integral parts of the depositional setting. For example, pyrite formed syndepositionally that indicates an anoxic depositional setting, or syndepositional length-slow chalcedony that suggests an evaporitic depositional setting. Dolomitization is also excluded.

4.1.1 Silty Mudstone - F1

The silty mudstone lithofacies (F1) is a finely laminated, black to dark gray, organic-rich silty mudstone with up to 10% quartz grains, which range from coarse to fine silt size and are subangular, poorly sorted, and erratically distributed (figure 4.1). Bioclasts are mostly thin, disarticulated ostracod shell fragments, many with preserved fish-hook shape terminations (Scholle and Ulmer-Scholle, 2003) that are 0.3 to 0.5 mm in length and aligned parallel to stratification. These shells form densely packed coquinas with thicknesses of 0.5 to 1 mm (figure 4.1B). These layers are interbedded with lean, organic-poor clay layers and laminae that appear light gray in hand specimens. Scarce dewatering structures truncate some laminations (figure 4.1C).

Depositional environment. Clay sized material was deposited in a low-energy setting below fair-weather wave base, probably in a distal sublittoral to profundal environment, allowing for accumulation of sediment from suspension. Preservation of organic matter (black area in thin section, figure 4.1B) and the absence of bioturbation suggest an anoxic depositional environment likely developed by thermal and/or chemical lake water stratification (Collinson, 1979; Long, 2006; Boehrer and Schultze, 2008; Tucker and Wright, 2009), whereby deposition of the organic-rich layers took place below the chemocline. On the other hand, the lean clay laminae likely represent periods of low organic matter production and/or vertical fluctuations of the chemocline paired with increased fresh water inflow via river(s).

Table 4.1. *Summary of lithofacies identified between the D and C shales.*

Facies #	Facies Name	Lithology	Bioclasts	Other Carbonate Grains	Sedimentary Structures	Clastic Material	Environment
1	Silty mudstone	Silty mudstone	Ostracod shell fragments	--	Planar parallel, wavy discontinuous	Clay	Distal sublittoral to profundal
2	Lime mudstone	Dolomudstone	Scarce ostracod shell fragments	Scarce peloids	Structureless	Coarse silt subangular quartz grains and clay	Distal littoral - sublittoral carbonate mud flats
3	Ostracod wackestone	Dolowackestone	Ostracod shells, scarce fish bones, and charophytes	Peloids	Massive, plane parallel	Scarce silt quartz grains	Littoral
4	Peloid wackestone-packstone	Silty dolowackestone-dolopackstone	Scarce ostracods and fish bones	Peloids	Wavy discontinuous, plane parallel	Coarse silt subangular quartz grains and clay	Littoral
5	Mollusc wackestone-floatstone	Wackestone-packstone	Pelecypods, gastropods, and ostracods	--	Massive	Scarce silt quartz grains	Littoral - sublittoral
6	Interclast grainstone-packstone	Dolograinstone-dolopackstone	Scarce ostracod shell fragments	Intraclasts	Structureless	--	Littoral shoreline
7	Ooid grainstone-packstone	Dolograinstone-dolopackstone	Ostracods and rare charophytes	Ooids, scarce peloids, oncoids, and intraclasts	Massive, cross lamination	--	Littoral shoreline
8	Ostracod grainstone-packstone	Dolograinstone-dolopackstone	Ostracods	Scarce ooids and peloids	Structureless, wavy discontinuous	Coarse silt subangular quartz grains and clay	Littoral near shore and shoreline
9	Brown claystone	Arenaceous claystone	Scarce ostracod shall fragments and fish bones	--	Plane parallel	Coarse silt rounded quartz grains	Distal littoral
10	Coal	Coal	Plant fragments	--	--	--	Supralittoral swamps

Table 4.2. *Lithofacies correlation between Logan and others (2016) and this project.*

This research		Logan and others (2016)	
Facies #	**Facies Name**	**Facies #**	**Facies Name**
1	Silty mudstone	**18**	Laminated silty oil shale
2	Lime mudstone	**17**	Argillaceous mudstone
3	Ostracod wackestone	**3**	Ostracod lime mudstone-wackestone
4	Peloid wackestone-packstone	**5**	Oolitic lime mudstone-wackestone
5	Mollusc wackestone-floatstone	**4**	Mulluscan lime wackestone-packstone
		11	Bioclastic lime floatstone to rudstone
6	Interclast grainstone-packstone	**6**	Intraclastic ostracod lime packstone-grainstone
7	Ooid grainstone-packstone	**9**	Oncolite-ooid lime packstone-grainstone
8	Ostracod grainstone-packstone	**7**	Ostracod lime packstone-grainstone
9	Brown claystone	--	--
10	Coal	**15**	Carbonaceous shale
--	--	**1**	Grey/green siltstone
--	--	**2**	Lime to dolomitic mudstone
--	--	**8**	Oolitic lime grainstone-packstone
--	--	**10**	Ooid-pisolite lime packstone-grainstone
--	--	**12**	Ostracod bearing sandstone
--	--	**13**	Structureless to laminated sandstone
--	--	**14**	Cross-stratified sandstone
--	--	**16**	Laminated illitic claystone

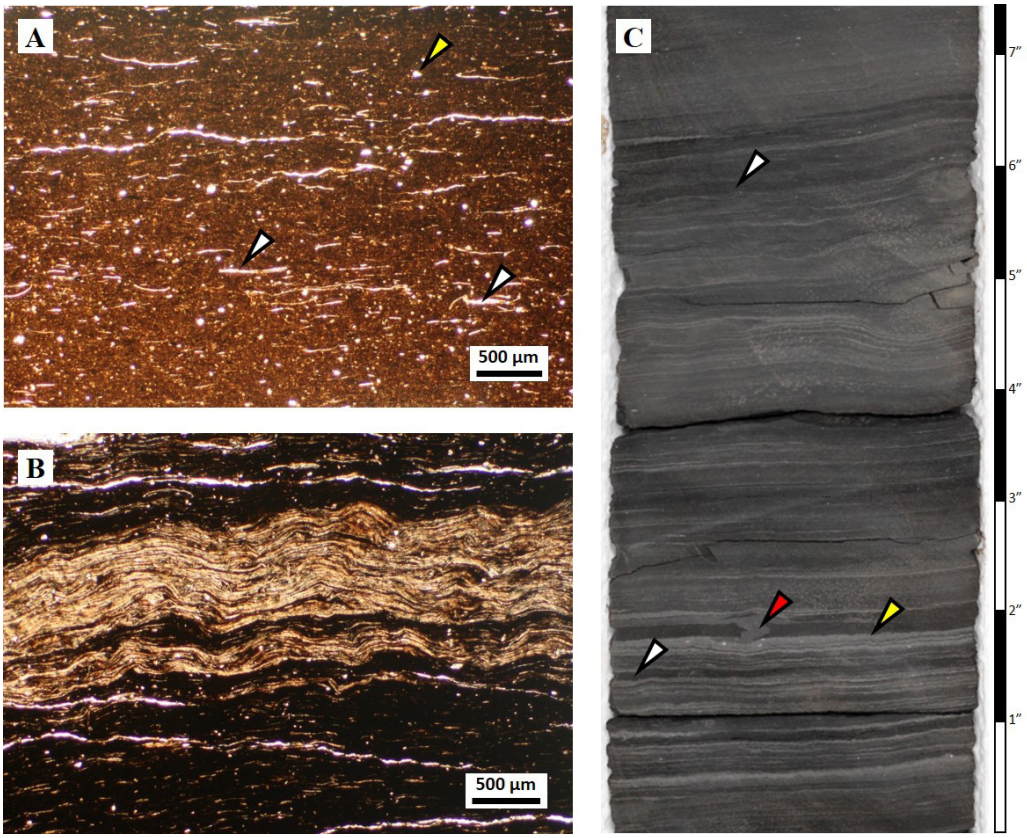

Figure 4.1. *Facies F1 – Silty mudstone.* ***A.*** *Transmitted light photomicrograph (TLP) of an organic poor bed with ostracod shell fragments (white arrows); aligned parallel to stratification (horizontal axis), silt material is mainly quartz (yellow arrow); well: BBC 14-1, sample 24, 6672.8 ft; plane polarized light (PPL).* ***B.*** *TLP of densely packed shell fragments (light yellow band) interbedded with organic-rich mudstone (dark areas); well: BBC 14-1, sample 7, 6705.3 ft; PPL.* ***C.*** *Core photograph of silty mudstone facies interbedded with organic-rich laminae (white arrow), densely packed shell laminae (yellow arrow), and organic-poor silt laminae (light gray), and dewatering structures (red arrow); well: BBC 14-1, 6705.3 ft to 6705.9 ft.*

4.1.2 Lime Mudstone – F2

The lime mudstone lithofacies (F2) is light brown, commonly homogeneous, microcrystalline dolomitized lime mudstone with ostracodal shell fragments and generally comprised of 3% clay minerals, and rounded, poorly sorted grains of quartz ranging from fine to medium silt (figure 4.2). Accessory minerals are microcrystalline pyrite (less than 3%), occasional authigenic, euhedral, prismatic, and microcrystalline quartz (less than 1%), and quartzine (length-slow chalcedony) crystals filling intraparticle pores. Bioclast content is low, generally less than 3%, and is mainly composed of articulated or fragmented calcite ostracod shells ranging in size from 0.05 to 0.2 mm (figure 4.2A). This facies shows massive to planar parallel stratification, and rare bioturbation structures are present in core. This facies is occasionally interbedded with thin laminae consisting of irregular or lenticular carbonate grains, such as peloids (likely steinkerns) and scarce ooids, that form lenses of peloidal grainstones (figure 4.2B).

Depositional environment. The microcrystalline matrix that makes up most of this facies type probably crystallized directly from lake water as lime mud suggesting a low energy setting. Furthermore, excellent preservation of disarticulated and unbroken ostracod shells (figure 4.2A) implies that the bioclasts were not transported, suggesting a low-energy environment with quiet water below the fair-weather wave base. Moreover, the low content of clays (≤ 3%) suggests a depositional environment located relatively far away from the source of siliciclastic fluvial input and/or represents times of significantly reduced influx from rivers. Peloidal grainstone lenses that interfinger with lime beds may indicate periods of mechanical reworking or storm events that disrupted the generally calm setting (figure 4.2B). The presence of quartzine likely represents brief periods of subaerial exposure and evaporation (further discussed in Chapters 5 and 6).

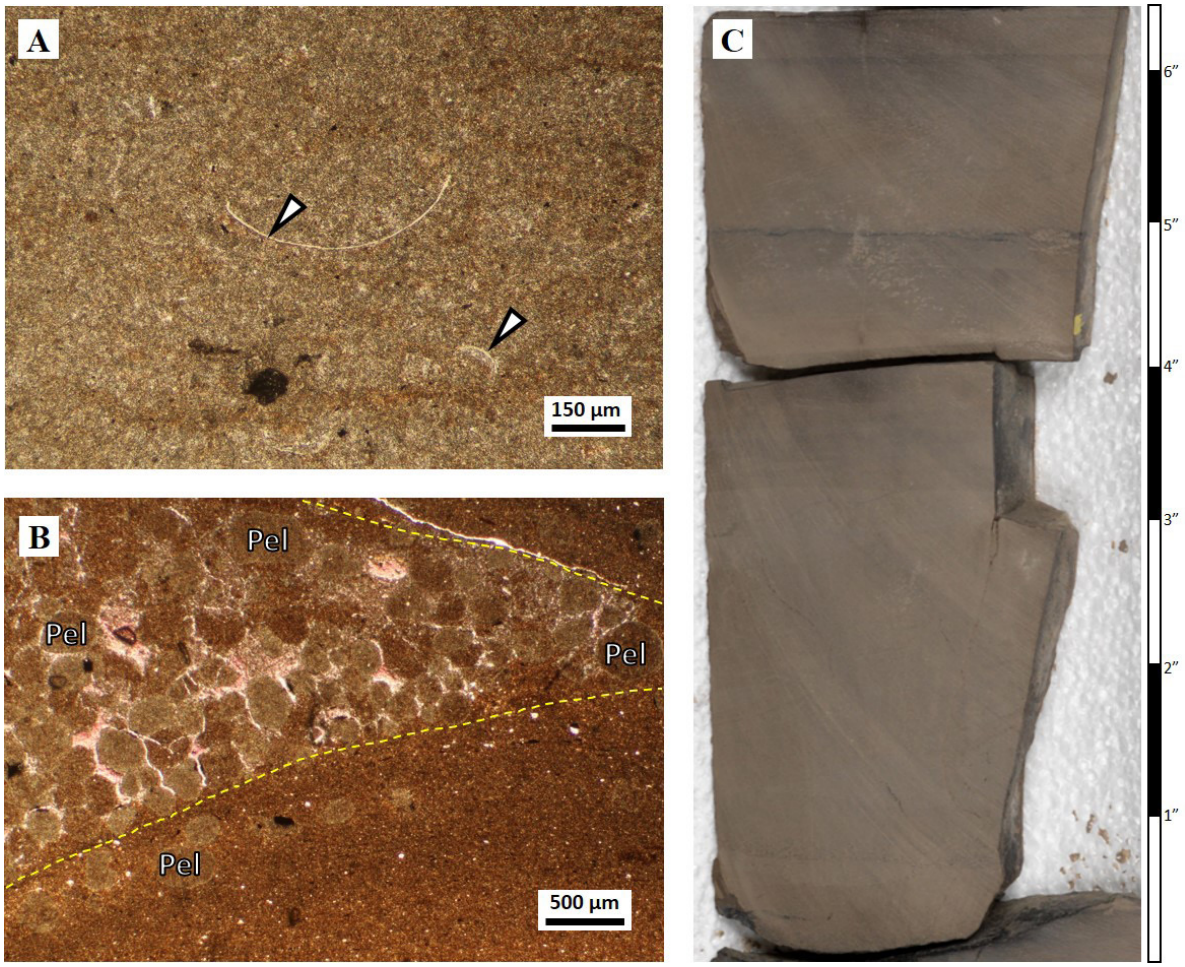

Figure 4.2. *Facies F2 – Lime mudstone.* ***A.*** *TLP of lime mudstone with scarce and well-preserved disarticulated ostracods shells (arrows); well: BBC 14-1, sample 17, 6692.6 ft; PPL.* ***B.*** *TLP of interbedded lenses (yellow dashed lines) of dolomitized peloids (Pel) embedded in microsparitic calcite cement (stained pink); bitumen (?) between peloids (dark areas); well: N-628, sample 3, 8205.6 ft; PPL.* ***C.*** *Core photograph of lime mudstone facies characterized by massive and planar stratification; well: BBC 14-1, 6702.7 ft to 6703.3 ft.*

4.1.3 Ostracod Wackestone – F3

The ostracod wackestone lithofacies (F3) is brown and composed of a microcrystalline matrix with <10 vol-% of siliciclastic material. Primary grains consist of disarticulated ostracod shells (figure 4.3A), but fish bones and elliptical gyrogonites [charophytes female reproduction organ (Flügel, 2010)] are minor to rare, and range in size from 0.02 to 0.05 mm (figure 4.3B). Dolomitized peloids are also relatively common and range from 0.01 to 0.05 mm in size. Stratification is mostly planar or slightly wavy, whereas some layers are bioturbated. Accessory minerals are microcrystalline pyrite (less than 1 vol-%) and scarce quartz grains. This facies hosts conspicuous chert nodules with irregular shapes and sizes, commonly with cm-dimensions and elongated parallel to bedding (figure 4.3C).

Depositional environment. The most important differences between facies F2 and F3 are the relative abundance of peloids and ostracods in facies F3, and the chert nodules that appear to be absent in facies F2. Again, the microcrystalline matrix that makes up most of facies F3 probably crystallized directly from lake water as lime mud. The setting is probably distal littoral below the fair-weather wave base. In-situ deposition of benthic ostracods (figure 4.3A) indicate an oxygenated environment. Furthermore, gyrogonites (figure 4.3B) also point to shallow water depths within a littoral setting (Håkanson and Jansson, 1983; Flügel, 2010), whereas the association of ostracods with charophytes (gyrogonites) suggests brackish lake water (Flügel, 2010). Chert nodules with quartzine suggests episodic evaporitic conditions (Folk and Pittman 1971; Pittman and Folk, 1971; Eugster and Hardie, 1978; Scholle and Ulmer-Scholle, 2003; Warren, 2006; Flügel, 2010). The chert nodules thus can be interpreted as an integral part of the depositional setting even though, in the strictest sense, they are a diagenetic feature (as is the dolomite that now makes up the matrix).

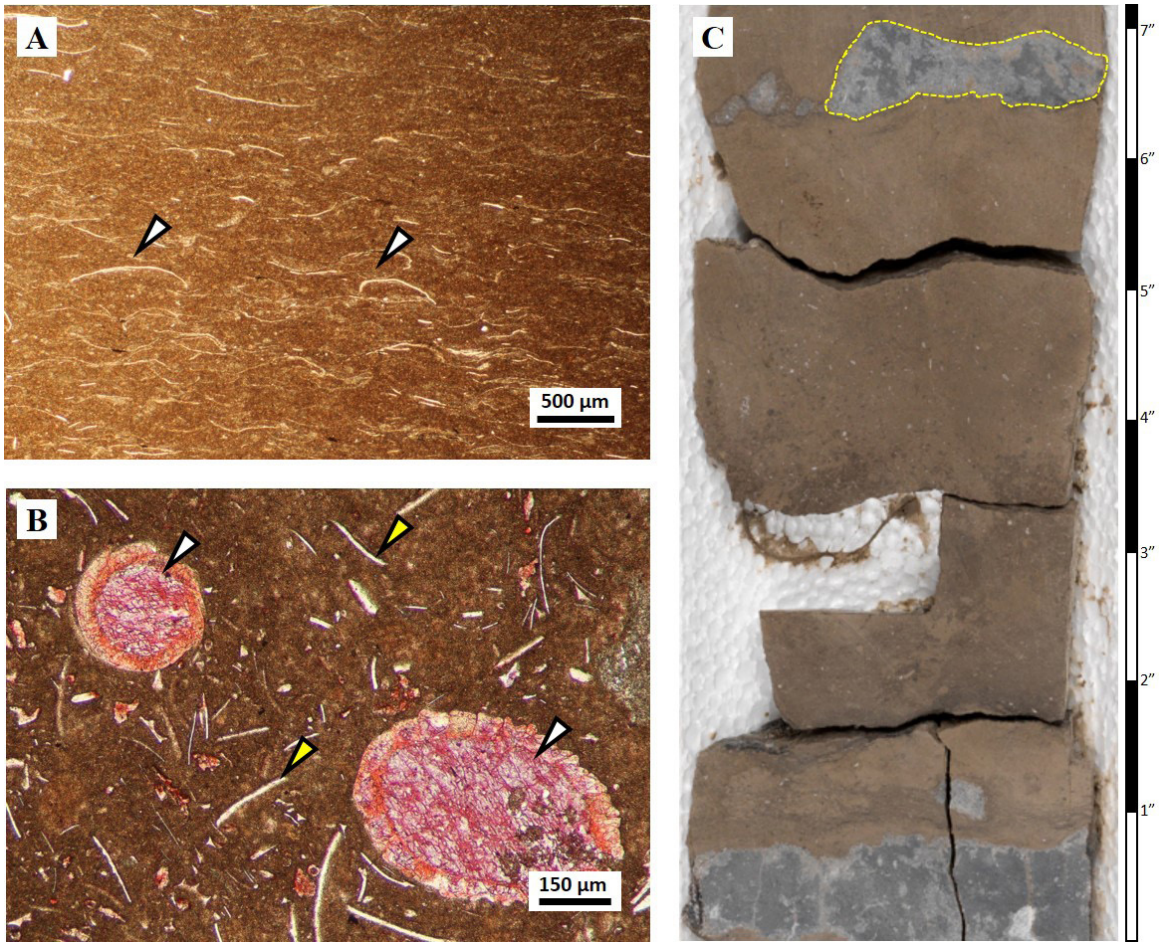

Figure 4.3. *Facies 3 – Ostracod wackestone-packstone.* ***A.*** *TLP of ostracod wackestone with disarticulated ostracods shells (arrows) aligned to bedding; well UT 15-13, sample 12, 7016.4 ft; PPL.* ***B.*** *TLP of gyrogonite (white arrows) associated with ostracod shell fragments (yellow arrows); well: 14-3, sample 27, 7373.65 ft; PPL.* ***C.*** *Core photograph of ostracod wackestone facies characterized by massive stratification and elongated chert nodules/bed (yellow dashed outline); well: BBC 14-1, 6685.3 ft to 6686 ft.*

4.1.4 Peloid Wackestone-Packstone – F4

The peloid wackestone-packstone lithofacies (F4) is light brown, consists of a dolomitized matrix, and contains less than 5% of well sorted silt-sized quartz grains. The most abundant carbonate grains are peloids that are light green to gray in color and elongated in shape, with a grain size from 0.05 to 1 mm (figure 4.4A and B). Bioclasts are mostly disarticulated and fragmented ostracod shells and fish bones. Euhedral, prismatic, and microcrystalline authigenic quartz is present as an accessory mineral. F4 hosts chert nodules with irregular shapes and sizes, commonly parallel to bedding. Pyrite is present as very fine scattered crystals. Frequent bioturbation structures are present in this facies.

Depositional environment. The most important differences between facies F3 and F4 are the lack of gyrogonites and the relative abundance of peloids in facies F4 (figure 4.4A and B). The occurrence of angular and dolomitized peloids suggests energy changes (such as storms), with the peloids being imported from different depositional settings within the lake. Laminae disrupted by bioturbation (figure 4.4A) suggests the lake bottom substrate was relatively oxygenated. Similar to F3, this facies presents scarce and scattered authigenic euhedral quartz suggesting evaporitic environments (Folk and Pittman, 1971; Folk and Siedlecka, 1974; Ulmer-Scholle and others, 1993; Flügel, 2010). The peloidal wackestone-packstone facies shares similar sedimentological features as the ostracod hosted wackestone-packstone facies (F3) deposited in the littoral zone above fair-weather wave base.

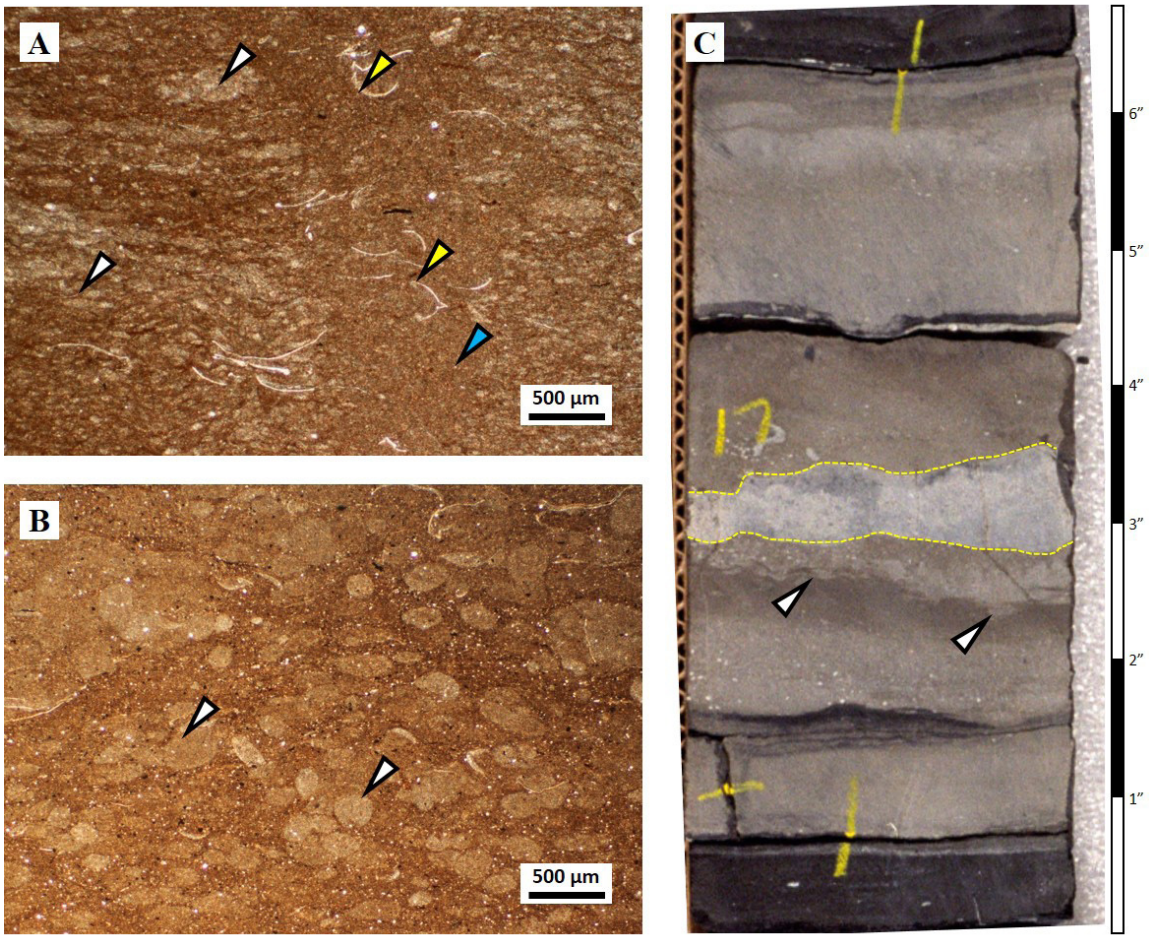

Figure 4.4. *Facies F4 – Peloidal wackestone-packstone.* ***A.*** *TLP of peloidal (white arrows) wackestone with scarce and disarticulated ostracods shells (yellow arrows); stratification disrupted by biological activity (blue arrow); well: N 6-28, sample 9, 8542.5 ft; PPL.* ***B.*** *TLP of peloids (arrows) within a microcrystalline dolomite matrix and clay material; well: UT 15-13, sample 13, 7017.4 ft; PPL.* ***C.*** *Core photograph of peloidal wackestone - packstone facies showing bioturbation structures (arrows) and chert nodule (yellow dashed outline); well: UT 15-13, 7017.1 ft to 7017.7 ft.*

4.1.5 Mollusc Wackestone-Floatstone – F5

The mollusc wackestone-floatstone lithofacies (F5) is light to dark gray with a micritic matrix. Bioclasts mainly consist of elongated and tubiform gastropods, centimeter-size pelecypods (0.1 to 3 cm), and ostracods shells that are typically disarticulated and aligned sub-parallel to bedding. Of them, gastropods are the most abundant fossil and seemingly larger than fragmented ostracod shells (figure 4.5A and B). In general, the bioclasts are well preserved and occur as dense thin layers of coquina interbedded with floatstone (figure 4.5C). Accessory minerals are microcrystalline pyrite and anhedral microcrystalline dolomite (less than 5%). Scarce quartz detritus particles (<3%) range from medium to very fine silt size and are poor to moderately sorted. Beds are typically structureless and usually have sharp, non-erosive contacts at the top. Partial silicification of gastropods and pelecypods is present in this facies (figure 4.6).

Depositional environment. F5 represents an environment that was subject to frequent changes in high to low energy on the basis of variable grain sizes and fossil indicators (figure 4.5). Lacustrine pelecypods and gastropods are usually distributed in nearshore or flood plain settings where high to low energy occurs (Cohen, 2003; Flügel, 2010). In contrast, microcrystalline calcite probably precipitated from lake waters during low energy times, as a product of biophysiochemical processes operating within the water column. Alternating couplets of mollusc wackestone and coquina layers (figure 4.5C; figure 4.6) implies rapid changes in lake water energy. The F5 facies was likely deposited in sublittoral to littoral environments with well oxygenated water above the storm-weather wave base. In addition, *Australorbis* and *Physa* gastropods (LaRocque, 1956) indicate fresh water conditions (Picard, 1955; LaRocque, 1956; Williamson and Picard, 1974).

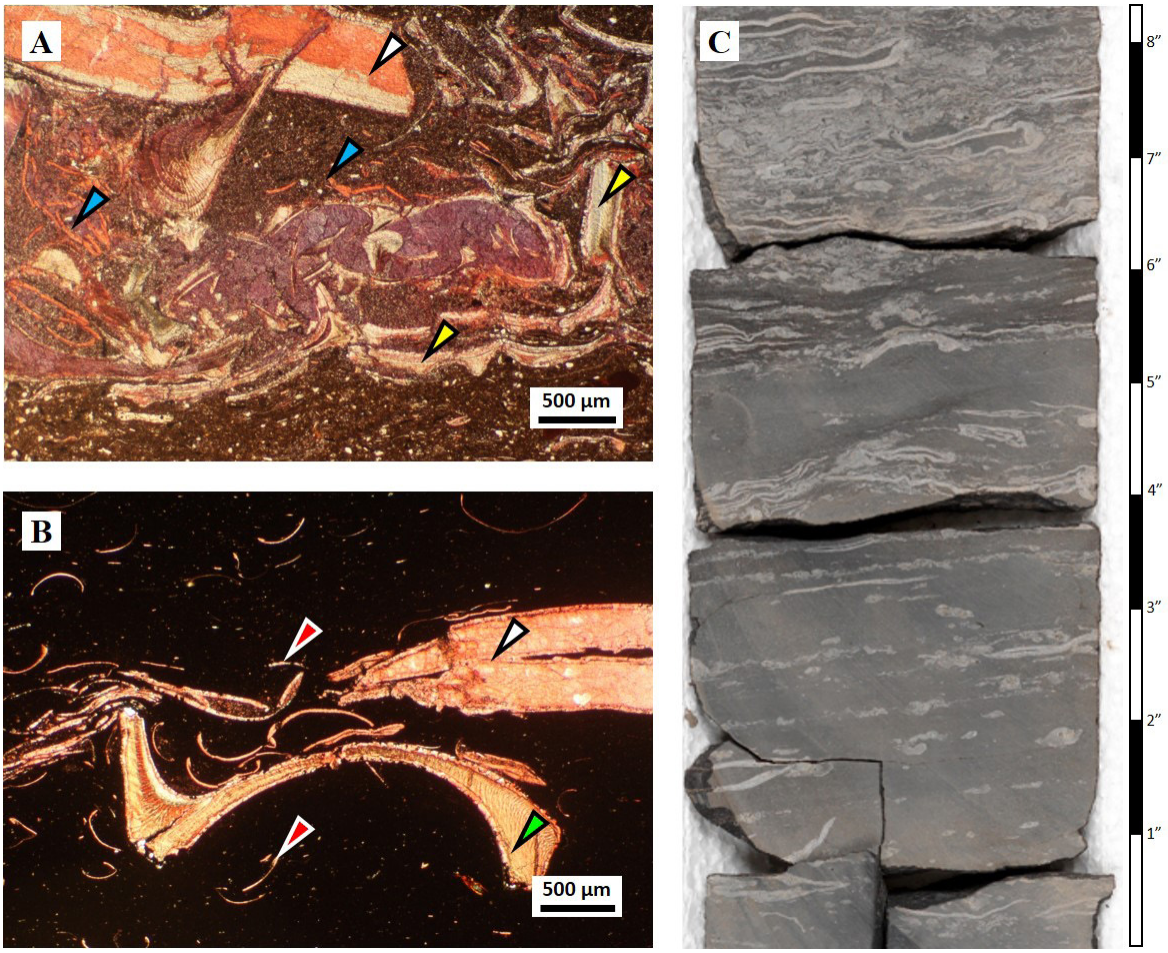

Figure 4.5. *Facies F5 – Molluscan bearing wackestone-floatstone.* ***A.*** *TLP of molluscan bearing floatstone with centimeter-size shells of pelecypods (white arrow), gastropods (yellow arrows), and disarticulated ostracods shells (blue arrows); well: PW 13-06, sample 5, 5537.3 ft; PPL.* ***B.*** *TLP of organic rich wackestone with pelecypods (white arrow), gastropods (green arrow); and ostracods (red arrows); black colour in matrix due to high organic matter content; well: N 6-28, sample 8, 8234.6 ft; PPL.* ***C.*** *Core photograph of interbedding coquina layer (at the top) with molluscan floatstone (at the base); well: BBC 14-1, 6696.1 ft to 6697.1 ft.*

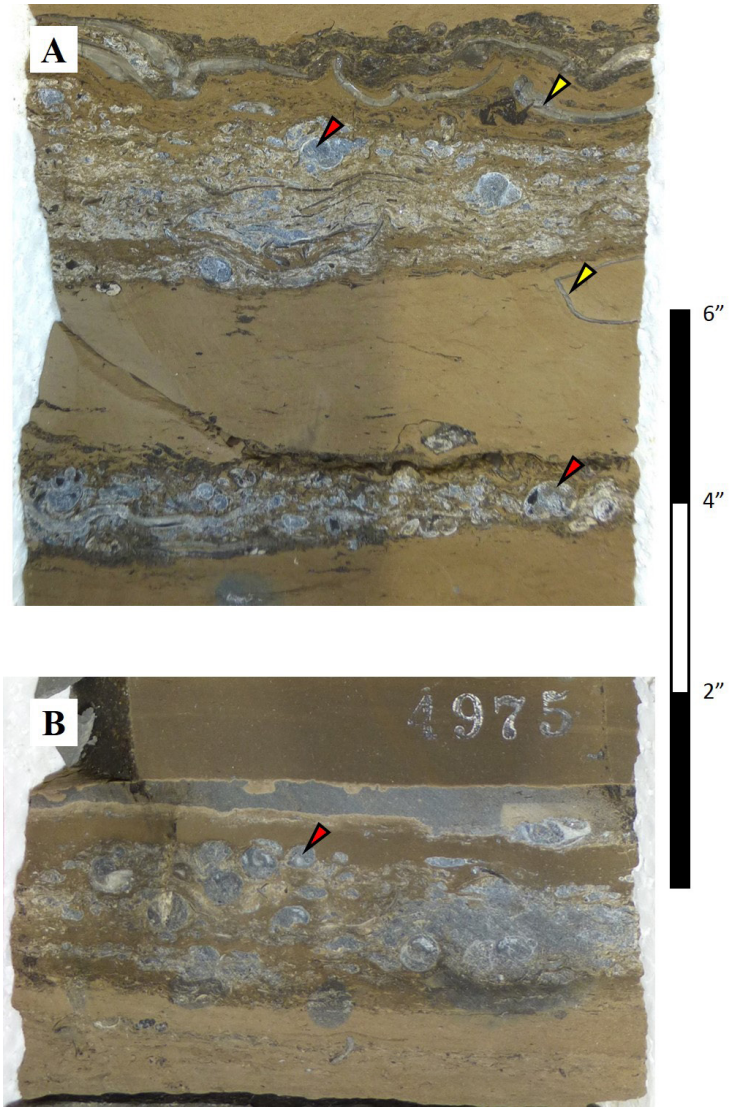

Figure 4.6. *Core photograph of molluscan limestone facies (F5) with partial silicification of gastropods (red arrows) and pelecypods (yellow arrows); well UT 11-20, depth:* ***A.*** *4974.2 to 4974.7 ft,* ***B.*** *4975 to 4975.3 ft.*

4.1.6 Intraclast Grainstone-Packstone – F6

The intraclast grainstone-packstone lithofacies (F6) is light brown and mainly comprised of dolomitic intraclasts and peloids, and minor ooids. Bioclasts are mainly ostracod shell fragments erratically distributed (figure 4.7A and B). Intraclasts are angular to well-rounded, poorly sorted, and particle size ranges from 0.2 mm to 10 mm. The intraclasts are composed of microcrystalline dolomite in the matrix and shells (likely ostracods). Furthermore, intraclasts show circum-granular cracks around irregular to globular particles of microcrystalline dolomite. The cracks are filled with blocky calcite cement (figure 4.7A). Peloids are composed exclusively of microcrystalline dolomite and display elongated shapes. Bioclasts are mainly disarticulated and fragmented ostracod shells (figure 4.7B). There are also rare silt-size quartz particles (1%).

Depositional environment. Rock texture and carbonate grain sizes (from 0.2 mm to 10 mm) are characteristics of a high energy environment. Intraclast particles have a different texture and color in comparison to the texture features of facies F6, which suggests deposition, dolomitization, and partial lithification took place in a different depositional setting, likely in the littoral to supralittoral environment. Moreover, intraclasts show pedogenesis features such as circum-granular cracks (figures 4.7A) that imply the intraclasts were exposed to eogenetic processes (Esteban and Klappa, 1983; Freytet and Verrecchia, 2002; Flügel, 2010). After exposure, the partially indurated sediments were ripped up and transported by storm events. Part of this material was subjected to reworking by wave action which caused them to evolve into well-rounded grains (figure 4.7B). Lithofacies F6 was probably located in nearshore areas influenced by wave action.

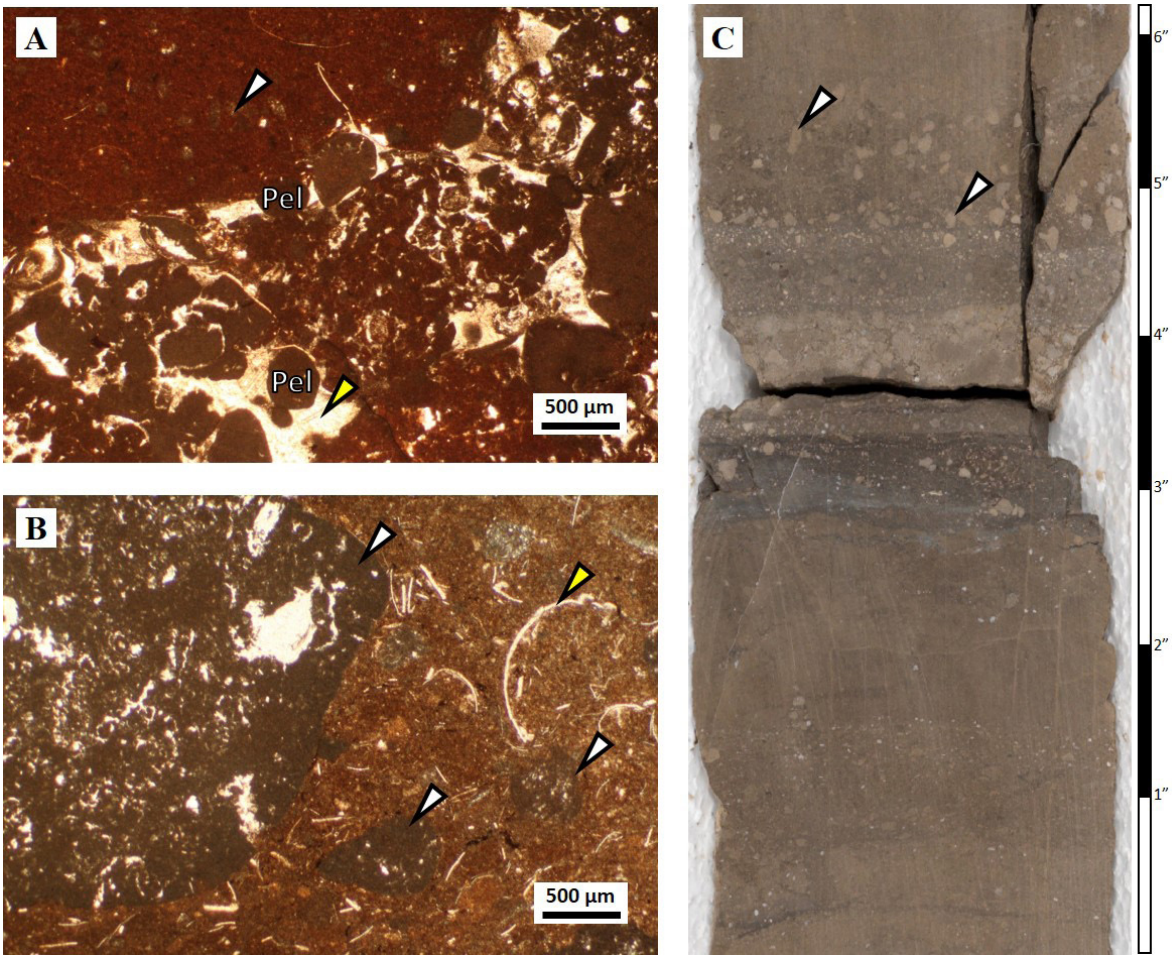

Figure 4.7. *Facies F6 – Intraclast peloid packstone-grainstone.* ***A.*** *TLP of centimeter-size dolomitized intraclasts (white arrow), peloids (Pel), and blocky calcite cement (yellow arrow); well: 14-1, sample 12, 6683.95 ft; PPL.* ***B.*** *TLP of well-rounded intraclasts (white arrows), ostracods shell fragments (yellow arrow) within a dolomitized matrix; well: BBC 14-1, sample 13, 6684.90 ft; PPL.* ***C.*** *Core photograph of intraclastic peloidal facies. Rip-up intraclast particles (white arrows) within a dolomitized micrite (?) matrix; well: BBC 14-1, 6684.9 ft to 6685.4 ft.*

4.1.7 Ooid Grainstone-Packstone – F7

The ooid grainstone-packstone lithofacies (F7) is dark brown and comprised of well-sorted and completely dolomitized ooids, peloids, and intraclasts, and rare (<2%) ostracod shells. Ooids show spherical to sub-spherical shapes with concentric layers of dolomitized micrite (figure 4.8A). Some ooids were altered by micritization (figure 4.8B). The core of ooids is composed of bioclasts (ostracod shell fragments), quartz particles, peloids, and intraclasts. Ooid size ranges from 0.2 to 1.5 mm. Accessory minerals are euhedral, microcrystalline, double-terminated, authigenic quartz and microcrystalline pyrite. F7 facies present massive stratification (figure 4.8C).

Depositional environment interpretation. The concentric and well-defined internal structure of the ooids (figures 4.8A and B) and lack of detrital grains suggest that the ooid grainstone-packstone facies (F7) was deposited in a high energy environment close to the shore area, influenced by wave agitation with low input of siliciclastic material and above the fair-weather wave base. Micritization of ooids may indicate that high microbial activity occured in the photic zone. Additionally, authigenic, euhedral and double-terminated quartz precipitation within interparticle pores indicate a probable saline environment (Flügel, 2010).

4.1.8 Ostracod Grainstone-Packstone – F8

The ostracod grainstone-packstone lithofacies (F8) is light brown with carbonate grains mainly of densely packed, articulated, and deformed ostracod shells (40–50%); subordanite dolomicrite pellets; and scarce peloids. The internal cavity of ostracods is typically filled with dolomitized micrite and pellets (?) (figure 4.9A). Some ostracods shells are micritized. Siliciclastic material

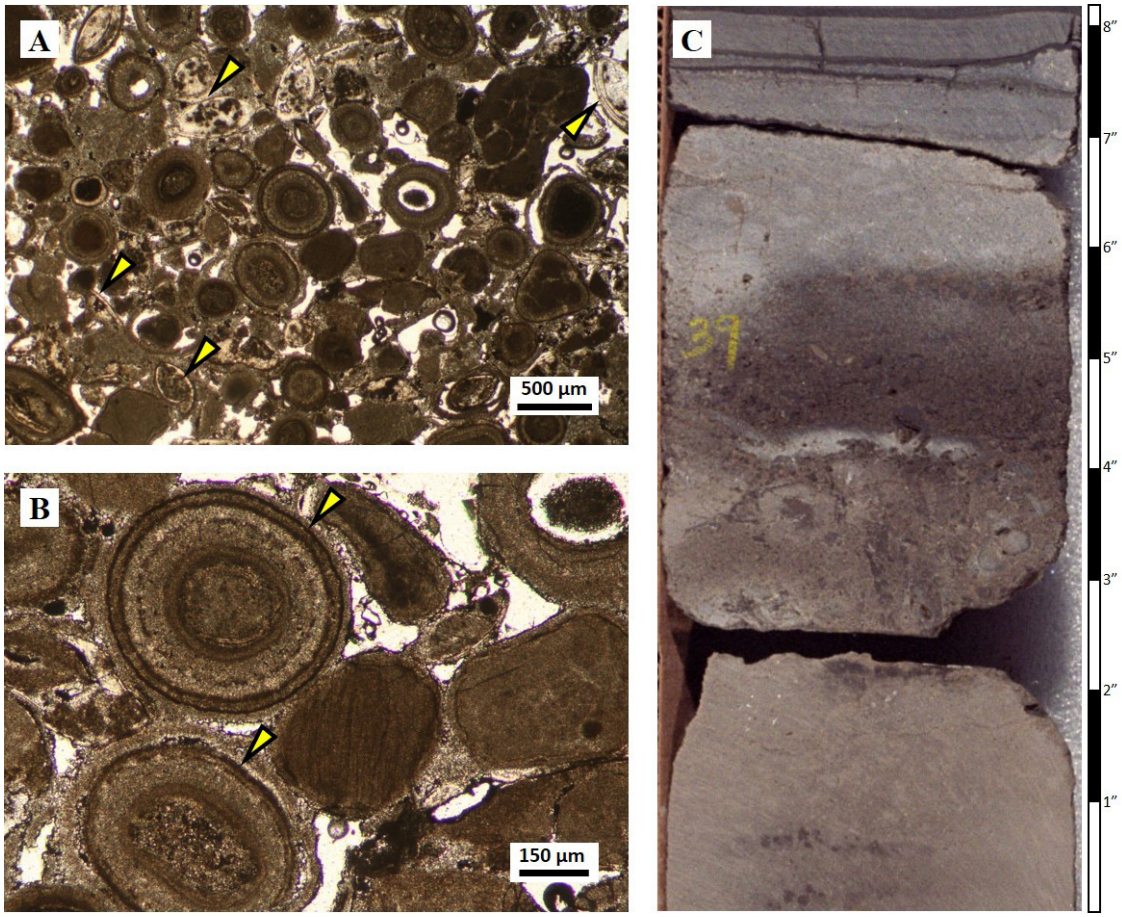

Figure 4.8. *Facies F7 – Ooid grainstone-packstone.* ***A.*** *TLP of ooid grainstone with ooids partially dissolved and scarce articulated ostracods shells (yellow arrows); well: PW 13-06, sample 6, 5539.5 ft; PPL.* ***B.*** *Detail of microphotograph (A) that shows micritization of ooids (yellow arrow). Note ooids are completely dolomitized; PPL.* ***C.*** *Core photograph of ooid grainstone facies with massive stratification; well: PW 13-06, 5539.25 ft to 5539.9 ft.*

is scarce (<2%) and consists of medium silt to very fine subangular quartz. Microcrystalline pyrite is present as an accessory mineral. Some layers host chert nodules, mainly composed of quartzine, that have elongated shapes and variable sizes, commonly with cm-dimensions, parallel to bedding (figure 4.9C). In core, F8 presents parallel and massive stratification.

Depositional environment. The depositional environment of ostracod grainstone-packstone lithofacies (F8) is interpreted to be a shallow setting with moderate to high energy, probably located in mud flats within littoral environments. The abundance of ostracods was likely promoted by optimal lake water conditions that boosted the ostracod reproduction rate. Additionally, shell constructive micritization was probably generated by algae (Flügel, 2010). In this case, this environment must be in the euphotic zone with high nutrient concentration (Scholle and Ulmer-Scholle, 2003; Flügel, 2010). Quartzine in chert nodules suggests evaporitic conditions (Folk and Pittman 1971; Pittman and Folk, 1971; Eugster and Hardie, 1978; Scholle and Ulmer-Scholle, 2003; Warren, 2006; Flügel, 2010).

4.1.9 Brown Claystone – F9

The brown claystone facies (F9) is characterized by light brown to grey arenaceous claystone, in places fissile, containing up to 15% quartz grains. These particles are well sorted, subangular to rounded, with sizes that range from very fine to fine sand. Bioclasts are mainly thin and disarticulated fragments of shells (likely ostracod shells) and fish bones with particle sizes varying from 0.05 to 0.3 mm (figure 4.10A). This facies is interbedded with laminae of ostracod coquinas (figure 4.10B). Facies F9 shows plane parallel and wavy stratification; thicknesses vary from about 0.1 to 2.5 m. Scarce bioturbation is present in facies F9.

Depositional environment. The arenaceous claystone facies is vertically associated with thin coal seams and is present only at the landward area of the basin (Willow Creek outcrop). This association suggests a low energy environment close to the shoreline setting (Ryder and others, 1976) and close to the siliciclastic input areas (deltas). Interbedded claystone and coquina layers indicate episodic ostracod blooms. Bioturbation indicates an oxygenated environment.

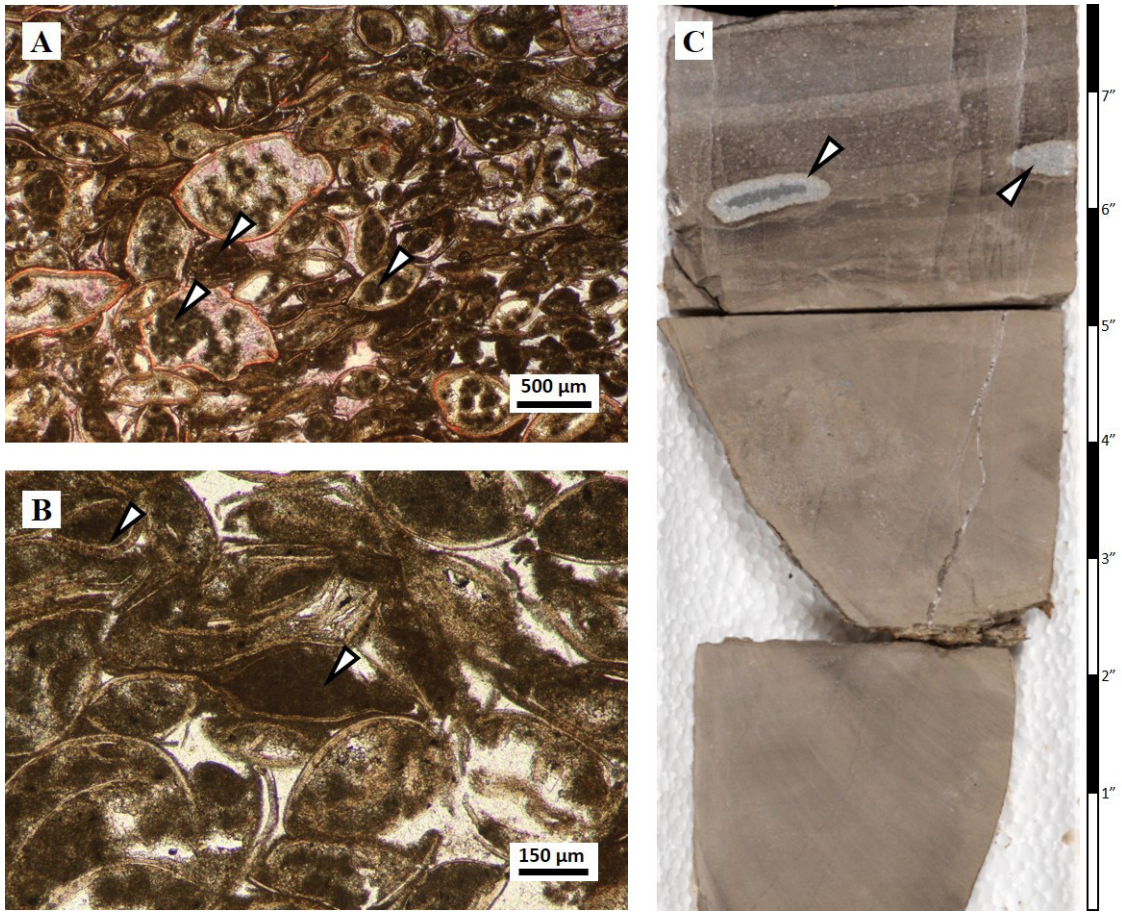

Figure 4.9. *Facies F8 – Ostracod grainstone-packstone.* ***A.*** *TLP of ostracod grainstone. The internal voids of ostracods are partially filled with dolomitized pellets (?) and micrite (white arrows); the resting voids were filled with blocky ferroan calcite cement (pale purple areas); well: DS 11-20, sample 11, 4998.5 ft; PPL.* ***B.*** *TLP of ostracod grainstone facies. Microcrystalline dolomite partially fills the internal cavity of articulated ostracods shells (white arrows); well: DS 11-20, sample 11, 4998.5 ft; PPL.* ***C.*** *Core photograph of ostracod grainstone facies with chert nodules (white arrows); well: BBC 14-1, 6680.0 ft to 6680.7 ft.*

4.1.10 Coal – F10

Coal facies (F10) is defined by dark brown to black coal seams with average bed thickness of 3.0 cm (figure 4.11). Some recognizable plant structures are present. Coal seams are associated vertically with the brown arenaceous claystone facies (F9) and ostracod wackestone (F3). The F10 facies is present only in outcrop at Willow Creek Canyon.

Depositional environment. The coal seam facies represents a swamp environment close to the lacustrine basin (Uinta Basin). This setting is likely the inland expression of a cyclic rising of the water table caused by transgression events (Reinson, 1992; Keighley and others, 2003).

4.2 Facies Associations

A typical vertical succession of facies is shown in figure 4.12. The associated facies allow for the recognition of lacustrine depositional environments on a larger relative to wave base levels and water depth (Tänavsuu-Milkeviciene and Sarg, 2012). Grouping of facies into genetically related units is based on vertical and lateral association, rock textures, and sedimentary structures. The main depositional environments are defined by the lake water column: (1) supralittoral zone located above the lake water table and subjected to subaerial weathering and cyclic flooding, (2) littoral zone, which is highly influenced by wave activity and limited at the base by the fair-weather wave base (FWWB); (3) sublittoral zone, which is between the FWWB and the storm wave base (SWB); and (4) profundal zone that is below the SWB (Tänavsuu-Milkeviciene and Sarg, 2012) (figure 4.13). The facies associations are therefore related to depositional environments as shown in figure 4.13. The littoral and sublittoral zones are located within the photic zone. Facies associations are summarized in table 4.3.

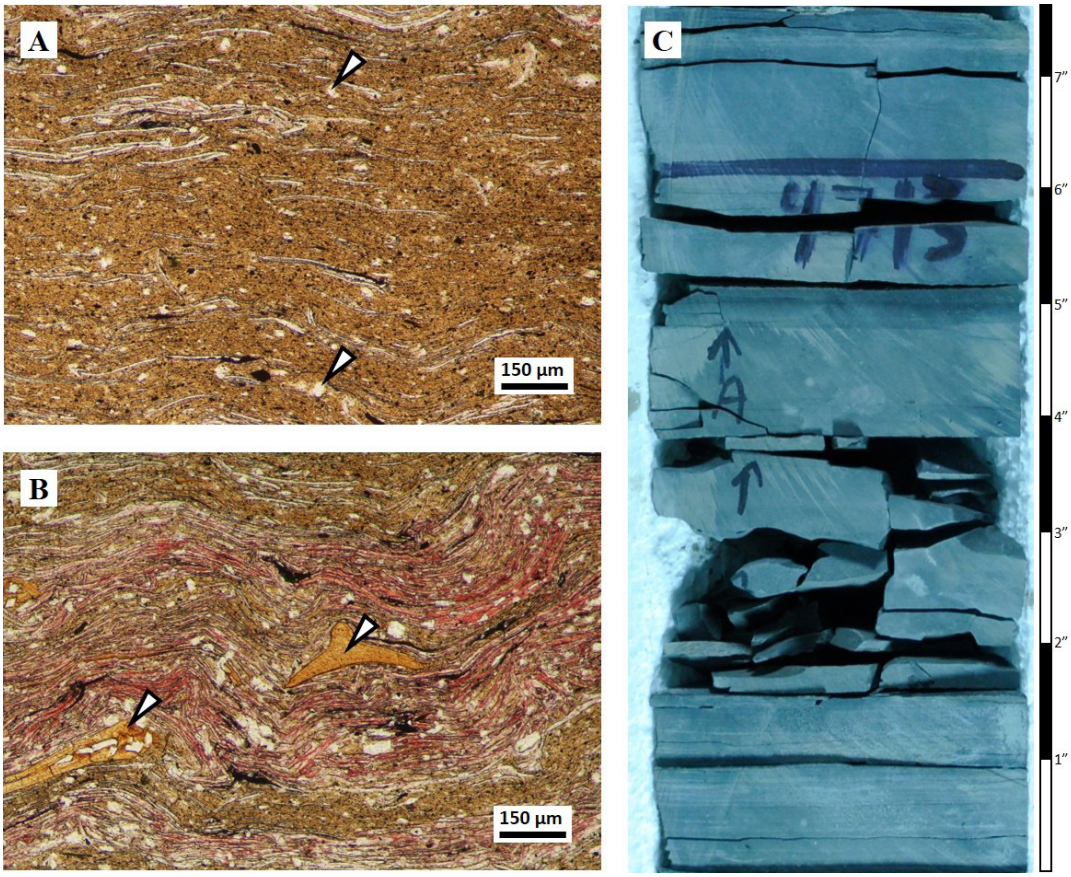

Figure 4.10. *Facies F9 – Brown arenaceous claystone.* ***A.*** *TLP of brown claystone with disarticulated ostracod shell fragments aligned subparallel to bedding, with subangular to rounded and very fine sand quartz grains (white arrows); well: UI 16, sample 16, 4713.2 ft; PPL.* ***B.*** *TLP of interbedded laminae of coquinas (pale pink-red) and arenaceous claystone (light brown area), and fish bones (arrows); well: UI 16, sample 16, 4713.2 ft; PPL.* ***C.*** *Core photograph of brown and fissile claystone; well: UI 16, 4712.9 ft to 4712.5 ft.*

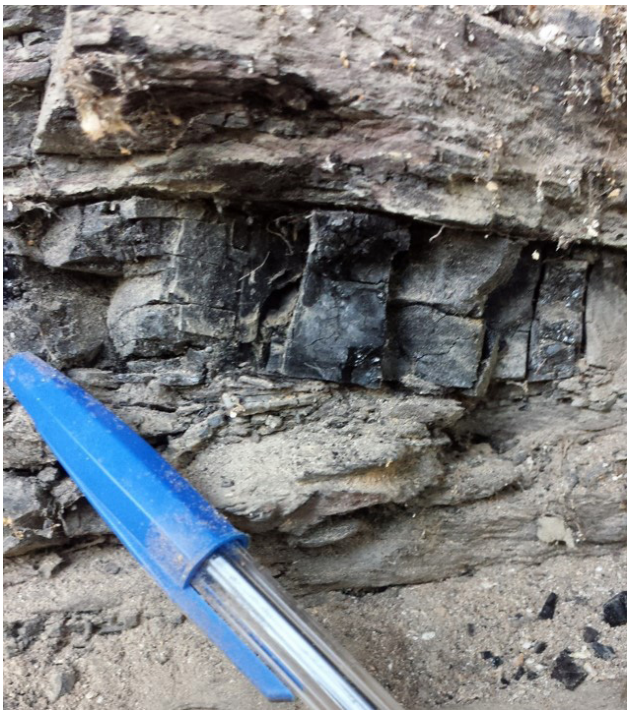

Figure 4.11. *Facies F11 – Coal. Thin coal seam in Willow Creek Canyon outcrop. Seam coals are vertically associated with claystone (F9) (base) and ostracod wackestone (F3) (top).*

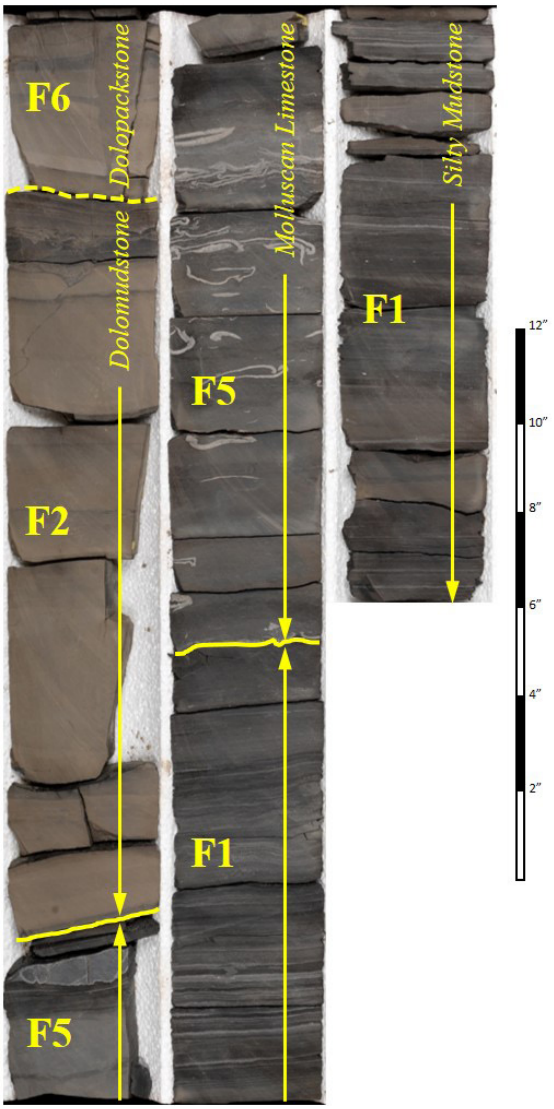

Figure 4.12. *Vertical succession of facies from organic-rich silty mudstone (F1) at the base, mollusc wackestone-floatstone (F5), and lime mudstone (F2) coarsening upward to interclast grainstone-packstone (F6) at the top. Photograph of well BBC 14-1, 6702 ft to 6706.1 ft.*

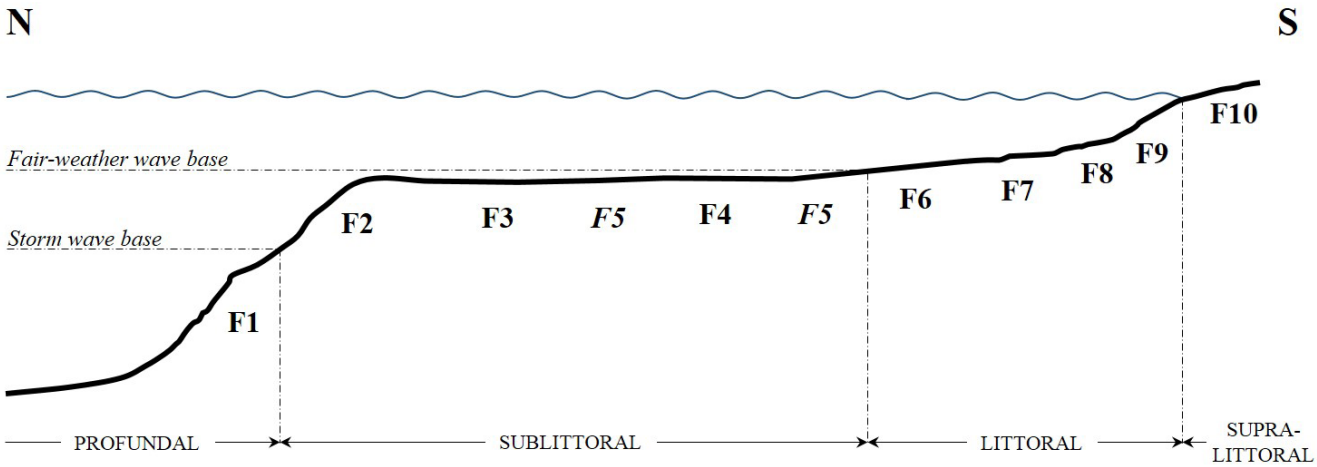

Figure 4.13. *Schematic representation of the lateral facies distribution in the Uinta Basin profile. Time of deposition of the molluscan wackestone-floatstone facies (F5) is different from the time of deposition of the other carbonate facies (F2, F3, F4, F6, F7, and F8). F5 was deposited in a fresh water setting during the initial stage of regression, whereas the facies F2, F3, F4, F6, F7, and F8 were deposited during the maximum regression (see Chapter 4, Sections 4.3 and 4.4 for further discussion).*

Table 4.3. *Associations relating to genetic vertical and horizontal relation, sedimentary structures, and rock textures.*

Facies associations			
Code	**Name**	**Facies**	**Environment**
A	Marginal swamps	F9, F2, F3, F10	Supralittoral
B	Marginal carbonates	F2, F6, F7, F8	Littoral to sublittoral
C	Massive carbonates	F2, F3, F4, F5	Littoral to sublittoral
D	Laminated mudstones	F1	Profundal

4.2.1 Marginal Swamp (A)

Marginal swamp environment is defined by a vertical association of brown claystone (F9), lime mudstone (F2), ostracod wackestone (F3), and coal (F10) facies. The paleogeographic location for this association could be placed out of the lake basin (landward), bordering the coast line. Moreover, coal seam (F10) and lacustrine deposit (F2 and F3) associations were created likely by transgression events that made swamps which later transitioned to ostracod wackestone lacustrine facies deposition in the supralittoral environment.

4.2.2 Marginal Carbonates (B)

Marginal carbonate environments are defined by lateral association of intraclast grainstone-packstone (F6), ooid grainstone-packstone (F7), and ostracod grainstone- packstone (F8) facies, which indicate a high energy environment influenced by wave action (Gierlowski-Kordesch, 2010). Eventually, part of this zone was subaerially exposed by regression of lake water. The exposed areas were subjected to weathering and erosion that generated intraclastic carbonate grains. This facies association occurs at the top of dolomite layer PZ1 in well PW 13-06 (landward) and at the top of dolomite layer PZ1 in well BBC 14-1 (basin ward), suggesting an isolated, extensive, and flat carbonate ramp having very low or no interaction with siliciclastic sediments, deposited in the littoral setting. Based on ooid and pisoid abundance, cycle thickness, and comparison to modern lacustrine stromatolites, Ryder and others (1976) estimated the water depth for this environment ranged from 10 cm to 9 m.

4.2.3 Massive Carbonates (C)

This facies association is composed of lime mudstone (F2), ostracod wackestone (F3), peloid wackestone-packstone (F4), and mollusc wackestone-floatstone (F5). The vertical association of facies F3 with F2 suggests that they were deposited in adjacent and probably overlapping depositional environments. Furthermore, similar sedimentary structures and the vertical association of facies F3 and F4 also suggests close depositional environments. This facies association is characterized by massive carbonates with a high matrix to grains ratio, fine-size carbonate grains, and scarce to moderate ostracod shell fragments and fish bones. Grain size of carbonate grains and increment of matrix percentage suggest an environment of moderate to low energy between the FWWB and the SWB. This environment was ideal for benthic organisms (ostracods mainly) that reworked sediments. The biological activity partially obliterated primary sedimentary structures and indicates an oxygenated setting. This environment was influenced by episodic storms that formed lenses of peloidal grainstone interfingering with lime mudstones (figure 4.2B).

4.2.4 Laminated Oil-Rich Mudstones (D)

This facies association is characterized by laminated oil-rich mudstones interbedded with laminae of lean silty mudstone and coquina laminae. The high organic matter content values suggest an anoxic environment located below the SWB within the anoxic zone where lack of oxygen and light created adverse conditions for organisms and allowed for preservation of organic matter. However, periodic water level and oxygen fluctuations promoted deposition of some light gray, organic-poor mudstone.

4.3 Facies Successions and Cyclicity

Individual facies are arranged vertically, defining repetitive cycles or successions that help to determine the basin's evolution thoughout the deposition of the UBm. Thickness of these cycles ranges from 22.9 ft landward up to 39 ft basinward. Fluctuations in lake level are recorded by the vertical variation of facies.

Each cycle is generally defined at the base by organic-rich mudstone (F1), followed by a mollusc wackestone-floatstone (F5), and topped by an intraclast grainstone-packstone (F6), ooid grainstone-packstone (F7), or an ostracod grainstone-packstone (F8) (figure 4.12). The cycle is repeated five times between the D and C shales and has local variations (figure 4.14).

Transgression events result from either a period of flooding promoted by an increased rate of water inflow than outflow or by a higher accommodation rate than sediment supply (tectonism) (Ryder and others, 1976; Carrolls and Bohacs, 1999). As a result, deposition of the silty mudstone facies (F1) transgressed landward (Ryder and others, 1976). At the same time, the wackestone-floatstone facies (F5) moved landward as well. A rise in lake level probably increased te water table near the lake margin and inundated the supralittoral zone that established swamps and marshes, and favored deposition of lenticular coal seams. After a period of flooding, lake level fell and depositional environments regressed basinward, partially exposing the grainstone-packstone deposits to subaerial conditions. Pedogenic characteristics, such as circumgranular cracks (figure 4.7A and B), were developed at the top of layer PZ1 in wells PW 13-06 and N 6-28, which supports this interpretation.

This interpretation is consistent with the findings by Tänavsuu-Milkeviciene and others (2017) who defined three major depositional cycles for the entire section of the GRF. The section of interest here might be correlated with the first depositional cycle defined by Tänavsuu-Milkeviciene and others (2017), which was controlled by short climate variations. During increased moisture episodes (high inflow), lake level rose pushing the marginal facies associations landward. In contrasts, dry episodes (low inflow) caused a lake water drop moving back the marginal facies basinward (Tänavsuu-Milkeviciene and others, 2017).

The idealized depositional cycles represent a period of deposition of about 10 to 16 thousand of years (ky) (table 4.4). This time interval was calculated based on the average sediment accumulation rate defined by Smith and others (2008) at the base of the GRF. Smith (2008) defined a deposition rate of about 150 mm/ky for the basin-margin areas (Indian Canyon outcrop, southwest of the study area close to the Nine Mile Canyon outcrop described in this project). The cyclicity was likely controlled by periodic climate variations having the same time interval (10 to 16 ky).

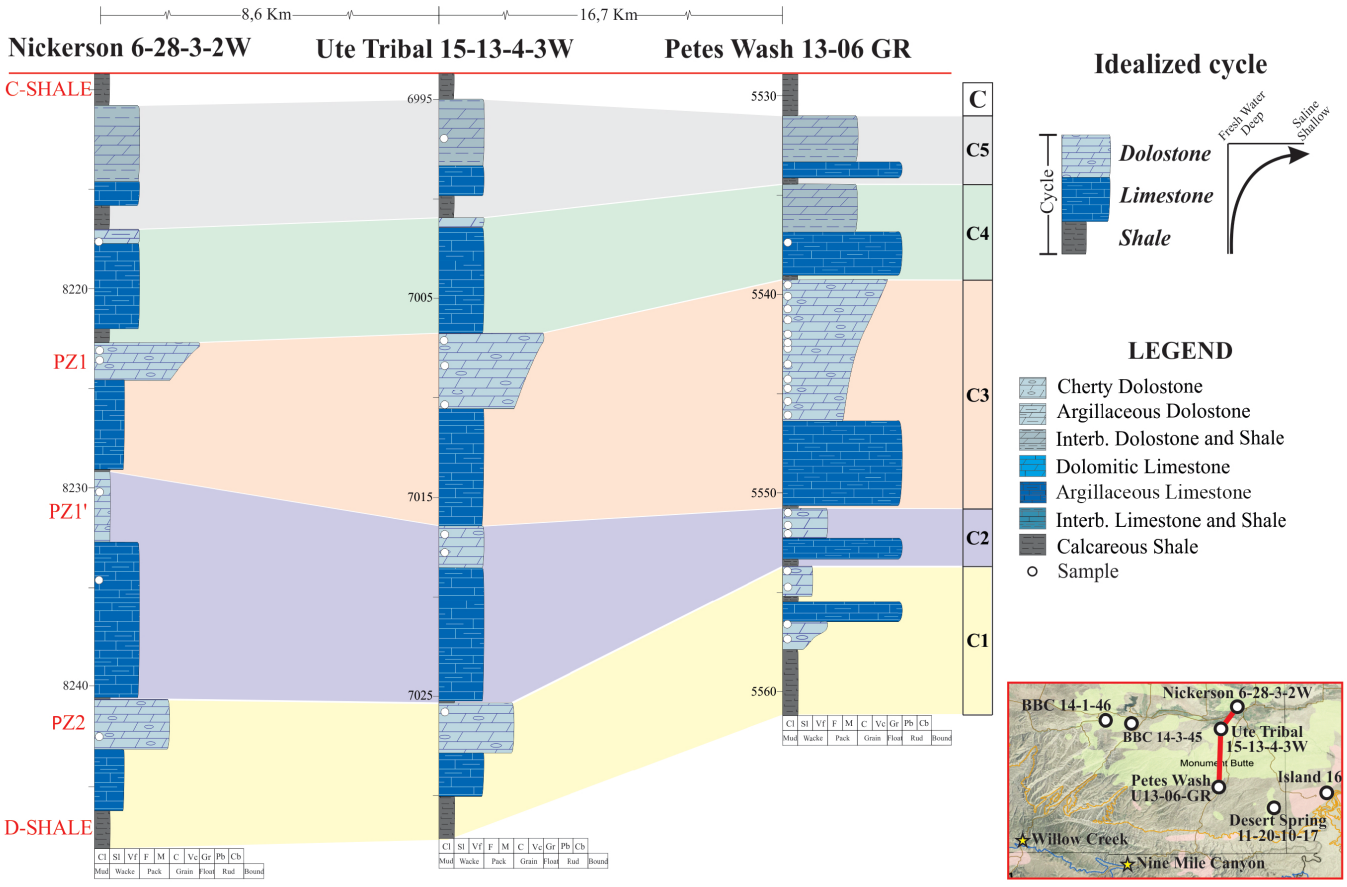

Figure 4.14. *Correlation of stratigraphic cycles C1 to C5 (right column) within D and C shales.*

Table 4.4. *Thickness and calculated time of deposition for each idealized cycle identified within D and C shales. TAve: Thickness average of each cycle; thickness in ft.*

Cycle	Thickness of cycles								Time (ky)
	BBC 14-1	BBC 14-3	N 6-28	UT 15-13	PW 13-06	DS 11-20	IU 16	TAve	
C5	8.0	6.4	6.2	6.0	3.4	1.5	3.0	4.9	10.0
C4	3.9	5.8	5.7	5.8	4.8	7.3	8.0	5.9	12.0
C3	8.0	9.6	6.5	9.7	11.5	3.2	7.4	8.0	16.2
C2	8.8	8.0	11.4	9.1	2.9	3.6	4.9	6.8	14.1
C1	7.3	4.0	7.5	6.8	7.5	6.0	3.6	6.5	12.4

4.4 Facies and Dolomitization

Facies and dolomitization relationships show three main factors: (i) pervasive matrix dolomitization occurred in facies F2, F3, F4, F6, F7 and F8; (ii) the underlying and fresh water mollusc wackestone-floatstone facies (F5) was not dolomitized; and (iii) dolomitization took place at the top of each cycle (figure 4.14).

All carbonate facies were dolomitized to variable degrees except for F5. The relative percentages of dolomite and calcite in each facies (figure 4.15) suggest that dolomitization crosscut facies boundaries, having taken place from the sublittoral environment (lime mudstone facies–F2) to the littoral (near shore) environment (ostracod grainstone-packstone facies–F8) (figure 4.16). However, the fresh water mollusc wackestone-floatstone facies (F5) was not dolomitized (dolomite volume <10%).

The vertical variation of facies from F1 (base of the cycles) grading toward facies F5 (fresh water molluscan wackestone-floatstone) and the occurrence of the dolomitized facies F2, F3, F4, F6, F7, and F8 (top of the cycles), suggest that deposition was controlled by transgressive/regressive cycles. Thereby, facies F1 represents the maximum flooding event or lake expansion and a deeper depositional setting (profundal). After the transgression maximum, the lake water dropped and the depositional environment changed from a profundal to a sublittoral setting, allowing for the precipitation/deposition of micrite in a fresh water setting (as evidenced by the fossil associations). During this period, dolomitization of already deposited carbonate sediments (facies F5) was not possible because of a relatively low Mg/Ca ratio and low temperature of the lake water (fresh water setting). Near the maximum regression of the lake water, the depositional environment changed to an overall shallow littoral/sublittoral setting in which the already deposited carbonate sediments were partially dolomitized. Dolomitization was likely driven by increased Mg/Ca ratio and temperature of the lake water (see Chapter 6 for further discussion).

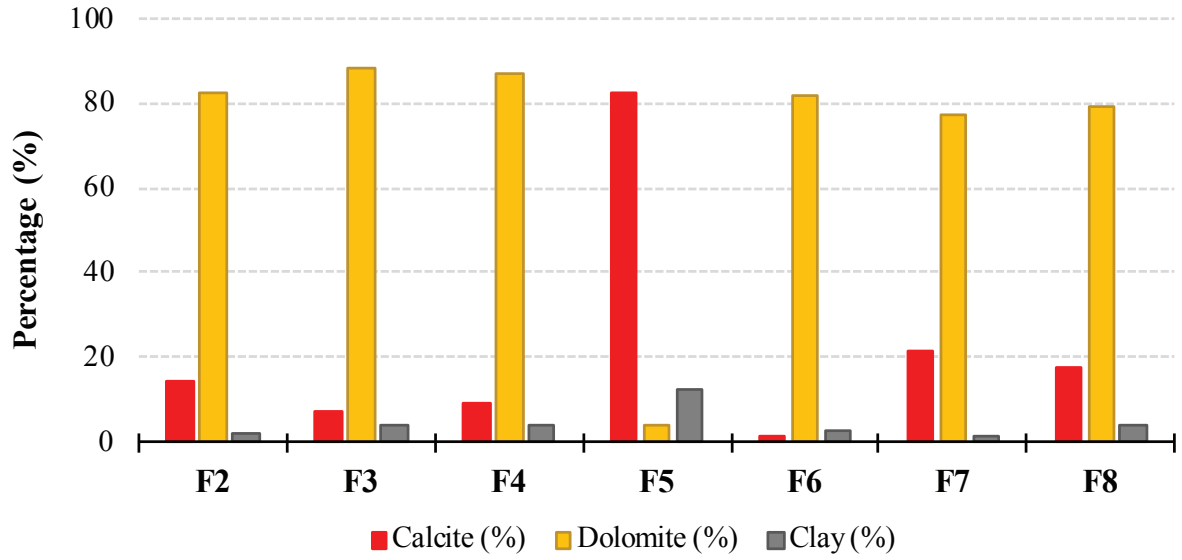

Figure 4.15. *Mineralogical composition for carbonate facies. Volume percentage (vertical axis) estimated from thin sections using semi-quantitative charts (Baccelle and Bosellini, 1965).*

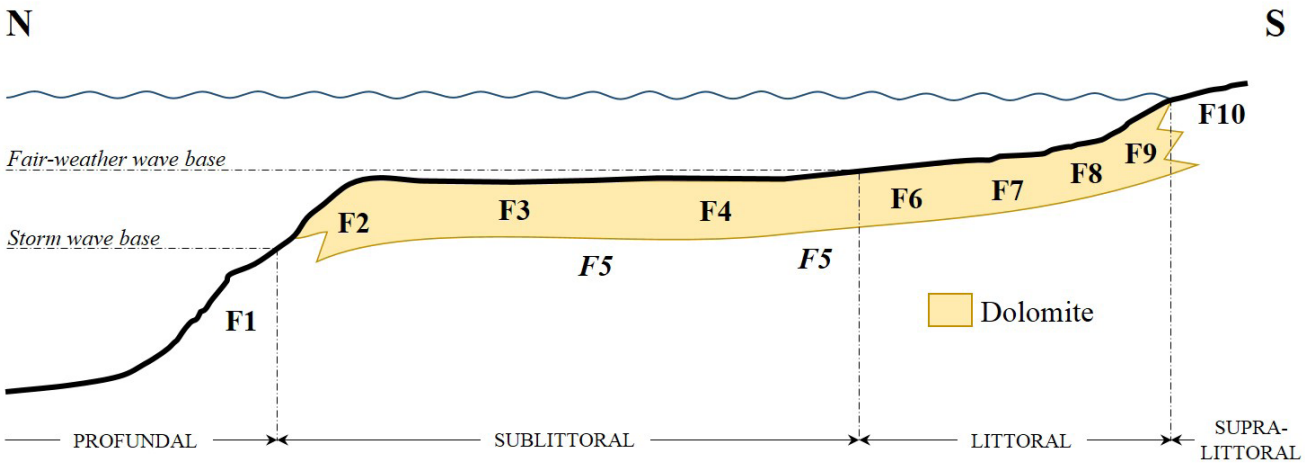

Figure 4.16. *Schematic representation of facies distribution and dolomitization. F5 was not dolomitized.*

CHAPTER 5 DIAGENESIS

The stratigraphic interval of study shows a composite of diagenetic events from near-surface to deep burial diagenetic settings. Special attention was paid to dolomitization, i.e., how this process is related to the petrophysical properties (porosity and permeability) of petroliferous dolomite layers PZ1, PZ1′, and PZ2. Additional diagenetic processes such as mechanical compaction, cementation, dissolution, fracturing, and stylolitization were also considered because they also modified the reservoir quality.

Fifteen diagenetic events were identified based on thin section petrographic descriptions. The relative timing of the diagenetic features was interpreted based on textural relationships. However, the duration of some events remains uncertain because of diagenetic complexity. A summary of diagenetic events and their temporal relationships are given in table 5.1, a paragenetic sequence chart (Section 5.1.2).

5.1 Diagenetic History from Core and Thin Section Petrography

5.1.1 Petrographic Observations

This section describes the characteristics of the diagenetic features according to their temporal occurrence from the earliest to the latest diagenetic products. Dolomite textural description and classification were completed following Gregg and Sibley's (1984) and Sibley and Gregg's (1987) dolomite textural classification modified by Wright (2001) (figure 5.1). Four types of dolomite textures were identified using thin section and scanning electron microscopy (SEM). These were classified as planar-e, planar-s, nonplanar-a, and cement categories. Detailed descriptions of texture and crystal size on the SEM scale are presented in Section 5.2.1.1 and 5.2.1.2.

Additionally, mineral crystal size and carbonate grain size follow the classification proposed by Folk (1962) (figure 5.2).

5.1.1.1 Cracks – Phase 1a

Cracks are usually random with no preferential direction and are polygonal in shape. Cracks do not crosscut but rather preferentially skirt carbonate grains, becoming circumgranular cracks (figure 5.3A). Sub-millimetre-sized cracks are present in dolomitized micrite rock fragments (figure 5.3A to C) and are filled with calcite cement (figure 5.3C). These intraclasts are exclusively present at the top of layer PZ1 toward the basin center in wells BBC 14-1, BBC 14-3, and N 6-28. Larger and wider cracks are present exclusively in the Nine Mile outcrop in ostracod dolopackstone (figure 5.3D) and show the same pattern as the smaller scale features.

5.1.1.2 Meniscus cement – Phase 1b

Meniscus cement precipitated at carbonate grain contacts (figure 5.3E), partially filling interparticle pores. Meniscus cement shows a geographical variation in its relative abundance as follows: in nearshore areas, meniscus cement is preferentially developed within intraclastic grainstone, ooid grainstone, and ostracod grainstone facies (F6, F7, and F8), in which the meniscus cement is more abundant in well PW 13-06 at the top of layer PZ1. Basinward meniscus cement is not present. The original carbonate mineral that precipitated as meniscus cement was replaced by dolomite, which obliterated the original texture of meniscus cement.

Table 5.1. *Paragenetic sequence. Phases 1 (cracks and meniscus cement), 2 (molds and equant-blocky calcite cement), 3b (dolomite cement), and 8 (equant calcite cement) took place along the near shoreline area only. These diagenetic products are highlighted red.*

PHASE	PRODUCTS	54 My — EARLY	10 My	0 My — LATE
1a	Cracks			
1b	Meniscus cement			
2a	Molds I			
2b	Blocky calcite cement			
2c	Variably lithified sediment			
3a	Replacive dolomite			
3b	Dolomite cement			
4	Molds II			
5a	Isopachous quartz rims			
5b	Chert nodules			
5c	Euhedral quartz			
6	Pyrite			
7	Mechanical compaction features			
8	Equant calcite			
9	Molds III and vugs			
10	Blocky ferroan calcite cement			
11	Subhorizontal stylolites and sutured seams			
12	Oil impregnation			
13	Subvertical stylolites and sutured seams			
14	Subvertical fractures			
15	Drusy calcite cement			
PHASE	PRODUCTS	NEAR SURFACE	SHALLOW / INTERMEDIATE / DEEP	INTERMEDIATE

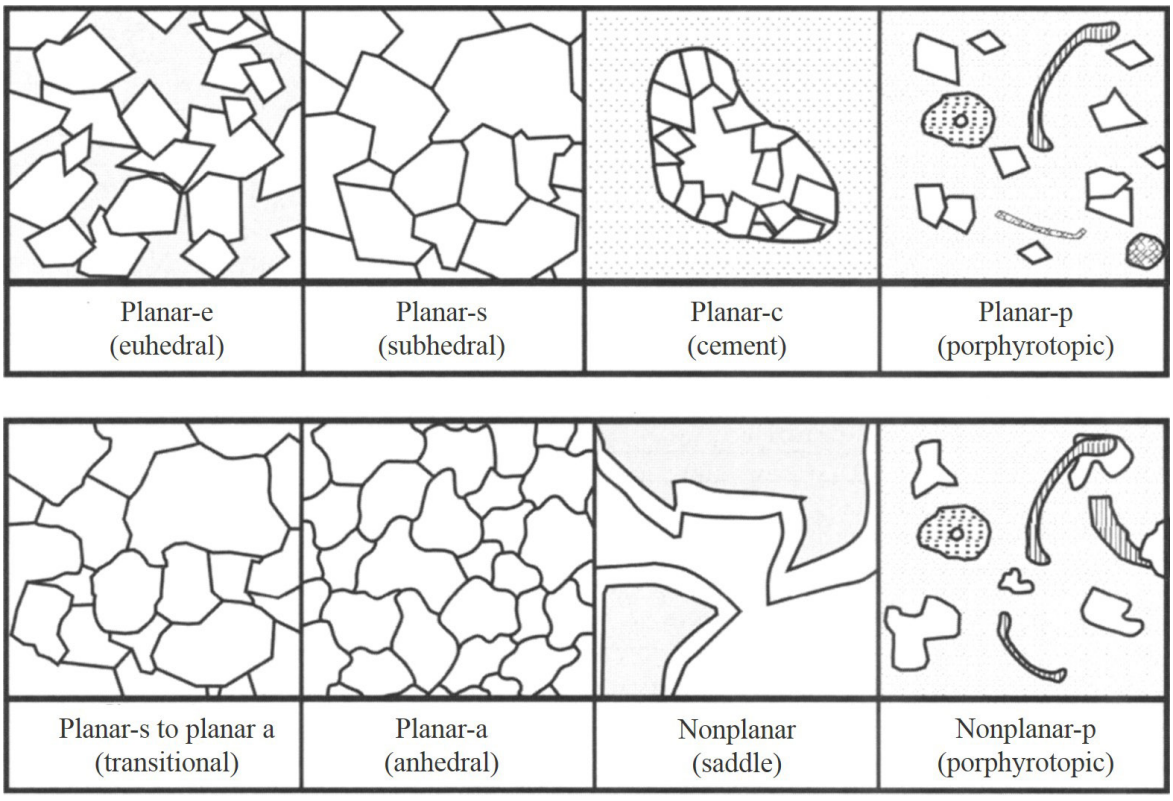

Figure 5.1. *Dolomite textural classification proposed by Gregg and Sibley (1984) and Sibley and Gregg (1987). Image modified from Machel (2004).*

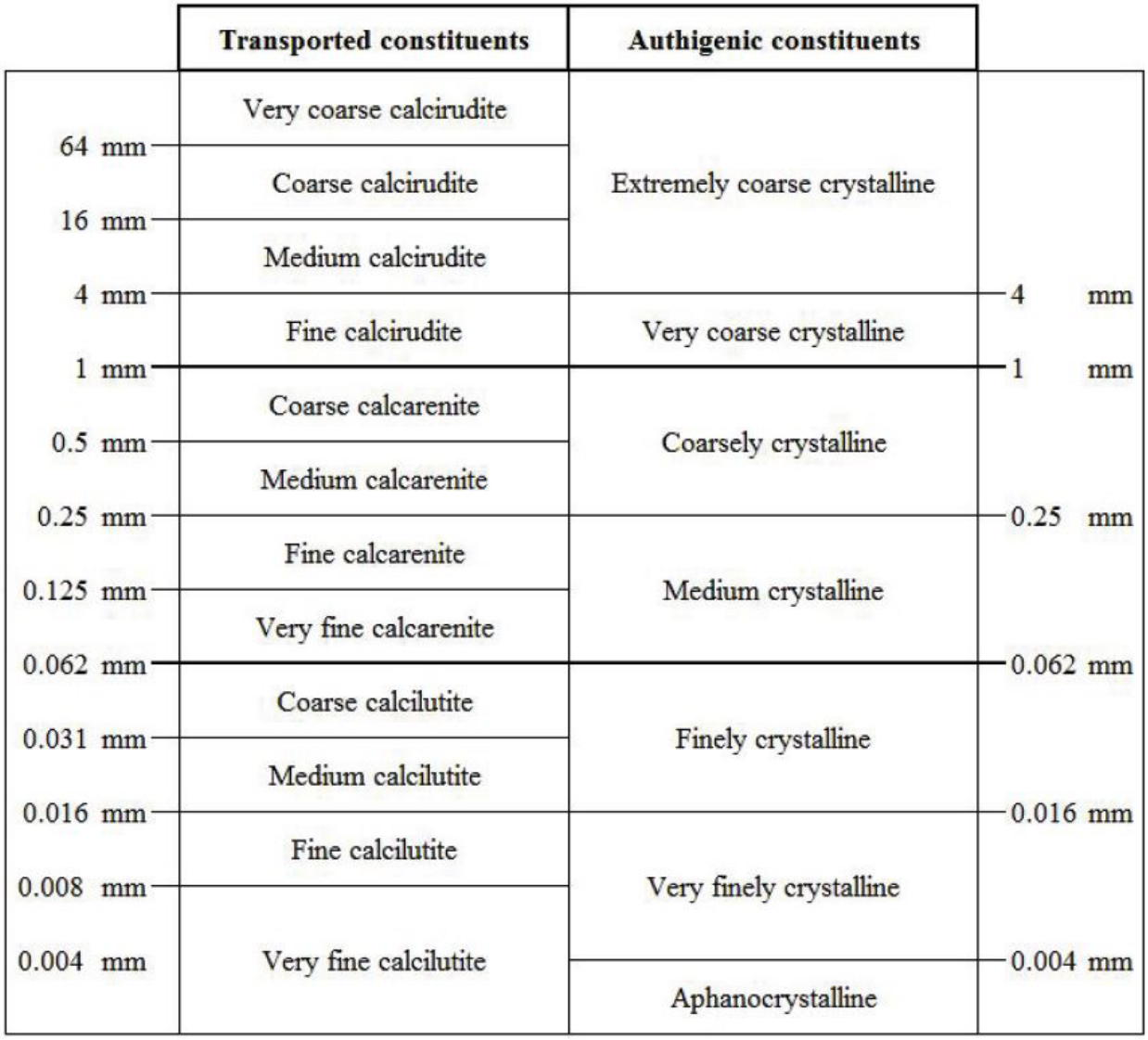

Figure 5.2. *Carbonate grain size and mineral crystal size classification; from Folk (1962).*

5.1.1.3 Molds I – Phase 2a

Molds were created by dissolution of mainly mollusk shells (figure 5.3F). Such molds are present only within dolomitized intraclasts (Facies F6) and are filled with calcite cement. These molds have preserved the original shapes without any evidence of mechanical deformation (figure 5.3F).

5.1.1.4 Blocky calcite cement – Phase 2b

Blocky calcite crystal ranges from medium to coarse crystalline in size. This cement fills moldic porosity and cracks (figure 5.3A to D) in intraclastic grainstone and ostracod grainstone facies (F6 and F8).

5.1.1.5 Variably lithified sediment – Phase 2c

Sediment can often undergo variable lithification by early meniscus and blocky calcite cement.

5.1.1.6 Replacive dolomite – Phase 3a

This section provides petrographic observations on the thin section scale; however, characterization of individual dolomite crystals is not possible using the petrographic microscope because the crystals are too small. This characterization was therefore conducted using SEM images (see Sections 5.2.1.1 and 5.2.2.1 for further analysis). Replacive dolomite is brown to green in colour, with crystal size ranging from aphanocrystalline to very finely crystalline. Replacive dolomite is found in the matrix (figure 5.4A), as well in peloids, intraclasts (figure 5.4B), ooids, and pellets; however, dolomite generally does not replace bioclasts (figure 5.4C).

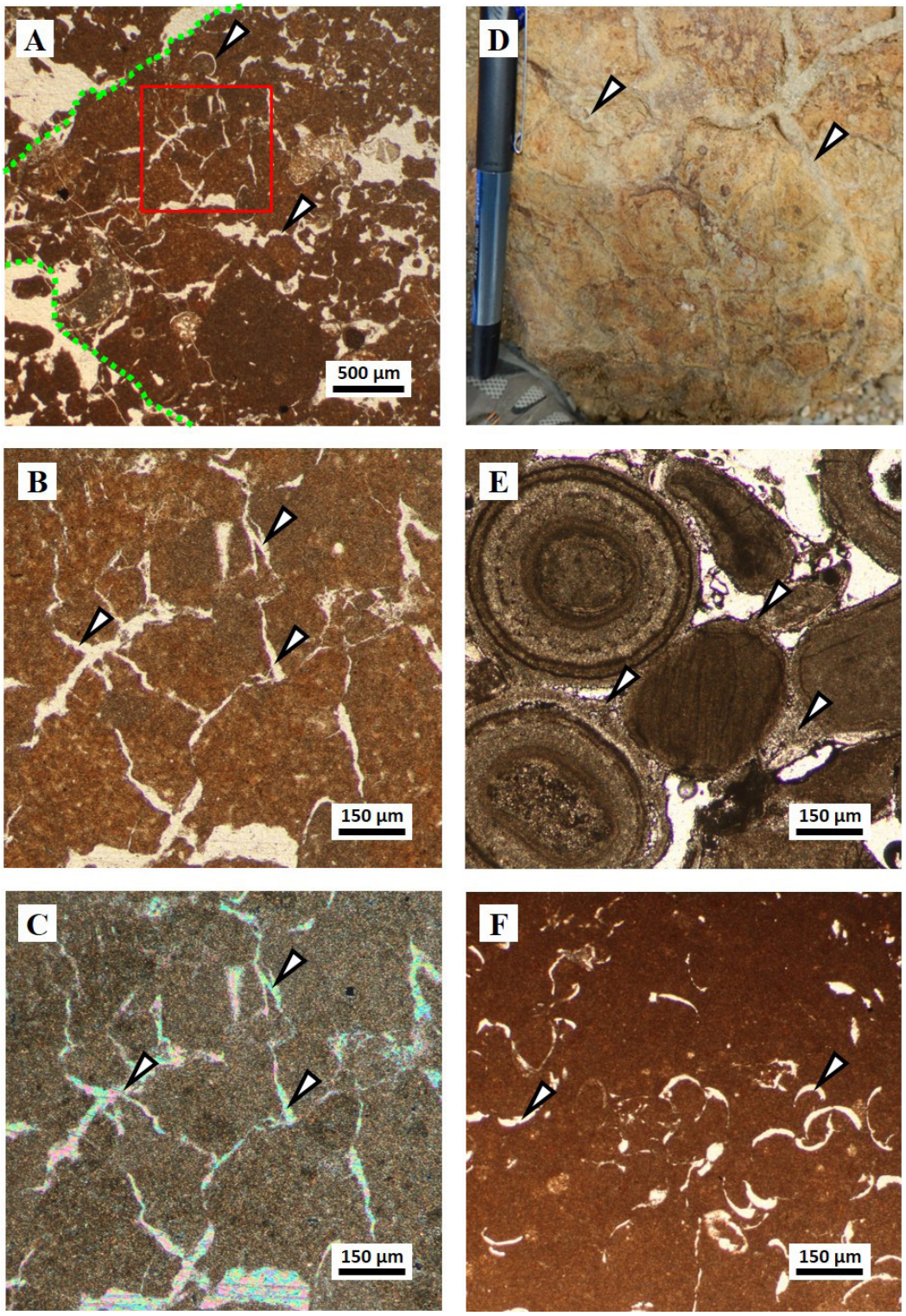

Figure 5.3. A. *TLP of intraclast (green dash outline) with cracks that surround peloids (arrow) and crosscut dolomitized matrix; well: N 6-28, sample: 5, 8223.2 ft; plane polarized light (PPL).* ***B.*** *Detail of photomicrograph (A). Polygonal micro-cracks (arrows) cross-cutting microcrystalline dolomitized matrix (brown area), cracks are completely filled with blocky calcite cement; PPL.* ***C.*** *Crossed-polarized photomicrograph (XPL) (B), blocky calcite cement fills cracks (arrow).* ***D.*** *Cracks present in the nearshore area are filled with blocky calcite cement (arrows); Nine Mile outcrop, pen for scale.* ***E.*** *TLP of ooid dolograinstone with microcrystalline meniscus cement at grain contacts (arrows); well: PW 13-06, sample 6, 5539.5 ft; PPL.* ***F.*** *TLP of molds of bioclasts filled with blocky calcite cement (arrow); well: UT 15-13, sample 5, 6982.2 ft; PPL.*

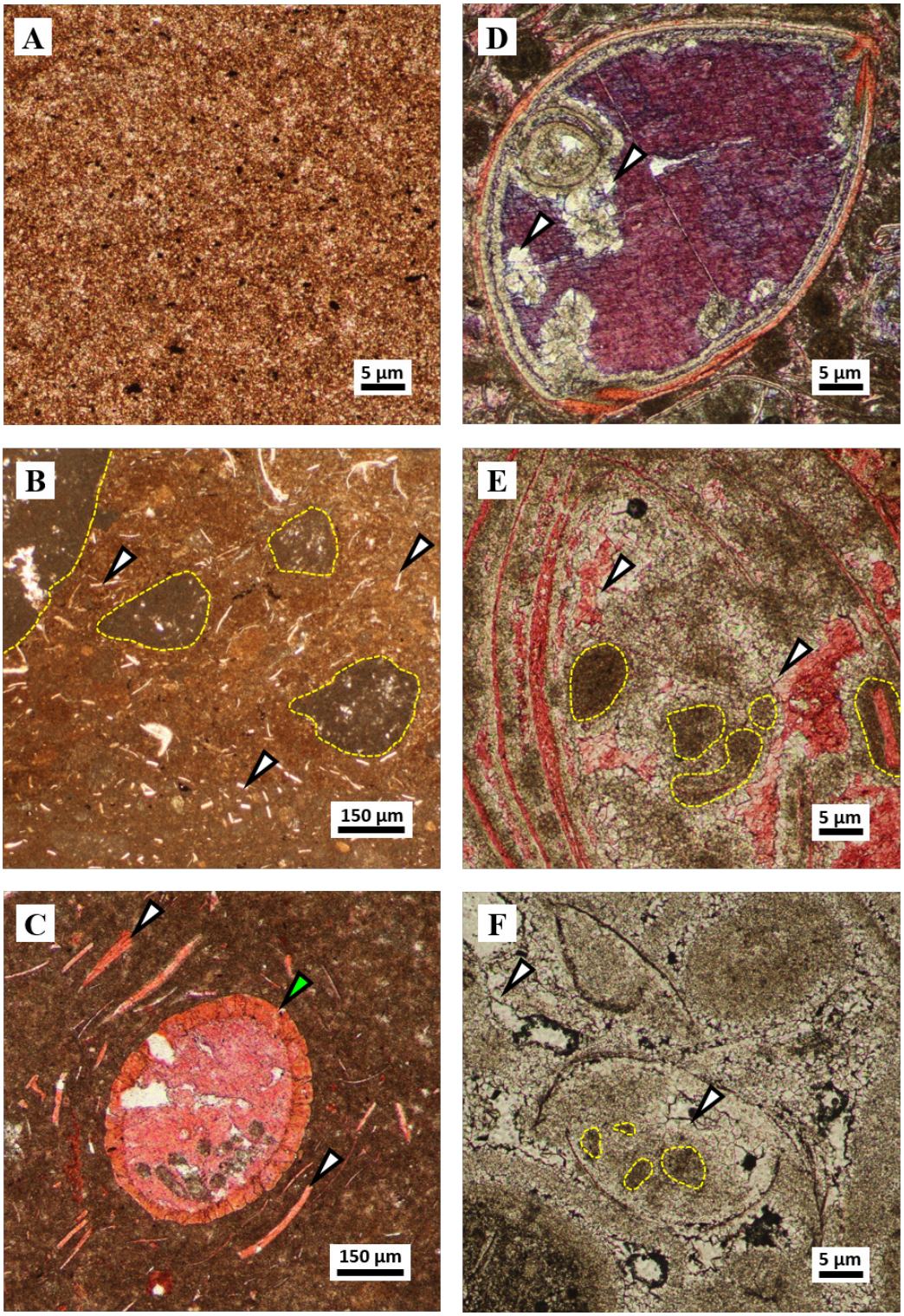

Figure 5.4. A. *TLP of very fine dolomite in matrix; pyrite and hydrocarbon droplets (black spots); well: BBC 14-1, sample: 17, 6692.6 ft; PPL.* ***B.*** *TLP of very fine dolomite in matrix (light brown area) and dolomitized intraclasts (yellow dashed outlines), bioclasts (arrows) not dolomitized; well: BBC 14-1, sample: 13, 6684.9 ft; PPL.* ***C.*** *TLP of matrix-selective dolomitization (dark brown area), shell fragments (white arrows) and gyrogonite bioclast (green arrow) not dolomitized; well: BBC 14-3, sample: 27, 7373.6 ft; PPL.* ***D.*** *TLP of planar-c dolomite cement (arrows) partially fills intraparticle pore; well: IU 16, sample: 14, 4729.9 ft; PPL.* ***E.*** *TLP of rims of planar-c dolomite cement (arrows) grow around dolomitized peloids and ooids (yellow dashed outlines); well: DS 11-20, sample 12, 4999.35 ft; PPL.* ***F.*** *TLP of planar-c dolomite cement (arrows) around dolomitized peloids (?) within ostracod shells; well: PW 13-06, sample: 6, 5539.5 ft; PPL.*

5.1.1.7 Dolomite cement – Phase 3b

Dolomite cement is comprised of microcrystalline crystals and partially fills intraparticle pores, usually present as overgrowth of dolomitized internal sediment (figure 5.4D to F). Most crystals are euhedral to subhedral, and crystal size varies from 10 to 20 µm. Dolomite cement preferentially developed at nearshore areas within the ostracod grainstone and ooid grainstone facies (F8 and F9). In contrast, the basinward facies (F3, F4, and F5) do not display this type of cement.

5.1.1.8 Molds II – Phase 4

Molds were developed by partial to complete dissolution of calcite bioclasts (figures 5.5A to C). Dissolution of bivalves not previously filled with mud were later filled with fibrous chert (figures 5.5A and B), whereas bivalves filled with mud formed molds only as narrow as the shells (figure 5.5C).

5.1.1.9 Isopachous quartz cement rims – Phase 5a

This phase is characterized by quartz crystals with sizes ranging from 5 to 20 µm and bladed to equant shapes. The quartz cement lines interparticle pores (figures 5.5D and E) and in rare cases intraparticle pores (figure 5.5F). This cement preferentially developed in the nearshore area within the intraclast, ooid, and ostracod grainstone facies (F6, F7, and F8).

5.1.1.10 Chert nodules – Phase 5b

Silica forms elongated and irregular chert nodules (up to several decimetres in dimension) within dolomite layers PZ1, PZ1′ and PZ2. The nodules are composed of assorted silica varieties: length-fast and length-slow (quartzine) chalcedony (Flöerke and others, 1991), megaquartz (Folk and Weaver, 1952), and granular microcrystalline quartz (Knauth, 1994). Colourless, fibrous, and aphanocrystalline chalcedony cement also fills intraparticle pores (figures 5.5A and B) and vugs.

Both length-slow (figures 5.6A to C) and length-fast (figures 5.6D and E) chalcedony display a spherulitic fibrous habit and/or a radial fibrous to feathered habit (figures 5.5B, 5.6B and E) nucleated along pore walls. Megaquartz crystals show a polygonal crystal habit with irregular interlocking crystals located at the centers of voids and filling remaining space (figure 5.6F). Granular microcrystalline quartz (anhedral quartz crystals around bioclast in figure 5.6A to D) composes most of the volume of the chert nodules.

5.1.1.11 Euhedral quartz – Phase 5c

Quartz of phase 5c is colourless, clean, commonly hexagonal and double–terminated euhedral crystals of quartz that vary in size from 5 to 20 µm. Euhedral quartz crystals contain very fine crystalline dolomite inclusions (figure 5.7A). They formed around chert nodules and within bioclasts (figures 5.7B and C) and are overall in random distribution within the dolomitized matrix of facies F2, F3, and F4.

5.1.1.12 Pyrite – Phase 6

Phase 6 is characterized by very fine crystalline and octahedral pyrite crystals associated with calcite within chert nodules (figure 5.7D). Crystal size varies from 10 to 100 µm. Some pyrite crystals encase very fine crystalline and planar-e dolomites (figure 5.7E). There are also disseminated crystals of very fine to fine crystalline pyrite within very fine crystalline dolomite (matrix) (figure 5.7F). Pyrite crystals range in size from 5 to 10 µm.

5.1.1.13 Mechanical compaction features – Phase 7

Several mechanical compaction features are present: (i) broken and flattened bioclasts (figures 5.8A, and 5.9A and B), (ii) peloids elongated and/or amalgamated parallel to bedding (figure 5.8B), (iii) concavo-convex contacts between grains, and (iv) breakage of ooids and peloids.

5.1.1.14 Equant calcite – Phase 8

Equant calcite forms mosaics of mostly anhedral crystals with sizes varying from 10 to 50 µm. This calcite also fills interparticle pores as cement and is more abundant toward nearshore areas (facies F6, F7, and F8), especially within the ostracod grainstone-packstone facies (F8) (figure 5.8C). Equant calcite cement is not present toward the basin center (F2, F3, and F4 facies).

5.1.1.15 Molds and vugs – Phase 9

Phase 9 is characterized by partial dissolution of equant calcite-cement-created vugs, which were filled with ferroan calcite cement in Phase 10 (figures 5.8D and E). Partial dissolution of bioclasts (preferentially pelecypods and gastropods) created moldic pores, which were also filled by ferroan calcite cement (figure 5.8F).

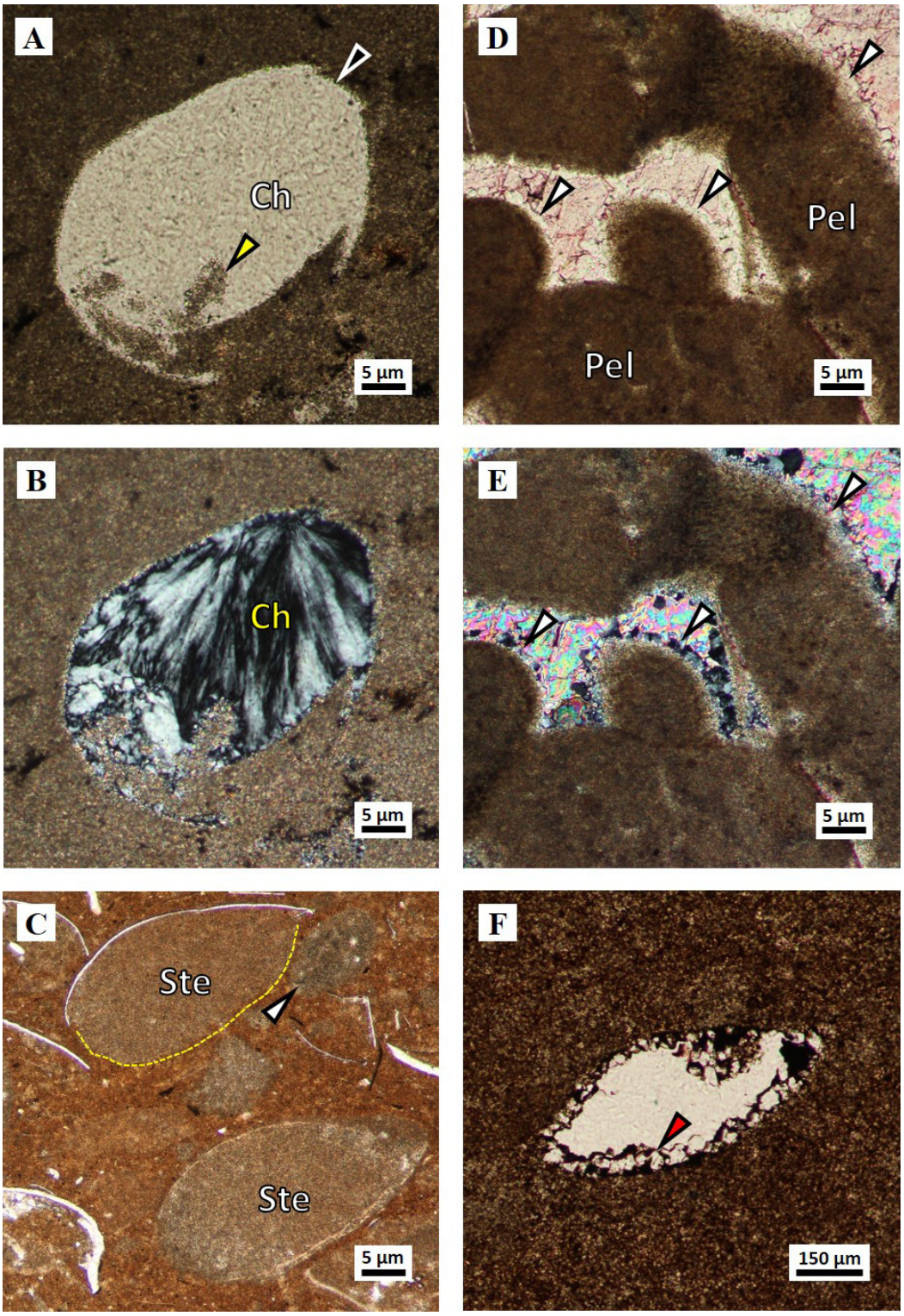

Figure 5.5. A. *TLP of ostracod mold (black arrow) filled with dolomite (yellow arrow) and chalcedony (Ch); well: PW 13-06, sample: 8, 5543.5 ft; PPL.* ***B.*** *Crossed-polarized light image of (A). Feathered texture of the chalcedony that fills internal ostracod (?) pore; XPL.* ***C.*** *Partial (yellow dashed line) and complete dissolution (arrow) of ostracod shells; steinkerns (Ste) within an aphanocrystalline dolomitized matrix; well BBC 14-1, sample: 9, 6680.1 ft; PPL.* ***D.*** *TLP of rims of very fine crystalline quartz as cement (arrows) around dolomitized peloids (Pel); well: BBC 14-1, sample: 12, 6683.95 ft; PPL.* ***E.*** *Crossed-polarized light image of (D). Quartz cement (arrows), and calcite cement (yellow, green, and blue area); XPL.* ***F.*** *TLP of rims of equant quartz cement (arrow) in intraparticle pore. Dark brown and black spots are hydrocarbons; well: N 6-28, sample: 7, 8230.2 ft; PPL.*

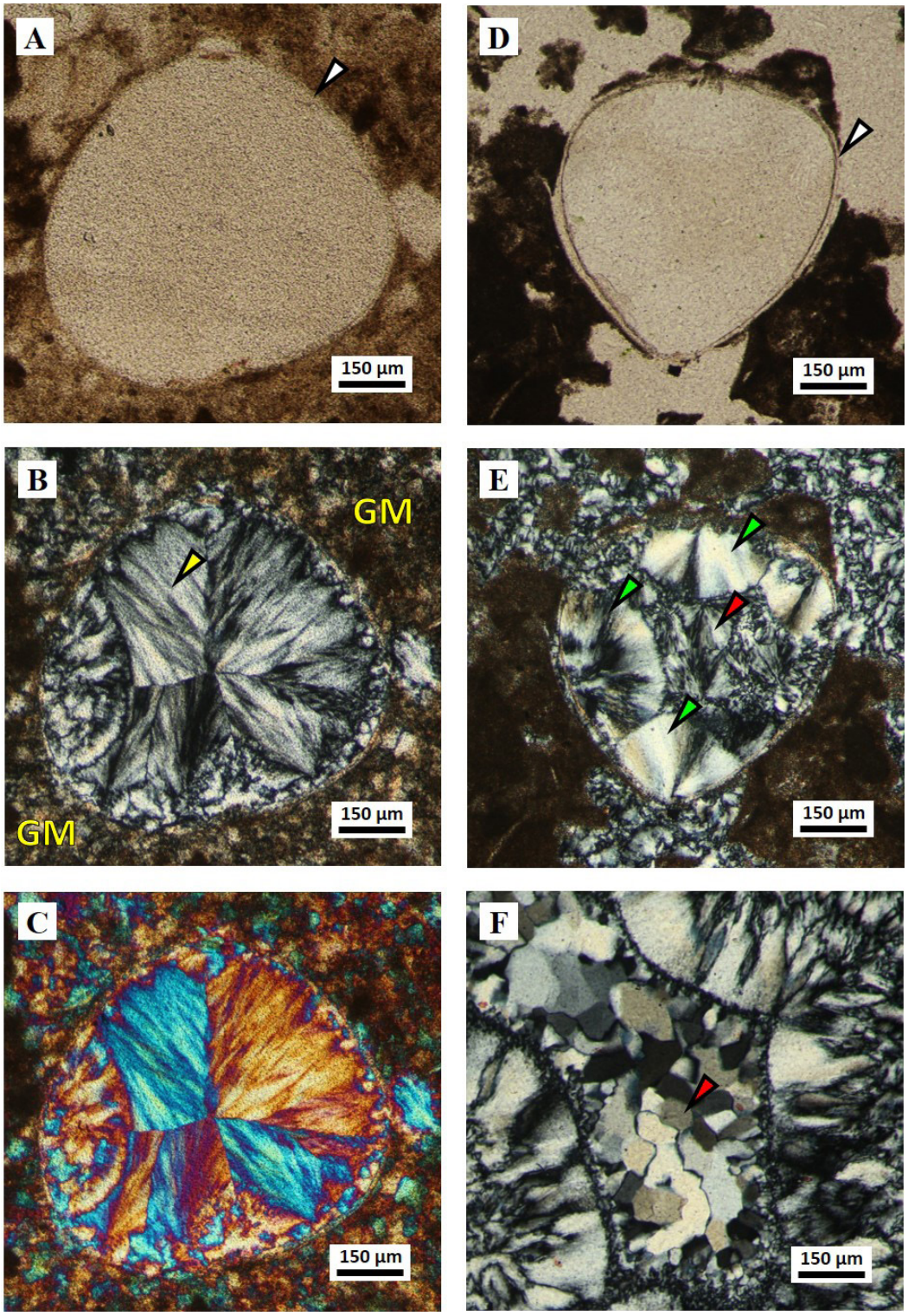

Figure 5.6. A. *TLP of a chert nodule. Ostracod shells (arrow) mimetically replaced by microcrystalline quartz. Intraparticle pore filled by chalcedony (light brown area); well: BBC 14-3, sample: 28, 7374 ft; PPL.* ***B.*** *Crossed-polarized light image of (A), quartzine (arrow) nucleated at the walls of the ostracod shells. Granular microcrystalline quartz (GM) precipitated around bioclasts; XPL.* ***C.*** *Same image (A) and (B); XPL + gypsum plate.* ***D.*** *TLP of a chert nodule with an articulated ostracod (arrow) partially replaced by quartz and dolomite, internal void filled with chalcedony; well: BBC 14-3, sample: 29, 7375 ft; PPL.* ***E.*** *Crossed-polarized light image of (D), several chalcedonies nucleated along the internal walls of the ostracod shell (green arrows); some chalcedony have radial fibrous to feathered habit (red arrow); XPL.* ***F.*** *TLP of megaquartz crystals (red arrow) fill a void post-dating chalcedony cement (feathered crystals); well: BBC 14-3, sample: 29, 7375 ft; XPL.*

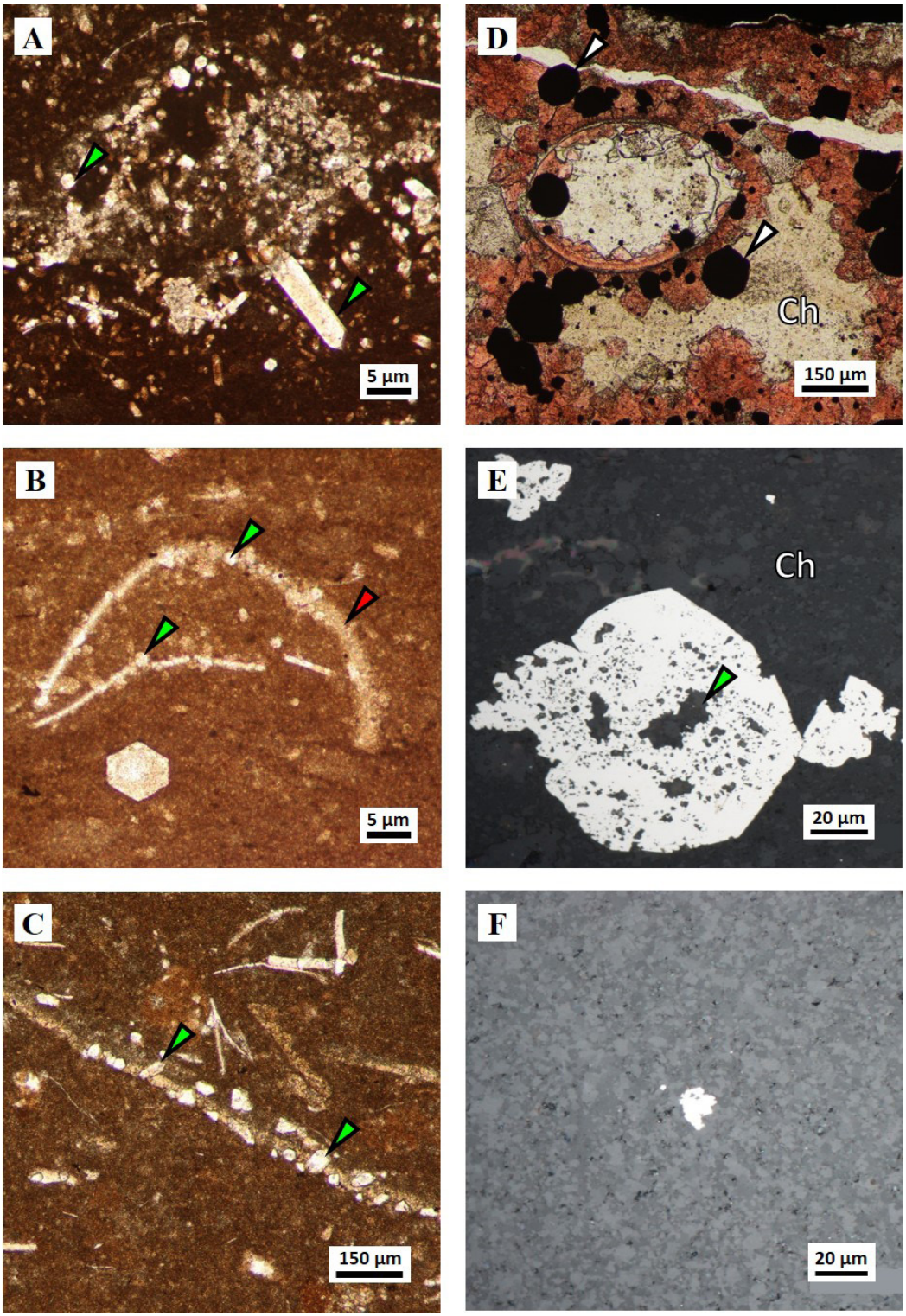

Figure 5.7. A. *TLP of euhedral quartz (arrows) within an aphanocrystalline dolomite matrix (dark brown area). Quartz crystals with dolomite inclusions; well: UT 15-13, sample: 11, 7009.9 ft; PPL.* ***B.*** *and* ***C.*** *TLP of euhedral quartz within aphanocrystalline dolomite matrix (light brown area). Some quartz (green arrows) crystallized along shells (red arrow); (B) Well: UT 15-13, sample: 11, 7009.9 ft; PPL. (C) Well: BBC 14-3, sample: 28, 7374.05 ft; PPL.* ***D.*** *TLP of fine crystalline pyrite with cubic and octahedral shape (arrows) associated with calcite (red areas) within a chert nodule (Ch); well: PW 13-06, sample: 11, 5552.3 ft.* ***E.*** *Reflected light photomicrograph of medium to coarse pyrite with octahedral shapes (bright area) that encloses aphanocrystalline dolomite (arrow) within a chert nodule (Ch); well: N 6-28, sample: 6, 8223.7 ft.* ***F.*** *Reflected light photomicrograph of very fine crystalline and framboidal pyrite (bright area) within dolomitized matrix; well: PW 13-06, sample: 10, 5545.3 ft.*

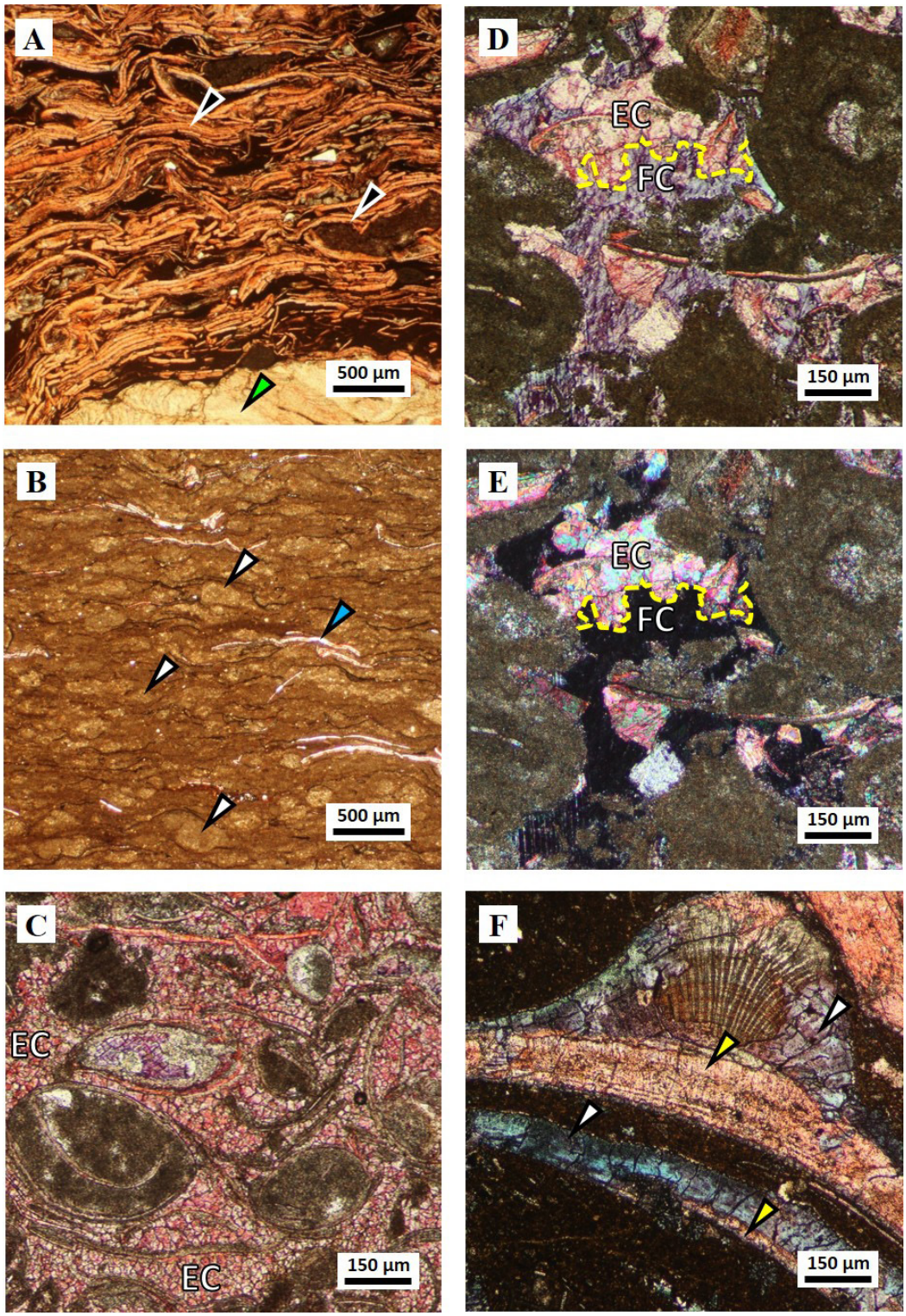

Figure 5.8. A. *TLP of densely packed ostracod (black arrows) and gastropod shell (yellow arrow); well: DS 11-20, sample 14, 5017 ft; PPL.* ***B.*** *TLP of elongated and dolomitized peloids (steinkerns?) (white arrows), and flattened ostracod shells (yellow arrow) aligned parallel to bedding; well: UT 15-13, sample: 7, 6989 ft; PPL.* ***C.*** *TLP of equant calcite (EC) in interparticle pores. Crystal size ranges from 10 to 20 µm; well: IU 16, sample: 14, 4729.9 ft; PPL.* ***D.*** *TLP of equant calcite cement (EC) and ferroan calcite cement (FC) in contact along a possible dissolution front (yellow dashed line); well: DS 11-20, sample: 13, 5000.3 ft; PPL.* ***E.*** *Crossed-polarized image of (D).* ***F.*** *TLP of partial dissolution of bioclast. Original metastable calcium carbonate of gastropod shell fragments (yellow arrows), which was partially dissolved and then filled by blocky ferroan calcite cement (white arrows); well: PW 13-06, sample: 14, 5565.9 ft.*

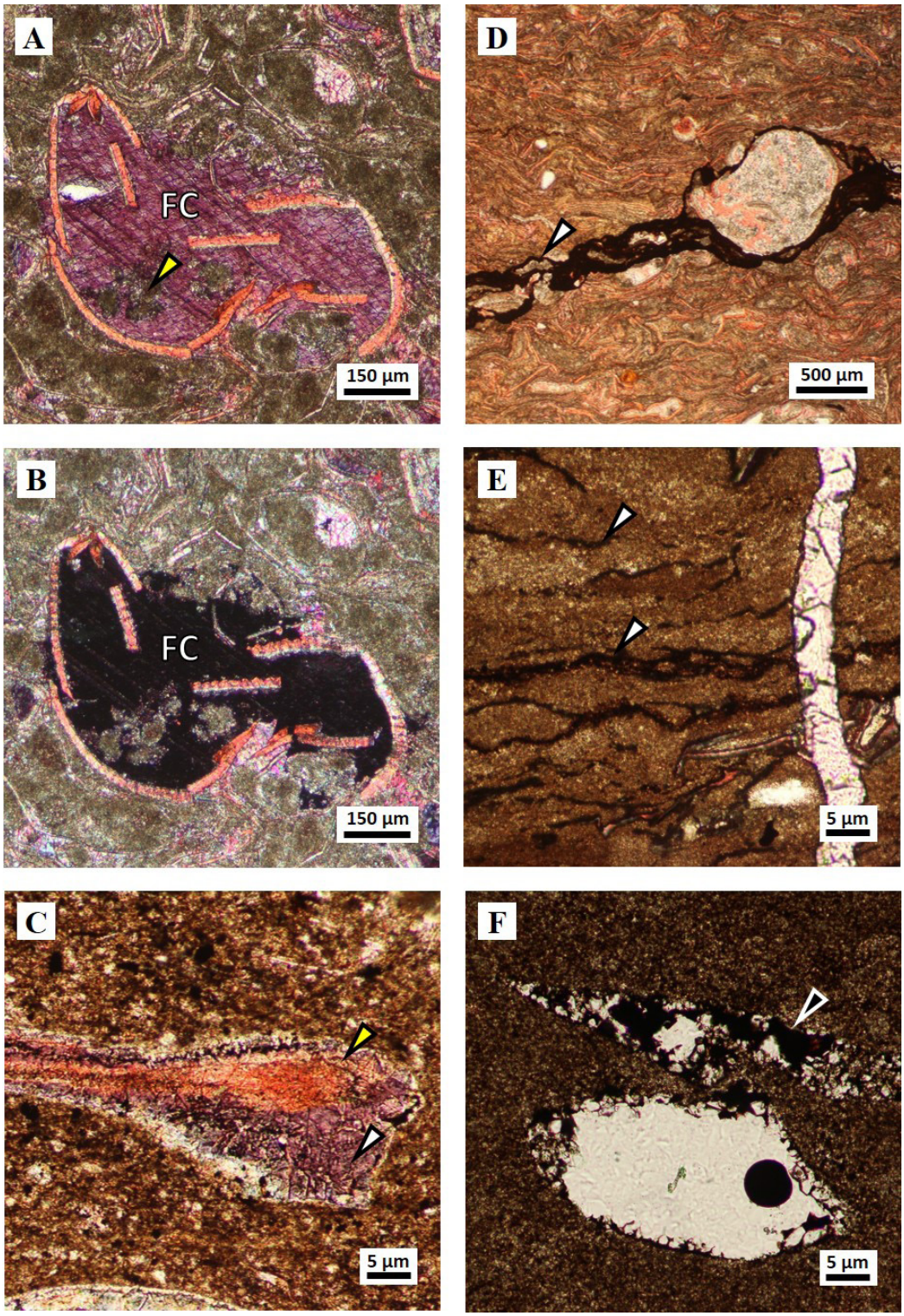

Figure 5.9. A. *TLP of blocky ferroan calcite cement (FC) in ostracod intraparticle pore (dark purple), encasing patches/clusters of microcrystalline dolomite (arrow); well: IU 16, sample: 14, 4729.9 ft; PPL.* ***B.*** *Crossed-polarized light image of (A).* ***C.*** *TLP of blocky ferroan calcite cement (white arrow) in space developed by partial dissolution of shell fragment (yellow arrow); well: BBC 14-1, sample: 6, 6666.5 ft; PPL.* ***D.*** *TLP of irregular to hummocky subhorizontal stylolites forming an anastomosing set (arrow); well: IU 16, sample: 16, 4733.2 ft; PPL.* ***E.*** *TLP of swarms of microstylolites or sutured seams (arrows), subvertical fracture post-dates stylolites and is filled by blocky calcite cement; well: UT 15-13, sample: 6, 6983.9 ft; PPL.* ***F.*** *TLP of hydrocarbon within intercrystal pores of dolomitized matrix and moldic pores; well: N 6-28, sample: 7, 8230.2 ft; PPL.*

5.1.1.16 Blocky ferroan calcite cement – Phase 10

Blocky ferroan calcite is a cement with crystals that vary in size from 50 to 200 µm. Ferroan calcite cement mainly fills intraparticle and interparticle pores and is usually associated with equant calcite cement of phase 8 (figures 5.9A and B). In some cases, this type of cement fills pores that resulted from the dissolution of shells of pelecypods and gastropods (figure 5.9C).

5.1.1.17 Subhorizontal stylolites and sutured seams – Phase 11

Subhorizontal stylolites and sutured seams are nearly parallel to bedding. Subhorizontal stylolites have an irregular to hummocky shape (Logan and Semeniuk, 1976) with amplitudes up to 20 µm and in some cases, compose an irregular anastomosing set (figure 5.9D). Swarms of microstylolites or sutured seams are common in dolostones (figure 5.9E).

5.1.1.18 Oil impregnation – Phase 12

Black oil (liquid phase) fills intercrystal, interparticle, and moldic pores (figure 5.9F), fractures, stylolites, and solution seams. Oil is present in all carbonate facies (F2 to F8). Textural relationships between oil impregnation and blocky calcite cement (phase 15) does not clarify the timing between these phases.

5.1.1.19 Subvertical stylolites and solution seams – Phase 13

Vertical stylolites are characterized by sharp to wavy boundaries and commonly columnar to wave-like peak stylolites (Logan and Semeniuk, 1976) with amplitudes up to 2500 µm, which crosscut bedding planes and carbonate grains (figure 5.10A). Subvertical stylolites are associated with subvertical fractures (figure 5.10A) and occur in both limestone and dolostone. Insoluble material has thicknesses ranging from 50 to 200 µm (figure 5.10B). These stylolites are preferentially developed toward the basin center in wells BBC 14-1, BBC 14-3, N 6-28, and UT 15-13.

5.1.1.20 Vertical fractures – Phase 14

Single or cluster vertical fractures are characterized by straight, branching, and stepped profiles nearly perpendicular to stratification (figure 5.10C). Fractures display apertures up to 50 µm. Fractures crosscut carbonate grains, chert nodules, and stylolites. Fractures are partially to filled with calcite cement of phase 15. There is no evidence of relative movement along the fractures.

5.1.1.21 Drusy calcite cement – Phase 15

Drusy calcite cement is made up of fibrous to bladed calcite crystals that vary from medium crystalline to blocky and very coarse crystalline in size (center of the void) and have well-defined twining (figures 5.10D and E). Calcite cement fills vertical fractures (phase 14) and stylolites (phase 13). These calcite crystals commonly contain hydrocarbons (oil) in fluid inclusions (figure 5.10F).

5.1.2 Interpretation

The paragenetic sequence defined in table 5.1 chronologically lists the products that were formed over the entire stratigraphic section of interest. The top of the table shows timing from early (after deposition) to late (present). Additionally, the base of the table shows diagenetic environments proposed by Machel (1999). The near-surface diagenetic setting occurs between zero and a few meters of depth and is controlled by surface waters, whether marine, fresh, or evaporitic. The shallow burial diagenetic setting is below the near-surface diagenetic setting down to about 1000 m, still heavily influenced, if not controlled by, surface-derived waters. The intermediate burial diagenetic setting is between about 1000 and 3000 m in depth, and the base coincides with the top of the liquid oil window, which varies in depth and is controlled by the geothermal gradient and kerogen type. Finally, the deep burial diagenetic setting encompasses the liquid oil window and extends down to the top of the metamorphic realm (Machel, 1999).

This section offers an interpretation of the diagenetic processes that created the various diagenetic products described in the previous section (5.1.1?) and provides an interpretation of the temporal designation for each diagenetic product based on textural relationships such as crosscutting features and cement textures. The term ‘phase’ is defined here as the time interval during which a particular diagenetic process created the product(s) listed in table 5.1.

5.1.2.1 Phase 1a–1b

Diagenesis transformed precursor lime sediments just after deposition in the near-surface diagenetic setting. The first diagenetic processes formed two products: cracks (phase 1a) and meniscus cement (phase 1b). These features were likely developed by subaerial exposure of unlithified sediment, in which, due to pore water evaporation, soft sediment shrinkage produced crack networks and/or circumgranular cracks (Esteban and Klappa, 1983). This process took place along the shoreline area, presumably during periods of subaerial exposure, although the observed cracks may also have formed subaqueously due to syneresis.

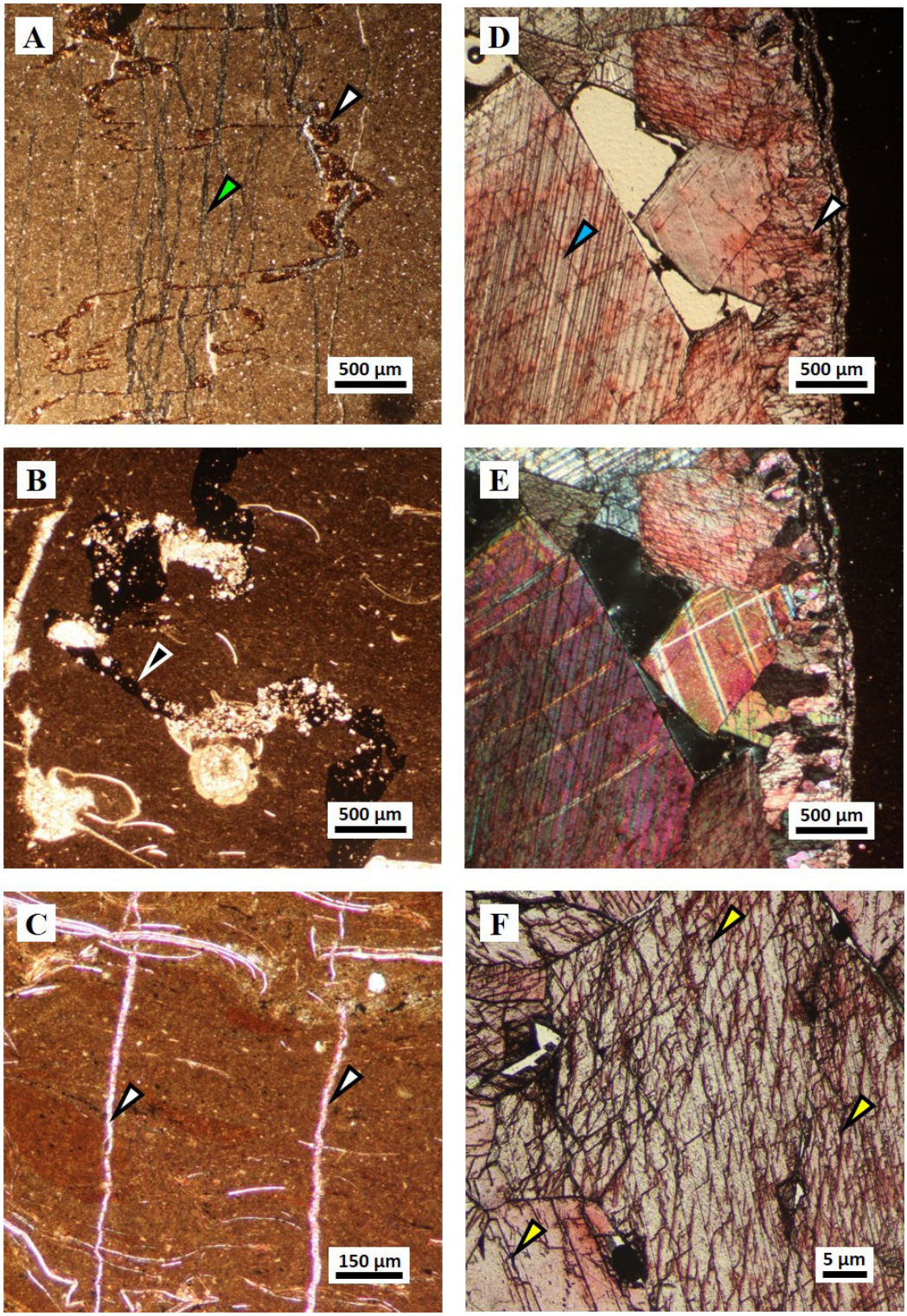

Figure 5.10. A*. TLP of subvertical serrated stylolites (white arrow) with amplitude up to 2500 µm associated to subvertical fractures (green arrow); well: N 6-28, sample: 1, 8199.3 ft; PPL.* ***B.*** *TLP of anastomosing sutured seam (arrow) that crosscuts stratification (horizontal axis); well: N 6-28, sample: 8, 8234.6 ft; PPL.* ***C.*** *TLP of subvertical fractures (arrows) that crosscut stratification (horizontal axis) and ostracod shells. Fractures filled by blocky calcite cement; well: BBC 14-1, sample: 20, 6701.4 ft; PPL.* ***D.*** *TLP of drusy calcite cement with crystal size increasing from medium crystalline (white arrow) at the stylolite wall toward a very coarse crystalline (blue arrow) in the center; well: N 6-28, sample: 12, 8267.4 ft; PPL.* ***E.*** *Crossed-polarized light image of (A).* ***F.*** *TLP of hydrocarbon (arrows) as inclusions in calcite crystals (entire photomicrograph); well: N 6-28, sample: 12, 8267.4 ft.*

The progressive evaporation of pore water in the vadose zone allowed crystallization of calcite as meniscus cement (James and Choquette, 1984) at or near carbonate grain boundaries. Vadose diagenesis took place only along the shoreline area located near the southern limits of the study area.

5.1.2.2 Phase 2a–2b–2c

Vertical fluctuations in the water table formed several diagenetic products. In phase 2a, meteoric water probably promoted dissolution of metastable carbonate minerals (Scholle and Ulmer-Scholle, 2003), forming molds and vugs. Cracks that had formed in phase 1 as well as molds and vugs of phase 2a were then filled with equant calcite cement. The dissolution of bioclasts and subsequent precipitation of equant and blocky calcite cement suggest early diagenesis within the meteoric-phreatic zone (Pingitore, 1976; Scholle and Ulmer-Scholle, 2003), which overlaps the near-surface and shallow burial diagenetic settings defined by Machel (1999).

Also during phase 2, lime mud was likely lithified to limestone (here identified as phase 2c), perhaps only partially and variably depending on proximity to the fluctuating lake shoreline, thereby forming semi-lithified carbonate material by virtue of an interplay of recrystallization (stabilization of metastable aragonite and/or high-magnesium calcite) and minor intergranular cementation (blocky calcite cement). Based on the petrographic evidence available, the degree of mineralogical stabilization and induration of the sediments prior to phase 3 cannot be determined.

5.1.2.3 Phase 3a–3b

Dolomite was formed by two different processes: the replacement of the precursor micrite matrix (phase 3a), and crystallization as cement (phase 3b). Moreover, dolomite cement crystals overgrew dolomite replacement crystals. This relationship suggests that these products (replacement and cements) precipitated from the same parental dolomitized fluid. Furthermore, the preservation of the parental limestone textures (figures 5.3, 5.4, and 6.8) and the fact that dolomitization was stratiform and created layers PZ1, PZ1′, and PZ2 that alternate with limestone layers suggests that dolomitization was a nearly synsedimentary process in the near-surface diagenetic environment. As such, the UBm dolomite layers conform to the type of dolomite known as penecontemporaneous (Budd, 1997; Warren, 2000; Machel, 2004). Dolomite formation likely was driven by slight to moderate degrees of evaporation, as further discussed in Section 5.2 and Chapter 6, Section 6.3.

5.1.2.4 Phase 4

Molds were created by the dissolution of bioclasts. This process occurred in the near- surface diagenetic environment where fluids dissolved ostracod shells and fragments (figures 5.5A to C). The dissolution of bioclasts may have been a by-product of dolomitization. Alternatively, and perhaps more likely, incursions of relatively fresh lake water and/or rain water during periods of subaerial exposure facilitated dissolution of non-dolomitized bioclasts.

5.1.2.5 Phase 5a–5b–5c

Bioclast dissolution and quartz crystallization likely took place at the same time (Maliva and Siever, 1989) and nearly contemporaneously with dolomitization and/or very soon thereafter. Furthermore, considering that silicified bioclasts do not show any reworking (disarticulated shells) or mechanical deformation (broken shells), silicification took place prior to mechanical compaction, thus also in the near-surface diagenetic environment. Primary calcium carbonate matrix and carbonate grains (intraclasts and peloids) now contained within chert nodules consist of dolomite, which indicates that dolomitization predated silicification.

Quartzine within chert nodules suggests that the silicification process was probably driven by evaporation (Folk and Pittman, 1971; Siedlecka, 1972; Heaney, 1995; Warren, 2006). The source of silica was likely the river water that fed the lake, and thereby from the eroding hinterland. Furthermore, the only recognizable evaporite mineral in the stratigraphic interval of interest is chert, and it is present as nodules encapsulating dolomite crystals within the PZ layers.

5.1.2.6 Phase 6

Pyrite can be formed as a by-product of either bacterial sulfate reduction (BSR) or thermochemical sulfate reduction (TSR) (Machel, 2001). BSR occurs at low temperatures commonly between 60° to 80°C, whereas TSR occurs in deep burial diagenetic settings at temperatures between 100°C to 140°C (Machel, 2001). In the UBm, pyrite formation must have taken place within the near-surface to shallow burial diagenetic settings. This interpretation is based on the textures and the occurrence of pyrite in the paragenetic sequence, as well as the maximum burial temperature of the study area. According to Schamel (2015), the maximum temperature was likely near 110°C based on burial history curves, which is too low for thermochemical sulfate reduction. The fact that pyrite is overall very low in abundance likely reflects that the lake water had a very low sulfate concentration, rather than low concentrations of iron or organic matter, both of which were abundant.

5.1.2.7 Phase 7

Mechanical compaction deformed the entire stratigraphic section of interest, generating densely packed mollusc layers, broken bioclasts, and elongation parallel to the bedding of semi-lithified components. Mechanical compaction likely took place throughout the near-surface and shallow burial diagenetic settings. The fact that many bioclasts show evidence of breakage further suggests that early diagenetic lithification was rather 'weak' overall, thus leaving many semi-plastic sedimentary layers in the shallow burial diagenetic setting (see phase 2c above). Phase 7 might have overlapped with dolomitization (phases 3a and 3b), silicification (phases 5a, 5b, and 5c), and pyritization (phase 6).

5.1.2.8 Phase 8

Equant calcite cementation likely occurred during and after mechanical compaction. The temporal interpretation of the calcite cement is based on crystal morphology and superposition with other diagenetic products.

5.1.2.9 Phase 9

A third generation of mold formed along with some vugs during phase 8, considering the types of cements that fill them (figure 5.8D to F), notably ferroan calcite. The cause for this dissolution phase cannot be ascertained but may have been another temporal freshening of the pore water after previous phases of evaporation that had formed dolomite and/or chert.

5.1.2.10 Phase 10

Ferroan calcite cement filled the remaining pores left by partial dissolution of calcite cement (figures 5.8D to F and 5.9C). The precipitation of ferroan calcite cement requires a reducing environment, which preferentially develops within intermediate and deep burial diagenetic settings (Machel, 1999; Scholle and Ulmer-Scholle, 2003; Flügel, 2010). The textural relationship of ferroan calcite cement with previous diagenetic products confirms this interpretation.

5.1.2.11 Phase 11

Continuous burial led to the development of subhorizontal stylolites and sutured seams caused by chemical compaction. Stylolitization took place in the intermediate and deep burial diagenetic settings (Machel, 1999; Flügel, 2010).

5.1.2.12 Phase 12

Oil was generated likely in the upper levels of the deep burial diagenetic setting, considering the (lacustrine) type of kerogen [types I and II; Schamel, 2015)] contained in the Green River Basin. According to Schamel (2015), the stratigraphic interval of interest underwent differential burial, in which the maximum depth for the northern part of the study area (depocenter) is estimated at 3700 m, and for the southern part of the study area (nearshore line) is around 2550 m. Schamel (2015) estimated that the northern part of the study area is presently within the wet gas window.

5.1.2.13 Phase 13

The subvertical stylolites were likely created by a tectonic compressive event (Ebner and others, 2010), in which the direction of the maximum compressive stress was likely subhorizontal, probably associated with the fast uplift and/or erosion rates (Schamel, 2015).

5.1.2.14 Phase 14

Vertical fractures may have formed during tectonic compression in a tri-axial stress field, or during uplift and/or erosion that took place 0.5 million years ago (Mya) (Schamel, 2015). Considering the current post-uplift depth of the strata of interest, phase 14 is placed into the intermediate burial diagenetic environment.

5.1.2.15 Phase 15

Drusy calcite cement partially fills some open subvertical fractures and stylolites (figures 5.10D to F). Calcite crystal sizes and texture variation suggest an intermediate burial diagenetic setting (Machel, 1999). Along the walls of subvertical stylolites and/or fractures, calcite crystals are medium crystalline with bladed texture, whereas at the center of the void, calcite crystals are very coarse crystalline with blocky texture.

5.1.3 Burial History

Schamel (2015) designed a burial history model for the GRF. In this model, the base of the GRF is defined by the UBm, which is located at the base of the GR-7 unit (figure 5.11). The maximum temperature that unit GR-7 reached was between 95°C and 120°C at a geothermal gradient of 25°C/km. However, the highest temperature of 120°C does not apply to the current study area because it was calculated for a synthetic well located farther north, representing the region of maximum burial.

Considering that the current study area is located between the depocenter and the nearshore settings of the Uinta Basin, the maximum burial temperature in the current study area is estimated to be ~110°C [based on extrapolation of Schamel's (2015) model] (figure 5.11).

The burial curve (figure 5.11) describes a high burial rate in the time interval from 55 to 40 Ma. Most of the identified diagenetic phases took place in the near-surface and shallow diagenetic settings from phase 1 through phase 9 between the time of deposition at about 55 Ma and 52 Ma; all of them took place in the first three million years (My) of deposition. Later, phases 10 and 11 occurred in the intermediate diagenetic setting between about 52 and 40 Ma. Thereafter, the burial rate decreased, as defined by reduction of the negative slope at 40 Ma, reaching the maximum burial depth around 3050 m at 20 Ma. Schamel (2015) estimated that the liquid oil window (phase 12) was passed between about 40 and 30 Ma (black dots in figure 5.11). The oil generation window defines the intermediate–deep diagenetic settings boundary (Machel, 1999) located around 2550 and 2850 m, followed by an extended period of no additional burial, as described by the horizontal contours between 20 and 10 Ma. Uplift of the basin started at about 10 Ma with an abrupt slope change at around 0.5 Ma, likely generated by high erosion rates (Schamel, 2015).

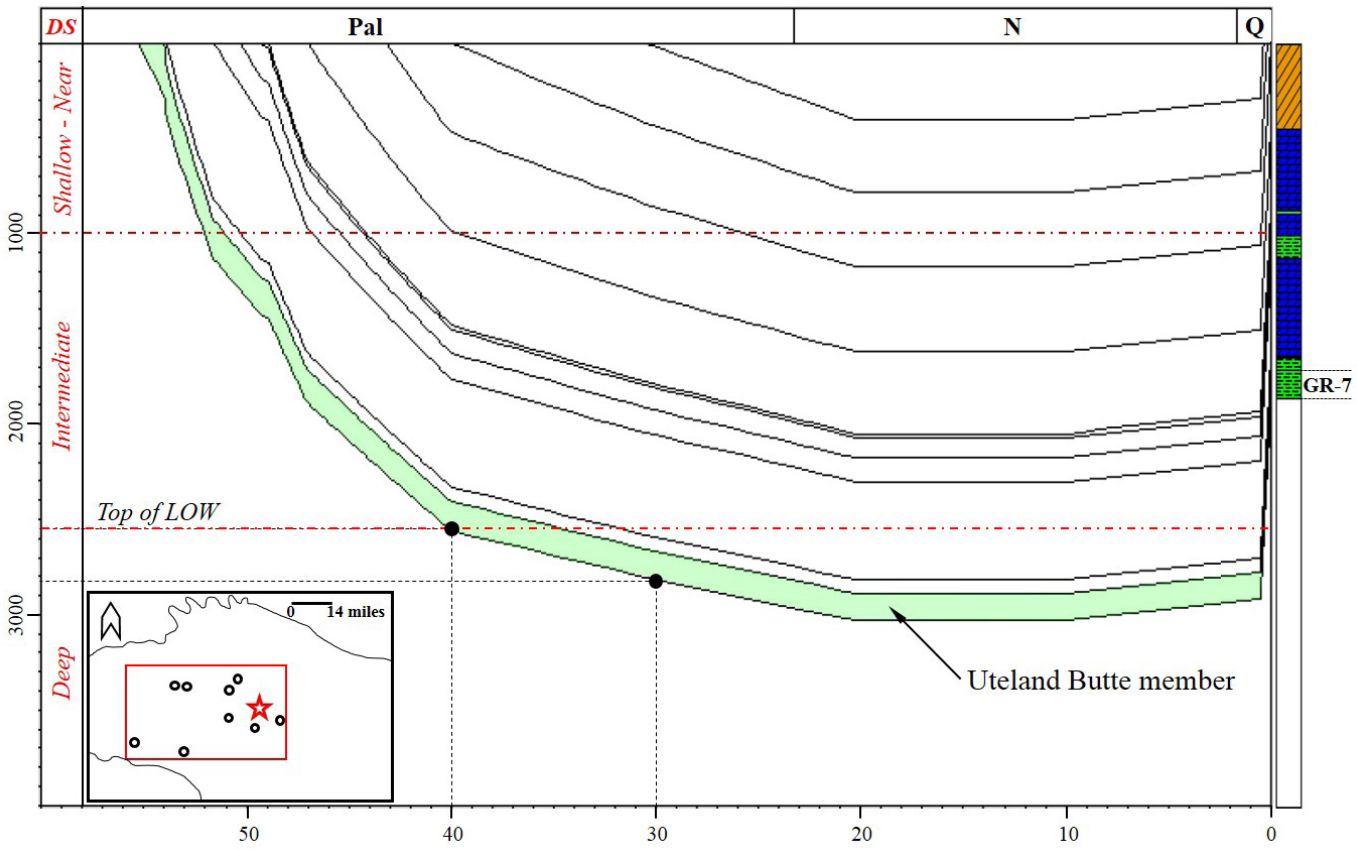

Figure 5.11. *Burial curve of a synthetic well located within the study area (red star in the inset map) correlated with diagenetic environments as identified in this study (left column), modified from Schamel (2015); DS: Diagenetic settings based on Machel's (1999) diagenetic environments, Pal: Paleogene, N: Neogene, Q: Quaternary, LOW: Liquid oil window.*

5.2 Dolomite

5.2.1 Observations

This section presents petrographic characteristics of dolomite obtained by scanning electron microscopy and cathodoluminescence microscopy, as well as compositional data such as Ca^{2+} content and cation ordering, and stable isotope and elemental composition.

5.2.1.1 Crystal shapes

A dip cross section to identify variations in dolomite textures from the nearshore areas toward the basin center was made using wells N 6-28, UT 15-06, and PW 13-06. Three thin sections were selected for PZ1, four thin sections were selected for PZ1′, and three thin sections were selected for PZ2 (figure 5.12).

PZ1, PZ1′, and PZ2 layers display four dolomite textures: planar-e (figure 5.13A), planar-s (figure 5.13B), nonplanar-a (figure 5.13C), and planar-c (figure 5.13D). Intercrystal voids are present in planar-s and nonplanar-a dolomites, probably from dissolution of calcium carbonate cores in phase 4 and/or phase 9 (table 5.1).

These textures display a distinctive distribution across the study area. For layer PZ1, planar-e dolomite is predominant in well PW 13-06 located nearshore, while nonplanar-a dolomite is more common in well UT 15-13 located in an intermediate zone. PZ1′ consists entirely of planar-e dolomite in the nearshore area (well PW 13-06) and near the basin center (well N 6-28), while nonplanar-a and planar-s dominate are at an intermediate zone. The PZ2 layer presents a different pattern in which the most abundant texture is planar-s dolomite in all three well locations (figure 5.14).

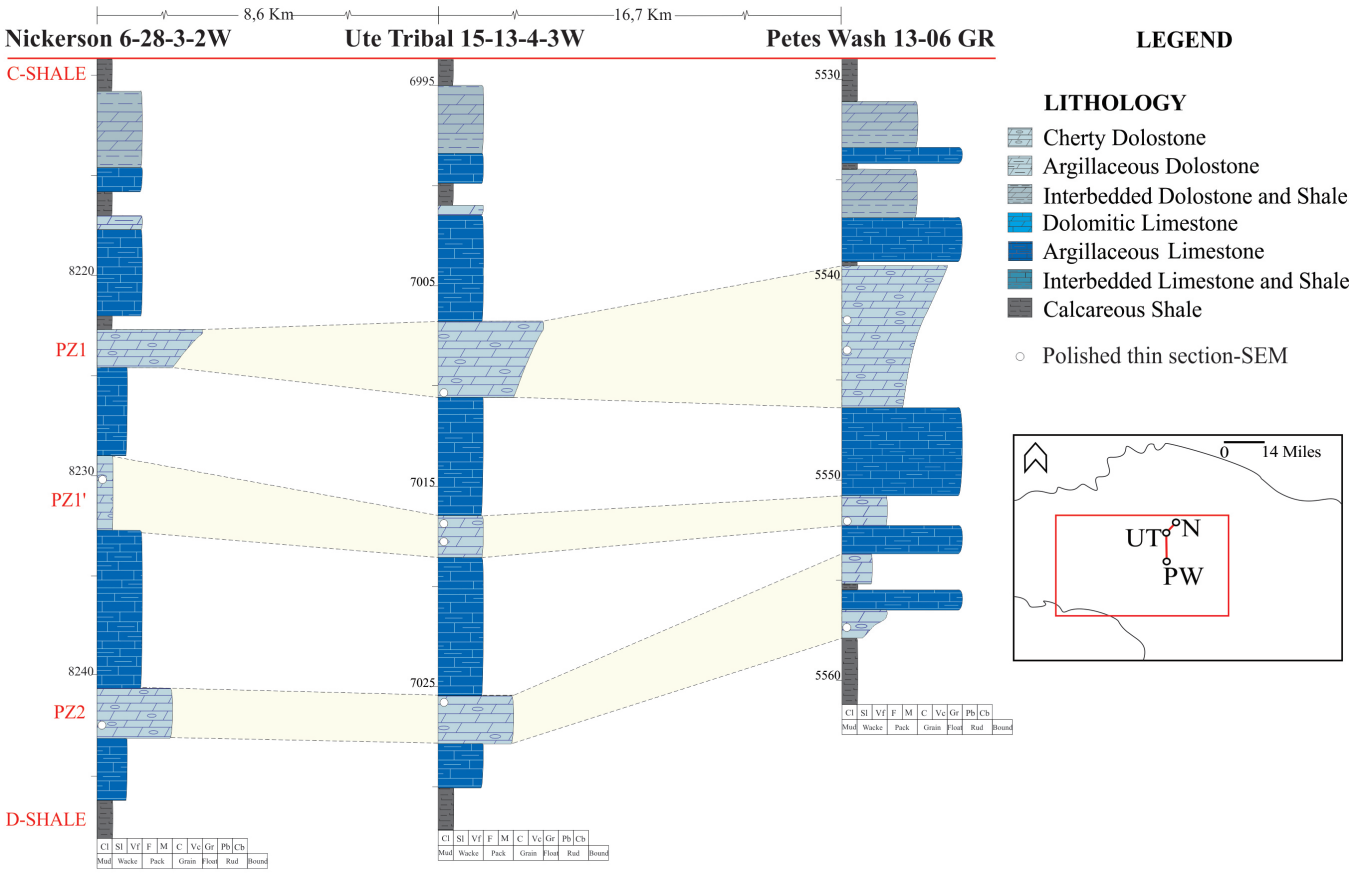

Figure 5.12. *Stratigraphic correlation of PZ layers with location (depth) of selected polished thin section for layers PZ1, PZ1', and PZ2. Numbers in the inset map stand for wells/outcrops as 1: BBC 14-1, 2: BBC 14-3, 3: N 6-28, 4: UT 15-13, 5: PW 13-06, 6: DS 11-20, 7: UI 16, 8: WCC, and 9: NMC.*

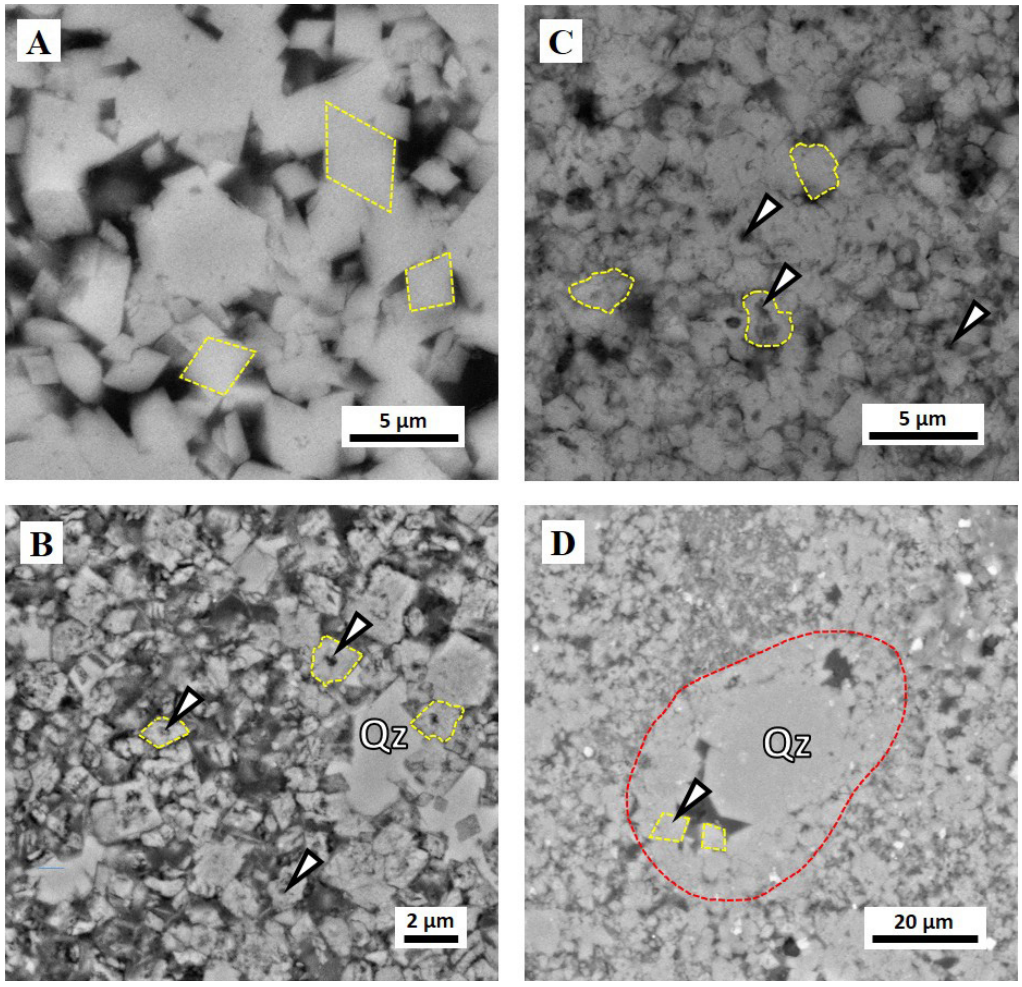

Figure 5.13. A. *SEM image of planar-e dolomite texture. Note the straight dolomite faces and well defined rhombohedral habit (yellow dashed lines); well: N 6-28, sample: 7, 8230.2 ft.* ***B.*** *SEM image of planar-s dolomite, some dolomite crystals have irregular faces (yellow dashed lines) and internal holes (white arrows); post-dolomitization authigenic quartz (Qz) encases some dolomite crystals; well: PW 13-06, sample: 12, 5557.4 ft.* ***C.*** *SEM image of nonplanar-a dolomite, dolomite crystals have irregular and lobate crystal faces (yellow dashed outlines) and internal holes (white arrows); well: UT 15-13, sample: 11, 7009.9 ft.* ***D.*** *SEM image of planar-c dolomite; interparticle pore (red dashed line) partially filled by dolomite cement (yellow dashed outlines) and authigenic quartz (Qz); well: N 6-28, sample: 9, 8242.5 ft.*

5.2.1.2 Crystal sizes

Identification of dolomite crystal sizes was based on the following steps. First, individual dolomite crystal size was measured according to crystal shape. For euhedral and subhedral crystals, two of the straight edges of the rhomb were measured. For anhedral crystals, the largest and shortest crystal diameter were measured. Secondly, the crystal sizes were grouped according to crystal size frequency distribution. Clustering dolomite crystal sizes using frequency distribution was inconclusive because the histograms do not show natural breaks (valleys). The Jenks natural breaks classification method was used because it minimizes the standard deviation of the selected group and maximizes the standard deviation between groups (Jenks, 1967).

As a result, three dolomite crystal populations emerged: population one (POP 1), ranging from 0.25 to 1.5 µm; population two (POP 2), ranging from 1.5 to 3.0 µm; and population three (POP 3), ranging from 3.0 to 6.0 µm. POP 1 is the most abundant with 53.7%, followed by POP 2 with 37.7%, and POP 3 with 8.6 % (figure 5.15). These three dolomite populations are present in all measured samples in about the same relative proportion. The means and standard deviations of the measured crystals are summarized in table 5.2, grouped by dolomite layer. The dolomite crystal size populations do not present any preferential distribution along the N-S cross section of figure 5.12.

The dolomite crystal size distribution (CSD) shows a right-skewed distribution with major crystal size concentration around the lowest values (0.25 µm to 2.5 µm) and a tail located at the highest values (6 µm) (figure 5.16). The peak around 0.25 µm to 2.5 µm is composed of POP 1 and POP 2, whereas the tail (3 µm to 6 µm) is composed mainly of POP 3. All dolomite PZ layers display the same distribution.

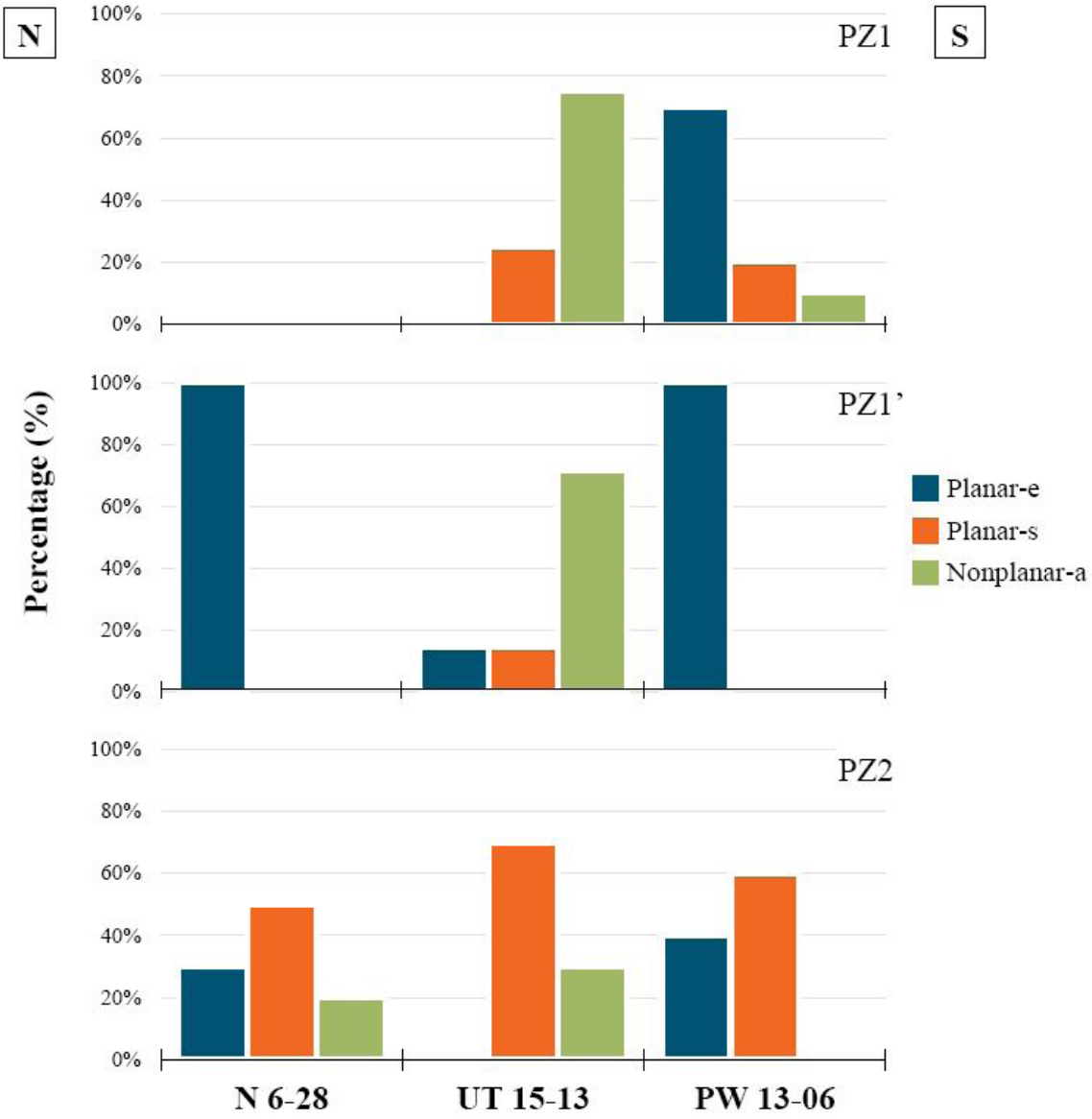

Figure 5.14. *Distribution of dolomite textures for each PZ layer. N: North, S: South. The cross section is shown in figure 5.12.*

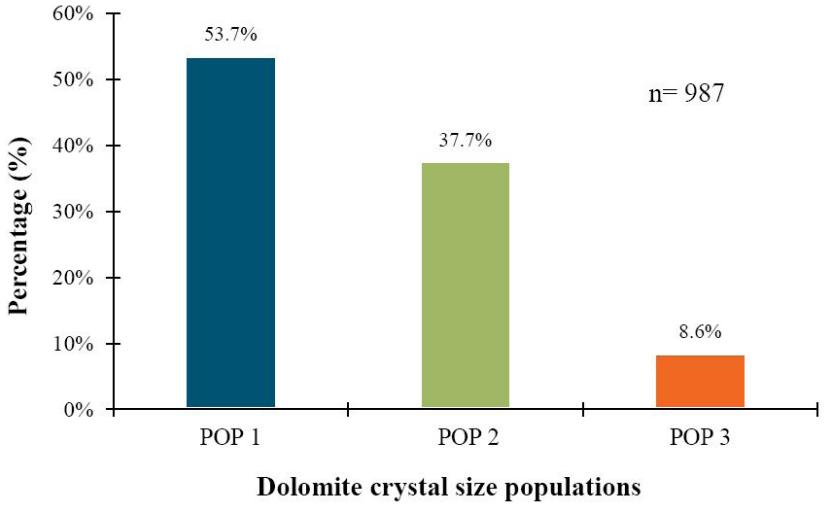

Figure 5.15. *Percentage distribution of dolomite crystal size populations. POP 1: 0.25 µm to 1.5 µm, POP 2: 1.5 µm to 3.0, POP 3: 3.0 µm to 6.0 µm.*

Table 5.2. *Mean size and standard deviation (St.Dev) of dolomite crystals.*

Well	Sample	Depth (ft)	Layer	Mean size (µm)	St.Dev (µm)	n
UT 15-13	11	7009.9	PZ1	1.3	0.67	193
PW 13-06	7	5541.9	PZ1	2.4	0.94	80
PW 13-06	8	5543.5	PZ1	2.2	0.98	86
N 6-28	7	8230.2	PZ1'	2.0	0.90	78
UT 15-13	12	7016.4	PZ1'	1.6	0.80	125
UT 15-13	13	7017.4	PZ1'	1.5	0.50	54
PW 13-06	11	5552.3	PZ1'	2.7	1.11	19
N 6-28	9	8242.5	PZ2	1.7	0.78	100
UT 15-13	14	7025.2	PZ2	1.4	0.65	128
PW 13-06	12	5557.4	PZ2	1.3	0.54	124

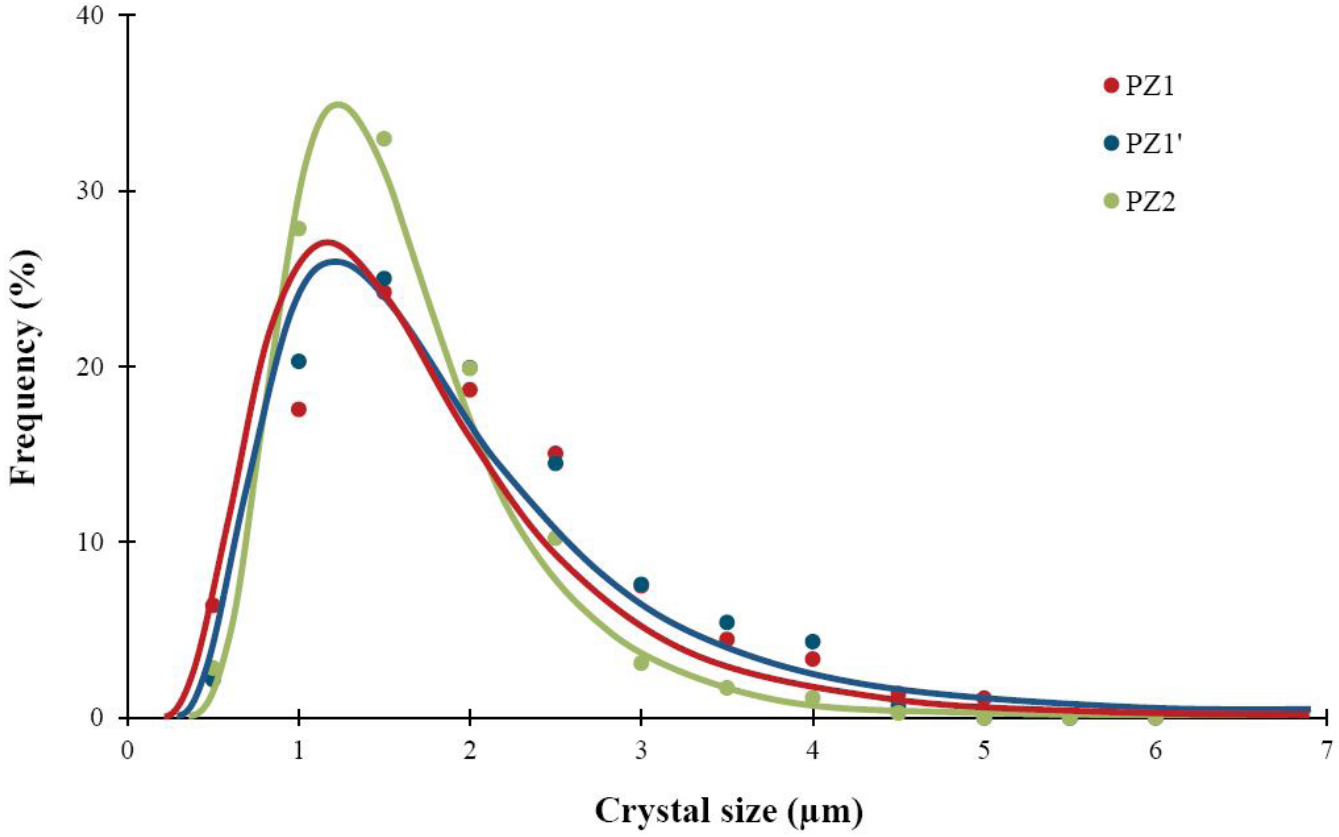

Figure 5.16. *Dolomite crystal size distribution for each PZ layer. All PZ layers present a right-skewed and left tail distribution.*

The right-skewed and left tail distribution was validated through the Anderson-Darling statistical test (Anderson and Darling, 1954), considering the normal distribution as the null hypothesis. In figure 5.17A, the data (red dots) deviate from the normal probability (blue line), obtaining an AD (Anderson-Darling) value of 16.301. In contrast, in figure 5.17B most of data (red dots) fit with the lognormal probability (blue line), with an AD value of 1.617. Comparing AD values of both cases (A and B), the normal distribution has the highest AD value. In this case, the null hypothesis (CDS as normal distribution) is rejected. Dolomite CSD for PZ layers presents a better approach to a lognormal distribution.

5.2.1.3 Cathodoluminescence

The electron beam excitation on the surface of dolomite crystals does not display any visible luminescence characteristics either through a microscope (figure 5.18) or through the cathodoluminescence (CL) detector attached to the SEM.

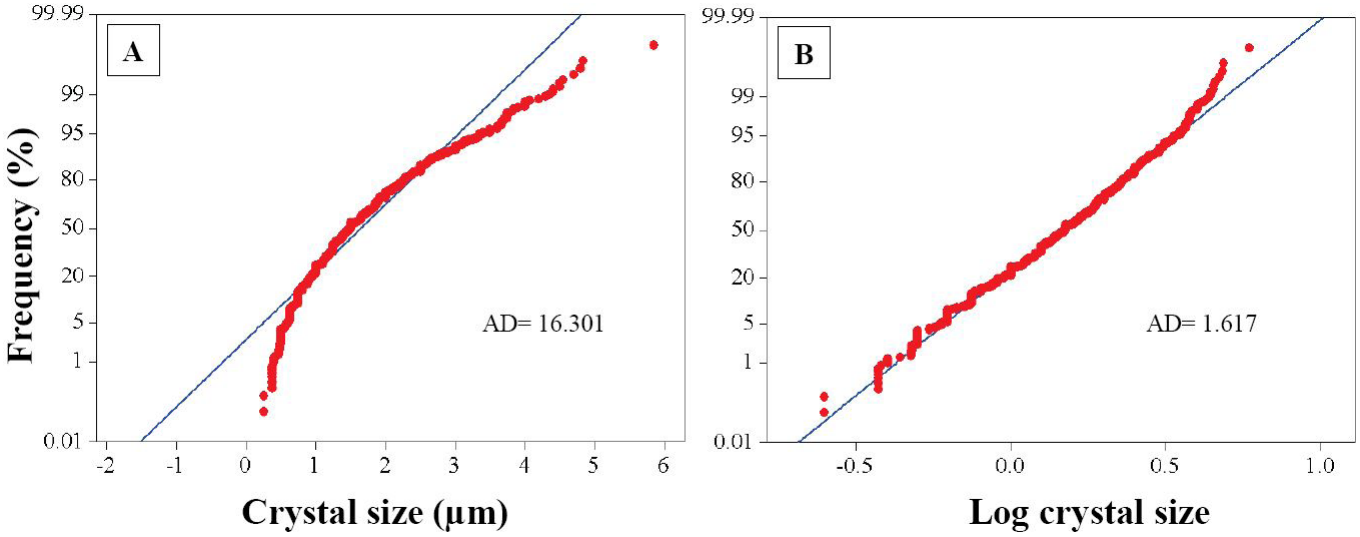

Figure 5.17. *Validation of dolomite CSD: A. normal and B. lognormal distributions. AD: Anderson-Darling value.*

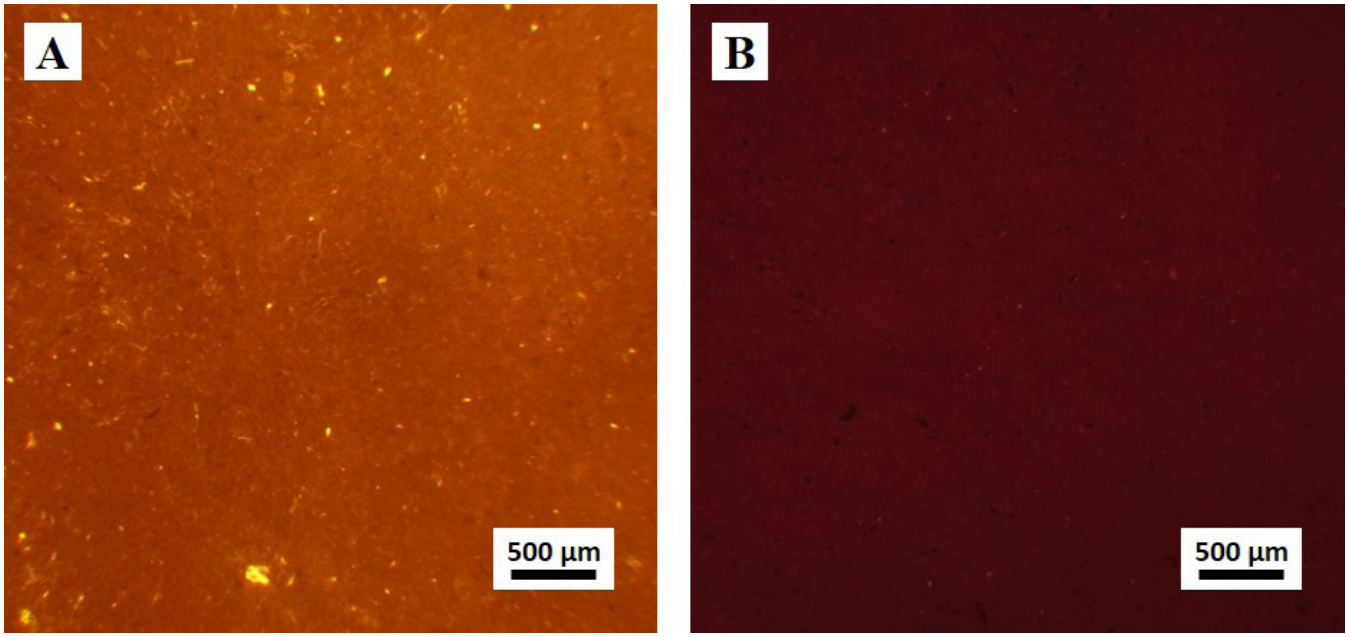

Figure 5.18. A. *TLP of dolomudstone at the base of PZ1 with dolomite crystals in matrix (dark red area); well: PW 13-06, sample: 10, 5545.3 ft.* ***B.*** *Cathodoluminescence photomicrograph of the same area in (A) with no visible luminescence contrast.*

5.2.1.4 Stoichiometry

Dolomite stoichiometry was identified by XRD and EMPA data. This section compares the dolomite calcium mole percentage from XRD and EMPA. The XRD data is from Indiana University because the diffractograms from this lab show the greatest detail (split peaks, asymmetries). Comparison and discussion of XRD data from different laboratories is detailed in appendix E.

The high resolution diffractograms from Indiana University display three remarkable characteristics: (i) a d_{104} dolomite peak is displaced toward lower 2θ values relative to the ideal dolomite peak; (ii) the d_{104} dolomite peak is usually split into "subpeaks" with side humps (asymmetrical peak); and (iii) the d_{104} dolomite peak is rather broad (figure 5.19). All dolomite samples run at Indiana University (14 samples) show the same or similar pattern.

The observed XRD diffraction pattern could be related to: (i) iron substituting for magnesium, (ii) calcium substituting for magnesium, and/or (iii) different dolomite chemical populations (Kaczmarek and Sibley, 2011). Both Fe^{2+} and excess Ca^{2+} cations within the crystal lattice causes a shift of the d_{104} dolomite peak toward lower 2θ values.

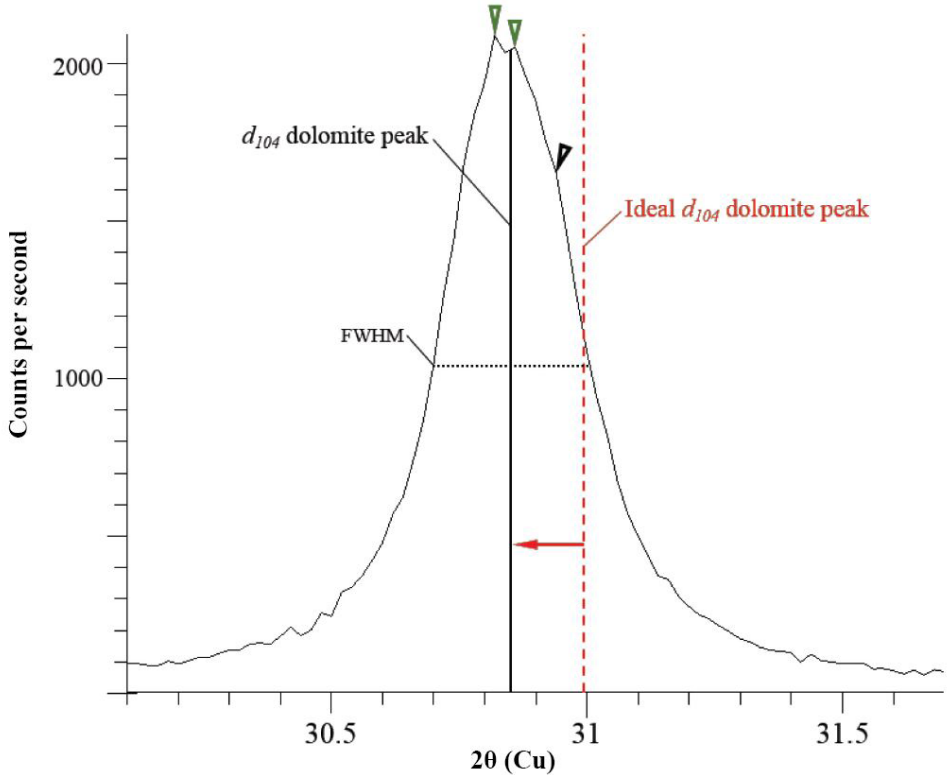

Figure 5.19. *High-resolution diffractogram of the* d_{104} *dolomite peak that displays three remarkable characteristics: (i)* d_{104} *peak (30.86°2θ represented by vertical black line) shifted toward lower 2θ values (ideal dolomite* d_{104} *peak, red dashed line), in this particular sample = 0.13°2θ (left red arrow); (ii) split* d_{104} *peak (green arrows) and side humps (black arrow) that define an asymmetrical* d_{104} *reflection; and (iii) wide peak with a full width of half maximum intensity (FWHM) of 0.31°2θ, higher that the ideal dolomite [FWHM= 0.155°2θ for Eugui dolomite (Jones and others, 2001)]. Well PW 13-06, sample: 8, 5543.5 ft. XRD diffractogram from Indiana University (Cukα radiation).*

The possibility of Fe^{2+} causing the observed broadening and/or the shifting of the d_{104} peak can be discounted on the basis of energy-dispersive X-ray spectroscopy (EDS), EMPA, and ICP-MS data (appendices 4, 6, and 7 respectively), none of the which showed Fe^{2+} values higher than 1% Fe (EDS = 0.2%, EMPA = 0.2%, ICP-MS = 0.9%; all values are arithmetic means). Hence, the observed patterns are interpreted as resulting from Ca^{2+} excesses. Furthermore, the split in the d_{104} dolomite peak is likely generated by at least two calcian dolomite populations (e.g., Jones and others, 2001).

The dolomite calcium mole percentage ($\%Ca_{Dol}$) was calculated using the equation proposed by Lumsden (1979), in which there is a direct correlation between the Ca^{2+} mole percentage and the position of the d_{104} peak of dolomite crystals:

$$NCaCO_3 = 333.33 * d - 911.99 \quad (1)$$

where $NCaCO_3$ is the dolomite calcium content in mole percentage, and d is the d-spacing of the d_{104} peak, calculated using the Bragg law:

$$\text{Sin } \theta = \lambda/2d \quad (2)$$

where θ is the reflected angle, λ is the wavelength of Cu Kα radiation, and d is the spacing value between crystal lattices. Equation 2 in 1:

$$NCaCO_3 = [333.33 * (\lambda/2*\text{Sin } \theta)] - 911.99 \quad (3)$$

The resulting $\%Ca_{Dol}$ values for all samples analyzed are listed in appendix E. The calculated $\%Ca_{Dol}$ values, obtained using Lumsden's equation, are subject to errors as neither Equations 1 nor 3 consider other features that affect the d-spacing. These features include heterogeneous cation replacement that causes an estimated error between 1 to 2.5 $\%Ca_{Dol}$ (Reeder and Sheppard, 1984). However, the error could be even larger given the presence of several dolomite populations, each with a different $\%Ca_{Dol}$ composition (Reeder and Sheppard, 1984).

For the dolomites of the UBm, an estimation of the $\%Ca_{Dol}$ error using the Lumsden equation was performed by comparing the $\%Ca_{Dol}$ values calculated from XRD data to the $\%Ca_{Dol}$ values measured from EMPA data (table 5.3 and figure 5.20). The EMPA $\%Ca_{Dol}$ values were taken as base of reference because (1) the precision and accuracy (0.4 to 0.5 $\%Ca_{Dol}$) is considerably smaller than the XRD data and (ii) EMP is able to measure individual dolomite crystals. Previous to the measurement, the EMPA was calibrated against the dolomite (internal) standard for Ca, Mg, Sr, Fe, and Mn. The calculated $\%Ca_{Dol}$ values from EMPA data were determined by the relationship between the Ca and Mg molar fraction as defined:

$$\%Ca_{Dol} = ({}^{m}Ca / ({}^{m}Ca + {}^{m}Mg)) \times 100 \quad (4)$$

where m is the molar fraction.

The frequency distribution of the EMPA data was plotted for each sample (figure 5.20B). Each bin represents a different $\%Ca_{Dol}$ population (Bin in table 5.3, "B" in figure 5.20B). The arithmetic mean of each bin was compared to the probable correlative $\%Ca_{Dol}$ population (from XRD data) represented by sub-peaks and humps recorded in each diffractogram (blue vertical lines in figure 5.20A). The calculated difference of $\%Ca_{Dol}$ (arithmetic mean) between EMPA and XRD is 0.5 %Ca. As a result, the difference between EMPA and XRD data from Indiana University laboratory is considered negligible.

This affirmation is additionally confirmed by the strong positive correlation (R^2=0.7) between the $\%Ca_{Dol}$ (EMPA data) versus the d_{104} spacing (calculated from XRD data using equation 2) (figure 5.21). As result, the XRD data from Indiana University laboratory is considered the base of reference between the University of Alberta and Western Michigan University laboratories.

The UBm dolomites display a wide range of $\%Ca_{Dol}$, from 49% to 59%. The $\%Ca_{Dol}$ distribution for each PZ layer is shown in figure 5.22. Each dolomite layer displays a different frequency distribution. PZ1 has a multimodal $\%Ca_{Dol}$ distribution with the near stoichiometric mode between 49 and 52 $\%Ca_{Dol}$ (14%), followed by a strong mode between 53 and 55 $\%Ca_{Dol}$ (83%), and a third mode between 58 and 59 $\%Ca_{Dol}$ (3%). PZ1′ displays a multimodal $\%Ca_{Dol}$ distribution with three different modes: a near stoichiometric mode between 51 and 54 $\%Ca_{Dol}$ (65%), a second mode between 55 and 56 $\%Ca_{Dol}$ (23%), and a third one between 57 and 58 $\%Ca_{Dol}$ (12%). In contrast, PZ2 describes a bimodal distribution with a broad mode between 51 and 55 $\%Ca_{Dol}$ (85%) and a second mode between 56 and 58 $\%Ca_{Dol}$ (15%) (figure 5.22).

Combining all data, the dolomites form two major populations: (i) Population 1 ($POP1_{\%Ca}$) varies widely from 49 to 56 $\%Ca_{Dol}$, and (ii) Population 2 ($POP2_{\%Ca}$) ranges from 56 to 59 $\%Ca_{Dol}$ (figure 5.23). $POP1_{\%Ca}$ contains 92% of all data. These dolomites are calcium-rich (or calcian) dolomites according to Gregg and others (2015) definition.

Table 5.3. *Comparison of $\%Ca_{Dol}$ values obtained from XRD (Indiana University) and EMPA. The difference of the %Ca between XRD and EMPA (Δ) was calculated taking as base of reference the values from EMPA data. EMPA-XRD arithmetic mean = 0.5.*

	XRD			**EMPA**			**Δ**
	Subpeak	d_{104} (2θ)	$\%Ca_{Dol}$	Bin	n	$\%Ca_{Dol}$	EMPA-XRD
6-28-7	P1	30.92	51.22	B4	48	52.6	1.4
	P2	30.88	52.43	B5	60	53.3	0.9
	P3	30.86	53.04	B6	4	54.3	1.3
15-13-14	P1	30.90	51.83	B3	8	51.7	-0.1
	P2	30.88	52.43	B4	28	52.5	0.1
	P3	30.84	53.65	B5	4	53.8	0.1
	P4	30.82	54.27	B7	1	55.8	1.5
13-06-8	P1	30.94	50.61	B2	1	50.9	0.3
	P2	30.90	51.83	B3	5	51.6	-0.2
	P3	30.85	53.35	B4	9	52.7	-0.6
	P4	30.82	54.27	B5	22	53.5	-0.7
	P5	30.78	55.49	B6	22	54.4	-1.1
	P6	30.75	56.41	B7	1	55.0	-1.4
13-06-11	P1	30.86	53.04	B7	6	55.5	2.5
	P2	30.82	54.27	B8	18	56.5	2.2
	P3	30.78	55.49	B9	22	57.5	2.0
	P4	30.74	56.72	B10	4	58.3	1.6

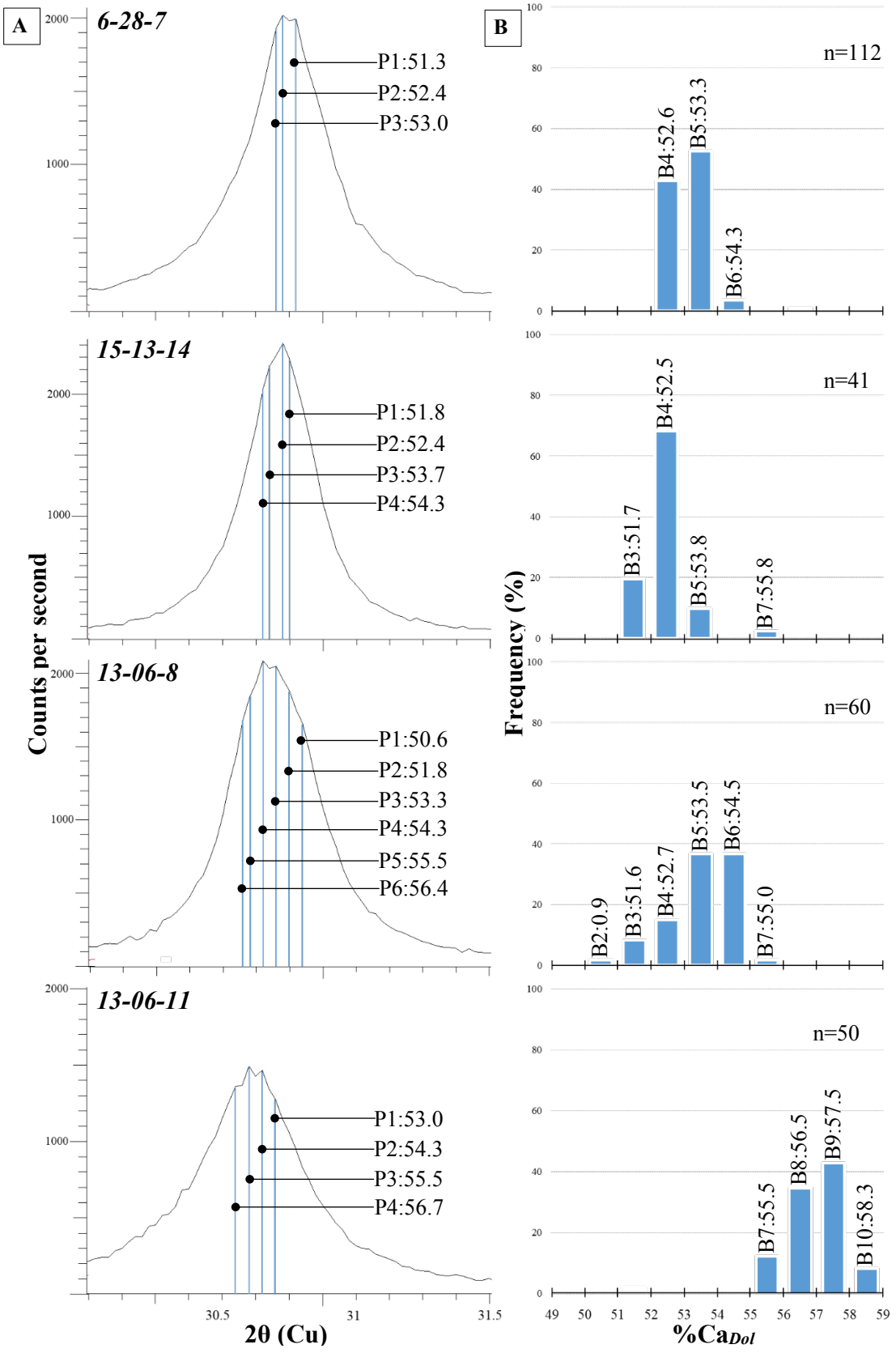

Figure 5.20. *Graphic comparison between the %Ca_{Dol} values calculated from (A) XRD data and (B) EMPA data.* ***A.*** *All samples show a split* d_{104} *peak with one or several humps, each of them possibly represents a different %Ca_{Dol} population with a unique* d_{104} *at different 2θ value. Each* d_{104} *"subpeak" is represented by a blue line. The calculated value of %Ca_{Dol} for each inferred population is indicated at the right side of each* d_{104} *"subpeak".* ***B.*** *%Ca_{Dol} frequency distribution for each sample measured by EMPA. The %Ca_{Dol} arithmetic mean for each population is indicated at the top of each bin.*

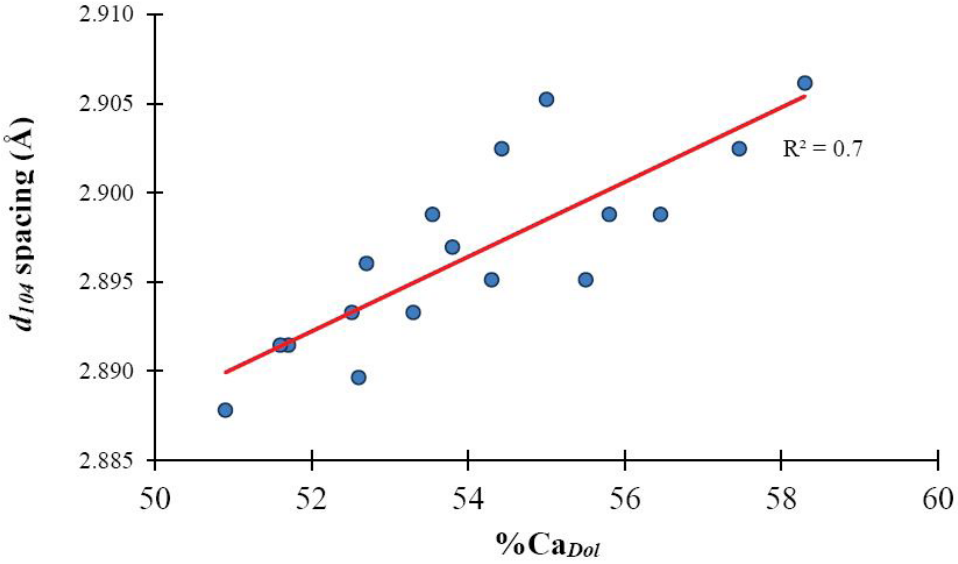

Figure 5.21. *Correlation between* d_{104} *(vertical axis) calculated from XRD data and %Ca*$_{Dol}$ *(horizontal axis) calculated from EMPA data. Red line: linear regression.*

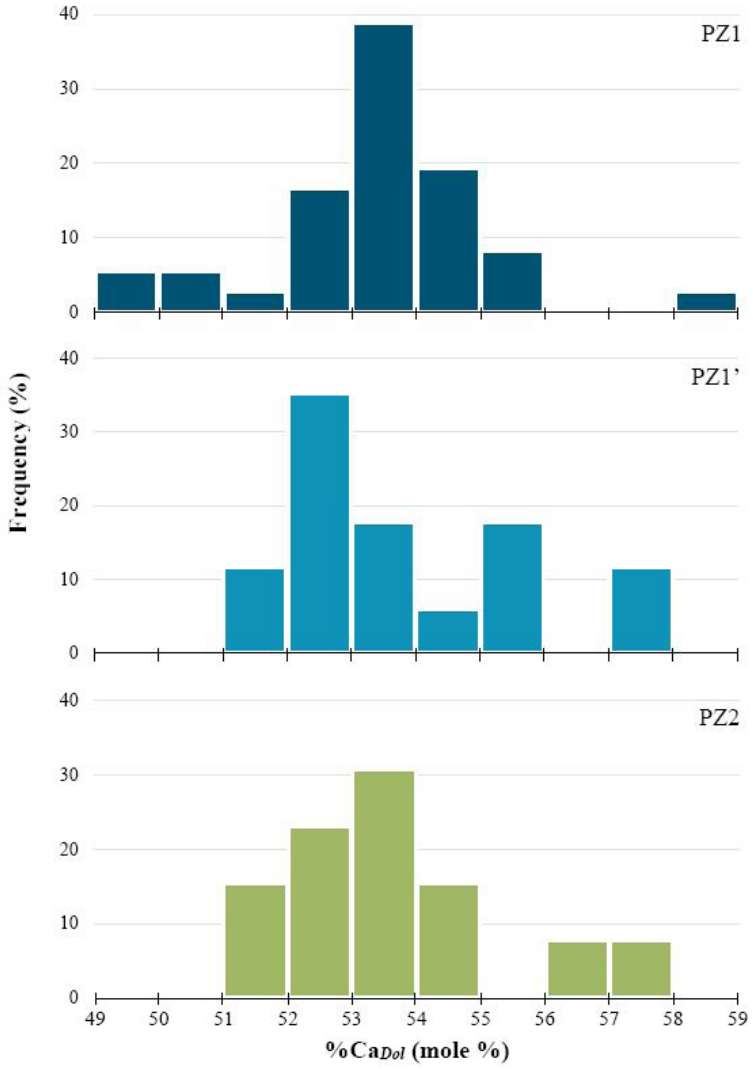

Figure 5.22. *Frequency distribution of calcium mole percentage in dolomite crystals (%Ca*$_{Dol}$*) for each PZ layer. %Ca*$_{Dol}$ *calculated by mean of the equation by Lumsden (1979).*

Calcium excess in dolomite crystals also displays a vertical trend in which the more stoichiometric dolomite crystals are preferentially at the top of the PZ layers, whereas the non-stoichiometric dolomite crystals are preferentially at the base of the PZ layers (figure 5.24). This trend is clearly defined in the PZ1 layer, well PW 13-06, in which there is a strong correlation between $\%Ca_{Dol}$ and depth (R^2=0.8) (figure 5.25).

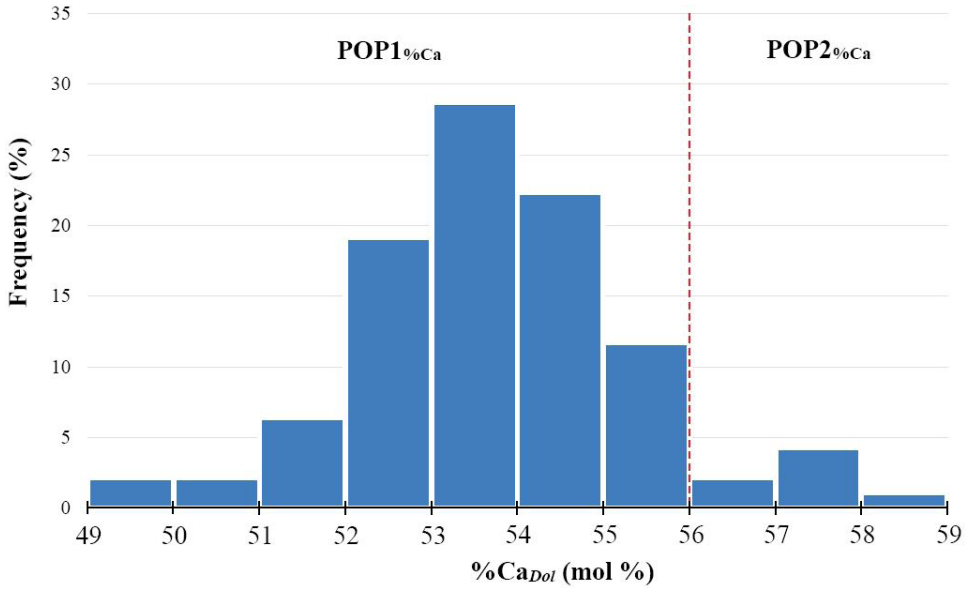

Figure 5.23. *$\%Ca_{Dol}$ populations. $POP1_{\%Ca}$ fluctuates between 49 to 56.5 %Ca and $POP2_{\%Ca}$ fluctuates between 56.5 to 59 %Ca. $POP1_{\%Ca}$ is the most abundant (92%).*

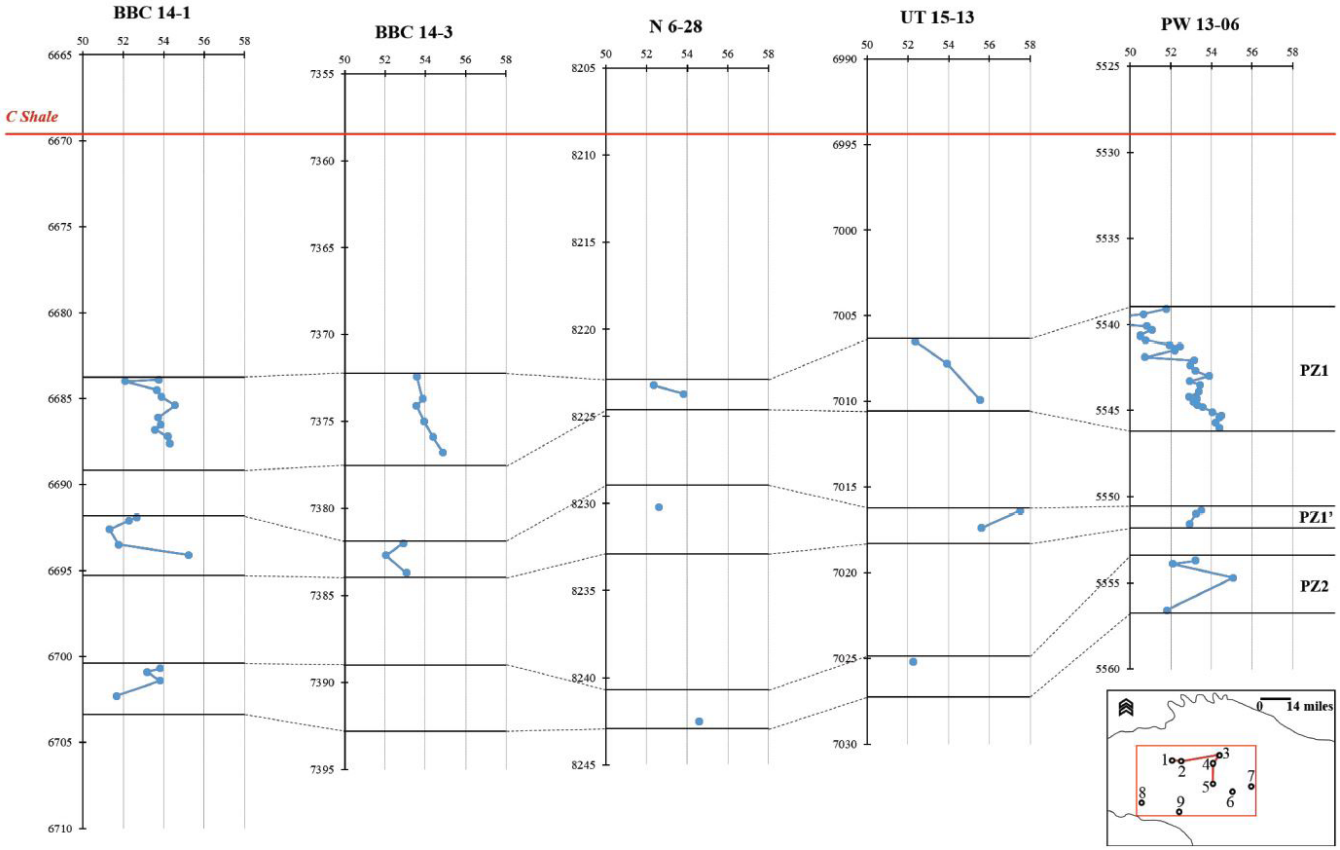

Figure 5.24. *Dolomite stoichiometry variation in depth; horizontal axis: $\%Ca_{Dol}$ (%), vertical axis: depth (ft). See map inset for well locations; numbers in the inset map stand for wells/outcrops as 1: BBC 14-1, 2: BBC 14-3, 3: N 6-28, 4: UT 15-13, 5: PW 13-06, 6: DS 11-20, 7: UI 16, 8: WCC, and 9: NMC.*

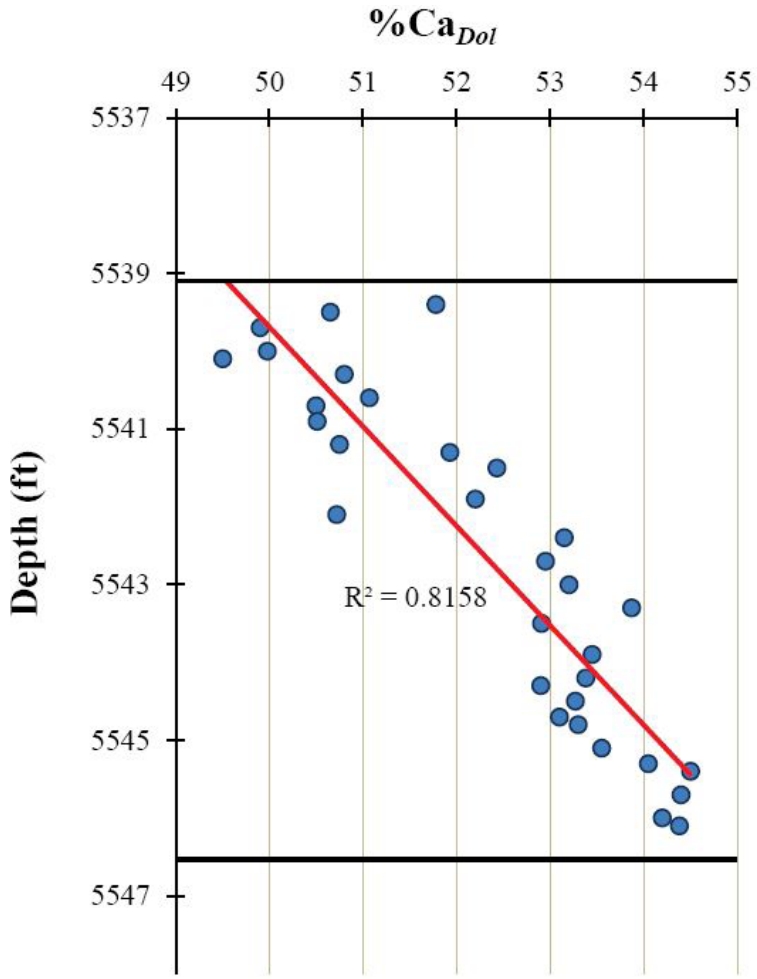

Figure 5.25. *$\%Ca_{Dol}$ variation with depth. Data for PZ1 layer, well PW 13-06. Black horizontal lines: top and base of the PZ layer, red line: linear regression.*

5.2.1.5 Ordering

The XRD diffractogram also offers information on dolomite cation ordering characteristics. Goldsmith and Graf (1958) defined a calcium-magnesium bearing carbonate mineral as dolomite if the crystal displays d_{110}, d_{015}, and d_{021} ordering peaks relative to the 100% of d_{104} dolomite peak. The degree of cation ordering was calculated according to the Goldsmith and Graf (1958) definition (d_{015} / d_{101}).

Intensities of d_{015} and d_{101} peaks were obtained from XRD data. Dolomites are thus characterized by low cation ordering values varying from 0.1 to 0.5, with a mean of 0.27 and standard deviation of 0.03 (table 5.4). The dolomite cation ordering and $\%Ca_{Dol}$ relationship shows a trend in which the highest cation ordering values (>0.3) are from nearly stoichiometric dolomites (49 to around 54 %Ca) and the lowest cation ordering values (0.1 to 0.3) are from calcium-rich dolomite (around 54 to 58 %Ca) (figure 5.26).

Ordering also varies with depth in which the more ordered dolomites are located at the top of the PZ layers and the disordered dolomites are preferentially located at the base of the PZ layers. This trend is also well defined in the PZ1 layer, well PW 13-06, in which there is a strong correlation between ordering and depth (R^2=0.7) (figure 5.27).

5.2.1.6 Conventional carbon and oxygen isotope data

The carbon and oxygen isotope values for all dolomite PZ layers display a wide spectrum. $\delta^{13}C$ of dolomite ($\delta^{13}C_{Dol}$) varies from 6.0‰ to -5.2‰ relative to Vienna Pee Dee Belemnite (VPDB), and $\delta^{18}O$ of dolomite ($\delta^{18}O_{Dol}$) varies from 0.9‰ to -10.4‰ (VPDB). In contrast, carbon and oxygen isotopic values for the selected limestone samples show smaller ranges: $\delta^{13}C$ of calcite ($\delta^{13}C_{Cal}$) varies from -1.0‰ to 1.0‰ (VPDB), and $\delta^{18}O$ of calcite ($\delta^{18}O_{Cal}$) varies from -10.1‰ to -5.8‰ (VPDB). Table 5.5 shows the summary of the isotopic composition for each dolomite layer and limestone samples.

Table 5.4. *Cation ordering and %Ca_{Dol} by well and PZ layer (n = 64). Data from XRD.*

Well	PZ	Ordering		
		Mean	St.Dev	n
BBC 14-1	PZ1	0.21	0.05	10
	PZ1'	0.34	0.06	5
	PZ2	0.28	0.06	4
BBC 14-3	PZ1	0.21	0.01	6
	PZ1'	0.25	0.03	3
N 6-28	PZ1	0.27	0.03	2
	PZ1'	0.30		1
	PZ2	0.24		1
UT 15-13	PZ1	0.29	0.08	3
	PZ1'	0.24		1
	PZ2	0.33		1
PW 13-06	PZ1	0.32	0.09	12
	PZ1'	0.25	0.03	3
	PZ2	0.33	0.03	3
DS 11-20	PZ1	0.27		1
	PZ1'	0.22		1
	PZ2	0.20		1
I16	PZ1	0.23	0.03	2
	PZ1'	0.27	0.00	2
	PZ2	0.24	0.04	2

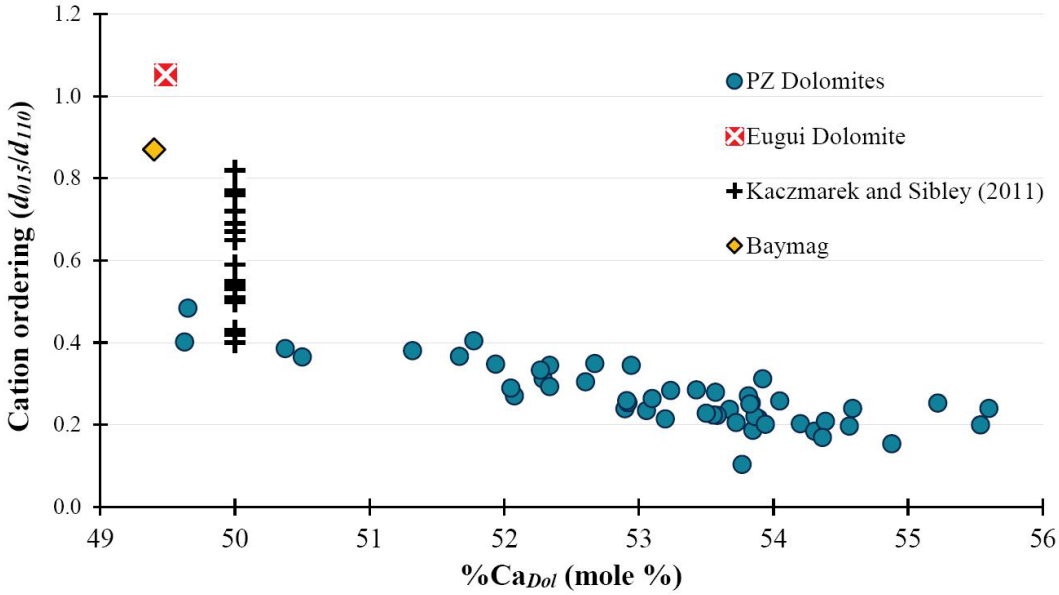

Figure 5.26. *Correlation between cation ordering and %Ca_{Dol} populations for all PZ layers combined. Baymag dolomite, synthetic dolomites (Kaczmarek and Sibley, 2011), and Eugui dolomite (www.rruff.info) values plotted as reference.*

Assuming isotopic equilibrium, the broad $\delta^{13}C_{Dol}$ distribution can be separated in two groups: (i) a set of $\delta^{13}C_{Dol}$ values depleted by 1‰ to 6‰ relative to $\delta^{13}C_{Cal}$ (left arrow figure 5.28), and (ii) a set of $\delta^{13}C_{Dol}$ values enriched by 1‰ to 6‰ relative to $\delta^{13}C_{Cal}$ (right arrow figure 5.28).

The $\delta^{18}O_{Dol}$ values are generally significantly less depleted than those from the limestones (figure 5.29). Moreover, dolomites of PZ1 display the highest $\delta^{18}O_{Dol}$ mean value (-2.6‰ VPDB), whereas dolomites in PZ2 show the lowest $\delta^{18}O_{Dol}$ mean value (-3.4‰ VPDB). However, the $\delta^{18}O_{Dol}$ value range of the PZ1 is broader (8.2‰) than those from PZ2 (5. 3‰).

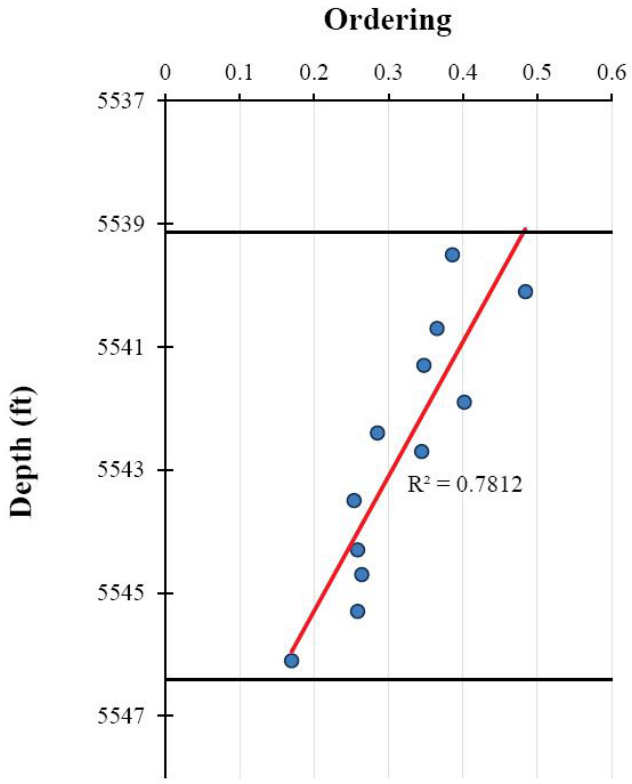

Figure 5.27. *Ordering variation with depth. Data for PZ1 layer, well PW 13-06. Black horizontal lines: top and base of the PZ layer, red line: linear regression.*

Table 5.5. *Isotopic signatures for PZ layers and interbedded limestone layers.*

Layer	Mineral	$\delta^{13}C$ (VPDB)			$\delta^{18}O$ (VPDB)		
		Values (‰)	Range	Mean	Values (‰)	Range	Mean
PZ1	Dolomite	-5.4 to 4.8	10.2	1.8	-7.3 to 0.9	8.2	-2.6
PZ1'	Dolomite	-3.3 to 5.2	8.5	1.5	-6.2 to 0.1	6.3	-3.0
PZ2	Dolomite	-1.1 to 6.0	7.1	1.3	-6.0 to -0.7	5.3	-3.3
Limestone	Calcite	-1.0 to 1.0	2.0	-0.3	-10.1 to -5.8	4.3	-7.7

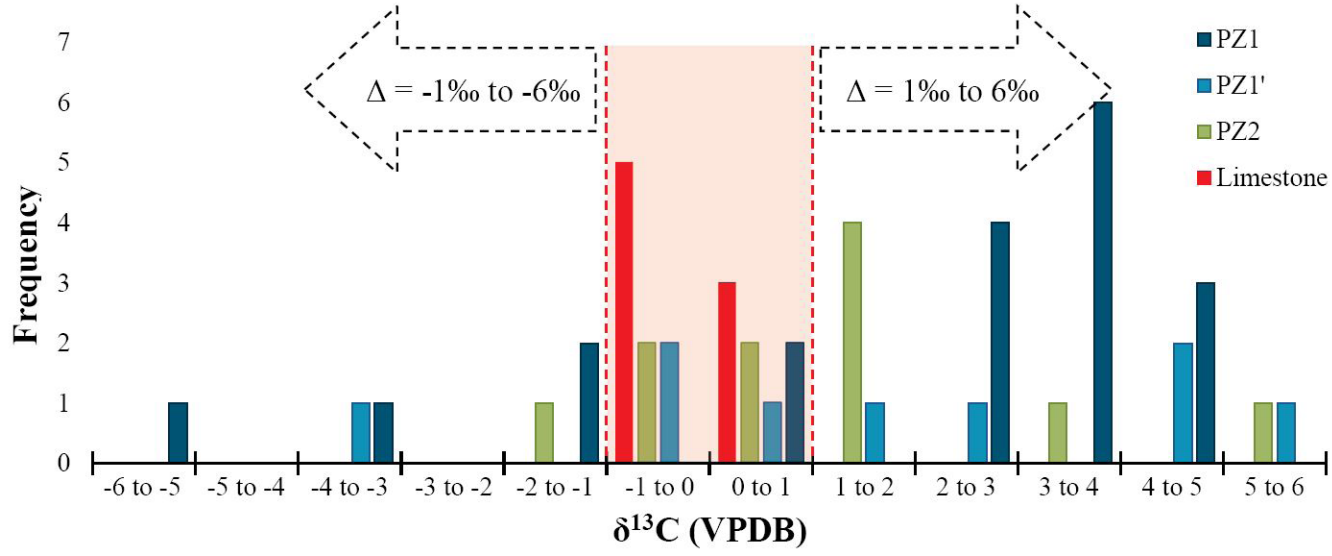

Figure 5.28. *$\delta^{13}C$ frequency distribution for dolomites (all PZ dolomite layers) and calcites (interbedded limestones).*

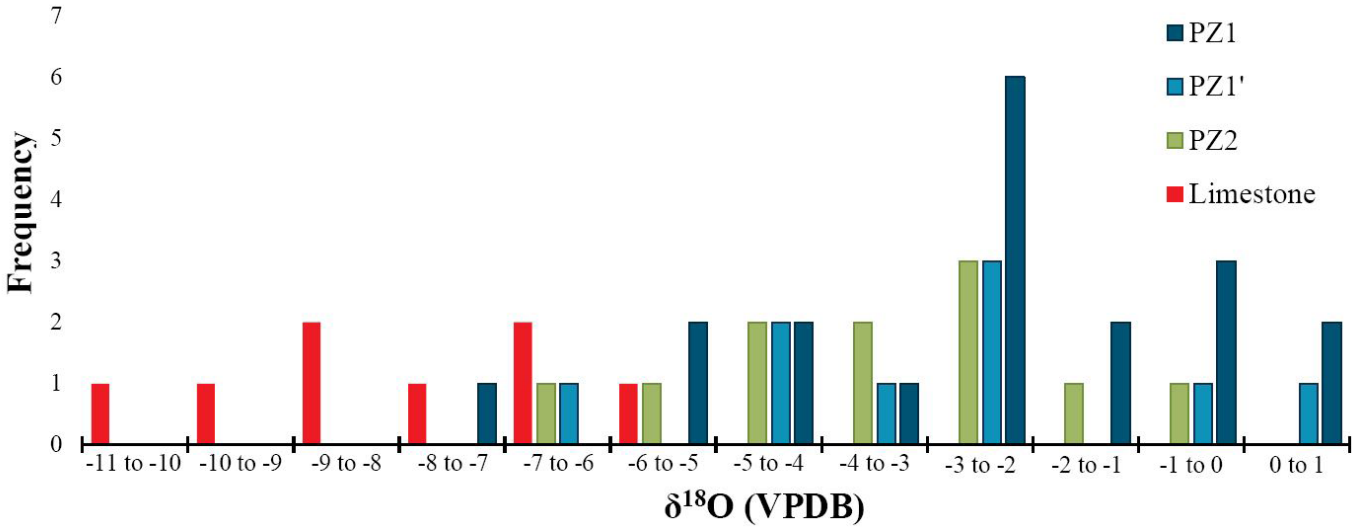

Figure 5.29. *$\delta^{18}O$ frequency distribution of dolomite (all PZ dolomite layers) and calcite (interbedded limestone). $\delta^{18}O_{Dol}$ increment from parental $\delta^{18}O$ calcite from -5‰ and 1‰ (VPDB).*

5.2.1.7 Clumped-isotopes thermometry

A different method for determining the temperature of dolomitization is from the clumped-isotopes technique. According to this method, the calculated temperature of dolomite formation varies from 30 to 59°C. Furthermore, the calculated temperature of calcite formation is higher than dolomite temperature and varies from 79 to 84°C (table 5.6).

5.2.1.8 Elemental compositions

The major elements Ca and Mg and the trace elements Na, Al, Fe, Mn, Si, Zn, Sr, and Pb were measured in 43 dolomite samples (from dolostones) and seven calcite samples (from limestones). The Na, Al, Fe, Mn, Si, Zn, Sr, and Pb concentration values are presented graphically in figure 5.30 and tabulated in appendix G.

Sodium: Dolomites have higher Na values than calcites. Dolomite values range from 528 to 2412 ppm (average 1113 ppm), and calcite values range from 348 to 1338 ppm (average 812 ppm) (figure 5.30). Furthermore, the higher Na values are located toward the near shore area (figure 5.31A).

Strontium: Dolomites show lower Sr values than calcites. Dolomite values range from 497 to 1991 ppm (average 1092 ppm), and calcite values range from 977 to 1765 ppm (average 1348 ppm) (figure 5.30). There is a Sr trend in which the highest values are located toward the centre of the basin in wells N 6-28, UT 15-13, and PW 13-06 (figure 5.31B).

Iron: Dolomites have lower Fe values than calcites. Dolomite values range from 1404 to 21044 ppm (average 5861 ppm), and calcite values range from 4162 to 12397 ppm (average 7598 ppm) (figure 5.30). There is no discernible geographical distribution for Fe (figure 5.31C).

Manganese: Dolomites have lower Mn values than calcites. Dolomite values range from 91 to 1642 ppm (average 322 ppm), and calcite values range from 265 to 929 ppm (average 583 ppm) (figure 5.30). There is no discernible geographical distribution for Fe (figure 5.31D).

Aluminum: Dolomites have relatively lower Al values than calcites. Dolomite values range from 44 to 2599 ppm (average 664 ppm), and calcite values range from 407 to 2456 ppm (average 1224 ppm) (figure 5.30). Furthermore, there is an Al trend in which the higher values are located toward the near shore area (figure 5.32A).

Silicon: Dolomites have around the same Si values as calcites. Dolomite values range from 697 to 8856 ppm (average 2475 ppm), and calcite values range from 1227 to 3131 ppm (average 2241 ppm) (figure 5.30). There is no discernible geographical distribution for Si (figure 5.32B).

Table 5.6. *Calculated dolomitizing fluid temperature (T) for PZ layers in wells PW 13-06 and N 6-28. Litho: Lithology, L: Limestone, D: Dolostone, %Dol: Dolomite percentage in the carbonate fraction.*

Sample	Depth	Litho	PZ Layer	%Dol	$\delta^{13}C$ (VPDB)	$\delta^{18}O$ (VPDB)	Δ_{47}	T (°C)
13-06-5	5537.3	L		1.8%	-0.46	-9.74	0.555	79
					-0.51	-9.77		
13-06-7	5541.9	D	PZ1	100%	3.30	-4.54	0.679	30
					3.31	-4.43		
					3.30	-4.37		
13-06-12	5557.4	D	PZ2	100%	1.34	-4.60	0.599	59
6-28-1	8199.3	D		100%	0.55	-2.39	0.609	55
					0.58	-2.36		
6-28-7	8230.2	D	PZ1'	100%	4.57	-2.30	0.627	48
					4.56	-2.22		
6-28-8	8234.6	L		5.3%	0.72	-10.40	0.545	84
					0.72	-10.36		

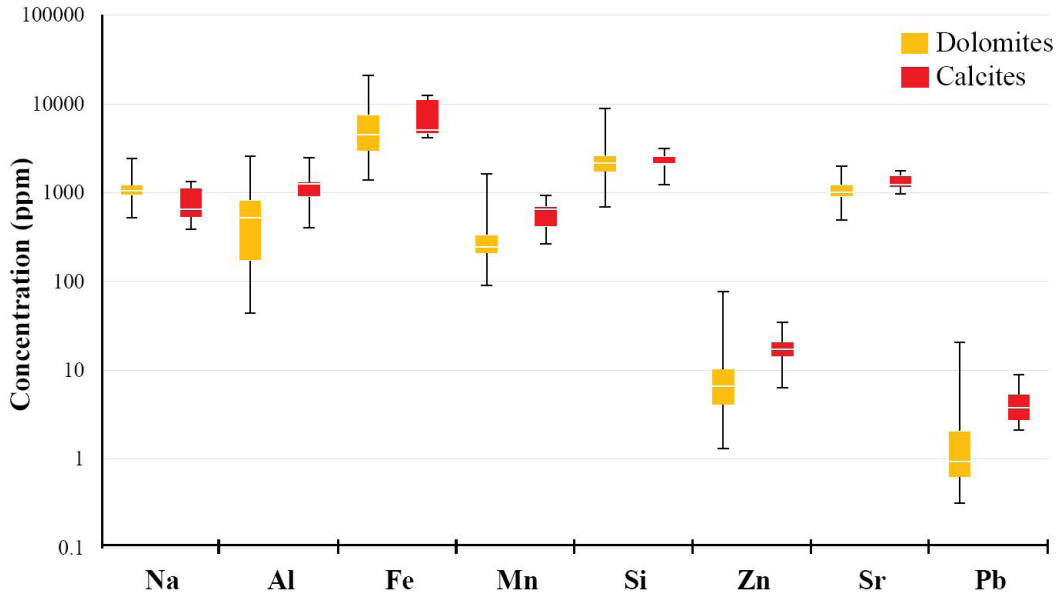

Figure 5.30. *Elemental compositions of dolomite and calcite.*

Zinc: Dolomites show lower Zn values than calcites. Dolomite values range from 1.3 to 76.4 ppm (average 12.09 ppm), and calcite values range from 6.3 to 34.8 ppm (average 18.4 ppm) (figure 5.30). There is no discernible geographical distribution for Zn (figure 5.32C).

Lead: Dolomites show lower Pb values than calcites. Dolomite values range from 0.32 to 20.67 ppm (average 2.12 ppm), and calcite values range from 2.11 to 8.98 ppm (average 4.45 ppm) (figure 5.30). There is no discernible geographical distribution for Zn (figure 5.32D).

5.2.2 Interpretations

5.2.2.1 Crystal shapes

Proper identification of dolomite texture and crystal size is very important for making interpretations about dolomitizing fluid characteristics (Gregg and Sibley, 1984; Sibley and Gregg, 1987; Warren, 2000; Machel, 2004). The coexistence of planar-e, planar-s, and nonplanar-a textures suggests either a variation over time in the composition of the dolomitizing fluid (Sibley and Gregg, 1987), or different dolomitization phases, each from different fluid (Sibley and Gregg, 1987; Machel, 2004), or inheritance of crystal size variations from the lime(stone) precursors.

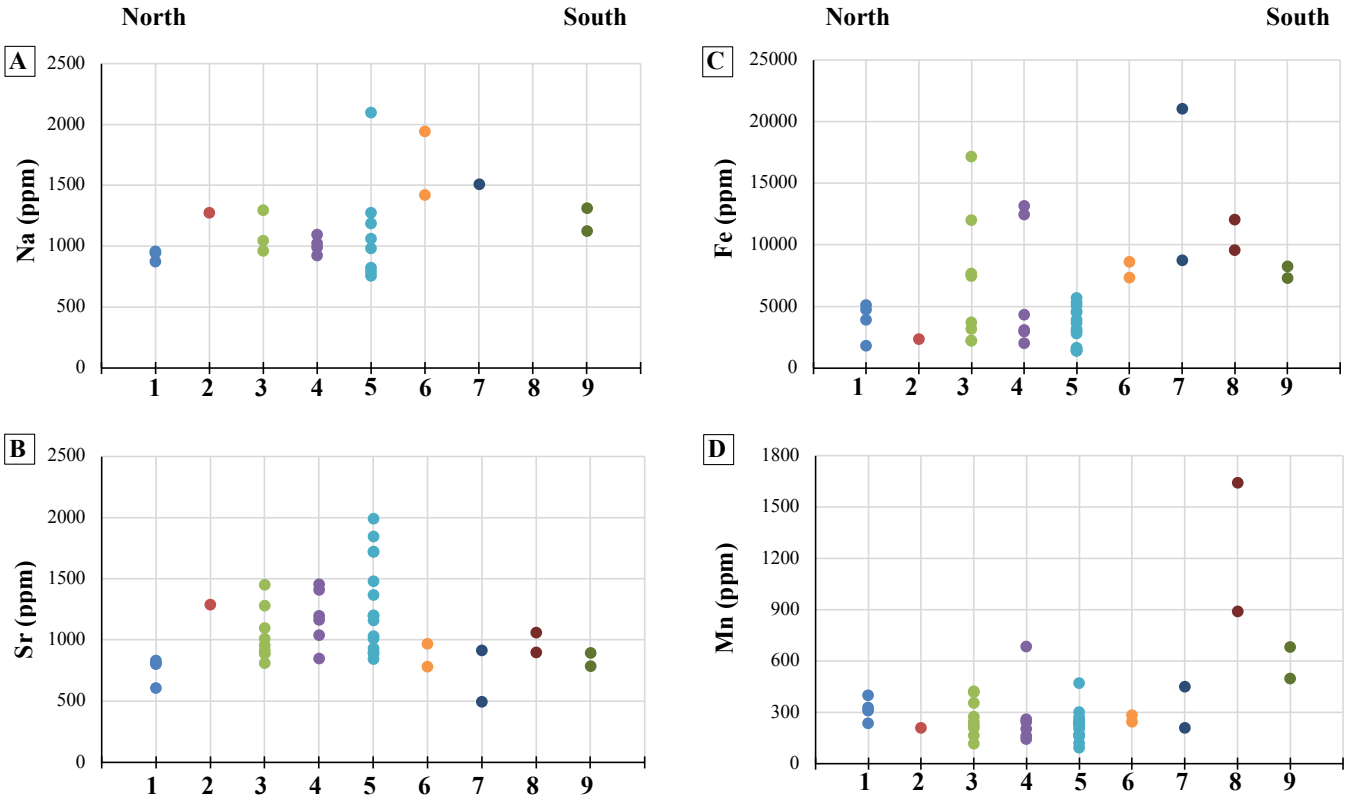

Figure 5.31. *Na, Sr, Fe, and Mn concentration in dolomite and geographical distribution. Numbers in the horizontal axis stand for wells/ outcrops as; 1: BBC 14-1, 2: BBC 14-3, 3: N 6-28; 4: UT 15-13; 5: PW 13-06; 6: DS 11-20; 7: I 16; 8: WCC; 9: NMC.*

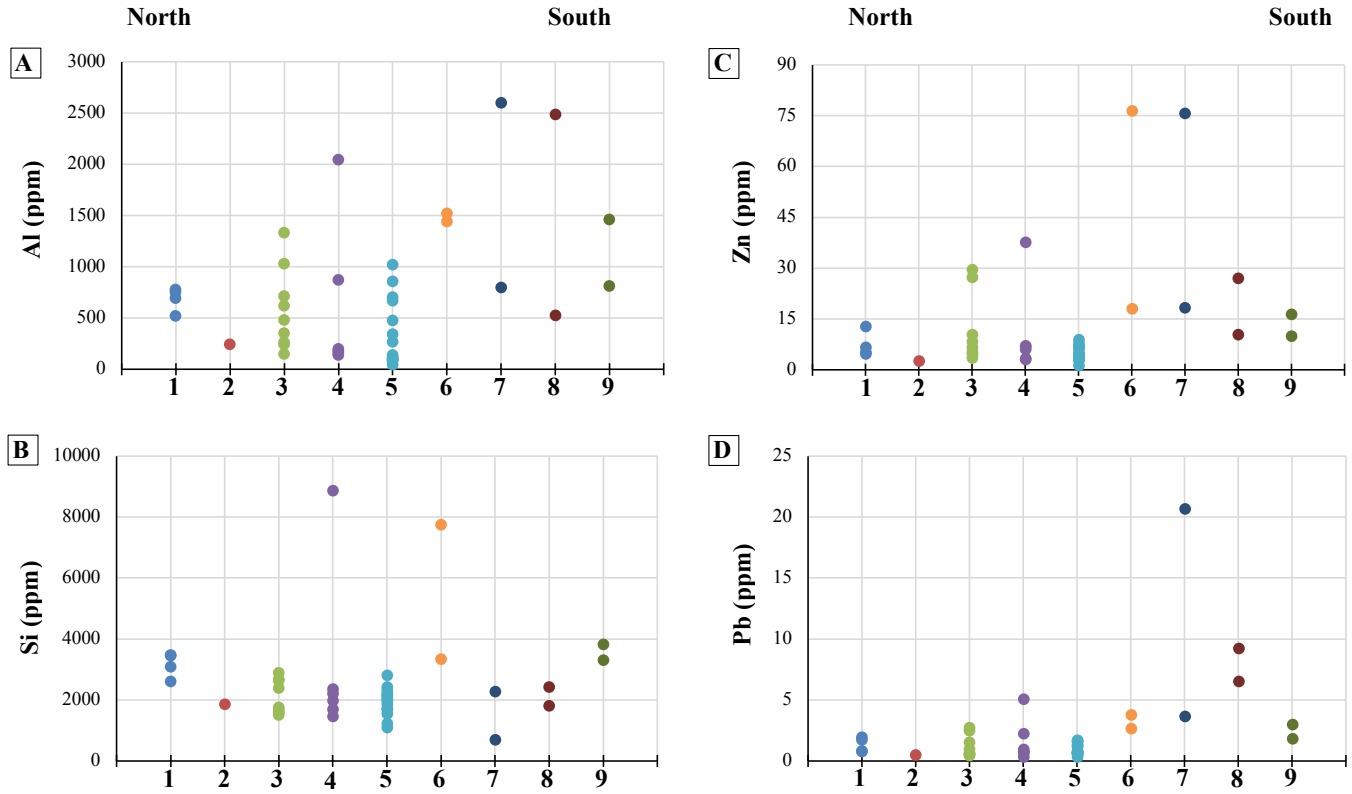

Figure 5.32. *Al, Si, Zn, and Pb concentration in dolomite and geographical distribution. Numbers in the horizontal axis stand for wells/ outcrops as; 1: BBC 14-1, 2: BBC 14-3, 3: N 6-28; 4: UT 15-13; 5: PW 13-06; 6: DS 11-20; 7: I 16; 8: WCC; 9: NMC.*

Sibley and Gregg (1987) recognized that the crystal shapes of dolomite correlate with supersaturation of the dolomitizing fluids and with the temperature of dolomitization. Straight crystal faces in planar-e dolomite commonly tend to develop at "low supersaturation and/or low temperatures" (Sibley and Gregg, 1987, p. 968). In contrast, nonplanar-a textures tend to develop from highly supersaturated fluids and/or at "high" temperatures (Sibley and Gregg, 1987), for example, at temperatures higher than the so-called "critical roughening temperature," which is around 50 to 100°C for dolomite (Sibley and Gregg, 1987).

Regional distribution of dolomite textures (figure 5.14) can be interpreted to be the result of geographic variations of the chemical composition of the dolomitizing fluid. In nearshore areas, the fluid composition may have been only slightly supersaturated with respect to dolomite, leading to the development of mainly planar-e textures, whereas in the intermediate zone between the nearshore and basin center areas the dolomitizing fluid was probably more highly supersaturated, thus creating planar-s textures. However, more data must be acquired to confirm this interpretation.

5.2.2.2 Crystal size

Dolomite crystal sizes and populations offer important information about the history of diagenesis related to dolomitization events or recrystallization. Dolomite crystal size populations may be inherited or controlled by the crystal sizes of the precursor limestone, by recrystallization of metastable dolomite precursor mineral phases, or by different dolomitization events (Sibley and Gregg, 1987; Sibley and others, 1993; Machel, 2004).

The right-skewed dolomite crystal size distribution (figure 5.16) probably was created by recrystallization, which involves an increase of crystal size (Sibley and others, 1993; Gregg and Shelton, 1989; Gregg and others, 1992). This is likely the case of the dolomite in all PZ layers in which the original crystal size was modified from small crystals size (POP1 and POP2) to larger crystals size (POP3).

5.2.2.3 Cathodoluminescence

According to Machel and others (1991), luminescence in the carbonate minerals is the emission of light (photons) from certain elements (mainly Mn^{2+}, Rare Earth Elements, and Pb^{2+}). Photon emission is produced when an external source of energy (such as an electron beam) excites an electron, moving it toward a higher energetic band. When the exited electrons lose energy, they return to lower energy levels and release energy difference as photons (Boggs and Krinsley, 2006).

The lack of luminescence in the dolomite crystals of this study can be attributed to either or both of the following:

(i) Low concentrations of activator Mn^{2+} and sensitizer Pb^{2+} elements (Machel, 1985; Machel and Burton, 1991; Machel, 2000) coupled with a high concentration of quencher Fe^{2+}. Machel (1995) indicates that luminescence is related to the activator-sensitizer and quenchers concentration ratio up to the point that high concentrations of Fe^{2+} (principal quencher) may constrain luminescence behaviour. To identify luminescence using a standard luminescence microscope, Machel (2000) suggests a minimum concentration of 10 to 20 ppm for Mn^{2+} coupled with a concentration of 150 ppm for Fe^{2+} (Mn/Fe = 0.1). A higher Fe^{2+} concentration creates a lower Mn/Fe ratio, which quenches luminescence. The Mn/Fe ratio was calculated from EMPA data with a value of 0.05, and from ICP-MS data with a value of 0.06. The low Mn/Fe ratio likely is the reason for the absence of cathodoluminescence.

(ii) A later recrystallization event that destroyed the initial activator-sensitizer and quenchers zonation (Machel, 2000).

5.2.2.4 Stoichiometry

Dolomite calcium percentages can be related to environments of dolomitization (Lumsden and Chimahusky, 1980; Gregg and others, 1992; Searl, 1994). In general, evaporitic settings correlate with nearly stoichiometric dolomites (50–52 $\%Ca_{Dol}$) and non-evaporitic settings correlate with non-stoichiometric dolomites (55–56 $\%Ca_{Dol}$). However, a potential recrystallization event, which is probably reflected by the left-skewed CSD (figure 5.16), might have altered the original $\%Ca_{Dol}$ chemical signature (Mazzullo, 1992; Machel, 1997; Gregg, and others, 2015) from non-stoichiometric dolomite ($POP2_{\%Ca}$) to nearly stoichiometric dolomite ($POP1_{\%Ca}$).

5.2.2.5 Ordering

Based on experimental data (synthetic dolomite), Kaczmarek and Sibley (2011) concluded that dolomite cation ordering and stoichiometry characteristics are related to parental fluid composition. They argue that the more supersaturated the dolomitizing fluid is, the higher the Mg content in dolomite, despite variable dolomite cation ordering. Some of the synthetic dolomite crystals resulting from the Kaczmarek and Sibley experiments are plotted in figure 5.26. These dolomite crystal series precipitated from supersaturated fluids (Mg/Ca molar ratio ≥1) with a wide range of cation ordering from about 0.4 to 0.8 (figure 5.26).

Cation ordering values are relatively low (0.27 ±0.07) compared to those of ideal dolomite (~0.87 in figure 5.26 for Baymag dolomite). According to Kaczmarek and Sibley (2011), the first replacement phase during dolomitization (very high magnesium calcite or protodolomite) invariably displays a very low degree of cation ordering. If these metastable phases are allowed to recrystallize over time, they assume increasingly higher degrees of ordering (and lower Ca^{2+} excess). Hence, it is reasonably inferred that the observed ranges in cation ordering represents various "stages" of progressive recrystallization which did not go to completion, except for the nearly stoichiometric dolomites in $POP1_{\%Ca}$.

5.2.2.6 Conventional carbon and oxygen isotope data

Environmental interpretations are based on calcite and dolomite isotopic composition relationships. The reference for interpretation of dolomite formation is the $\delta^{13}C$ and $\delta^{18}O$ values of the calcite (matrix) of the limestones. This assumption is valid only if the calcite (matrix) in limestone did not undergo recrystallization.

$\delta^{13}C$ values of calcite ($\delta^{13}C_{Cal}$) are close to the Vienna Pee Dee Belemnite standard with a narrow variation (±1‰ PDB) (figure 5.28). Assuming isotopic equilibrium, this value can be taken to represent the dissolved organic carbon of the lake water (DIC_W).

On the other hand, the $\delta^{13}C_{Dol}$ enrichment (from 1‰ to 6‰ PDB, figure 5.28) is interpreted to have resulted from one or both of the following two processes:

(i) A $\delta^{13}C_{Dol}$ enrichment can be caused by high organic activity. In this process organisms preferentially take up ^{12}C, which increases the $\delta^{13}C$ values of the DIC_W. Consequently, dolomite formed in isotopic equilibrium with the lake water has elevated $\delta^{13}C_{Dol}$ values. This interpretation is supported by the total organic carbon (TOC) and S2 values in the dolomite PZ layers (figure 5.33). In well N 6-28, taken as representative of the other wells, there is a remarkable contrast between the limestone and dolomite PZ layers because the dolomite layers consistently have higher TOC and S2 values than the interbedded limestones. The dolomite layers reach the highest TOC values, expressed as wt% HC (see figure 5.33).

(ii) Organic matter decay may also play an important role in the $\delta^{13}C_{Dol}$ enrichment. This process could be represented by [?] the breakdown reaction of organic matter (acetate):

$$CH_3COOH \rightarrow CO_2 + CH_4 \quad (5)$$

where acetate is fermented to carbon dioxide and methane with a significant isotopic fractionation between the two products (e.g., Irwin and others, 1977; Tucker and Wright, 1990).

According to Irwing and others (1977), acetate fermentation releases CO_2 with $\delta^{13}C$ values around +15‰ PDB, while the concomitantly formed CH_4 may have $\delta^{13}C$ values around -50‰ PDB. Dolomite that formed in isotopic equilibrium with CO_2 from acetate fermentation may be significantly enriched in ^{13}C, whereby the amount of enrichment depends on the relative proportions of DIC_W and CO_2 from fermentation.

In contrast, six samples have $\delta^{13}C_{Dol}$ values significantly depleted relative to calcite (figure 5.28). This depletion is interpreted as the result of organic matter oxidation as represented by:

$$CH_4 + SO_4^{2-} \rightarrow HCO_3^- + HS^- + H_2O \quad (6)$$

$$2CH_2O + SO_4^{2-} \rightarrow H_2S + 2HCO_3^- \quad (7)$$

Biochemical methane (CH_4) oxidation, as represented by Reaction 6 (Tucker and Wright, 1990) and carbohydrates ($2CH_2O$) oxidation by sulphate-reducing bacteria (Berner and others, 1985; Machel 2001) described by Reaction 7 (Berner and others, 1985) leads to the simultaneous formation of ^{13}C-depleted carbonates (from the HCO_3^-) and pyrite (from the HS^-) (figure 5.34), if Ca^{2+}, Mg^{2+} and Fe^{2+} are available. The carbohydrates oxidation process, products (Reaction 7), and by-products are represented in figure 5.34.

In either case (Reaction 6 or 7), the source of oxygen is the dissolved sulfate (SO_4^{2-}) present in the lake water. Tuttle and Goldhaber (1993) suggested that sulfate anions in the Uinta Basin were supplied by river input and derived from weathering of Jurassic marine evaporite minerals. This interpretation is supported by the occurrence of framboidal pyrite crystals associated with the dolomite crystals (figure 5.7F).

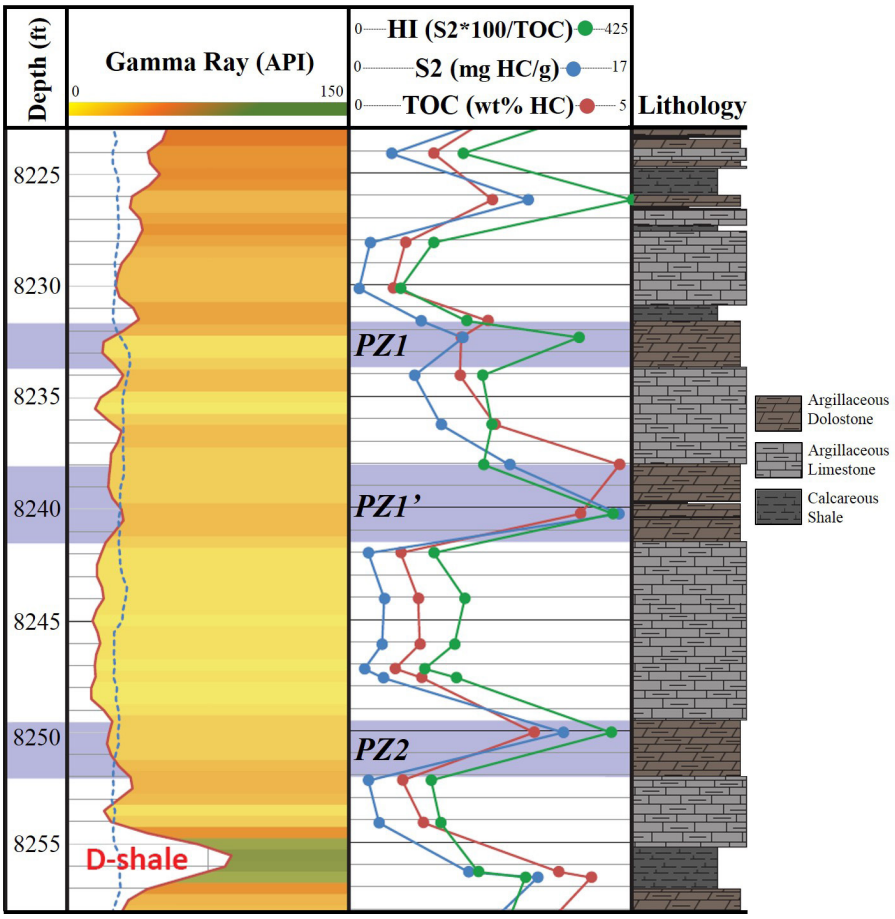

Figure 5.33. *Total organic carbon (TOC) and S2 logs of well N 6-28. Dolomite PZ layers are highlighted in blue.*

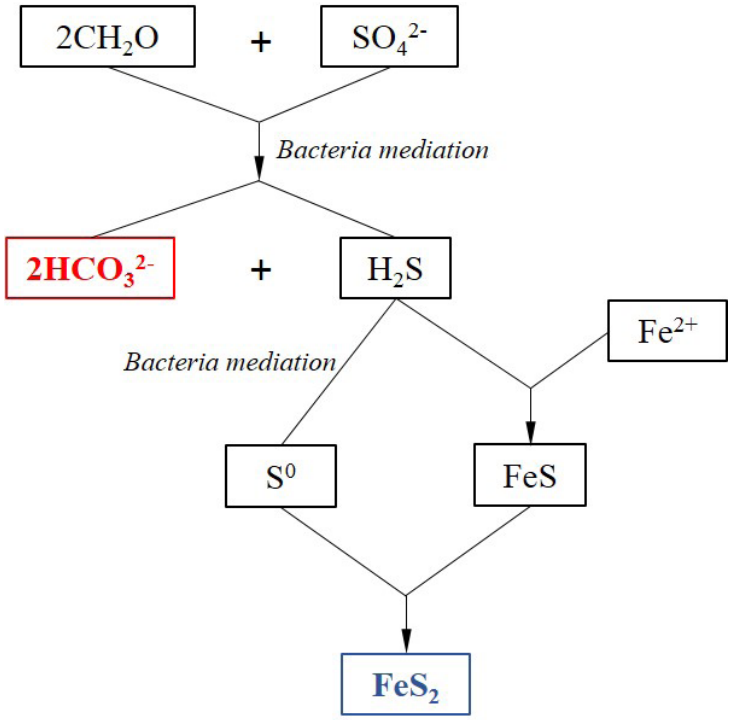

Figure 5.34. *Idealized processes that may have created low $\delta^{13}C$ values in dolomites: Oxidation of low $\delta^{13}C$ organic matter [-25 to -30‰ PDB (e.g., Tucker and Wright, 1990; Machel, 2001)] created ^{13}C-depleted bicarbonate anions (red rectangle). Pyrite (blue rectangle) formed as by-product from the hydrogen sulfide and detrital iron (Fe^{2+} in lake water) reaction. Modified from Berner and others (1985).*

$\delta^{18}O$ values of dolomite ($\delta^{18}O_{Dol}$) can provide information concerning the temperature of dolomite formation. The low $\delta^{18}O_{Cal}$ values suggest that calcite crystallized in isotopic equilibrium from fresh lake water. This interpretation is supported by fossil associations presented in the mollusc wackstone-floatstone facies (F5). According to LaRocque (1956), the pelecypod and gastropod fossils recorded at the base of the GRF (correlated to the UBm) are fresh water mollusc species. Moreover, the wide range of the $\delta^{18}O_{Cal}$ values (from -10.1 to -5.8‰ VPDB, mean: -7.7‰, range: 4.3‰) suggests fluctuations on fluvial inflow rates, variable degrees of rock-water interaction, or variable temperature during subsequent burial recrystallization, or a combination of all three processes/factors.

MacGinitie (1969) described the fossil floral record in the GRF and calculated the average temperature for the coldest months as 12°C, with a minimum temperature of about 3°C. Assuming lake water temperatures from 3°C to 12°C and precipitation in isotopic equilibrium, the oxygen isotopic composition of the lake water ($\delta^{18}O_W$) might have fluctuated between -13.13‰ and -6.38‰ SMOW (Standard Mean Oceanic Water) (table 5.7), with an arithmetic mean of -9.55 ±1.9‰.

The isotopic water composition was calculated using the temperature equation for the calcite-water system proposed by Friedman and O'Neil (1977):

$$10^3 Ln\alpha = 2.78 * (10^6/T^2) - 2.89 \quad (8)$$

A variation from the $\delta^{18}O$ values of calcites to the higher $\delta^{18}O$ values in dolomites (figure 5.29) was probably caused by a combination of temperature increase and/or evaporation. During evaporation, the water composition is controlled by equilibrium and kinetic effects (Tucker and Wright, 1990; Gat, 1995; Davis and others, 2009). For the kinetic effect, the lighter water molecules ($^1H^{16}O$) diffuse more easily to the atmosphere. For the equilibrium effect, the lighter water molecules have higher vapor-pressure values, making it easier for them to pass into the atmosphere. As a result, the lake water becomes enriched in δ^2H and $\delta^{18}O$. Consequently, dolomite crystals that form in isotopic equilibrium with lake water are also enriched in ^{18}O.

The water/fluid temperatures calculated for dolomitization are listed in table 5.8, based on the measured $\delta^{18}O$ of dolomites and the estimated $\delta^{18}O$ isotopic composition, using the dolomite-water system isotopic fractionation proposed by Sheppard and Schwarcz (1970):

$$10^3 Ln\alpha = 3.23 * (10^6/T^2) - 3.29 \quad (9)$$

Pitman (1996), working in the depocenter of the Uinta Basin, estimated the $\delta^{18}O$ values of fresh lake water setting (for calcite precipitation) between -12‰ and -6‰ SMOW, which are close to the range calculated for the calcites in this study (see table 5.7). Furthermore, Pitman (1996) estimates that the $\delta^{18}O_W$ was around -5‰ SMOW for a slightly evaporated environment. By comparison, Long (2006) estimated the $\delta^{18}O_W$ of fresh lake water setting (calcite precipitation) around -9‰ and -2‰ SMOW, and the $\delta^{18}O_W$ for evaporated setting (dolomite precipitation) around -11‰ and -4.5‰ (SMOW) in the southwest margin of the Uinta Basin. Long (2006) calculated these values assuming a constant temperature of 25°C for calcite and dolomite precipitation.

Estimation of the $\delta^{18}O_W$ during dolomitization considers the $\delta^{18}O_W$ values proposed by Pitman (1996) but extends the $\delta^{18}O_W$ range in ±5‰ SMOW, from -10‰ to 0‰ SMOW. The calculated $\delta^{18}O_W$ values proposed by Long (2006) are not included in this analysis because he estimated the calcite and dolomite precipitation at the same temperature of 25°C. This cannot be accurate for several reasons, one of them flagged by his assertion that the $\delta^{18}O_W$ for dolomitization was lower than $\delta^{18}O_W$ for calcite precipitation.

On the contrary, the higher $\delta^{18}O$ values of dolomite versus calcite suggest that dolomitization was probably caused by somewhat evaporated lake water with higher $\delta_{18}O_W$ from evaporation. Therefore, the temperature of dolomitization must also have been higher than that of the fresh water setting (12°C).

Based on these considerations, the lake water $\delta^{18}O$ isotopic composition during dolomitization is evaluated in three different $\delta^{18}O_W$ settings: (i) $\delta^{18}O_W$ = -10‰ (SMOW), (ii) $\delta^{18}O_W$ = -5‰ (SMOW), and (iii) $\delta^{18}O_W$ = 0‰ (SMOW) (table 5.8).

$\delta^{18}O_W$ = -10‰ (SMOW) was not a probable alternative during dolomitization because the majority of the calculated temperatures are lower than 13°C (values in red, table 5.8), with some values below 0°C. Similarly, $\delta^{18}O_W$ = 0‰ (SMOW) was not a probable water isotopic composition during dolomitization because the majority of the calculated temperatures are higher than 40°C (values in red, table 5.8). On the other hand, an intermediate $\delta^{18}O_W$ = -5‰ (SMOW) yields reasonable temperatures between 13°C to 36°C with four exceptions (in red, table 5.8).

Table 5.7. *Calculated $\delta^{18}O$ of lake water ($\delta^{18}O_W$) for calcite precipitation, assuming lake water temperatures between 3°C and 12°C (MacGinitie, 1969).*

Well	Sample	$\delta^{18}O_{Cal}$ (PDB)	$\delta^{18}O_W$ @ 3°C (SMOW)	$\delta^{18}O_W$ @ 12°C (SMOW)
BBC 14-1	14-1-19	-9.28	-12.27	-10.00
N 6-28	6-28-8	-8.02	-10.97	-8.71
PW 13-06	13-06-4	-8.39	-11.35	-9.09
PW 13-06	13-06-5	-7.48	-10.42	-8.16
PW 13-06	13-06-14	-10.11	-13.13	-10.86
PW 13-06	13-06-18	-6.42	-9.32	-7.06
DS 11-20	11-20-2	-6.47	-9.37	-7.11
I 16	16-5	-5.76	-8.64	-6.38

Current lakes around the Uinta Basin have similar temperatures (variably throughout seasons) (Eardley, 1938; Belovsky and others, 2011), and the calculated temperatures are similar to the estimated paleo-temperatures of Lake Uinta based on paleo-biological and paleo-climate studies (MacGinitie, 1969; Rasmussen and others, 1999).

A different estimation of the temperature along dolomitization is based on a comparison between the current lake water temperatures of Great Salt Lake (Utah, USA) and the estimated temperatures of the Eocene epoch in the study area. Great Salt Lake was chosen because it is located around the same latitude as ancient Lake Uinta. The reported maximum water temperature in the summer of Great Salt Lake varies between 26°C and 32°C (Eardley, 1938; Belovsky and others, 2011; www.usclimatedata.com). Furthermore, the relationship between lake water and air temperatures is positive and strong (high R^2) for the highest lake water-air temperatures (McCombie, 1959). On the other hand, Rasmussen and others (1999), using fossils of mammals, estimated that the coolest temperature during the middle Eocene was at least 4°C higher than current temperatures. Therefore, it is reasonable to assume that the water temperature of the ancient Lake Uinta could have reached at least 30°C. This temperature supports the notion that the lake water $\delta^{18}O$ isotopic composition fluctuated between -10‰ and 0‰ (SMOW) during dolomitization, and most likely was close to -5‰ SMOW.

5.2.2.7 Clumped-isotopes thermometry

The clumped-isotopes results (table 5.6) supplement the conventional oxygen isotope results as follows:

(i) The dolomite PZ1 layer presents a dolomitization temperature of 30°C (sample 13-06-7), which is close to its temperature of around 24°C estimated from conventional oxygen isotope geothermometry (see previous section). However, the dolomite PZ1′ and PZ2 layers show much higher dolomitization temperatures of 48°C (sample 6-28-7) and 59°C (sample 13-06-12), respectively. The discrepancy between the estimated temperature from conventional oxygen isotopes and clumped isotopes may be due to the following reasons: (1) analytical error (Bernasconi, personal communication, 2016); or (2) the higher "clumped" temperatures do not reflect the dolomitization process but are due to recrystallization.

(ii) Dolomitization temperatures in the two limestone samples analyzed are significantly higher than those calculated for dolomite samples (79°C for sample 13-06-5 and 84°C for sample 6-28-8). These temperatures cannot possibly reflect the lake water at the time of calcite formation and/or deposition but must be due to recrystallization during burial.

Considering that the calculated clumped-isotopes temperatures are in the range of the estimated maximum burial temperatures (from north to south) in the study area (see Section 5.1.3), it appears that the calcite for the limestone layers was prone to isotopic re-equilibrium during recrystallization near maximum burial whereas the dolomite of the dolostones was not.

5.2.2.8 Elemental compositions

Trace element concentration in dolomite crystals can be used for interpretations about the dolomitizing fluid, dolomitization environment, and/or recrystallization. The concentration of trace elements in minerals is defined by (i) trace element fluid concentration, (ii) water/rock ratio of the system, and (iii) the distribution coefficient (*D*) (Tucker and Wright, 1990). If an element has a *D* value >1, the resulting crystal is enriched in the concentration of trace elements (higher $^{m}Te/^{m}Ca$) more than the parent fluid. In contrast, if an element has a *D* value <1, the resulting crystal is less concentrated in trace elements (low $^{m}Te/^{m}Ca$) than the parent fluid (McIntire, 1963). However, distribution coefficients are not constant. Rather they might vary with the composition of the solid phase, temperature, pressure, and kinetic factors (McIntire, 1963; Veizer, 1983).

Table 5.8. *Calculated temperatures (T °C) of dolomitizing fluids based on estimated lake water $\delta^{18}O$ composition varying from -10‰ to 0‰ SMOW and measured $\delta^{18}O_{Dol}$ values from conventional isotopes analysis. Temperature values deemed unreasonable for dolomitization are highlighted in red color; temperatures calculated using the dolomite-water system isotopic fractionation equation proposed by Sheppard and Schwarcz (1970). See text for discussion.*

Well	Sample	$\delta^{18}O_{Dol}$ (PDB)	T (°C) @ $\delta^{18}O_W$ = -10‰ SMOW	T (°C) @ $\delta^{18}O_W$ = -5‰ SMOW	T (°C) @ $\delta^{18}O_W$ = 0‰ SMOW
			PZ1		
BC 14-1	14-1-14	-2.71	6.3	24.9	47.8
BBC 14-1	14-1-15	-5.05	14.8	35.3	60.9
N 6-28	6-28-5	-2.06	4.0	22.2	44.4
N 6-28	6-28-6	0.87	-5.3	10.8	30.4
UT 15-13	15-13-9	0.04	-2.8	13.9	34.1
UT 15-13	15-13-10	-1.63	2.6	20.4	42.2
UT 15-13	15-13-11A	-7.30	23.8	46.4	75.1
UT 15-13	15-13-11B	-2.59	5.8	24.3	47.1
PW 13-06	13-06-6	-1.55	2.3	20.1	41.8
PW 13-06	13-06-6B	-0.39	-1.4	15.5	36.2
PW 13-06	13-06-7	-2.62	6.0	24.5	47.3
PW 13-06	13-06-7B	-0.69	-0.4	16.7	37.6
PW 13-06	13-06-8	-2.85	6.8	25.5	48.5
PW 13-06	13-06-9	-2.18	4.4	22.6	45.0
PW 13-06	13-06-10	-4.33	12.1	32.0	56.7
PW 13-06	13-06-10A	-3.26	8.2	27.2	50.7
DS 11-20	11-20-4	-0.84	0.0	17.3	38.3
I 16	16-3	-5.61	17.0	37.9	64.3
I 16	16-4	-4.42	12.4	32.4	57.2
			PZ1'		
BBC 14-1	14-1-17	-2.37	5.1	23.5	46.0
N 6-28	6-28-7	-0.26	-1.8	15.0	35.6
UT 15-13	15-13-12	-4.63	13.2	33.3	58.4
UT 15-13	15-13-13	-4.83	13.9	34.2	59.5
PW 13-06	13-06-10B	-6.16	19.1	40.6	67.6
PW 13-06	13-06-11	-10.39	37.6	63.8	98.1
DS 11-20	11-20-5	-2.44	5.3	23.7	46.3
I 16	16-7	0.06	-2.8	13.8	34.1
I 16	16-8	-3.00	7.3	26.1	49.3
			PZ2		
BBC 14-1	14-1-20	-2.69	6.2	24.8	47.7
BBC 14-1	14-1-21	-0.71	-0.3	16.8	37.7
N 6-28	6-28-9	-2.11	4.2	22.4	44.6
UT 15-13	15-13-14	-1.31	1.5	19.1	40.6
PW 13-06	13-06-11A	-5.37	16.0	36.8	62.8
PW 13-06	13-06-11B	-4.84	14.0	34.3	59.6
PW 13-06	13-06-11C	-2.90	6.9	25.7	48.7
PW 13-06	13-06-12	-6.03	18.6	40.0	66.8
DS 11-20	11-20-8	-4.80	13.8	34.1	59.4
DS 11-20	11-20-9	-3.47	9.0	28.1	51.8
I 16	16-10	-3.62	9.5	28.8	52.7
I 16	16-11	-2.02	3.9	22.0	44.2

The trace element concentration in dolomite is defined by Equation 10 (Gregg and Shelton, 1989), which correlates the molar ratio of the trace element to that of Ca^{2+} and Mg^{2+} as follows:

$$[{}^{m}Te/({}^{m}Ca + {}^{m}Mg)]_s = D * [{}^{m}Te/({}^{m}Ca+{}^{m}Mg)]_l \quad (10)$$

where "m" is the molar concentration, "Te" stands for trace element, "*s*" represents the solid phase (calcite), "*D*" stands for the distribution coefficient, and "*l*" represents the liquid phase (or dolomitizing lake/pore water in this case). This equation is valid for systems in equilibrium and homogeneous distribution of trace elements during precipitation (Veizer, 1983).

Sr and Na concentrations of the dolomitizing fluids are compared to two specific reference waters: (i) a saline setting represented by the current Great Salt Lake concentration, and (ii) a fresh water setting represented by an average concentration of several lakes. Calculation was based on the distribution coefficients for dolomite proposed by Veizer (1983) (D_{Sr} = 0.025 to 0.07, D_{Na} = $2x10^{-5}$ to $2x10^{-4}$), the current Ca, Mg, Sr, and Na concentration of Great Salt Lake water (Whitehead and Feth, 1961), and the Ca, Mg, Sr, and Na average concentration of fresh lake water [Majid, 1983 in Veizer (1983)] (table 5.9 and figure 5.35).

Sr and Na are associated with the degree of salinity of the dolomitization fluids (Land and Hoops, 1973; Tucker and Wright, 1990). Assuming partition equilibrium during dolomitization and no recrystallization, the probable calculated Sr and Na concentrations of the dolomitizing fluid (ancient Lake Uinta water or pore waters derived from it) were greater than the waters references (figure 5.35), suggesting an evaporitic dolomitizing fluid. This interpretation is valid only if Na is incorporated within the dolomite lattice. Furthermore, the geographical variation of this data, with somewhat elevated values located toward the nearshore area (figure 5.31A), suggests that the lake/pore water had elevated salinities at least temporarily toward the near shore areas.

On the other hand, the Sr concentration in dolomite may be an indicator of dolomitizing fluid flow and Sr/Ca ratio of the dolomitizing fluid. In figure 5.36, the Sr concentration decreases with depth, which probably represents an upward dolomitizing fluid direction (see Chapter 6, section 6.1.3 for further discussion).

Fe and Mn concentrations are indicators of the reduction-oxidation potential of the dolomitization fluid (Tucker and Wright, 1990; Machel and Burton, 1991; Davison, 1993;) and the availability of these elements (Budd, 1997). For these elements to be incorporated into the dolomite lattice, they must be in their divalent forms, which requires a reducing redox potential (Machel and Burton, 1991). Fe and Mn concentrations higher than 1000 ppm and 50 ppm, respectively, suggests reducing pore waters and Fe-Mn external source (Budd, 1997). The average Fe and Mn concentration (5216 pp and 322 ppm, respectively) in the dolomite samples of this study (figures 5.31C and D) suggest a reducing lake/pore water setting. This interpretation is valid only if the current Fe and Mg concentrations in dolomite crystals are the original signature.

The Al and Si concentrations are taken as a proxy for the amount of "insoluble residue," i.e., essentially the clay mineral content in the samples because these elements cannot be incorporated into dolomite at low diagenetic temperatures (Weber, 1964). In the samples of this study, the Al concentrations have a spatial distribution in which the higher values are preferentially located in the nearshore area (figure 5.32A). This distribution was probably caused by deposition of most of the suspended sediment in the nearshore areas, which led to a decrease of clay sediments toward the basin center. In contrast, the Si concentration shows roughly the same concentration throughout the basin (figure 5.32B).

The Zn and Pb concentrations are commonly elevated in basinal brines (e.g., Morrow, 1982), and dolomites formed from them often are associated with galena and/or sphalerite. The PZ layers of the UBm do not have any of these characteristics. In contrast, the average Zn and Pb concentrations are low (12 ppm and 2 ppm, respectively) (figures 5.32C and D) in comparison with known basinal dolomites which reach values up to 14 ppm and 50 ppm, respectively (Luczaj and others, 2016).

Table 5.9. *Sr and Na concentrations and ratios to Ca^{2+} of calculated dolomitizing fluid compared to current fresh water from lakes in the region and saline water from Great Salt Lake.*

	Dolomitizing fluids	Freshwater - Lakes	Saline water - Great Salt Lake
Sr (ppm)	1300	0.07	15
Na (ppm)	1420	50	83600
Ca (ppm)	245701	8	241
Mg (ppm)	133081	6	7200
${}^{m}Sr/({}^{m}Ca+{}^{m}Mg)$	$2.66x10^{-2}$	$1.79x10^{-3}$	$5.66x10^{-4}$
${}^{m}Na/({}^{m}Ca+{}^{m}Mg)$	$9.69x10^{1}$	$1.28x10^{0}$	$3.16x10^{0}$

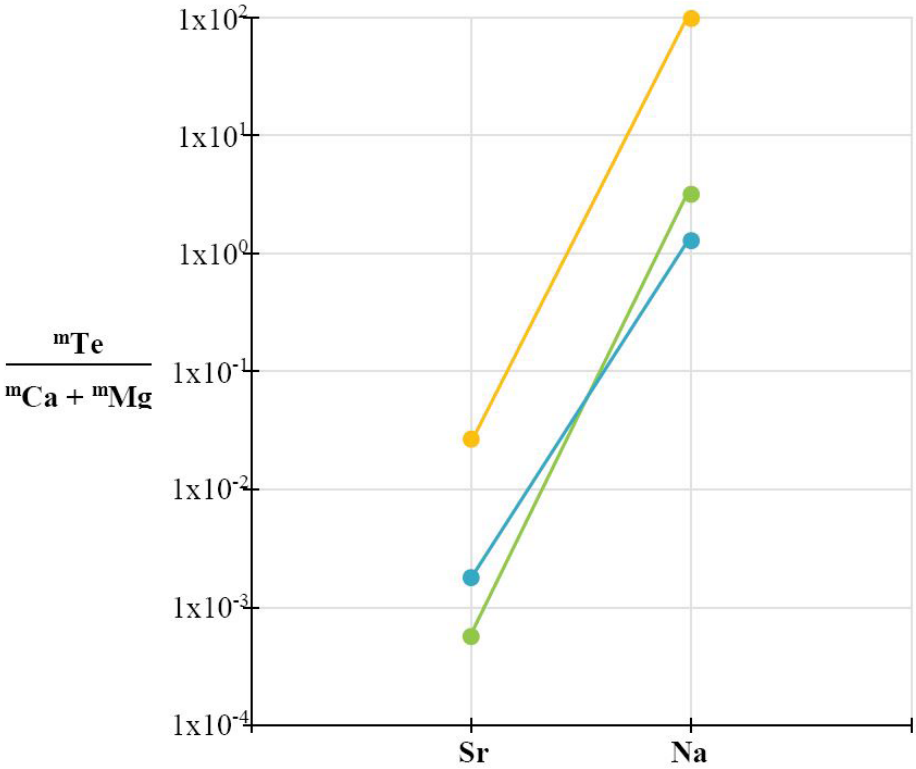

Figure 5.35. *Calculated Sr/Ca and Na/Ca molar concentration of the ancient Uinta Lake (yellow line), the Great Salt Lake (green line), and fresh lake waters (blue line).*

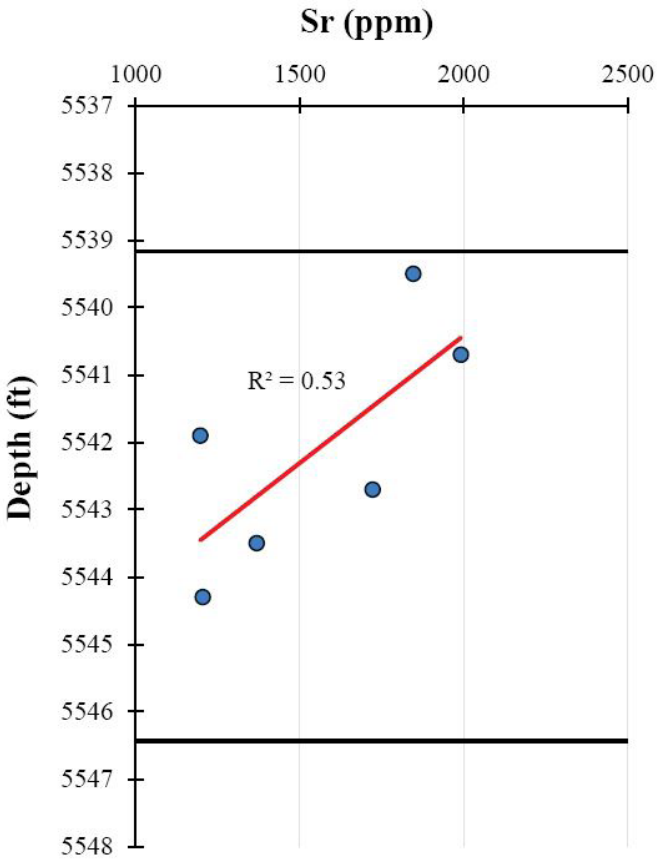

Figure 5.36. *Sr concentration variation of dolomite crystals with depth. PZ1 layer, well PW 13-06. Horizontal black lines: top and base of the PZ layer, red line: regression line.*

5.3 Porosity

This section presents porosity characteristics from different perspectives. First, porosity features are described by layer, then porosity is described according to its geographical and vertical distribution using well core-plug data, and finally porosity values from SEM images analysis are correlated to dolomite textures.

Core, thin sections, and SEM image petrographic descriptions show fabric and non-fabric selective porosity types (e.g., figures 5.5C, 5.4A). For fabric selective porosity, four different types are present: intercrystal (IC), moldic (MO), interparticle (IEP), and intraparticle (IAP). For non-fabric selective porosity, two different types are present: vug (VG) and fractures (FR). IAP is present only in grain-supported facies (ooid grainstone, F7) and some of these pores were occluded by calcite cement (phases 1b, 2b, and 8 in table 5.1) before oil migration (phase 12). Additionally, MO, IEP, and VG were partially occluded by carbonate and silica cementation phases (phases 2a, 4, 5a, 5b, and 9 in table 5.1).

Among the secondary pore types, IEP has the highest porosity values up to 20% (thin section estimation percentage); however, this porosity is exclusively present within the ooid grainstone facies (F7). FR porosity represents a very low porosity percentage (<1%) and most of the fractures are partially to completely filled by calcite cement (phase 15). In contrast, IC is the most abundant pore type in all PZ layers with a pore size that ranges from microporosity and mesoporosity types.

The geographic distribution of porosity was established based on extant core-plug data (table 5.10). According to the most abundant pore type identified in core, thin sections, and SEM images, porosity values measured from core plugs are assumed to largely represent the intercrystal porosity type.

PZ1 displays a wide porosity variation and has the highest porosity values of all PZ layers with an average of 17.7% (σ: 7.1%). Wells BBC 14-1, BBC 14-3, and N 6-28 have higher porosity variability in comparison with wells UT 15-13 and PW 13-06. In contrast, PZ1′ and PZ2 have the lowest porosity values with an average of 9.4% (σ: 5.9%) and 12.3% (σ: 7.1%), respectively.

Table 5.10. *Porosity values from plugs. Data from company reports obtained by UGS.*

Well	Depth (ft)	PZ	Porosity (%)
BBC 14-1	6684.0	PZ1	18.0
BBC 14-1	6685.5	PZ1	31.3
BBC 14-1	6686.2	PZ1	17.9
BBC 14-1	6687.0	PZ1	14.4
BBC 14-1	6688.2	PZ1	15.8
BBC 14-3	7373.7	PZ1	26.5
UT 15-13	7007.4	PZ1	17.8
UT 15-13	7008.2	PZ1	19.7
UT 15-13	7009.6	PZ1	24.8
PW 13-06	5540.1	PZ1	20.6
PW 13-06	5542.3	PZ1	21.9
BBC 14-1	6692.3	PZ1'	10.2
BBC 14-1	6694.0	PZ1'	11.7
BBC 14-3	7381.9	PZ1'	8.7
BBC 14-3	7382.6	PZ1'	2.6
N 6-28	8231.3	PZ1'	16.0
BBC 14-1	6701.6	PZ2	8.6
BBC 14-1	6703.0	PZ2	14.9
N 6-28	8241.1	PZ2	19.2
PW 13-06	5557.7	PZ2	12.6
DS 11-20	4990.5	PZ2	14.8
UI-16	4723.0	PZ2	4.0

The distribution of porosity in the PZ layers does not show distinctive trends laterally, i.e., along bedding. For PZ1, the correlation line (red dashed line in figure 5.37) between the average porosity values (white line within boxes) is roughly horizontal, but the maximum porosity values (high whiskers in figure 5.37) are located near the basin center (east-west section). PZ1′ has lower porosity values of all PZ layers near the basin center (east-west section) with highest porosity values in well N 6-28. PZ2 has the highest porosity variability, which varies from 20% near the basin center (well N 6-28) to 5% in the litoral-sublittoral zone (well UT 15-13) and increases up to 12% in the nearshore area (well PW 13-06) (figure 5.37).

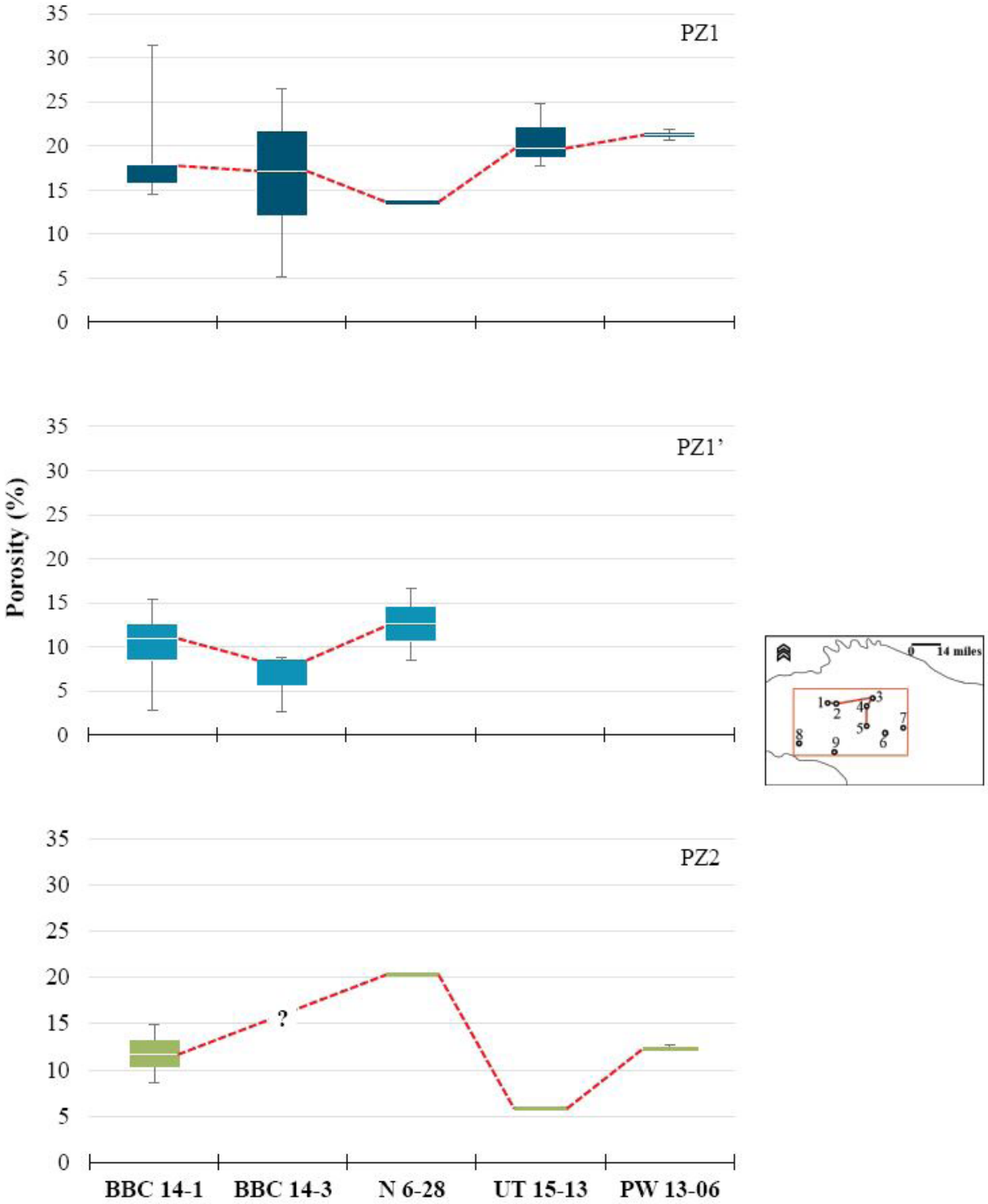

Figure 5.37. *Horizontal porosity variation for each PZ layer. Porosity values measured from core plug samples. Red dashed line represents porosity average correlation between wells. Numbers along the horizontal axes and in the inset map stand for wells/outcrops as follows: 1: BBC 14-1, 2: BBC 14-3, 3: N 6-28, 4: UT 15-13, 5: PW 13-06, 6: DS 11-20, 7: UI 16, 8: WCC, 9: NMC.*

The distribution of porosity does not show any distinctive vertical trends either. However, the highest porosity values are preferentially located near the top of the PZ layers, whereas the lowest porosity values are preferentially located near the base of the PZ layers (figure 5.38).

A different porosity measurement arises from SEM images by means of APS Assess 2.0 image analysis software. In this analysis, the darkest areas represent pores and the brightest areas represent dolomite crystals (figure 5.39). Three thin sections were selected for PZ1, four thin sections for PZ1′, and three thin sections for PZ2 (figure 5.12). A total of 32 SEM images were used to determine porosity in this manner. Porosity results are summarized in table 5.11.

The estimated porosity from SEM images shows a pattern similar to that of porsity from plugs. However, the porosity values estimated from image analysis are significantly higher than those measured from plugs. PZ1 has the highest porosity values with an average of 30.8% (σ: 10.1%) versus 17.7% from plugs. PZ1′ has a porosity average of 19.1% (σ: 4.8%) versus 9.4% from plugs, and PZ2 has a porosity average of 20.0% (σ: 6.6%) versus 12.3% from plugs. For this study, porosity measured from plugs is considered as base of reference. It is not possible to apply an appropriate correction to the porosity values estimated from SEM image analysis because both types of measurement were made on samples from different depths.

Porosity from well logs show remarkable differences between the PZ layers and the interbedded limestones, in that the dolomite PZ layers consistently have higher porosity values than the interbedded mollusc limestones by about 11%. The porosity of the PZ layers ranges from 8 to 26% with an average of 16%. In contrast, porosity of the interbedded limestones ranges from 2 to 11% with an average of 5% (figure 5.40).

The porosity values were calculated from the density logs via Equation 11 (Asquith and Gibson, 1982):

$$P_D = (\rho_m - RHOB) / (\rho_m - \rho_f) \quad (11)$$

where P_D is porosity (calculated from density log); ρ_m is the density of the matrix, which for dolomite is 2.87 g/cm^3 and for calcite is 2.71 g/cm^3; RHOB is the density data registered by the tool; and ρ_f is the density of the fluid. The oil in PZ layers is characterized as a highly paraffinic crude oil with API values between 30° and 40° (Birdwell and others, 2016). Therefore, the density value used for porosity calculation is 0.8 g/cm^3.

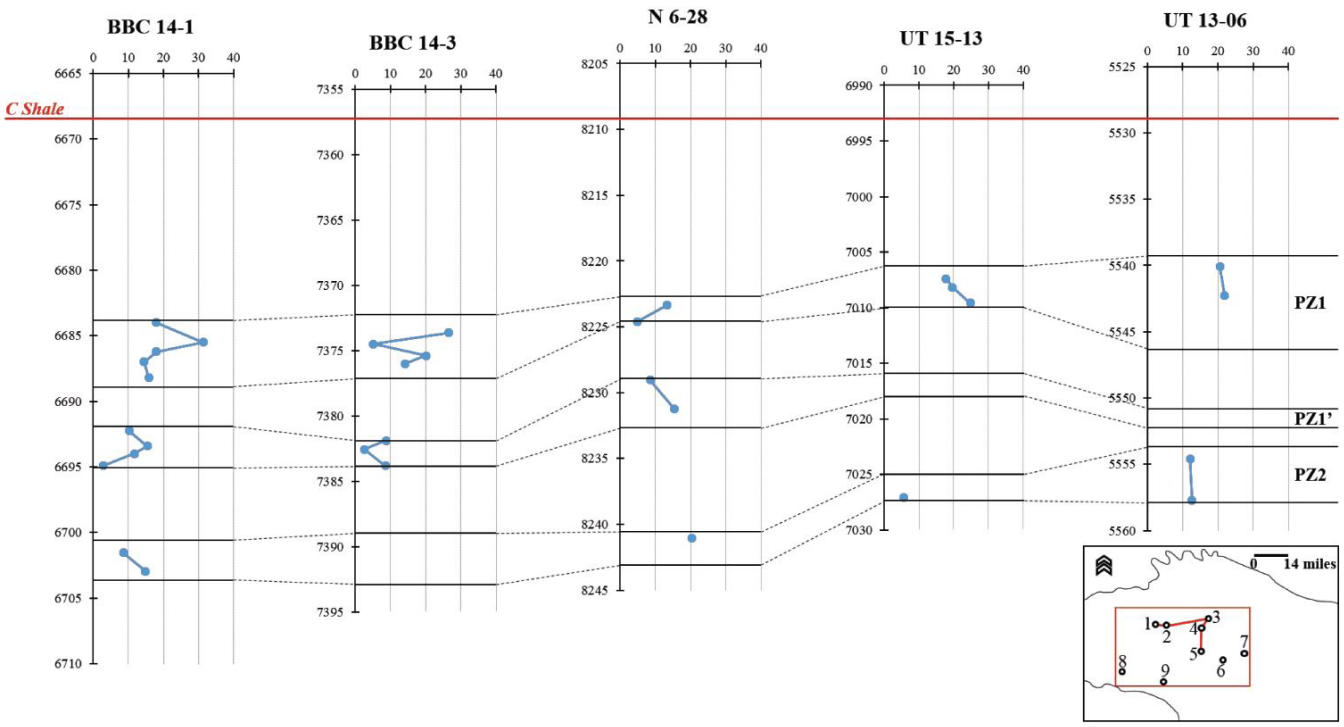

Figure 5.38. *Porosity variation with depth. Porosity values measured from core plugs; horizontal axis: porosity (%), vertical axis: depth (ft). Number in the inset map 1: BBC 14-1, 2: BBC 14-3, 3: N 6-28, 4: UT 15-13, 5: UT: 13-06, 6: DS 11-20, 7: UI 16, 8: WCC, 9: NMC.*

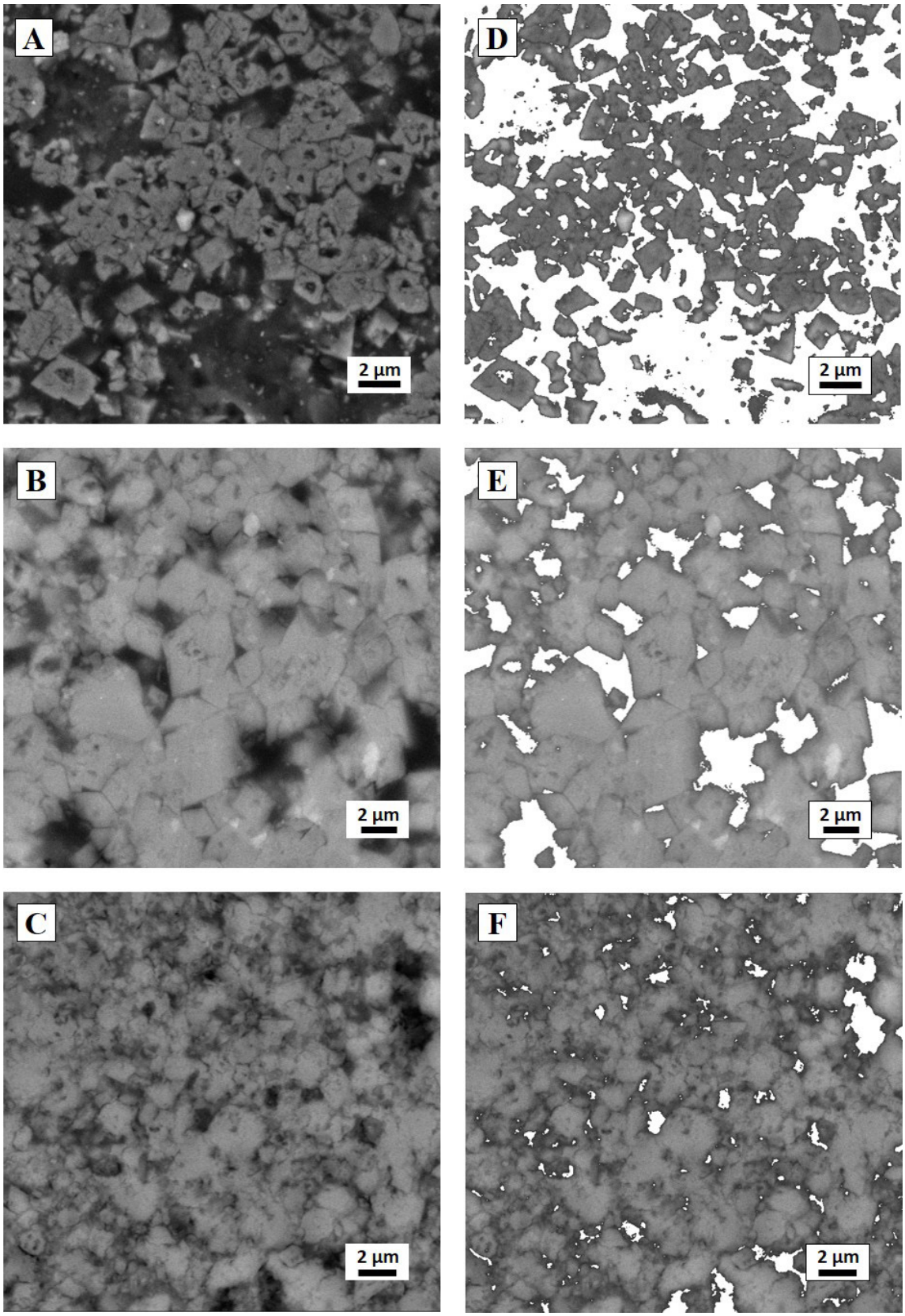

Figure 5.39. ***A.*** *SEM image of planar-e texture characterized by straight dolomite crystal faces; well: UT 15-13, sample: 13, 7017.4 ft, PZ1' layer.* ***B.*** *SEM image of planar-s texture characterized by straight and irregular dolomite crystal faces; well: N 6-28, sample: 9, 8242.5 ft, PZ2 layer.* ***C.*** *SEM image of nonplanar-a texture characterized by irregular dolomite crystal faces and more densely packed crystals; well: UT 15-13, sample: 11, 7009.9 ft, PZ1 layer.* ***D.*** *Same image as (A) highlighting porosity area (white area), estimated porosity: 43.38%.* ***E.*** *Same image as (B) highlighting porosity area, estimated porosity: 12.4%.* ***F.*** *Same image as (C) highlighting porosity area, estimated porosity: 7.82%.*

Table 5.11. *Porosity estimated from SEM images.*

Well	Sample	Depth (ft)	Image	Porosity (%)
		PZ1		
UT 15-13	15-13-11	7009.9	3	16.3
			4	13.7
			6	23.6
PW 13-06	13-06-07	5541.9	2	33.2
			3	44.2
	13-06-08	5543.5	2	32.2
			C1	39.6
			C2	38.6
			C3	29.5
			C5	37.3
		PZ1'		
N 6-28	6-28-7	8230.2	3	11.4
			4	21.4
			2	13.7
UT 15-13	15-13-12	7016.4	2	23.0
			6	18.1
			7	17.0
			8	17.0
			9	19.5
			4	21.8
PW 13-06	13-06-11	5552.3	1	27.9
		PZ2		
N 6-28	6-28-9	8242.5	3	12.5
			4	15.7
			5	12.4
			7	12.4
			9	22.7
			12	18.5
			13	18.9
UT 15-13	15-13-14	7025.2	1	17.4
			2	20.3
PW 13-06	13-06-12	5557.4	3	28.9
			1	30.3
			2	29.6

Porosity calculated from density logs shows the same pattern as porosity from plugs. PZ1 has the highest porosity values of all PZ layers with an average of 18.8% (σ: 4.0%), PZ1′ layer has the lowest porosity values with an average of 13.9% (σ: 1.5%), and PZ2 has an average of 15% (σ: 3.1%). Furthermore, the averaged porosity values calculated from logs are higher than the averaged porosity from plugs. For PZ1, porosity from logs is 1.0% higher than porosity from plugs. For PZ1′, porosity from logs is 4.5% higher than porosity from plugs. For PZ2, porosity from logs is 2.7% higher than porosity from plugs. However, an appropriated correction to the porosity from logs is not possible because the depth of measurement from logs is different than the plugs.

5.4 Permeability

Permeability data analysis is based on the extant data (table 5.12). The dolomitized PZ layers are characterized by very low permeability values that range from $1.2x10^{-4}$ to $2.9x10^{-1}$ mD. PZ1 has the highest permeability with an average of $8.1x10^{-2}$ mD; PZ1′ has the lowest permeability values with an average of $2.0x10^{-2}$ mD; and PZ2 has intermediate permeability that averages $5.4x10^{-2}$ mD.

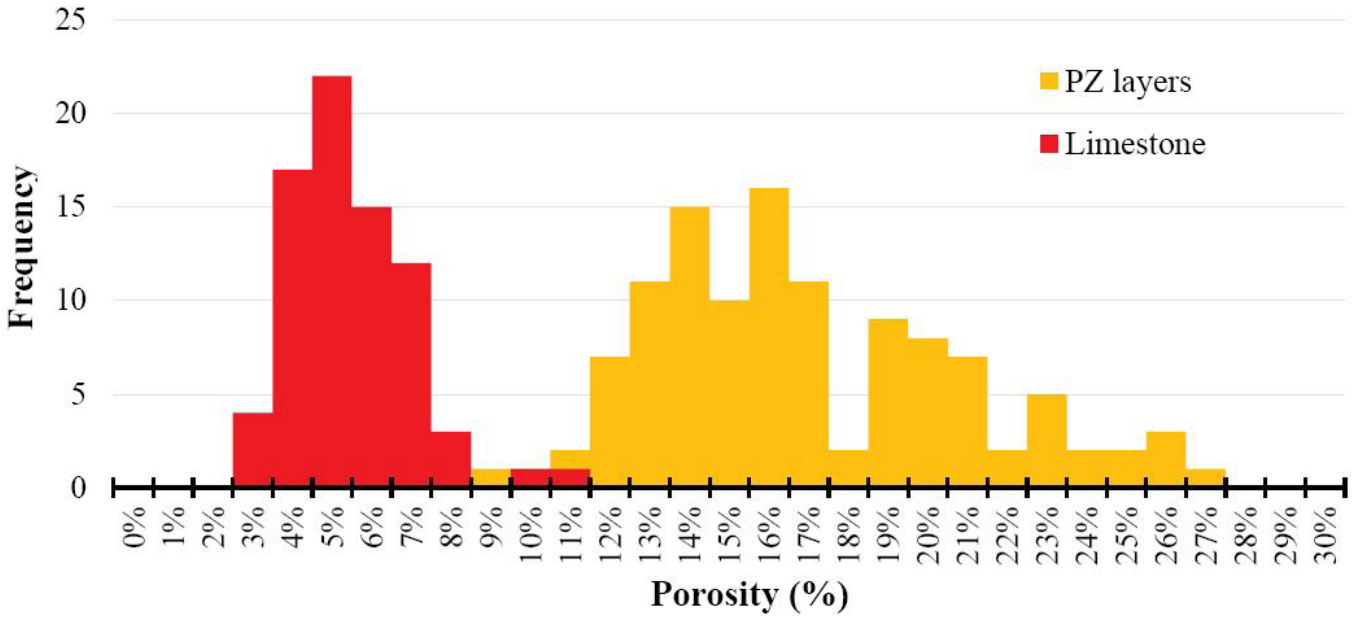

Figure 5.40. *Frequency distribution of porosity calculated from density logs for PZ layers and interbedded limestones.*

Table 5.12. *Permeability values from plugs. Data from company reports obtained by UGS.*

Well	Depth (ft)	Permeability (mD)	PZ
BBC 14-1	6684.0	0.03164	PZ1
BBC 14-1	6685.5	0.19893	PZ1
BBC 14-1	6686.2	0.02634	PZ1
BBC 14-1	6687.0	0.01842	PZ1
BBC 14-1	6688.2	0.00832	PZ1
BBC 14-3	7373.7	0.07700	PZ1
UT 15-13	7007.4	0.01559	PZ1
UT 15-13	7008.2	0.07056	PZ1
UT 15-13	7009.6	0.17472	PZ1
PW 13-06	5540.1	0.12667	PZ1
PW 13-06	5542.3	0.14943	PZ1
BBC 14-1	6692.3	0.00175	PZ1'
BBC 14-1	6694.0	0.07485	PZ1'
BBC 14-3	7381.9	0.00021	PZ1'
BBC 14-3	7382.6	0.00033	PZ1'
N 6-28	8231.3	0.02288	PZ1'
BBC 14-1	6701.6	0.00042	PZ2
BBC 14-1	6703.0	0.00398	PZ2
N 6-28	8241.1	0.29911	PZ2
PW 13-06	5557.7	0.00248	PZ2
DS 11-20	4990.5	0.02225	PZ2
UI-16	4723.0	0.00012	PZ2

Geographically, the permeability values of PZ1 are approximately the same along the chosen east-west and north-south cross sections (figure 5.41, top). In contrast, PZ1′ and PZ2 have an erratic distribution along the basin and do not show any discernible trends (figure 5.41, center and bottom).

On the other hand, the pore throat geometry varies systematically between dolomite textures. The planar-e and planar-s textures have a prismatic throat shape (space between the dolomite crystals) defined by straight and well-defined dolomite crystal faces (sheet-like). In contrast, the nonplanar texture has an irregular pore throat shape defined by irregular dolomite crystal faces (figure 5.42).

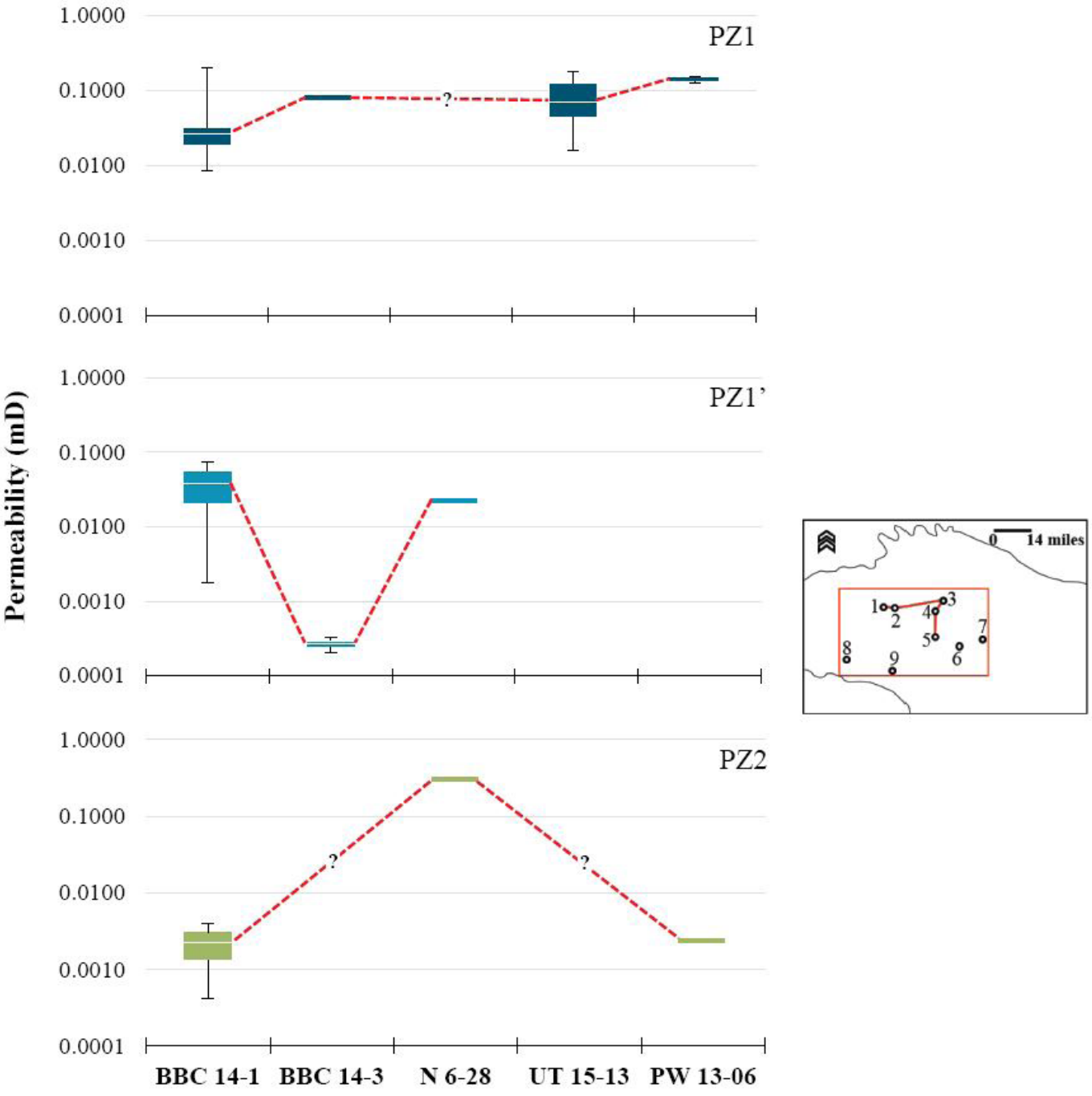

Figure 5.41. *Geographical distribution of permeability for each PZ layer. Data from core plug samples. Red dashed line represents permeability average correlation between wells. Numbers in the horizontal axis and in the inset map stand for wells/outcrops as 1: BBC 14-1, 2: BBC 14-3, 3: N 6-28, 4: UT 15-13, 5: PW 13-06, 6: DS 11-20, 7: UI 16, 8: WCC, 9: NMC.*

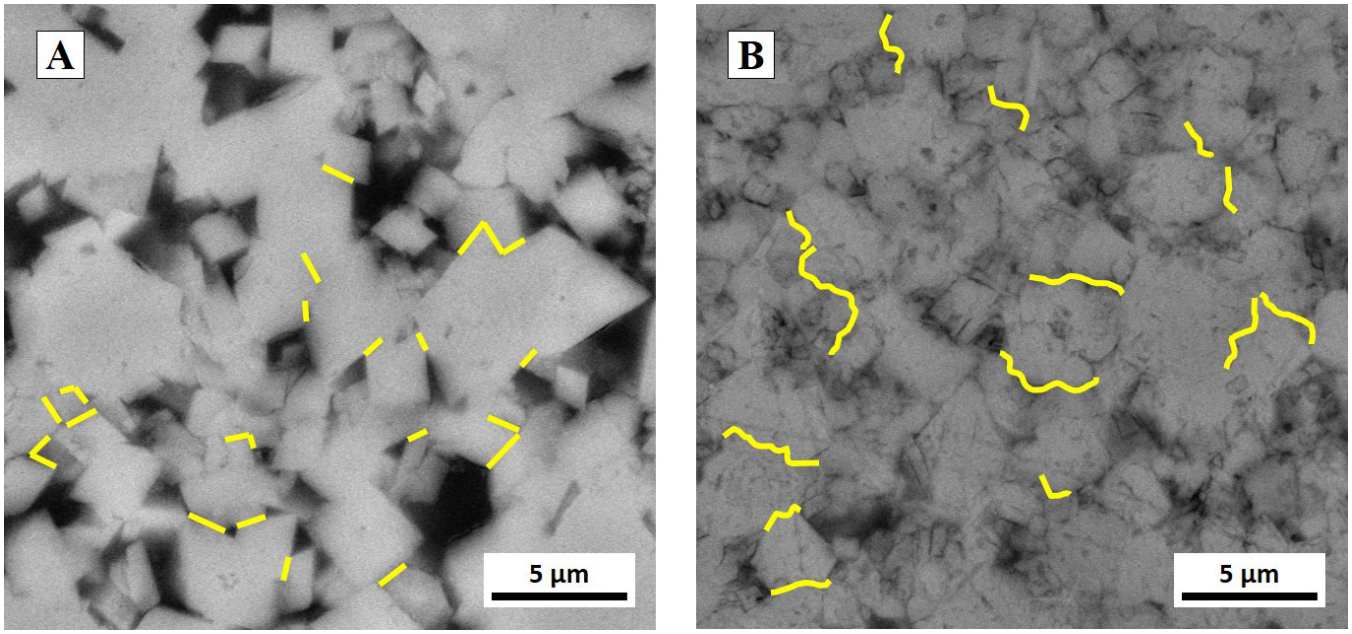

Figure 5.42. *Pore throat shapes.* ***A.*** *Sheet-like pore throat shape (yellow lines) between dolomite crystals in planar-e and planar-s textures; well: N 6-28, sample: 7, 8230.20 ft.* ***B.*** *Irregular pore throat shape (yellow lines) between dolomite crystals in nonplanar-a texture; well UT 15-13, sample: 11, 7009.90 ft.*

CHAPTER 6 DISCUSSION

This chapter provides an interpretation of dolomitization to account for the occurrence of petroliferous dolomite layers on various scales: (i) individual dolomite layers, (ii) the stratigraphic interval between D and C shales, and (iii) the context of regional paleogeography. An attempt to correlate dolomitization with reservoir characteristics is also discussed.

6.1 Individual Dolomite Layers

6.1.1 Dolomite: Replacement

The dolomite crystals of all PZ layers were created as replacement of lime mud and/or at least partially lithified lime mud. This replacement is shown by distinctive petrographic textural features such as partial or complete matrix-selective replacement and occurrence of microvugs (figure 5.4A) and molds (Tucker and Wright, 1990; Machel, 2004) (figure 5.4C to F and figure 6.8). These pores were probably generated by dissolution of metastable carbonate grains and/or crystals. Furthermore, there are no petrographic features to suggest direct precipitation of dolomite from the lake water. However, it cannot be ruled out that at least some of the dolomite in the PZ layers is a 'cement' or direct formation from aqueous solution.

6.1.2 Mg^{2+} Source

Dolomitization is favoured by several factors such as high Mg^{2+}/ Ca^{2+} ratio, high alkalinity, and high temperatures (Machel and Mountjoy, 1986; Machel and Mountjoy, 1987; Machel, 2004). Based on the geological setting of Lake Uinta during dolomitization (see Chapter 4, Section 4.2) and its burial history (see Chapter 5, Section 5.1.2), there were two potential Mg^{2+} sources: (i) transformation of clay minerals from the shales and (ii) lake water.

The interbedded shale beds are a potential source of Mg^{2+} due to the smectite-illite transformation that releases Mg^{2+} to the fluids, hence potentially favouring dolomitization (Kahle, 1965). However, this potential source of Mg^{2+} is discarded here because (i) petrographic evidence suggests dolomitization at very shallow depth and (ii) the calculated temperature is between ~ 23 to 30°C, with a maximum temperature of about 40°C (based on the conventional oxygen isotope thermometer; see Chapter 5, Section 5.2.2.6). This temperature range is much lower than the temperature of smectite-illite transformation of about 70°C (Pytte and Reynolds, 1989), which usually corresponds to a burial depth of about 1–2 km. Therefore, dolomitization occurred well before the release of Mg^{2+} from smectite-illite transformation.

Lacustrine environments generally have a low magnesium content between 2.4 ppm (Turkana Lake) to 756 ppm (Caspian Lake) (Nikanorov and Brazhnikova, 2004). Freshwater lakes can have Mg^{2+} concentrations below 1 ppm (Nikanorov and Brazhnikova, 2004) when the water inflow rate is higher than the water outflow in the absence of evaporation (Renaut and Gierloswki-Kordesch, 2010).

The most probable source of magnesium for dolomite formation in the UBm is from weathering of surrounding igneous rocks having abundant magnesium-rich minerals (pyroxenes and amphiboles) that released magnesium ions, which were then transported by rivers and groundwater. Igneous rocks that supply relatively high amounts of Mg^{2+} are gabbros, norites, pyroxenites, harzburguites, and dunites and their analogous. Such mafic rocks have high magnesium oxide content that varies between 6.73% for gabbro and 37.94% for dunite (Best, 1982). Thus, the Mg^{2+} for dolomitization likely was derived from the magnesium-rich igneous rocks that were located in and around the southwestern region of the Uinta Basin (Hunt, 1956) during deposition of the UBm, notably a Proterozoic metapyroxenite body located within the probable catchment area at the northwestern part of the Uncompahgre Uplift, where magnesium oxide (weight percent) is as high as 19.4 % (Case, 1991) (figure 6.1).

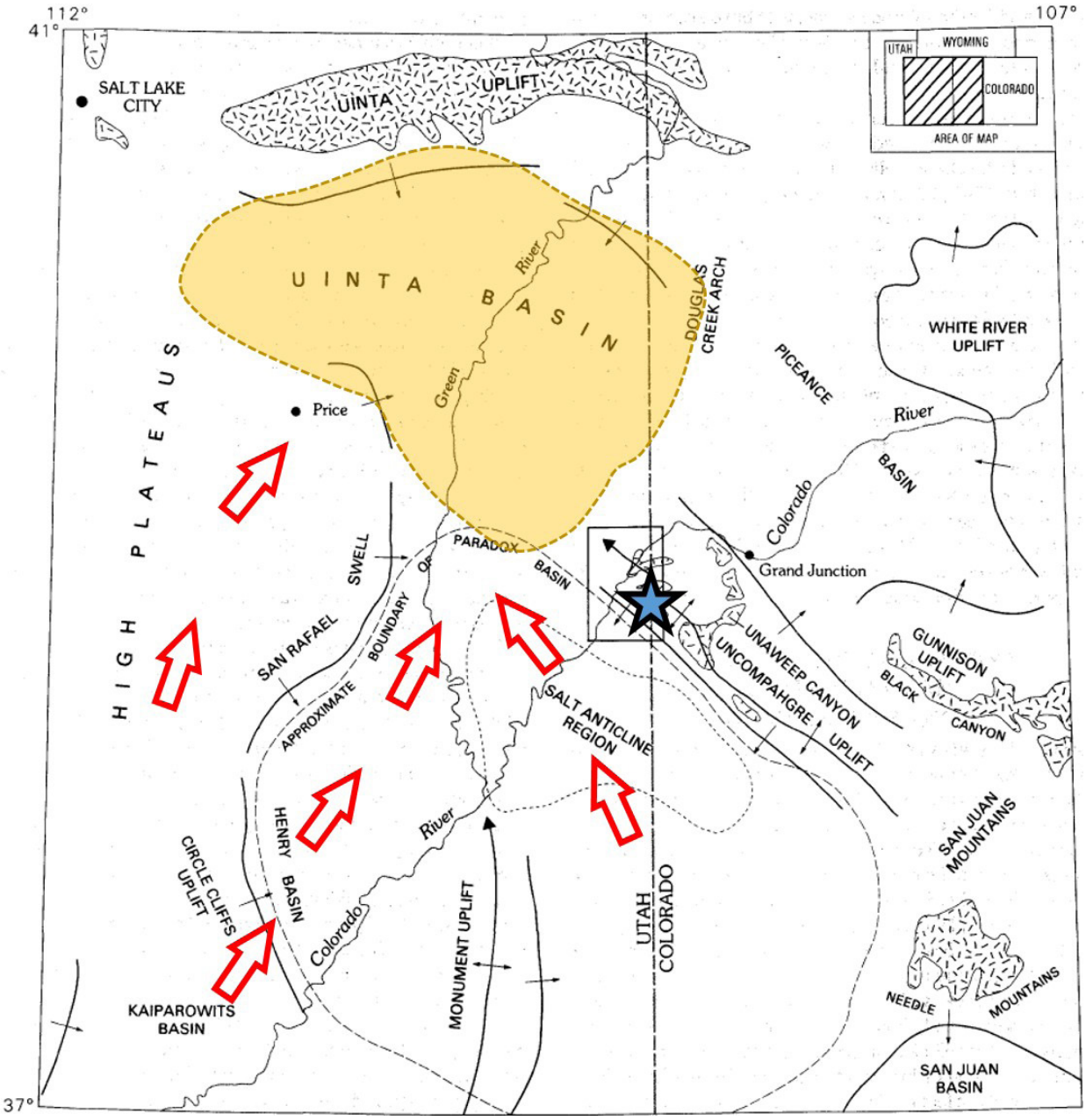

Figure 6.1. *Location of metapyroxenite (blue star) and the Uinta basin (yellow area). Additional potential sources of Mg^{2+} were located toward south/southwest of the Uinta Basin (Chapter 2, Section 2.2). Red arrow represents the probable paleo-river drainage. Figure modified from Case (1991).*

Chemical weathering is the main process that provides magnesium to surface waters (Nikanorov and Brazhnikova, 2004). An example of this process is defined in the reaction below (Broecker, 1971) in which enstatite ($MgSiO_3$), a common component of mafic and ultramafic intrusive rocks (Nesse, 1991), weathers in a subaerial environment as follows:

$$2CO_2 + 3H_2O + MgSiO_3 \rightarrow Mg^{2+} + H_4SiO_4 + 2HCO_3^- \quad (12)$$

Chemical weathering of mafic and ultramafic igneous bodies during deposition of the UBm may have been favoured by climate changes, specifically by relatively short term (10^3 to 10^5 years) periods of global warming with elevated atmospheric CO_2 values [higher than 2000 ppm (Pearson and Palmer, 2000)] that took place in the early Eocene epoch (Zachos and others, 2001) and likely enhanced the rate of the chemical weathering of igneous rocks in the region. In this global climate short-term scenario, the amount of rain increased during cooler periods (Robert and Kennett, 1992), whereas the atmospheric carbon dioxide values increased during warmer periods, such as during the Early Eocene Climatic Optimum (EECO), with CO_2 concentrations almost nine times the current values (Pearson and Palmer, 2000; Zachos and others, 2001). This suggests that the alternating limestone-dolostone layers in the UBm reflect cycles of cooler and warmer climate, with concomitant cyclical changes in temperature, amount of river recharge, evaporation, and Mg^{2+} input.

6.1.3 Interpretation and Model of Dolomitization

Most dolomite crystals (about 91%; Chapter 5, Section 5.2.1.2) are classified as aphanocrystalline, ranging between 0.25 to 3 μm in size. Dolomite crystal size is controlled by nucleation and growth rates that are directly regulated by temperature (Gregg and Sibley, 1984; Sibley and Gregg, 1987). The overall very small dolomite crystal size was likely caused by high nucleation rates paired with low growth rates, which are commonly associated with evaporitic (syndepositional) environments. Folk and Siedlecka (1974) stated that very fine dolomite crystals are an indicator of an evaporite cycle in schizohaline environments. Warren (2000) characterized syndepositional dolomite crystals in evaporite settings as very fine in size (< 10 μm). Budd (1997) characterized Holocene dolomites precipitated directly from seawater also as very fine crystalline (< 10 μm) and classified them as 'penecontemporaneous' dolomite.

In all of these cases, dolomitization was driven by evaporation that also favoured crystallization of evaporite minerals (such as quartzine and gypsum). While there is no evidence that sulfates were formed in the UBm, quartzine and other silica varieties are common (figures 5.6A to F), suggesting dolomitization occurred in an evaporitic environment. Furthermore, the mineralogical association of dolomite-silica and lack of gypsum suggest that the dolomitizing water in the UBm was Lake Uinta water that had very low sulfate concentration paired with relatively high Mg^{2+} concentration.

In addition, the north to south preferential distribution of dolomite textures (figure 5.14) suggest that the chemical composition of the dolomitizing water and its temperature changed over time. Relatively low dolomite-supersaturated water paired with relatively low temperature may have led to the development of rhombohedral dolomite crystals with planar-e texture, whereas high dolomite supersaturation paired with high temperature may have led to the development of planar-s and nonplanar textures (Sibley and Gregg, 1987). Hence, the observed textural distribution may have been generated by variations in dolomite saturation and temperature.

The lake water level was probably controlled by climate changes as well, and increased lake water temperature and evaporation paired with decreased river recharge promoted the drop in lake water level.

As a corollary, the lake water density also changed. Because of evaporation, the lake water became denser and Mg-saturated waters moved basinward and partially dolomitizing the already deposited calcium carbonate sediments. This mode of dolomitization conforms to the reflux model, first proposed by Adams and Rhodes (1960), in which metastable calcium carbonate is replaced by dolomite as sinking, denser, evaporated brines pass through unconsolidated lime mud.

This interpretation is supported by variations of excess calcium in the dolomites with depth. In the case of reflux dolomitization, nearly stoichiometric dolomite should be located near the top of each PZ layer, whereas calcium-rich dolomite should be preferentially located near the base of each PZ layer, as is observed in the data (figures 5.24 and 5.25). The level of supersaturation with respect to dolomite would have been highest at the beginning of dolomitization, forming nearly stoichiometric crystals very near to the source of the dolomitizing water—the sediment-water interface. Increasingly Ca-rich crystals would have formed from water with decreasing levels of supersaturation farther down into the sediment. However, later recrystallization would overprint this pattern, likely one of the reasons why the observed pattern in dolomite Ca-excess is not a regular top-down pattern (figure 5.24).

Furthermore, as Ca-excess and ordering are usually negatively correlated; the ordering of the PZ dolomites should decrease in each layer from the top downwards. The data appear to conform to this pattern, allowing for partial recrystallization. Differential reaction time and/or recrystallization probably created the observed variations in dolomite cation ordering with depth.

Moreover, layer-by-layer dolomite formation via reflux of the UBm implies a progressive increase in thickness of each PZ layer basinward; however, this pattern was not observed (further discussed in section 6.4.1). This finding suggests that reflux was not the only process responsible for dolomitization in the UBm.

A second process that was likely involved in dolomitization of the UBm took place diachronously from south to north in parts of the lake that became subaerially exposed during progressively falling water level, i.e., in the supralittoral zone (see Chapter 4). This setting likely experienced evaporative pumping of groundwater, with a vertical hydraulic gradient that allowed pore fluids to move upward (Hsü and Siegenthaler, 1969; Eugster and Surdam, 1973). This type of dolomitization conforms to the playa model that was first proposed for the GRF by Eugster and Surdam (1973). Evaporative pumping allowed at least partial recrystallization of the previously dolomitized sediments as well as the formation of additional dolomite.

The Sr concentrations of dolomite in the UBm can be interpreted as a record of ascending pore water flow. According to Machel (1999), if the dolomitizing fluid has a Sr/Ca ratio equal to or lower than that of the limestone, the Sr concentration in the dolomite should increase downflow. In contrast, if the dolomitizing fluid has a Sr/Ca ratio higher than that of the limestone, the Sr concentration in the dolomite should decrease downflow. Applying this concept, the evaporated and upward moving pore fluid probably had a Sr/Ca ratio equal to or less than that of the parental lime mud sediments (figure 5.36).

A third process that may have contributed to the current distribution of dolomite is mechanical reworking and redeposition of dolomite during episodic, perhaps even seasonal, flooding of the area. In this case, dolomite formed in the shallowest parts of the system was episodically washed into the deeper parts of the lake, as proposed by Eugster and Surdam (1973). This process is nearly impossible to verify and likely was of minor importance volumetrically. In any case, this process is not one of dolomitization (or dolomite formation, referring to dolomite that may have formed as 'cement' rather than replacement), and thus is excluded from the following discussion.

Be it reflux or evaporative pumping, dolomitization (or dolomite formation) was controlled by climate. In the warmer periods, freshwater input was diminished, and lake water evaporation was promoted, allowing dolomite to form. In the cooler periods, freshwater input increased, diluting the lake water, thereby inhibiting dolomitization. The inferred freshwater-brackish water changes are also recorded by fossil associations: freshwater molluscs (pelecypods and gastropods) are present in and/or dominate the floatstone layers, whereas more saline-tolerant organisms (ostracods and gyronites) characterize the dolomitized layers. Dolomitization in the UBm is thus interpreted as the result of cyclical fluctuations in lake water levels, salinity, and temperature, all driven by cyclical changes in climate, whereby each layer was dolomitized individually by two processes: reflux in the subaqueous part followed and/or overprinted by evaporative pumping in the subaerial (supralittoral) part. Furthermore, it is likely that most dolomitization took place during the lake level falls, i.e., while the climate was warming, although it cannot be ruled out that the basinward parts of each layer formed some dolomite and/or recrystallized dolomite also during the rise of the lake level following the lake level low stand.

An idealized representation of this scenario is illustrated in figure 6.2. This interpretation contemplates the hypothetical variation of the lake/pore water supersaturation with respect to dolomite and temperature at different time intervals (t_0 to t_5 in figure 6.2), coupled with physiographic changes such that the lake water level went down, and the lake decreased in size, thereby causing the shoreline to move toward the center of the lake.

In the freshwater setting (t_0), the lake water was undersaturated for dolomite and the temperature likely was below 12°C, based on the oxygen isotope data (Chapter 5, Section 5.2.2.6). In this setting lime mud was deposited and remained as calcium carbonate.

In the next phase (t_1), the reflux dolomitization started when the lake water had reached and/or exceeded supersaturation for dolomite, driven by increased evaporation and rising water temperature, paired with decreased fresh water inflow. Dolomitization during t_1 likely took place across all submerged lime mud sediments simultaneously, but only replaced them partially.

With continuous increase in temperature the lake water became warmer and possibly even more supersaturated with respect to dolomite (the level of supersaturation was governed by counteracting processes at this time: the increase in temperature and evaporation versus removal of Mg via ongoing dolomite formation). During phase (t_2) the lake water level dropped far enough such that the sediments located in the nearshore area were partially exposed. At this time reflux dolomitization continued in

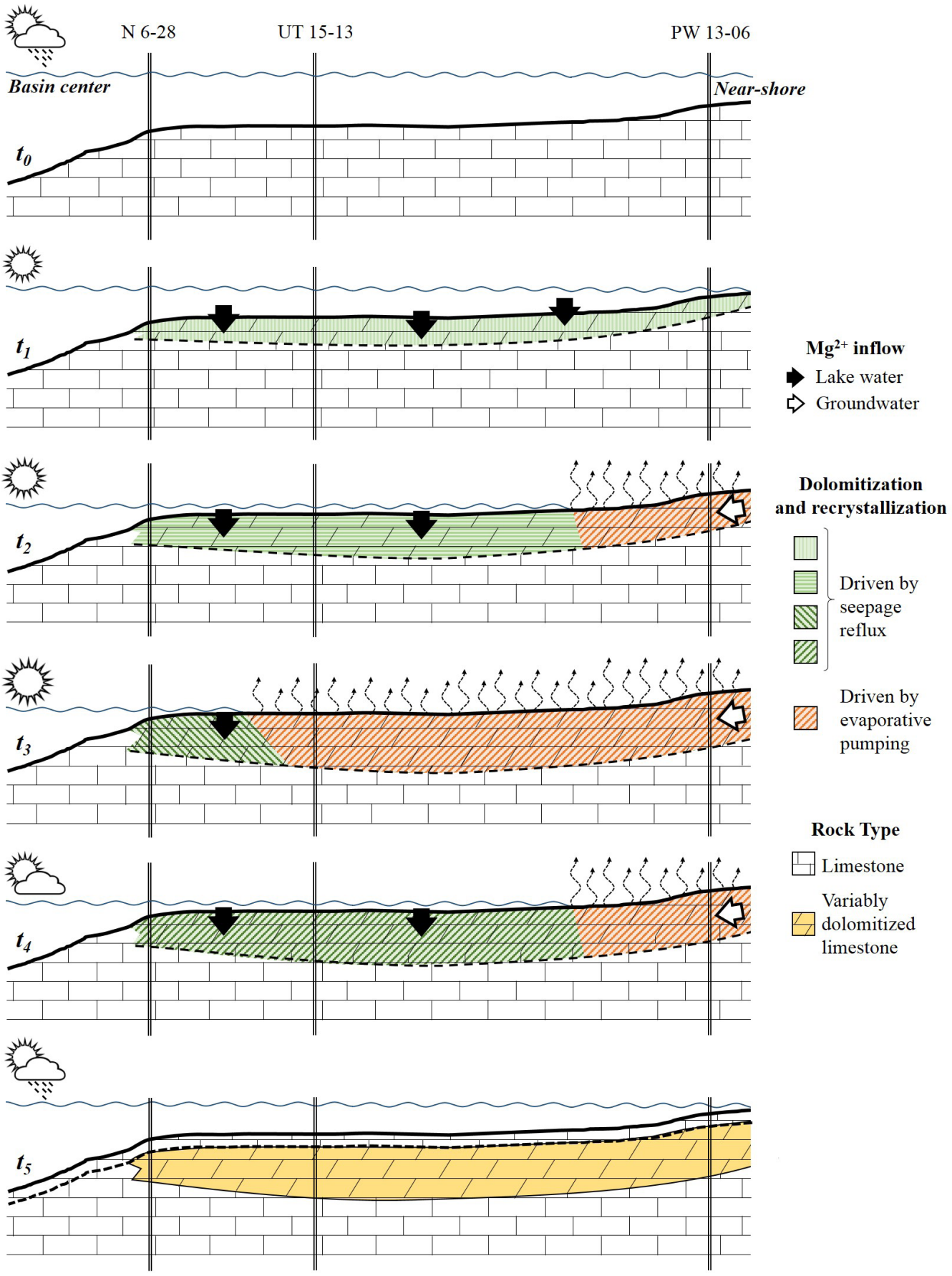

Figure 6.2. *Interpretation of dolomitization of an individual PZ-layer in the UBm. See text for discussion.*

the submerged sediments whereas evaporative pumping took place in the subaerially exposed lake sediments (t_2 in figure 6.2,). Therefore, reflux and evaporative pumping occurred at the same time.

At the maximum regression of the lake water table (t_3), the temperature reached the highest values at ~35°C based on the oxygen isotope data (Chapter 5, Section 5.2.2.6). The lake/pore water may have reached maximum supersaturation with respect to dolomite (supersaturation on $t_3>t_2>t_1$). Sediments deposited near the basin center that remained submerged were still subject to reflux dolomitization process, thus also for a longer period of time compared to the areas farther south that were exposed at this time and now subjected to evaporative pumping.

Following the warmest part of the climate cycle, the lake level rose due to increased river recharge and reduced evaporation, and the water temperature and level of dolomite supersaturation would decrease (t_4 in figure 6.2). Renewed flooding of the previously exposed sediments likely overprinted the already formed dolomites to a minor degree of recrystallization as long as the lake water temperature was warm enough to overcome kinetic barriers.

Finally (t_5), the system would return to the same or similar conditions that were present at the beginning of the cycle. Lime mud would now form on top of the dolomitized layer as long as the climate was cool and wet enough to allow for calcite precipitation.

Formation of the PZ layers by the combined seepage reflux and evaporative pumping processes necessitates that the inferred climate cycle took place at least as many times as there are dolostone-limestone couplets, i.e., this cycle was repeated at least five times (figure 4.14). Furthermore, it cannot be ruled out that there were higher order (shorter) climate cycles that are masked within the observed dolostone-limestone couplets, as inferred by Eugster and Surdam (1973) and Eugster and Hardie (1978), who found that certain lacustrine and/or playa phenomena (such as shrinkage cracks, crusts or nodules of a variety of evaporite minerals) are rather short lived and may not survive into the geologic record.

6.1.4 Calcite–Dolomite–Chert: Lake Water Chemical Evolution

The variation in the chemical composition of the lake water can be further characterized by the mineral association and timing between calcite, dolomite, and chert occurrence. The diagenesis of these minerals can be briefly described as: (i) calcite precipitation (deposition of lime mud), (ii) dolomitization of calcite (lime mud sediment and/or limestone), (iii) chert formation within PZ layers, and (iv) continued dolomitization. Precipitation of calcium carbonate occurred during the fresh water and relatively low temperature phases. Dolomite formation was caused by evaporation of lake/pore water driven by increased temperature (see Chapter 5, Sections 5.2.1.6 and 5.2.2.6). According to the estimation of lake water temperatures using $\delta^{18}O$ geothermometry (Chapter 5, Section 5.2.2.6), the calcite-dolomite mineral association suggests a gradual increase of the lake water temperature from about 12°C (calcite precipitation) up to about 36° to 40°C (dolomitization).

In the fresh water scenario, calcite precipitated likely by a decrease in CO_2 concentration either due to photosynthesis (high organic activity) or by lake water degassing (Eugster and Hardie, 1978; Tucker and Wright, 1990). Calcite precipitation led to an increase in the Mg/Ca ratio that, paired with an increase of lake/pore water temperature, favoured dolomitization. Chert, which is the only recognizable evaporite mineral in the stratigraphic interval of interest, likely precipitated at relatively advanced levels of evaporation of the lake/pore water (Eugster and Hardie, 1978) or by certain changes in the chemical composition of the lake water due to increased Si-input from run-off and associated pH changes (Eugster, 1967). Chert formation in Lake Magadi (Kenya) is a good analog for chert formation in the UBm, where syndepositional formation of chert is due to pH reduction of alkaline brines associated with periods of dilution/concentration stages of the lake water driven by periods of rainfall alternating with evaporation (Eugster 1967). Additionally, the position of chert formation within the paragenetic sequence of the UBm (see Chapter 5, Sections 5.1 and 5.2 and table 5.1) is crucial for the interpretation of dolomitization by virtue of enclosing earlier formed dolomite. Enclosed crystals of dolomite were isolated from the bulk formation water(s) during burial and thus may retain pristine isotopic signatures representing the conditions during dolomitization. Unfortunately, isotopic analysis of dolomite enclosed in chert could not be performed before completing this thesis.

The chemical variations of the lake/pore water proposed herein is in accordance with Eugster and Hardie's (1978) fluid evolution in a hydrologically 'closed' system. They proposed three main possible evolution pathways based on the $HCO_3^-/(Mg^{2+} + Ca^{2+})$ ratio. In the case of the UBm, the lack of sodium carbonates and calcium sulfates within the stratigraphic interval of interest suggests lake water had an equal bicarbonate (HCO_3^-) and $Mg^{2+}+ Ca^{2+}$ ratio. After precipitation of low-Mg calcite and dolomite, the lake water would have been impoverished in alkaline metals which favored silica precipitation likely as opal (Eugster and Hardie, 1978). The isopachous euhedral quartz cement rims (figures 5.5D and E) around the dolomitized peloids may represent silica precipitation by nearly complete pore water evaporation.

Last, a common way to characterize the chemistry and environment of dolomitization is by stoichiometry (or lack thereof) and ordering (Machel 2004). In the case of the UBm this approach yields a curious result. The dolomite crystals are characterized by a wide range in Ca-excess (Chapter 5, Section 5.2.1.4) paired with a low cation ordering (Chapter 5, Section 5.2.1.5), suggesting a very low degree, if not nearly the absence of, 'significant recrystallization' *sensu* Machel (1999). This is highly unusual for rocks of this age (Chapter 1, Section 2.4) and burial history (Chapter 5, Section 5.1.3).

The low and/or almost lacking recrystallization of the UBm dolomites is probably due to (i) low permeability of the PZ layers, (ii) low water to rock ratio, (iii) a nearly closed system during burial, or (iv) a combination of these alternatives. This interpretation is supported by the low permeability values of all PZ layers having average values that range from $8.1x10^{-2}$ mD for PZ1, $2.0x10^{-2}$ mD for PZ1′, and $5.4x10^{-2}$ mD for PZ2 (see Chapter 5, Section 5.4). On the other hand, Birdwell and others (2016) measured the pressure gradient in 42 intervals in or near the UBm and found six intervals with pressure gradients equal to greater than 0.5 psi/ft. Anderson and Roesink (2013) calculated the UBm pressure gradient with maximum values of 0.65 psi/ft.

According to the calculated and measured pressures of the UBm, the stratigraphic interval of interest is characterized as an overpressured reservoir [based on Dickinson's (1953) overpressure definition] with values equal to or higher than 0.5 psi/ft. The resulting low permeability and overpressure conditions of the unconventional reservoirs likely inhibited the dolomites from recrystallization, thereby preventing the calcium excess of the dolomites from being flushed out of the system.

6.2 Stratigraphic Interval D and C Shales

Periodic variations in climate are recorded by repetition of the idealized cycle (figures 4.14 and 6.2), which is present five times within the stratigraphic interval of interest. Dolomite formation was not possible without the changes in climate that drove the cyclicity. Thus, dolomitization was the result of cyclical variations in climate.

6.3 Regional Paleogeography

In addition to climate as the chief driving force of cyclicity and dolomitization in the UBm, tectonism has been recognized as a major factor controlling deposition and diagenesis in the region around the Uinta Basin (Davis and others, 2009; Gierlowski-Kordesch, 2010; Tänavsuu-Milkeviciene and others, 2017). Changes in depositional settings caused by climate variations occurred during relatively short periods of time, whereas changes driven by tectonism took longer periods of time (Tänavsuu-Milkeviciene and others, 2017).

Davis and others (2009) interpreted the evolution of the catchment area of the lacustrine intermountain and coexisting basins of Claron Lake, Lake Flagstaff, and Lake Uinta (figure 6.3). These authors identified shifts of the $\delta^{18}O$ values in carbonate samples of around +6‰ from the base (UBm) to the middle section (Douglas Creek Member) of the GRF (figure 6.3). Davis and others (2009) interpreted these shifts as resulting from changes in the hydrologic closure that led to the evaporation of Lake Uinta at the top of the GRF (saline facies). According to Davis and others (2009), the change in the catchment area was likely caused by post-depositional diachronous tectonic uplift that elevated the catchment area of the lake, which was probably higher than 2500 m at the time of deposition of the top of the GRF (saline facies). The $\delta^{18}O$ values of the dolomite layers in the UBm are consistent with the values reported by Davis and others (2009) and correspond to the values from the base of the GRF (figure 6.3C), in which the catchment area was probably lower in altitude.

The dolomite layers of the UBm do not record the regional tectonism because the latter occurred after UBm deposition and on a much larger time scale. The difference in the $\delta^{18}O$ values of the dolomite between the PZ2 and PZ1′ layers is only 0.3‰ PDB, and between the PZ1′ and PZ1 layers it is only 0.4‰ PDB (Chapter 5, Section 5.2.1.6).

6.4 Dolomitization and Reservoir Properties

6.4.1 Geometry of the Dolomite PZ Layers

The dolomite PZ layers display a lenticular geometry that is variable in thickness. The thickest sections are located in an intermediate position between the nearshore and basin center areas, and the layers pinch out basinward (north) and landward (south) (figures 6.4 to 6.6). PZ1 thickness varies from 1.9 ft (0.6 m) to 7.1 ft (2.2 m); PZ1′ from 1.5 ft (0.5 m) to 7.1 ft (1.2 m); and PZ2 from 1.5 ft (0.5 m) to 4 ft (1.2 m). The thickness variations in the PZ layers were probably controlled by several factors,

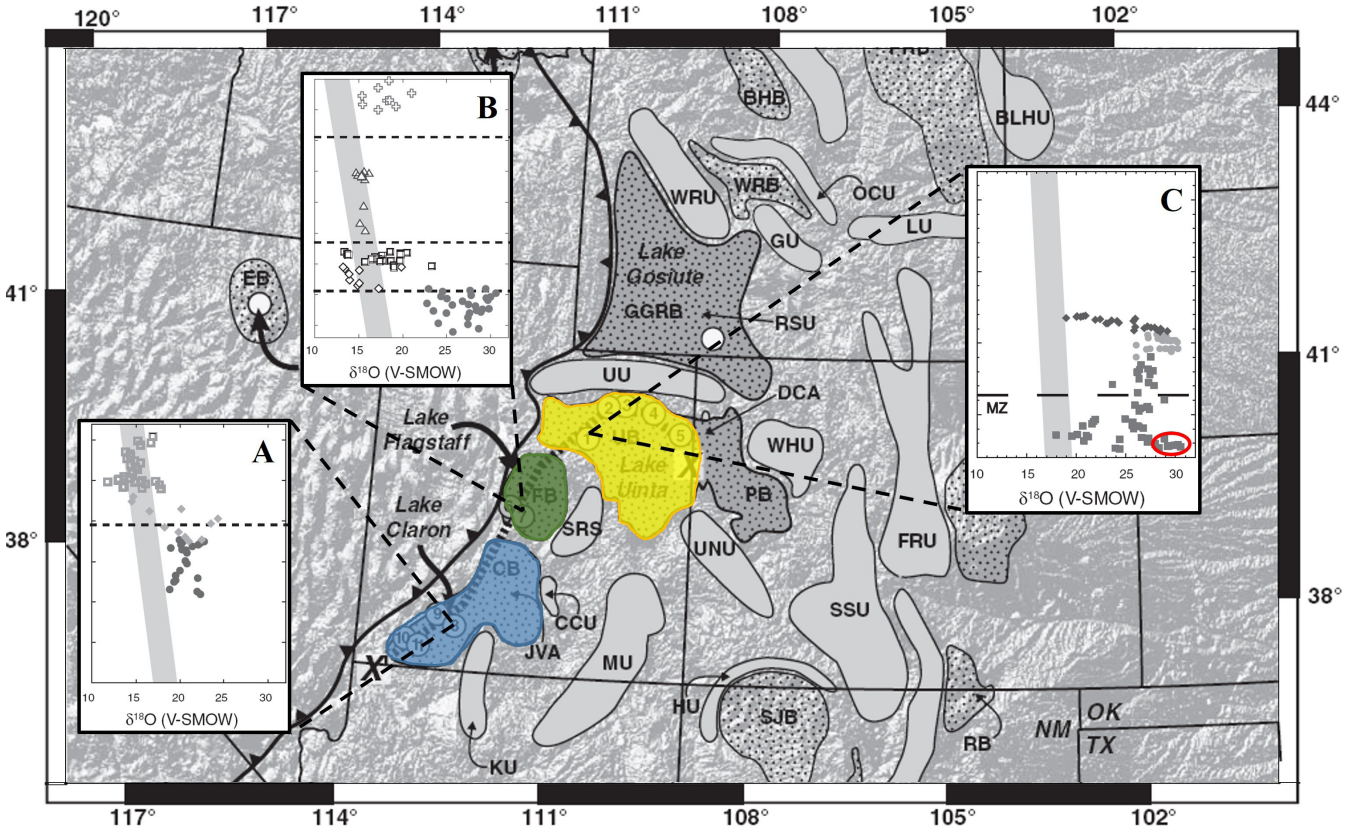

Figure 6.3. *Decrease of the $\delta^{18}O$ values for the Claron Basin (blue area) of about 5‰* ***A.****, Flagstaff Basin (green area) of about 7‰* ***B.****, and Uinta basin (yellow area) of about 6‰* ***C.****, probably caused by tectonism (Davis and others, 2009). (C) Tectonic uplifting took place after UBm deposition around 45 Ma. The $\delta^{18}O$ values of the dolomites in the PZ layers is highlighted by the red oval in the lower right corner of (C). Vertical axis in the inserted $\delta^{18}O$ plots is time (Ma), figure modified from Davis and others (2009).*

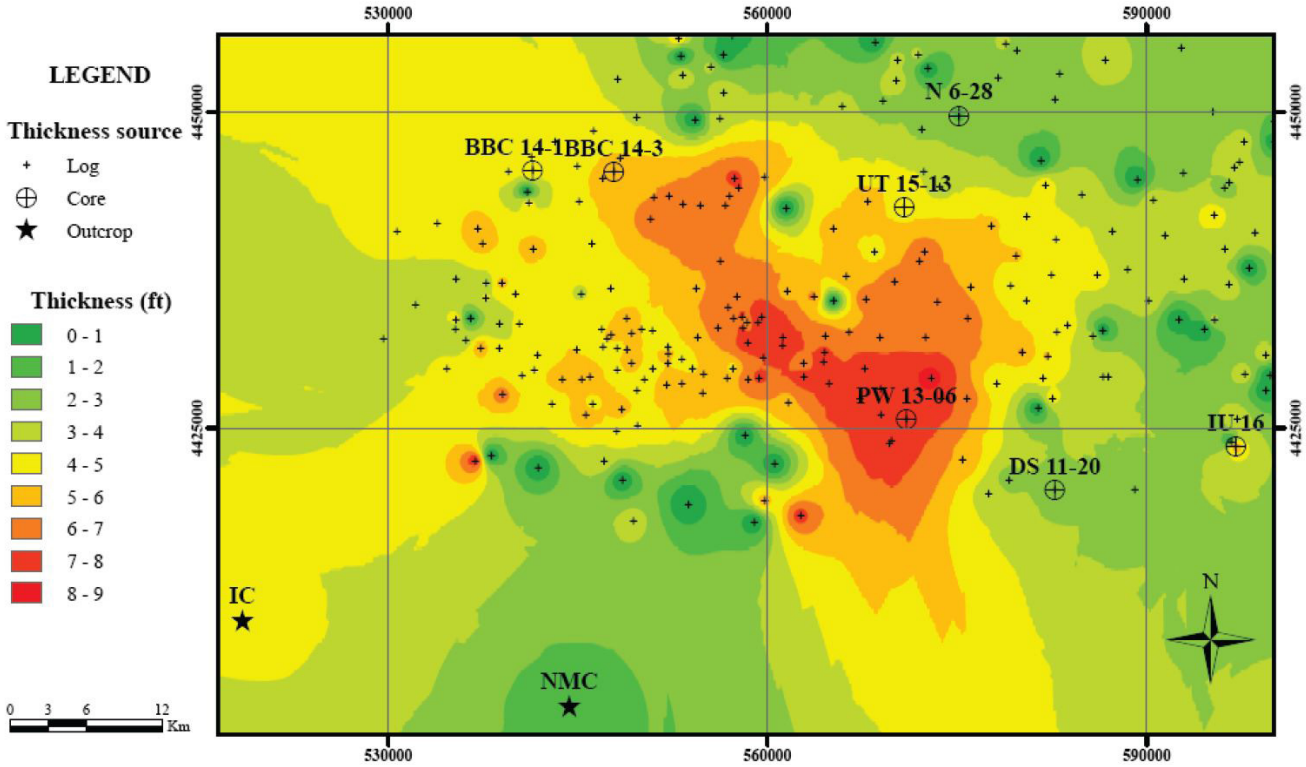

Figure 6.4. *Isopach map for PZ1 layer. Thickness measured from logs, cores, and outcrops.*

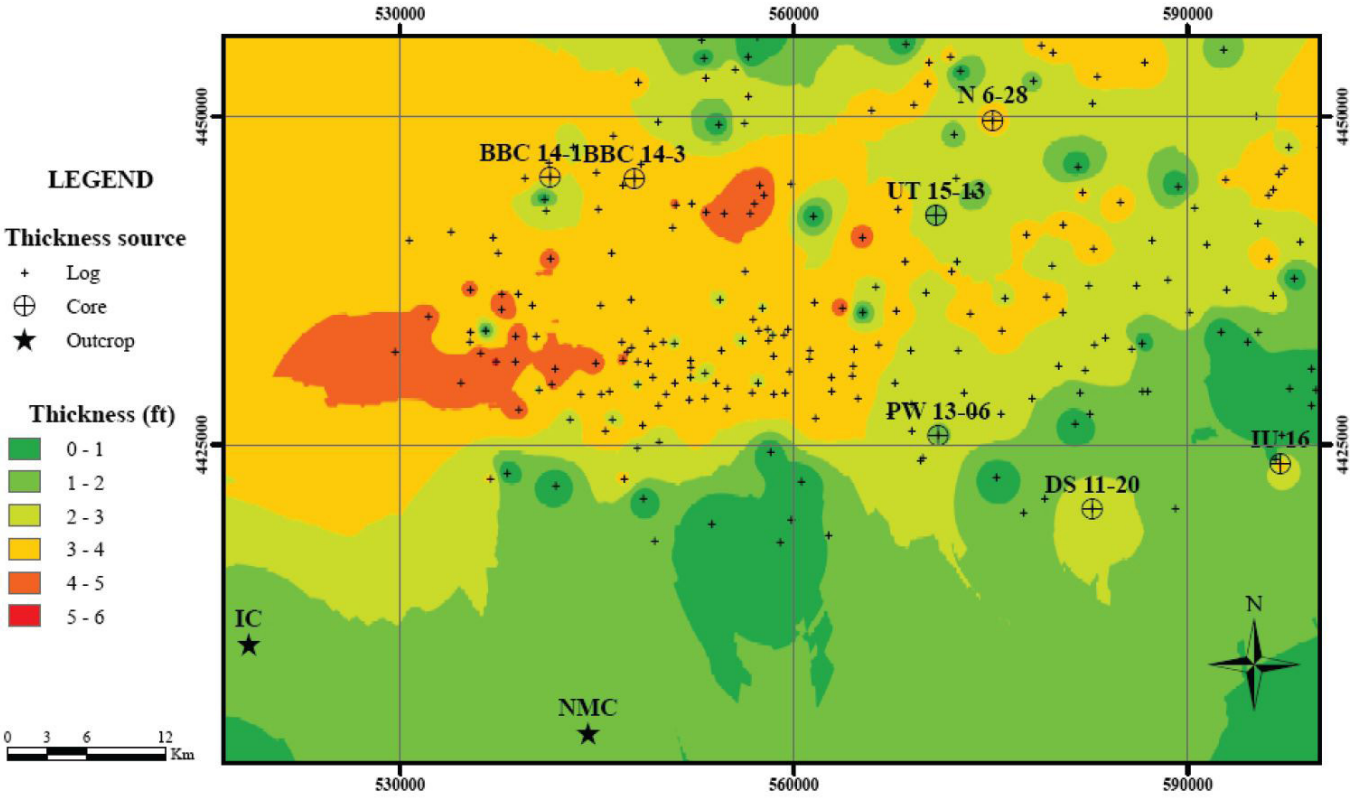

Figure 6.5. *Isopach map for PZ1' layer. Thickness measured from logs, cores, and outcrops.*

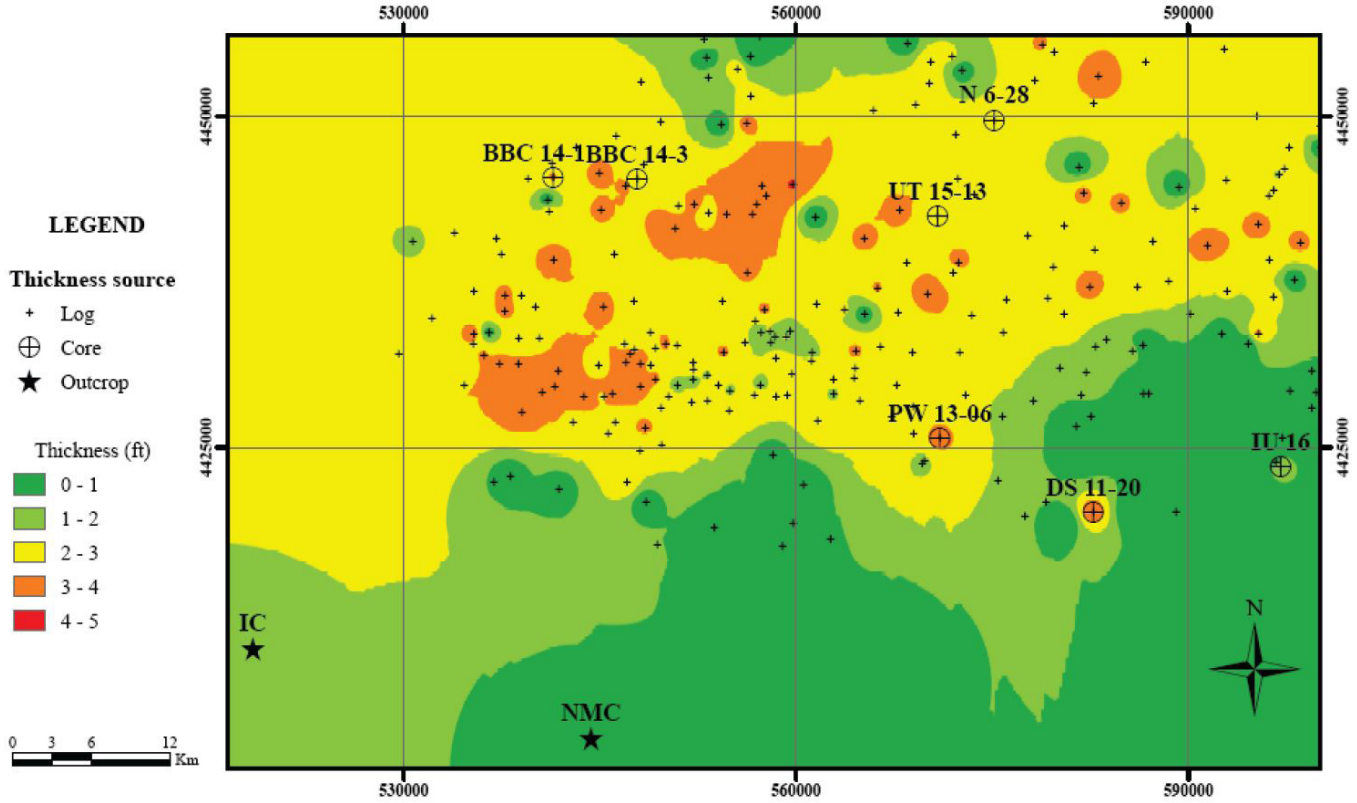

Figure 6.6. *Isopach map for PZ2 layer. Thickness measured from logs, cores, and outcrops.*

which include availability of dolomitizing fluids, Mg/Ca ratio, Mg^{2+} inflow (flux), paleobathymetry of Lake Uinta, porosity and permeability variations of the unconsolidated or partially consolidated lime mud, lake water level fluctuations, or a combination of these alternatives.

The paleobathymetry of the lake during dolomite formation likely was a shallow and flat littoral to sublittoral zone between the shoreline and the lake center (figures 4.13 and 6.2), possibly isolated at times from the lake center by carbonate shoals that were occasionally subaerially exposed. In this scenario, a "lagoon" would have been located between the shoal and the shoreline, wherein the thicker section of the dolomite PZ layers developed. In addition, and as noted before, it is possible that dolomite formed in the shallowest parts of the system was episodically washed into the deeper parts of the lake, either into the "lagoonal" area or farther toward the lake center, as proposed by Eugster and Surdam (1973), thus increasing the thickness of the PZ layers.

Another factor that defined the thickness of the dolomite PZ layers, at least in part, was porosity variations in the partially consolidated lime mud material. The more porous and more permeable material allowed dolomitizing water to percolate and/or get pumped upward more easily than through the less porous and/or less permeable material. Reduction of porosity and permeability of the partially consolidated sediments that took place prior to dolomitization was generated by calcite cementation phases (meniscus and blocky calcite cement) in the nearshore areas (Chapter 5, Sections 5.1.1.2 and 5.1.1.4).

In addition, variations of the lake water level, composition, and temperature, as described in Sections 6.1.3 and 6.1.4, may also have controlled the thickness of the PZ layers, at least partially. The greatest thickness of the PZ layers may correspond to areas where reflux and evaporative pumping superimposed each other for a long time and over a large extent.

A PZ1 isopachous map shows thickness trends southeast to northwest (figure 6.4). This trend is unique for PZ1. In contrast, the PZ1′ and PZ2 layers have an east-west thickness trend (figures 6.5 and 6.6). The southeast-northwest trend of thickness for PZ1 could be related to a major Mg^{2+} flux of groundwater coming from the paleorivers derived from the Uncompahgre Uplift, at the southeast area of the Uinta Basin (see figures 2.2 and 6.1), that favoured dolomitization around the area of the probable Mg^{2+} flux.

6.4.2 Porosity and Permeability

Dolomitization and porosity are closely related but there is no general rule that describes this relationship. Machel (2004) defined six potential sources of porosity enhancement related to dolomitization: so-called mole-per-mole replacement, calcite dissolution, dolomite dissolution, pH reduction in pore water, fluid mixing, and thermochemical sulfate reduction.

In the stratigraphic section of interest, dolomitization might have increased porosity as result of (i) the so-called mole-per-mole replacement that likely enhanced porosity due to volume loss, as represented by dolomitization (Reaction 13), in which two moles of calcite are replaced by one mole of dolomite (Machel 2004); (ii) calcite dissolution (micrite); and (iii) dissolution of metastable dolomite located in the core of the dolomite crystals (figures 5.13B and C, and 5.39A). Dissolution of these minerals was probably caused in the advanced stage of dolomitization after all available Mg^{2+} was exhausted and the fluid remained undersaturated in calcite; or when the fluid was close to the equilibrium and dolomite formation was kinetically inhibited while calcite dissolution was promoted (Machel, 2004).

$$2CaCO_3 + Mg^{2+} \rightarrow CaMg(CO_3)_2 + Ca^{2+} \quad (13)$$

On the other hand, there is a consistent difference in porosity between PZ layers and interbedded limestones (figure 6.7). Dolomitized sediments may have had higher porosity compared to those layers that are now present as limestones, or the limestone layers were more prone to lose primary porosity through diagenesis than the dolomite layers. If so, the porosity difference is likely due to differences in the mechanical and chemical behavior of theses rocks during mechanical and chemical compaction, respectively (Schmoker and Halley, 1982).

According to Hugman and Friedman (1979), grain size is the most important textural feature in carbonate rocks that controls the response during mechanical compression. Thus, the limestone and dolostone beds likely behaved similarly during mechanical compaction, given the same crystal size range for both minerals. In contrast, the susceptibility to dissolve under a stress field is different for calcite and dolomite. Calcite is more susceptible to dissolve than dolomite (Trurnit, 1968; Tada and Siever, 1989). Therefore, the limestone layers were more susceptible to chemical compaction (Phase 7), with or without the formation of stylolites. The latter form only when siliciclastic impurities are present in sufficient quantities.

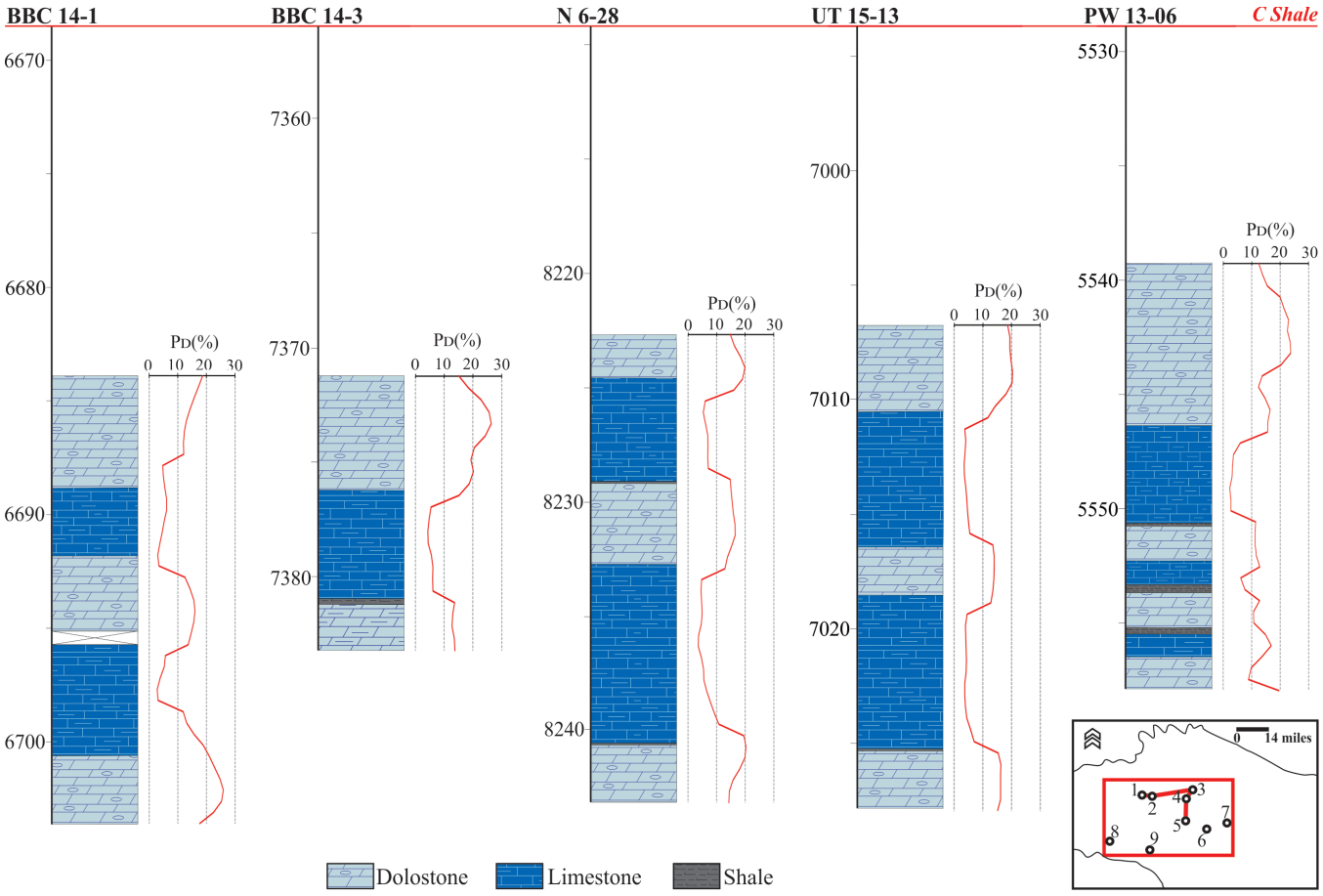

Figure 6.7. *Porosity (PD) calculated from density logs for PZ layers and interbedded limestones. Numbers in the inset map stand for wells/outcrops as 1: BBC 14-1, 2: BBC 14-3, 3: N 6-28, 4: UT 15-13, 5: PW 13-06, 6: DS 11-20, 7: UI 16, 8: WCC, 9: NMC.*

Additionally, the dolomitization timing also contributed to the preservation of the inherited porosity. According to the paragenetic sequence defined for the interval of interest (Chapter 5, Section 5.1.2), dolomitization (Phase 3) took place before mechanical compaction (Phase 7). This circumstance literally solidified the dolomite layers, converting them into a stronger framework and allowing for greater preservation of the porosity during subsequent compaction.

The preservation of the primary porosity is evident in the texture of the precursor limestones (figure 6.8). Conservation of the original textures was achieved by replacement of micrite (in matrix, peloids, ooids, and intraclasts) by dolomite crystals of about the same size as the parental micrite, otherwise the original texture (mudstone, wackestone, etc.) would have been obliterated.

Dolomite textures and porosity values show a positive correlation in some cases (Woody and others, 1996; Moore, 2001; Lucia, 2007). Woody and others (1996) correlated planar-e textures with high porosity and high permeability values. In contrast, there is a weak positive correlation between dolomite texture and porosity for the PZ layers of the UBm. However, planar textures (planar-e and planar-s) preferentially show the highest porosity values, whereas nonplanar-a texture shows the lowest porosity values (figure 6.9).

Dolomite texture and crystal shape are also correlated with permeability. The pore throat shape is inversely proportional to permeability and can be expressed by Equation 14 (England and others, 1987) as the tortuosity factor τ:

$$k = D * r^2 / \tau^2 \qquad (14)$$

where, k is permeability, *D* is a constant: 1/8, r is the mean pore radius, and τ is tortuosity.

Furthermore, tortuosity τ is also defined by the ratio of the length of the flow pathway relative to the length of the sample (Azar and others, 2008) (figure 6.10).

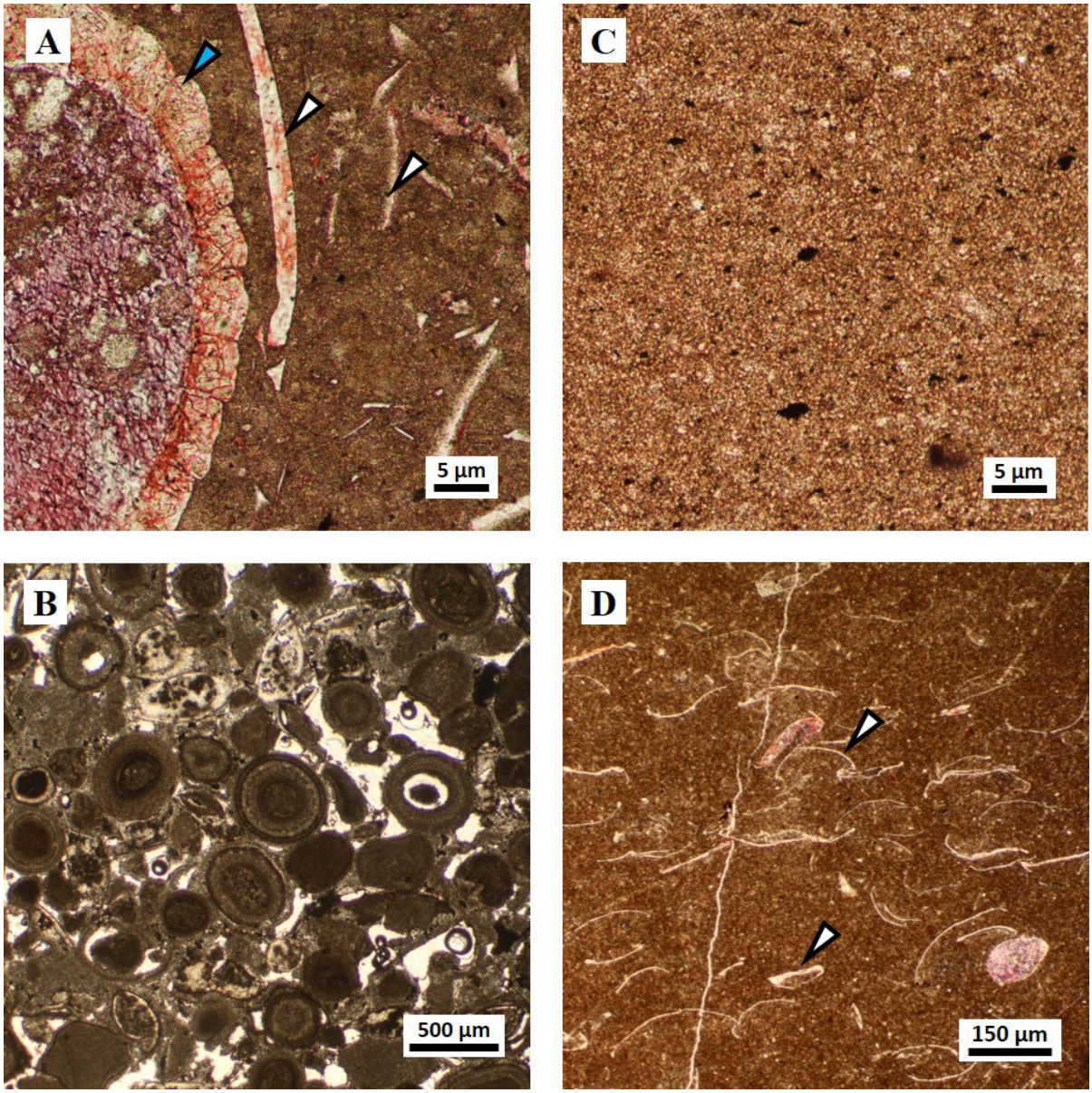

Figure 6.8. *Preservation of textures from the precursor limestone.* ***A.*** *TLP of dolopackstone, matrix-selective dolomitization, in which bioclasts (gyronite: blue arrow, ostracods shells: white arrows) were not replaced, well: BBC 14-3, sample: 28, 7374.05 ft.* ***B.*** *TLP of dolograinstone, mimetic dolomite replacement of ooids, well: PW 13-06, sample: 6, 5539.5 ft.* ***C.*** *TLP of dolomudstone, aphanocrystalline dolomite matrix and microvugs filled with hydrocarbons (arrows), well: UT 15-13, sample: 5, 6682.2 ft.* ***D.*** *TLP of intraclastic dolowackestone, matrix completely dolomitized; ostracod shell fragments (arrows) were not dolomitized; well: BBC 14-1, sample: 13, 6684.9 ft.*

Planar-e and planar-s textures commonly have short flow pathways (L_a) with pore throat shapes defined by prismatic volumes (figure 5.42A). These characteristics enhance permeability. In contrast, the nonplanar-a texture usually has longer flow pathways (L_a) associated with irregular pore throat shapes (figure 5.42B) that, coupled together, reduce permeability. However, the texture distribution, crystal size, and crystal shape in the PZ layers is highly variable, which is probably the result of superimposed dolomitization events (reflux and evaporative pumping) that overprinted the original texture and modified the dolomite crystal size and shape.

The high heterogeneity of porosity and permeability features of these unconventional oil reservoirs makes it difficult to predict "sweet spots" within the basin. Nevertheless, the PZ1 layer has the greatest thickness and highest porosity and permeability values of all PZ layers (figure 6.11).

The highest values of porosity and permeability of the PZ1 likely are related to the shapes of the dolomite crystals, which may have been controlled by temperature variations. The interpretation for dolomitization of the UBm as previously discussed is

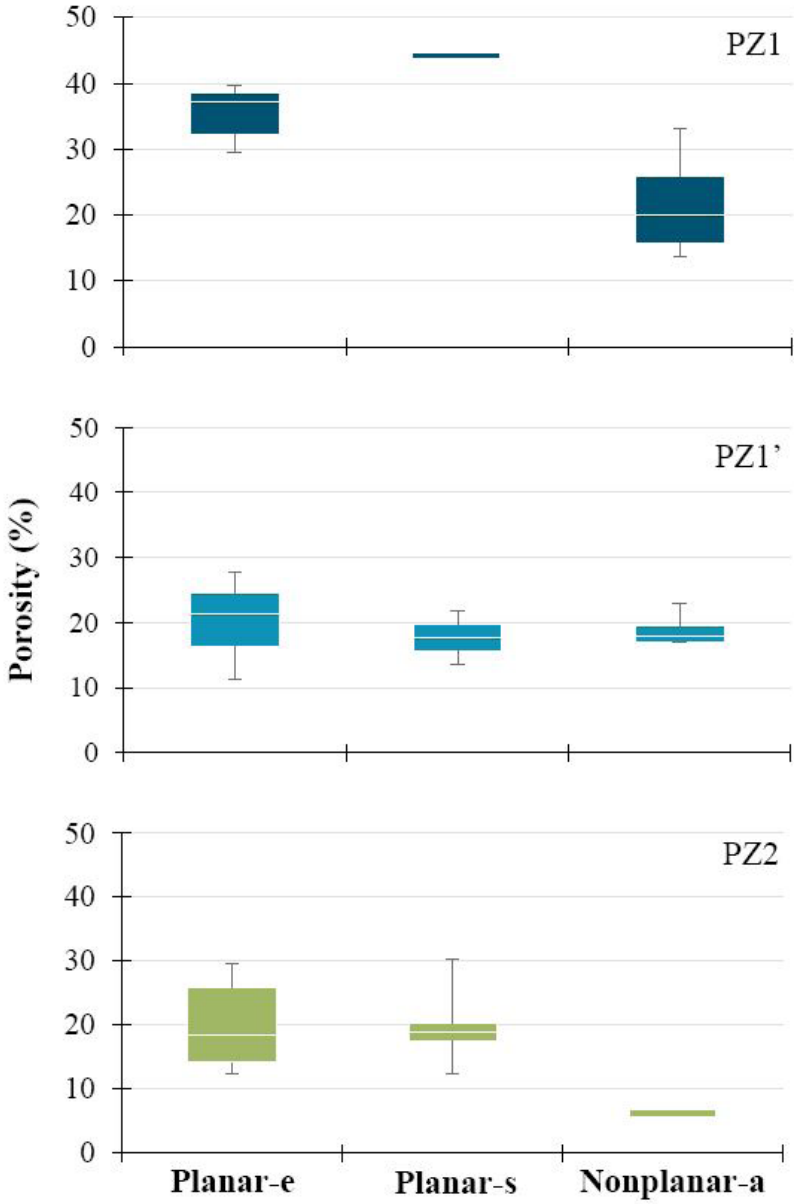

Figure 6.9. *Dolomite texture versus porosity for each PZ layer. Dolomite texture determined from SEM images and porosity estimated by image analysis software (Chapter 5, Section 5.3.1).*

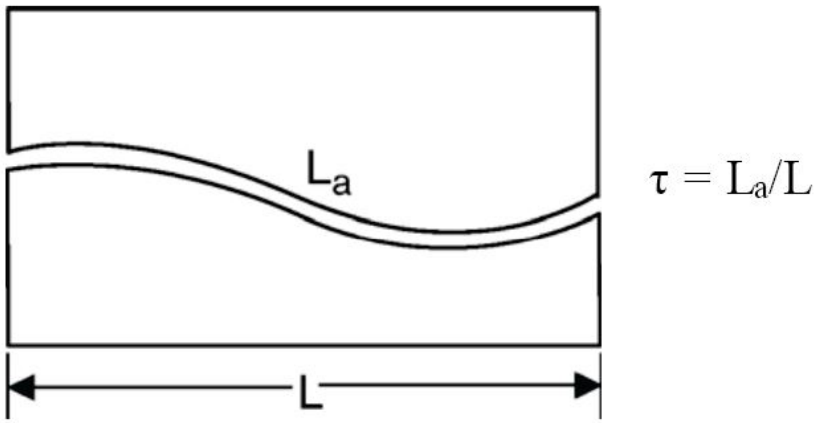

Figure 6.10. *Scheme representing the tortuosity factor (τ) as the ratio of the length of the fluid flow pathway (L_a) to the length of the sample (L). Image from Azar and others (2008).*

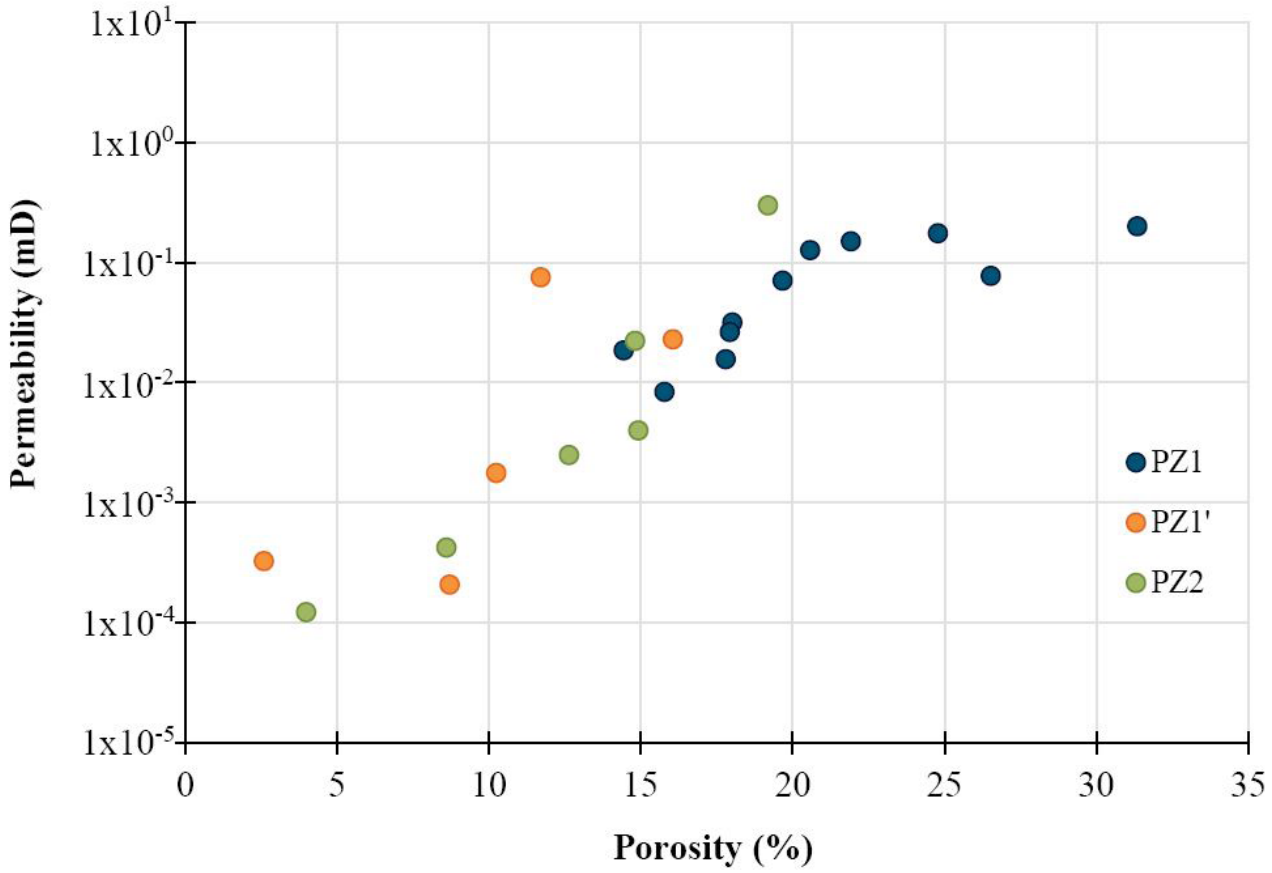

Figure 6.11. *Porosity vs. permeability plot of the PZ layers. Core plug data (Tables 5.10 and 5.12) from company reports obtained by UGS.*

a generalized interpretation of dolomite formation for all PZ layers; however, the dolomitizing temperatures are different for each layer. The average calculated temperature for the PZ1 is around 24°C, for PZ1′ around 26°C, and around 28°C for PZ2 (see Chapter 5, Section 5.2.2.6). The lower temperature of dolomitization for PZ1 favoured the preferential formation of euhedral and subhedral dolomite crystals (planar-e and planar-s textures), which enhanced its porosity- permeability properties (figure 6.12).

CHAPTER 7 CONCLUSIONS AND FUTURE WORK

7.1 Conclusions

The work conducted in the process of this thesis project successfully addressed the five research objectives outlined in Chapter 1.1 as follows.

Objective 1: *Characterization and analysis of facies types for the UBm as they relate to dolomitization.*
The UBm was deposited in a range of littoral to sublittoral environments, in which ten lithofacies were recognized. The eight carbonate facies are dolomitized to variable degrees and are characterized by (i) selective dolomitization of micrite matrix, peloids, ooids, and intraclast, and by (ii) variable preservation of the precursor limestone textures. However, bioclasts (mainly ostracods) are not dolomitized. The dolomitization process crosscut all facies boundaries from the distal sublittoral setting (mudstone facies, F1) toward the littoral nearshore area (intraclast grainstone-packstone (F6) through ostracod grainstone-packstone (F8) facies). Therefore, facies did not control dolomitization. Rather, dolomitization was favoured by variations in the composition and temperature of the lake and pore waters, ultimately driven by climate changes.

Objective 2: *Determination of the process(es) of dolomitization.*
Most, perhaps all, dolomites in the PZ layers formed by replacement of unconsolidated and/or at least partially lithified lime mud sediments, i.e., by matrix-selective replacement. Dolomites are aphanocrystalline with sizes that range from 0.15 to 6.0 µm. Ca-content ranges widely from 49% to 59%, and cation ordering (d_{015} / d_{101}) is generally low ranging from 0.1 to 0.5. The

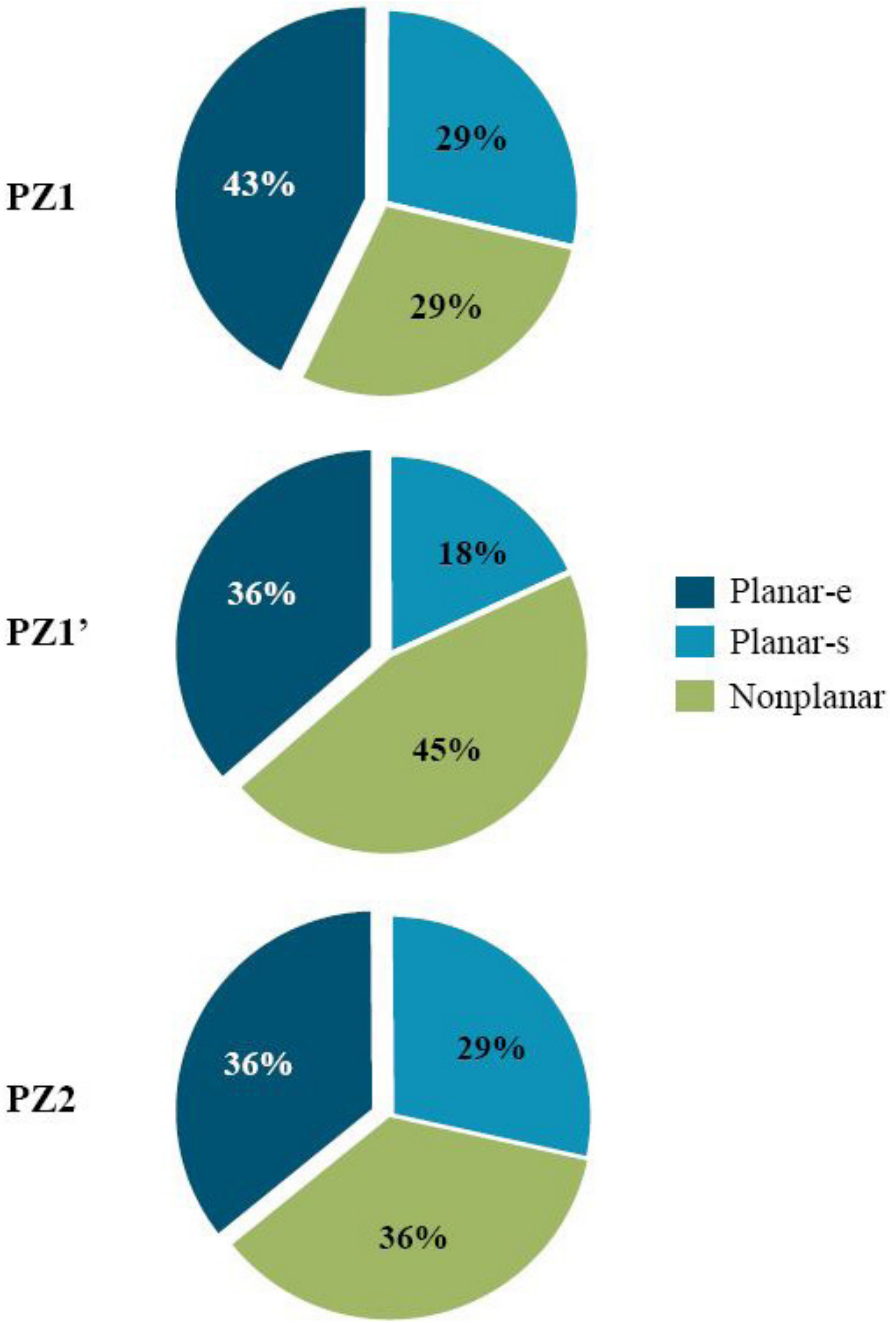

Figure 6.12. *Dolomite textures percentage for each PZ layer. PZ1 layer has the most abundant planar-e texture of all PZ layers. Data from SEM images petrography.*

PZ layers display a tabular geometry pinching out toward the basin center and the nearshore areas. All these features conform to the type of dolomite known as penecontemporaneous, thus they probably formed very early in the diagenetic history.

Dolomitization was driven by climate changes that created distinctive variations in the amount of precipitation, amount of river inflow, water temperature, evaporation, and lake and pore water chemistry. During the warmer climate periods, evaporation and reduced river inflow increased salinity sufficiently to create density-driven reflux of lake water in the subaqueous parts of the lake, which together with the attendant increases in temperature and Mg^{2+}/Ca^{2+} ratio in the lake water, resulted in dolomitization. At the same time the landward parts of the lake dried and formed a playa, which increased in size over time while the actual lake surface and volume shrank. In the playa area dolomite formed from evaporating groundwater by evaporative pumping. Over time this process overprinted the areas formerly affected by reflux. Dolomitization in the UBm is thus interpreted as the result of two different yet superimposed processes: density-driven reflux and evaporative pumping. Dolomitization stopped when the climate turned sufficiently cool again to refill the lake, thereby freshening and cooling the lake water to enable calcite precipitation again.

Objective 3: *Investigation of how porosity and permeability are related to dolomitization.*
Dolomitization contributed to the lithification of the lime mud sediments, which also contributed to preservation of the primary porosity inherited from the parental lime mud sediments/limestone. Furthermore, it is possible that the so-called mole-per-mole dolomite-calcite replacement enhanced the porosity of the PZ layers. Perhaps most importantly, the stratigraphic interval of interest is significantly overpressured, which inhibits both mechanical as well as chemical compaction, likely the main reason why the UBm has dolomite layers with porosity as high as about 45%, although permeability is generally low because of the small crystal size and shape.

Dolomite crystals' planar-e, planar-s and nonplanar textures are correlated with porosity and permeability. Planar textures (planar-e and planar-s) are associated with the highest values of porosity and permeability. However, dolomite texture, crystal size, and shape are highly variable throughout the PZ layers.

Objective 4: *Characterization of the geometry (lateral and vertical extent) of the dolomite layers in the study area*.
The thickest sections within the dolomitized PZ layers are developed between the nearshore and the basin center areas. These thickness variations were probably controlled by an interplay of paleobathymetry of Lake Uinta, regional variability of porosity and permeability of the parent lime mud sediments/limestones, fluctuations in the lake water temperature and chemical composition, and possibly by the presence of a sedimentary sill.

Objective 5: *Possible implications for petroleum reservoir development.*
Mapping of the most important reservoir characteristics, porosity and permeability, as well as identification of the dolomitization processes, has not led to the recognition of "sweet spots" for hydrocarbon exploration or extraction. Overall, the variations in porosity and permeability within each PZ layer and across the entire study area are too small to significantly influence exploration or development strategies. The best areas for exploration and development continue to be the highly overpressured areas generally toward the basin center.

7.2 Future Work

1. One of the most intriguing findings of this study is the relative compositional (high Ca-excess) and structural (low cation ordering) immaturity of the UBm dolomites. This finding is almost unheard of in dolomites of Tertiary age buried to ~3,000 m and with temperatures around 100°C. The interpretation of this finding given here, i.e., inhibition of recrystallization due to high overpressure, needs verification by further investigation. Does overpressure inhibit dolomite recrystallization elsewhere? Are all types of dolomite affected or only penecontemporaneous dolomites like those in the UBm? What roles do geothermal gradient and the rate of burial play?

2. Another intriguing finding is the discrepancy between the temperatures calculated by the conventional oxygen isotope method and the clumped isotope method. Related to this point is the finding that some temperatures from clumped isotope thermometry are significantly higher than the maximum burial temperature in the area. At this time, one is forced to conclude that the clumped isotope method needs refinement, or that at least some dolomite samples have experienced oxygen isotope exchange despite their compositional and structural immaturity (see point 1 above). Samples were taken of dolomite pairs within and outside of chert nodules. Dolomite encased in chert, and thus sheltered from fluid exchange during burial yield, will hopefully have more accurate and thus more reliable results of the temperatures of dolomite formation. Unfortunately, the samples taken for this part of the project could not be analysed before completion of this research.

REFERENCES

Adams, J.E., and Rhodes, M.L., 1960, Dolomitization by seepage refluxion: AAPG Bulletin, v. 44, no. 12, p. 1912–1920.

Al-Aasm, I.S., Taylor, B.E., and South, B., 1990, Stable isotope analysis of multiple carbonate samples using selective acid extraction: Chemical Geology—Isotope Geoscience Section, v. 80, no. 2, p. 119–125, DOI:10.1016/0168-9622(90)90020-D.

Anderson, J.G., and Roesink, J.G., 2013, Reservoir characterization of the Uteland Butte Formation in the Uinta Basin, American Association of Petroleum Geologists Search and Discovery Article #50888: Online, http://www.searchanddiscovery.com/pdfz/documents/2013/50888anderson/ndx_anderson.pdf.html.

Anderson, T.W., and Darling, D.A., 1954, A test of goodness of fit: Journal of the American Statistical Association, v. 49, no. 268, p. 765–769, DOI:10.1080/01621459.1954. 10501232.

Applied Geochemistry Group-Isotope Science Laboratory, undated, Analysis of ^{13}C and ^{18}O of carbonate minerals by CF-IRMS: Online, https://ucalgary.ca/uofcisl/techniques.

Asquith, G.B, and Gibson, C.R., 1982, Basic well log analysis for geologists: American Association of Petroleum Geologists—Methods in Exploration Series #5, 216 p.

Azar, J.H., Javaherian, A., Pishvaie, M.R., and Nabi-Bidhendi, M., 2008, An approach to defining tortuosity and cementation factor in carbonate reservoir rocks: Journal of Petroleum Science and Engineering, v. 60, no. 2, p. 125–131, DOI:10.1016/j.petrol.2007.05.010.

Baars, D.L., and Stevenson G.M, 1981, Tectonic evolution of western Colorado and eastern Utah, *in* Epis, R.C. and Callender, J.F., editors, Western Slope (Western Colorado)-New Mexico Geological Society 32nd Annual Fall Field Conference Guidebook: New Mexico Geological Society, p. 105–112.

Baccelle, L. and Bosellini, A., 1965, Diagrammi per la stima visiva della composizione percentuale nelle rocche sedimentary: Annali dell'Univrsità di Ferrara (Nuova Serie), Sezione 9, Scienze Geologiche e Paleontologiche, v. 1, no. 3, p. 59–62.

Barron, E.J., 1990, Climate and lacustrine petroleum source prediction, *in* Katz, B.J., editor, Lacustrine basin exploration: The American Association of Petroleum Geologists Memoir 50, p. 1–18.

Belovsky, G.E., Stephens, D., Perschon, C., Birdsey, P., Paul, D., Naftz, D., Baskin, R., Larkson, c., Mellison, C., Luft, J., Mosley, R., Marhon, H., Van Leeuwen, J., and Allen, D.V., 2011, The Great Salt Lake ecosystem (Utah, USA)—long term data and a structural equation approach: Ecosphere, v. 2, no. 3, p. 1–40, DOI:10.1890/ES10-00091.1.

Bereskin, S.R., Morgan, C.D., and McClure, K.P, 2004, Descriptions, petrology, photographs, and photomicrographs of core from the Green River Formation, south-central Uinta Basin, Utah: Utah Geological Survey Miscellaneous Publication 04-2, p. 1–38, https://doi.org/10.34191/MP-04-2.

Berner, R.A., De Leeuw, J.W., Spiro, B., Murchison, D.G., and Eglinton, G., 1985, Sulphate reduction, organic matter decomposition and pyrite formation [and discussion]: Philosophical Transactions of the Royal Society of London A—Mathematical, Physical and Engineering Sciences, v. 315, no. 1531, p. 25–38: Online, https://www.jstor.org/stable/37702.

Best, M.G, 1982, Igneous and metamorphic petrology: San Francisco, W. H. Freeman and Company, 630 p.

Birdwell, J.E., Vanden Berg, M.D. V., Johnson, R.C., and Brownfield, M.E., 2016, Geological, geochemical and reservoir characterization of the Uteland Butte member of the Green River Formation, Uinta Basin, Utah, *in* Dolan, M.P., Higley, D.H., and Lillis, P.G., editors, Hydrocarbon source rocks in unconventional plays, Rocky Mountain Region: The Rocky Mountain Association of Geologist, p. 352–378.

Boehrer, B., and Schultze, M., 2008, Stratification of lakes: Reviews of Geophysics, v. 46, no. 2, p. 1–27: Online, https://agupubs.onlinelibrary.wiley.com/doi/epdf/10.1029/2006RG000210.

Boggs, S.J., and Krinsley, D., 2006, Application of cathodoluminescence imaging to the study of sedimentary rocks: New York, Cambridge University Press, 165 p.

Bradley, W.H, 1931, Origin and microfossils of the oil shale of the Green River Formation of Colorado and Utah: U.S. Geological Survey Professional Paper 168, p. 1–58: Online, https://pubs.usgs.gov/pp/0168/report.pdf.

Broecker, W.S, 1971, A kinetic model for the chemical composition of sea water: Quaternary Research, v. 1, no. 2, p. 188–207, DOI:10.1016/0033-5894(71)90041-X.

Budd, D.A, 1997, Cenozoic dolomites of carbonate islands—their attributes and origin: Earth-Science Reviews, v. 42, no. 1-2, p. 1–47, doi:10.1016/S0012-8252(96) 00051-7.

Carroll, A.R., and Bohacs, K.M, 1999, Stratigraphic classification of ancient lakes—balancing tectonic and climatic controls: Geology, v. 27, no. 2, p. 99–102, DOI:10.1130/0091-7613(1999)027<0099:SCOALB>2.3.CO;2.

Case, J.E, 1991, Geologic map of the northwestern part of the Uncompahgre Uplift, Grand County, Utah, and Mesa County, Colorado, with emphasis on Proterozoic rocks: U.S. Geological Survey Map I-2088, 16 p. pamphlet, scale 1:24,000.

Cashion, W.B, 1967, Geology and fuel resources of the Green River Formation, southeastern Uinta Basin, Utah and Colorado: U.S. Geological Survey Professional Paper 548, p. 1–48: Online, https://pubs.usgs.gov/pp/0548/report.pdf.

Cohen, A.S, 2003, Paleolimnology—the history and evolution of lake systems: New York, Oxford University Press, 500 p.

Cole, R.D., and Picard, M.D, 1978, Comparative mineralogy of nearshore and offshore lacustrine lithofacies, Parachute Creek Member of the Green River Formation, Piceance Creek Basin, Colorado, and eastern Uinta Basin, Utah: Geological Society of America Bulletin, v. 89, no. 10, p. 1441–1454, DOI:10.1130/0016-7606(1978) 89<1441:CMONAO>2.0.CO;2.

Davis, S.J, 2008, Synorogenic evolution of large-scale drainage patterns—Isotope paleohydrology of sequential laramide basins: Stanford, California, Stanford University, Ph.D. dissertation, 204 p.

Davis, S.J., Mulch, A., Carroll, A.R., Horton, T.W., and Chamberlain, C.P, 2009, Paleogene landscape evolution of the central North American Cordillera—developing topography and hydrology in the Laramide foreland: Geological Society of America Bulletin, v. 121, no. 1-2, p. 100–116, DOI:10.1130/B26308.1.

Davison, W., 1993, Iron and manganese in lakes: Earth-Science Reviews, v. 34, no. 2, p. 119–163, DOI: 10.1016/0012-8252(93)90029-7.

Degens, E.T., and Epstein, S., 1964, Oxygen and carbon isotope ratios in coexisting calcites and dolomites from recent and ancient sediments: Geochimica et Cosmochimica Acta, v. 28, no. 1, p. 23–44, DOI:10.1016/0016-7037(64)90053-5.

Desborough, G.A., 1978, A biogenic-chemical stratified lake model for the origin of oil shale of the Green River Formation—An alternative to the playa-lake model: Geological Society of America Bulletin, v. 89, no. 7, p. 961–971, DOI:10.1130/0016-7606(1978)89<961:ABSLMF>2.0.CO;2.

Dickinson, G., 1953, Geological aspects of abnormal reservoir pressures in Gulf Coast Louisiana: AAPG Bulletin, v. 37, no. 2, p. 410–432: Online, http://archives.datapages.com/data/bulletns/1953-56/data/pg/0037/0002/0400/0410.htm.

Dickinson, W.R., Klute, M.A., Hayes, M.J., Janecke, S.U., Lundin, E.R., McKittrick, M.A., and Olivares, M.D., 1988, Paleogeographic and paleotectonic setting of Laramide sedimentary basins in the central Rocky Mountain region: Geological Society of America Bulletin, v. 100, no. 7, p. 1023–1039, DOI:10.1130/0016-7606(1988)100<1023:PAPSOL>2.3.CO;2.

Dickinson, W.R., Lawton, T.F., Pecha, M., Davis, S.J., Gehrels, G.E., and Young, R.A., 2012, Provenance of the Paleogene Colton Formation (Uinta Basin) and Cretaceous–Paleogene provenance evolution in the Utah foreland—Evidence from U-Pb ages of detrital zircons, paleocurrent trends, and sandstone petrofacies: Geosphere, v. 8, no. 4, p. 854–880, DOI:10.1130/GES00763.1.

Dickson, J.A.D, 1965, A modified staining technique for carbonates in thin section: Nature, v. 205, no. 4971, p. 587, DOI:10.1038/205587a0.

Doelling, H.H, 2002, Interim geologic map of the San Rafael Desert 30' x 60' Quadrangle, Emery and Grand Counties, Utah, scale 1:100.000.

Dunham, R.J, 1962, Classification of carbonate rocks according to depositional textures: The American Association of Petroleum Geologists Memoir 1, p. 108–121: Online, http://archives.datapages.com/data/specpubs/carbona2/data/a038/a038/0001/0100/0108.htm.

Dyni, J.R., Milton, C., and Cashion, W.B, 1985, The saline facies of the upper part of the Green River Formation near Duchesne, Utah, *in* Picard, M.D., editor, Geology and energy resources, Uinta Basin of Utah: Utah Geological Association Publication 12, p. 51–60: Online, https://archives.datapages.com/data/uga/data/055/055001/51_ugs550051.htm.

Eardley, A.J., 1938, Sediments of Great Salt Lake, Utah: AAPG Bulletin, v. 22, no. 10, p. 1305–1411: Online, http://archives.datapages.com/data/bulletns/1938-43/data/pg/0022/0010/1300/1305.htm?doi=10.1306%2F3D932FFA-16B1-11D7-8645000102C1865D.

Ebner, M., Toussaint, R., Schmittbuhl, J., Koehn, D., and Bons, P., 2010, Anisotropic scaling of tectonic stylolites—A fossilized signature of the stress field?: Journal of Geophysical Research, Solid Earth, v. 115, no. B6, DOI:10.1029/2009JB006649.

Embry III, A.F., and Klovan, J.E., 1971, A Late Devonian reef tract on northeastern Banks Island, NWT: Bulletin of Canadian Petroleum Geology, v. 19, no. 4, p. 730–781: Online, http://archives.datapages.com/data/cspg/data/019/019004/0730.htm.

England, W.A., Mackenzie, A.S., Mann, D.M., and Quigley, T.M., 1987, The movement and entrapment of petroleum fluids in the subsurface: Journal of the Geological Society, v. 144, no. 2, p. 327–347, DOI: 10.1144/gsjgs.144.2.0327.

Esteban, M., Klappa, C.F., 1983, Subaerial exposure environment, *in* Scholle, P.A., Bebout, D. G., and Moore, C.H., editors., Carbonate depositional environments: American Association of Petroleum Geologists Memoir, 33, p. 1–54.

Eugster, H.P., 1967, Hydrous sodium silicates from Lake Magadi, Kenya—Precursors of bedded chert: Science, v. 157, no. 3793, p. 1177–1180, DOI: 10.1126/science.157.3793.1177.

Eugster, H.P., and Hardie, L.A., 1978, Saline lakes, *in* Lerman A. and Baccini P., editors, Lakes—Chemistry, Geology, Physics, New York, Springer-Verlag, p. 237-293.

Eugster, H.P., and Surdam, R.C., 1973, Depositional environment of the Green River Formation of Wyoming—A preliminary report: Geological Society of America Bulletin, v. 84, no. 4, p. 1115–1120, DOI:10.1130/0016-7606(1973)84<1115:DEOTGR>2.0.CO;2.

Flöerke, O.W., Graetsch, H., Martin, B., Röeller, K., and Wirth, R., 1991, Nomenclature of micro- and non-crystalline silica minerals, based on structure and microstructure: Neues Jahrbuch Fuer Mineralogie, Abhandlungen, v. 163, no. 1, p. 19–42.

Flügel, E., 2010, Microfacies of carbonate rocks: Analysis, interpretation and application, second edition: Berlin, Springer, 984 p.

Folk, R.L., and Pittman, J.S., 1971, Length-slow chalcedony; a new testament for vanished evaporites: Journal of Sedimentary Petrology, v. 41, no, 4, p. 1045–1058. DOI:10.1306/74D723F1-2B21-11D7-8648000102C1865D.

Folk, R.L., and Siedlecka, A., 1974, The "schizohaline" environment—Its sedimentary and diagenetic fabrics as exemplified by Late Paleozoic rocks of Bear Island, Svalbard: Sedimentary Geology, v. 11, no. 1, p. 1–15, DOI:10.1016/0037-0738(74)90002-5.

Folk, R.L., and Weaver, C.E., 1952, A study of the texture and composition of chert: American Journal of Science, v. 250, p. 498–510, DOI:10.2475/ajs.250.7.498.

Foreman, B.Z., Heller, P.L., and Clementz, M.T., 2012, Fluvial response to abrupt global warming at the Palaeocene/Eocene boundary: Nature, v. 49, no. 7422, p. 92–95, DOI:10.1038/nature11513.

Fouch, T.D., 1976, Revision of the lower part of the Tertiary System in the central and western Uinta basin, Utah: Geological Society Bulletin 1405-C, p. C1–C7: Online, https://pubs.usgs.gov/bul/1405c/report.pdf.

Freytet, P., and Verrecchia, E.P, 2002, Lacustrine and palustrine carbonate petrography; an overview: Journal of Paleolimnology, v. 27 no. 2, p. 221–237.

Friedman, I., and O'Neil, J.R., 1977, Data of geochemistry—Compilation of stable isotope fractionation factors of geochemical interest: US Geological Survey Bulletin v.440-KK: Online, https://pubs.usgs.gov/pp/0440kk/report.pdf.

Gat, J.R., 1995, Stable isotopes of fresh and saline lakes, *in* Lerman, A., Imboden, D.M., and Gat, J.R., editors, Physics and chemistry of lakes: New York, Springer-Verlag Heidelberg, p. 139–165.

Ghosh, P., Adkins, J., Affek, H., Balta, B., Guo, W., Schauble, E.A., Scharg, D., and Eiler, J. M., 2006, 13C–18O bonds in carbonate minerals—A new kind of paleothermometer: Geochimica et Cosmochimica Acta, v. 70, no. 6, p. 1439–1456, DOI:10.1016 /j.gca.2005.11.014.

Gierlowski-Kordesch, E.H., 2010, Lacustrine carbonates, *in* Alonso-Zarzs A.M. and Tanner L.H, editors, Carbonates in continental settings—Facies, environments, and processes: Developments in Sedimentology 61, Oxford, Elsevier, p. 1–101.

Gierlowski-Kordesch, E.H., Jacobson, A.D., Blum, J.D., and Garćes, B.V., 2008, Watershed reconstruction of a Paleocene–Eocene lake basin using Sr isotopes in carbonate rocks: Geological Society of America Bulletin, v. 120, no. 1-2, p. 85–95, DOI:10.1130/B26070.1.

Goldsmith, J.R., and Graf, D.L., 1958, Structural and compositional variations in some natural dolomites: The Journal of Geology, v. 66, no. 6, p 678–693: Online, https://www.jstor.org/stable/30056855.

Gregg, J.M., and Shelton, K.L., 1989, Minor- and trace-element distributions in the Bonneterre Dolomite (Cambrian), southeast Missouri—evidence for possible multiple-basin fluid sources and pathways during lead-zinc mineralization: Geological Society of America Bulletin, v. 101, no. 2, p. 221–230, DOI:10.1130/0016-7606(1989)101<0221 :MATEDI>2.3.CO;2.

Gregg, J.M., and Sibley, D.F, 1984, Epigenetic dolomitization and the origin of xenotopic dolomite texture: Journal of Sedimentary Research, v. 54, no. 3, p. 908–931: Online, http://archives.datapages.com/data/sepm/journals/v51-54/data/054/054003/0908.htm.

Gregg, J.M., Bish, D.L., Kaczmarek, S.E., and Machel, H.G., 2015, Mineralogy, nucleation and growth of dolomite in the laboratory and sedimentary environment—A review: Sedimentology, v. 62, no. 6, p. 1749–1769, DOI:10.1111/sed.12202.

Gregg, J.M., Howard, S.A., and Mazzullo, S.J., 1992, Early diagenetic recrystallization of Holocene (< 3000 years old) peritidal dolomites, Ambergris Cay, Belize: Sedimentology, v. 39, no. 1, p. 143–160, DOI:10.1111/j.1365-3091.1992.tb01027.x.

Håkanson, L., and Jansson, M., 1983, Principles of lake sedimentology: Berlin, Springer-Verlag, 387 p.

Hansen, W.R., 1965, Geology of the Flaming Gorge area Utah–Colorado–Wyoming: U. S. Geological Survey Professional Paper 490, p. 1–196: Online, https://pubs.usgs.gov/pp/0490/report.pdf.

Hao, F., Zhou, X., Zhu, Y., Bao, X., and Yang, Y., 2009, Charging of the Neogene Penglai 19-3 field, Bohai Bay Basin, China—oil accumulation in a young trap in an active fault zone: AAPG Bulletin, v. 93, no. 2, p. 155–179, DOI:10.1306/09080808092.

Heaney, P.J., 1995, Moganite as an indicator for vanished evaporites—a testament reborn?: Journal of Sedimentary Research, Section A, Sedimentary Petrology and Processes, v. 65, no. 4, p. 633–638, DOI:10.1306/D4268180-2B26-11D7-8648000102C1865D.E.

Hintze, L.F., Willis, G.C., Laes, D.Y., Sprinkel, D.A., and Brown, K.D., 2000, Digital geologic map of Utah: Utah Geological Survey Map 179, scale 1:500.000, https://doi.org/10.34191/M-179.

Hsü, K.J., and Siegenthaler, C., 1969, Preliminary experiments on hydrodynamic movement induced by evaporation and their bearing on the dolomite problem: Sedimentology, v. 12, no. 1-2, p. 11–25, DOI: 10.1111/j.1365-3091.1969.tb00161.x.

Hugman III, R.H.H., and Friedman, M., 1979, Effects of texture and composition on mechanical behavior of experimentally deformed carbonate rocks: American Association of Petroleum Geologists Bulletin, v. 63, no. 9, p. 1478–1489.

Hunt, C.B., 1956, Cenozoic Geology of the Colorado Plateau: US Geological Survey Professional Paper 279, p. 1–99: Online, https://pubs.usgs.gov/pp/0279/report.pdf.

Irwin, H., Curtis, C., and Coleman, M., 1977, Isotopic evidence for source of diagenetic carbonates formed during burial of organic-rich sediments: Nature, v. 269, p. 209–213, DOI:10.1038/269209a0.

James, N.P., and Choquette, P.W., 1984, Diagenesis 9—Limestones—The meteoric diagenetic environment: Geoscience Canada, v. 11, no. 4, p. 161–194: Online, https://journals.lib.unb.ca/index.php/GC/article/view/3395.

Johnson, R.C., 1985, Early Cenozoic history of the Uinta and Piceance Creek basins, Utah and Colorado, with special reference to the development of Eocene Lake Uinta, *in* Flores R.M. and Kaplan, S.S., editors, Cenozoic paleogeography of the west-central United States: Rocky Mountain Section of SEPM, Rocky Mountain Paleogeography Symposium 3p. 247–276: Online, http://archives.datapages.com/data/rocky_sepm/data/023/023001/247_rocky_mount230247.htm.

Johnson, R.C., Birdwell, J.E., Mercier, T.J., and Brownfield, M.E., 2016, Geology of tight oil and potential tight oil reservoirs in the lower part of the Green River Formation, Uinta, Piceance, and greater Green River Basins, Utah, Colorado, and Wyoming: U.S. Geological Survey Scientific Investigations Report 2016–5008, 63 p.: Online, https://pubs.usgs.gov/sir/2016/5008/sir20165008.pdf.

Johnson, R.C., Birdwell, J.E., Mercier, T.J., Brownfield, M.E., Charpentier, R.R., Klett, T.R., Leathers, H.M., Schenk, C.J., and Tennyson, M.E., 2015, Assessment of undiscovered oil and gas resources in the Uteland Butte Member of the Eocene Green River Formation, Uinta Basin, Utah: U.S. Geological Survey Fact Sheet 2015–3052, p. 1–2, DOI:10.3133/fs20153052.

Johnson, R., Mercier, T., Brownfield, M., and Self, J., 2010, Assessment of in-place oil shale resources in the Eocene Green River Formation, Uinta Basin, Utah and Colorado: U.S. Geological Survey Digital Data Series DDS–69–BB: Online, https://pubs.usgs.gov/dds/dds-069/dds-069-y/REPORTS/69_Y_CH_1.pdf.

Jones, B., Luth, R.W., and MacNeil, A.J., 2001, Powder X-ray diffraction analysis of homogeneous and heterogeneous sedimentary dolostones: Journal of Sedimentary Research, v. 71, no. 5, p. 790–799: Online, http://archives.datapages.com/data/sepm/journals/v71/071005/0790.htm.

Kaczmarek, S.E., and Sibley, D.F., 2011, On the evolution of dolomite stoichiometry and cation order during high-temperature synthesis experiments—an alternative model for the geochemical evolution of natural dolomites: Sedimentary Geology, v. 240, no. 1, p. 30–40, DOI:10.1016/j.sedgeo.2011.07.003.

Kahle, C.F., 1965, Possible roles of clay minerals in the formation of dolomite: Journal of Sedimentary Research, v. 35, no. 2, p. 448–453.

Keighley, D., Flint, S., Howell, J., and Moscariello, A., 2003, Sequence stratigraphy in lacustrine basins: a model for part of the Green River Formation (Eocene), southwest Uinta Basin, Utah, USA: Journal of Sedimentary Research, v. 73, no. 6, p. 987–1006: Online, http://archives.datapages.com/data/sepm/journals/v73/data/073/073006/0987.htm.

Kluth, C.F., 1986, Plate tectonics of the ancestral Rocky Mountains, *in* Peterson, J.A., editor, Paleotectonics and Sedimentation in the Rocky Mountain Region, United States: American Association of Petroleum Geologists Memoir 41, p. 353–369: Online, http://archives.datapages.com/data/specpubs/structu1/data/a155/a155/0001/0000/0003.htm.

Knauth, L.P, 1994, Petrogenesis of chert, *in* Heaney, P.J., Prewitt, C.T., and Gibbs, G.V., editors, Silica—physical behavior, geochemistry and materials applications: Reviews in Mineralogy and Geochemistry, v. 29, no. 1 p. 233–258.

Land, L.S., and Hoops, G.K., 1973, Sodium in carbonate sediments and rocks—a possible index to the salinity of diagenetic solutions: Journal of Sedimentary Research, v. 43, no. 3, p. 614–617, DOI:10.1306/74D7281A-2B21-11D7-8648000102C1865D.

LaRocque, A., 1956, Tertiary mollusks of central Utah, *in* Peterson, J.A., editor, Geology and economic deposits of east central Utah: Intermountain Association of Petroleum Geologist, p. 140–145: Online, http://archives.datapages.com/data/uga/data/006/006001/140_ugs60140.htm.

Logan, B.W., and Semeniuk, V., 1976, Dynamic metamorphism—processes and products in Devonian carbonate rocks, Canning Basin, Western Australia: Geological Society of Australia Special Publication, v. 6, p. 1–138.

Logan, S.K., Sarg, J.F., and Vanden Berg, M.D., 2016, Lithofacies, deposition, early diagenesis, and porosity of the Uteland Butte member, Green River Formation, eastern Uinta Basin, Utah and Colorado: Utah Geological Survey Open File Report 652, 32 p.: Online, https://doi.org/10.34191/OFR-652.

Long, M., 2006, Origin of the Dolomite on the Green River Formation: Houston, Texas, University of Houston, Ph.D. dissertation 336 p.

Lucia, F. Jerry, 2007, Carbonate reservoir characterization—An integrated approach, Second edition: Berlin, Springer, 227 p.

Luczaj, J.A., McIntire, M.J., and Olson Hunt, M.J., 2016, Geochemical characterization of trace MVT mineralization in Paleozoic sedimentary rocks of northeastern Wisconsin, USA: Geosciences, v. 6, no. 2, p. 1–29, DOI:10.3390/geosciences6020029.

Lumsden, D.N., 1979, Discrepancy between thin-section and X-ray estimates of dolomite in limestone: Journal of Sedimentary Research, v. 49, no. 2. p. 429–436: Online, http://archives.datapages.com/data/sepm/journals/v47-50/data/049/049002/0429.htm.

Lumsden, D.N., and Chimahusky, J.S., 1980, Relationship between dolomite nonstoichiometry and carbonate facies parameters, *in* Zenger, D.h., Dunham, J.B., Ethington, R.L., editors, Concepts and models of dolomitization: SEPM Special Publication No. 28, p. 123–137: Online, http://archives.datapages.com/data/sepm_sp/SP28/Relationship_Between_Dolomite.htm.

MacGinitie, H.D., 1969, The Eocene Green River flora of northwestern Colorado and northeastern Utah: University of California Publications in Geological Sciences, v. 83, p. 1–203.

Machel, H.G, 1995, Magnetic mineral assemblages and magnetic contrasts in diagenetic environments—with implications for studies of palaeomagnetism, hydrocarbon migration and exploration, *in* Turner, P. and Turner, A., editors, Palaeomagnetic applications in hydrocarbon exploration and production: Geological Society of London, Special Publications, v. 98, p. 9–29, DOI:10.1144/GSL.SP.1995.098.01.02.

Machel, H.G., 1997, Recrystallization versus neomorphism, and the concept of significant recrystallization in dolomite research: Sedimentary Geology, v. 113, no. 3-4, p. 161–168, DOI:10.1016/S0037-0738(97)00078-X.

Machel, H.G., 1999, Effects of groundwater flow on mineral diagenesis, with emphasis on carbonate aquifers: Hydrogeology Journal, v. 7, no. 1, p. 94–107, DOI:10.1007/ s100400050182.

Machel, H.G., 2001, Bacterial and thermochemical sulfate reduction in diagenetic settings—old and new insights: Sedimentary Geology, v. 140, no. 1, p. 143–175, DOI:10.1016/ S0037-0738(00)00176-7.

Machel, H.G., 1985, Cathodoluminescence in calcite and dolomite and its chemical interpretation: Geoscience Canada, v. 12, no. 4, p. 139–147: Online, https://journals.lib.unb.ca/index.php/GC/article/view/3427.

Machel, H.G., 2000, Application of cathodoluminescence to carbonate diagenesis, *in* Pagel, M., Barbin, V., Blanc, P., and Ohnenstetter, D., editors, Cathodoluminescence in Geosciences: Springer-Verlag, p. 271–301.

Machel, H.G., and Mountjoy, E.W., 1987, General constraints on extensive pervasive dolomitization, and their application to the Devonian carbonates of western Canada: Bulletin of Canadian Petroleum Geology, v. 35, no. 2, p. 143–158: Online, http://archives.datapages.com/data/cspg/data/035/035002/0143.htm.

Machel, H.G., and Mountjoy, E.W., 1986, Chemistry and environments of dolomitization—a reappraisal: Earth-Science Reviews, v. 23, no. 3, p. 175–222, DOI:10.1016/0012-8252(86)90017-6.

Machel, H.G., Mason, R.A., Mariano, A.N., and Mucci, A., 1991, Causes and emission of luminescence in calcite and dolomite, *in* Barker, C.E. and Kopp, O.C., editors, Luminescence microscopy and spectroscopy—qualitative and quantitative applications: SEPM Short Course Notes, 25, p. 9–25.

Machel, H.G. and Burton, E.A., 1991, Factors governing cathodoluminescence in calcite and dolomite, and their implications for studies of carbonate diagenesis, *in* Barker, C.E. and Kopp, O.C., editors, Luminescence microscopy and spectroscopy—qualitative and quantitative applications: SEPM Short Course Notes, 25, p. 37–57.

Machel, H.G., 2004, Concepts and models of dolomitization—a critical reappraisal, *in* Braithwaite, C.J. R., Rizzi, G., and Darke, G., editors, The geometry and petrogenesis of dolomite hydrocarbon reservoirs: Geological Society, London, Special Publication 235, p. 7–63.

Maliva, R.G., and Siever, R., 1989, Nodular chert formation in carbonate rocks: The Journal of Geology, v. 97, no. 4, p. 421–433, DOI:10.1086/629320.

Mazzullo, S.J., 1992, Geochemical and neomorphic alteration of dolomite; a review: Carbonates and Evaporites, v. 7, no. 1, p. 21–37, DOI:10.1007/BF03175390.

McCombie, A.M., 1959, Some relations between air temperatures and the surface water temperatures of lakes: Limnology and Oceanography, v. 4, no. 3, p. 252–258, DOI:10.4319/lo.1959.4.3.0252.

McCrea, J. M., 1950, On the isotopic chemistry of carbonates and a paleotemperature scale: The Journal of Chemical Physics, v. 18, no. 6, p. 849–857, DOI:10.1063/1.1747785.

McIntire, W. L., 1963, Trace element partition coefficients—a review of theory and applications to geology: Geochimica et Cosmochimica Acta, v. 27, no. 12, p. 1209–1264, DOI:10.1016/0016-7037(63)90049-8.

McKenzie, J.A., 1991, The dolomite problem—An outstanding controversy, *in* Mueller, D.W., McKenzie, J.A., and Weissert, H., editors, Controversies in modern geology; Evolution of geological theories in sedimentology, Earth history and tectonics: London, Academic Press, p. 37–54, DOI:10.1063/1.1747785.

Mello, M.R., and Maxwell, J.R., 1990, Organic geochemical and biological marker characterization of source rocks and oils derived from lacustrine environments in the Brazilian continental margin: AAPG Memoir, v. 50, p 77–97: Online, http://archives.datapages.com/data/specpubs/basinar3/data/a133/a133/0001/0050/0077.htm.

Millán, M.I., Machel, H., and Bernasconi, S.M., 2016, Constraining temperatures of formation and composition of dolomitizing fluids in the Upper Devonian Nisku Formation (Alberta, Canada) with clumped isotopes: Journal of Sedimentary Research, v. 86, no. 2, p. 107–112, DOI:10.2110/jsr.2016.6.

Moore, C.H., 2001, Carbonate reservoirs—Porosity evolution and diagenesis in a sequence stratigraphic framework: Amsterdam, Elsevier, 461 p.

Morgan, C.D., and Bereskin, S.R., 2003, Characterization of petroleum reservoirs in the Eocene Green River Formation, Central Uinta Basin, Utah: The Mountain Geologist, v. 39, p. 111–127: Online, http://archives.datapages.com/data/rmag/mg/2003/morgan.htm.

Morrow, D.W., 1982, Diagenesis 2—Dolomite-Part 2—Dolomitization models and ancient dolostones: Geoscience Canada, v. 9, no. 2, p. 95–107: Online https://journals.lib.unb.ca/index.php/GC/article/view/3299.

Nesse, W.D, 1991, Introduction to optical mineralogy: New York, Oxford University Press.

Nikanorov, M., and Brazhnikova, L.V., 2004, Water chemical composition of rivers, lakes and wetlands, *in* M.G. Khublaryan, editor, Types and properties of waters, encyclopedia of life support systems (EOLSS): Oxford, Eolss Publishers Co., p. 42–79.

Pearson, P.N., and Palmer, M.R., 2000, Atmospheric carbon dioxide concentrations over the past 60 million years: Nature, v. 406, no. 6797, p. 695–9, DOI:10.1038/35021000.

Picard, M.D., 1955, Subsurface stratigraphy and lithology of Green River Formation in Uinta Basin, Utah: American Association of Petroleum Geologists Bulletin, v. 39, no. 1, p. 75–102. DOI:10.1306/5CEAE0E5-16BB-11D7-8645000102C1865D.

Pingitore, N.J., 1976, Vadose and phreatic diagenesis; processes, products and their recognition in corals: Journal of Sedimentary Petrology, v. 46, no. 4, p. 985–1006: Online, http://archives.datapages.com/data/sepm/journals/v42-46/data/046/046004/0985.htm.

Pitman, J.K., 1996, Origin of primary and diagenetic carbonates in the lacustrine Green River Formation (Eocene), Colorado and Utah: US Geological Survey Bulletin 2157, p. 1–17: Online, https://pubs.usgs.gov/bul/2157/report.pdf.

Pittman, J.S., and Folk, R.L, 1971, Length-slow chalcedony after sulphate evaporite minerals in sedimentary rocks: Nature Physical Science, v. 230, no. 11, p. 64–65: Online, https://www.nature.com/articles/physci230064a0.

Purser, B.H., Tucker, M.E., and Zenger, D.H., 1994, Problems, progress and future research concerning dolomites and dolomitization, *in* Purser, B.H., Tucker, M.E., and Zenger, D.H., editors, Dolomites—a volume in honour of Dolomieu: Blackwell Scientific Publications, p. 3–21.

Pusca, V.A., 2003, Wet/dry, terminal fan-dominated sequence architecture—A new, outcrop-based model for the Lower Green River Formation, Utah: Laramie, University of Wyoming, Ph. D. dissertation, 175 p.: Online, https://search.proquest.com/globalnews/docview/305284786/513A6C6E6A9942C6PQ.

Pytte, A.M., and Reynolds, R.C., 1989, The thermal transformation of smectite to illite, *in* Naeser N.D., and McCulloh T.H. editors, Thermal history of sedimentary basins: New York, Springer, p. 133–140.

Rasmussen, D.T., Conroy, G.C., Friscia, A.R., Townsend, K.E., and Kinkel, M.D., 1999, Mammals of the middle Eocene Uinta Formation, *in* Gillete, D.D., editor, Vertebrate paleontology in Utah: Utah Geological Survey Miscellaneous Publication 99-1, p. 401–420, https://doi.org/10.34191/MP-99-1.

Ray, J.S., and Ramesh, R., 1998, Stable carbon and oxygen isotope analysis of natural calcite and dolomite mixtures using selective acid extraction: Journal of Geological Society of India, v. 52, no. 3 p. 323–332: Online, http://www.geosocindia.org/index.php/jgsi/article/view/68815.

Reeder, R.J., and Sheppard, C.E., 1984, Variation of lattice parameters in some sedimentary dolomites: American Mineralogist, v. 69, no. 5-6, p. 520–527, DOI:10.1086/626547.

Reinson, G.E., 1992, Transgressive barrier island and estuarine systems, *in* Walker, R.G., and James, N.P., editors, Facies model—response to sea level change: Geological Association of Canada, p. 179–194.

Remy, R.R., 1992, Stratigraphy of the Eocene Part of the Green River Formation in the south-central part of the Uinta Basin, Utah: U.S. Geological Survey Bulletin, 1787-BB, p. 1–79: Online, https://pubs.usgs.gov/bul/1787bb/report.pdf.

Renaut, R.W., and Gierloswki-Kordesch, E.H., 2010, Lakes, *in* James, N.P. and Dalymple, R.W., editors, Facies models: Geological Association of Canada, p. 541–575.

Robert, C., and Kennett, J.P., 1992, Paleocene and Eocene kaolinite distribution in the South Atlantic and Southern Ocean—Antarctic climatic and paleoceanographic implications: Marine Geology, v. 103, no. 1-3, p. 99–110, DOI:10.1016/0025-3227(92)90010-F.

Roehler, H.W, 1991, Revised stratigraphic nomenclature for the Wasatch and Green River formations of Eocene age, Wyoming, Utah, and Colorado: U.S. Geological Survey Professional Paper 1506-B, 38 p.: Online, https://pubs.usgs.gov/pp/1506b/report.pdf.

Ryder, R.T., Fouch, T.D., and Elison, J.H., 1976, Early Tertiary sedimentation in the western Uinta basin, Utah: Geological Society of America Bulletin, v. 87, no. 4, p. 496–512, DOI:10.1130/0016-7606(1976)87<496:ETSITW>2.0.CO;2.

Schamel, S., 2015, Shale oil resource play potential of the Green River Formation, Uinta Basin, Utah: Utah Geological Survey Open-File Report 639, 65 p.: Online, https://doi.org/10.34191/OFR-639.

Schmoker, J.W., and Halley, R.B., 1982, Carbonate porosity versus depth—a predictable relation for south Florida: AAPG Bulletin, v. 66, no. 12, p. 2561–2570.

Scholle, P.A., and Ulmer-Scholle, D.S., 2003, A color guide to the petrography of carbonate rocks—grains, textures, porosity, diagenesis: AAPG Memoir 77, 459 p.

Searl, A., 1994, Discontinuous solid solution in Ca-rich dolomites—the evidence and implications for the interpretation of dolomite petrographic and geochemical data, *in* Purser, B., Tucker, M., and Zenger, D., editors, Dolomites—a volume in honour of dolomieu: International Association of Sedimentologists, Special Publication 21, p. 361–376.

Sheppard, S.M., and Schwarcz, H.P., 1970, Fractionation of carbon and oxygen isotopes and magnesium between coexisting metamorphic calcite and dolomite: Contributions to Mineralogy and Petrology, v. 26, no. 3, p. 161–198, DOI: 10.1007/BF00373200.

Sibley, D.F., and Gregg, J.M., 1987, Classification of dolomite rock textures: Journal of Sedimentary Petrology, v. 57, no. 6, p. 967–975: Online, http://archives.datapages.com/data/sepm/journals/v55-58/data/057/057006/0967.htm?doi=10.1306%2F212F8CBA-2B24-11D7-8648000102C1865D.

Sibley, D.F., Gregg, J.M., Brown, R.G., and Laudon, P.R., 1993, Dolomite crystal size distribution, *in* Rezak, R. and Lavoie, D.L., editors, Carbonate microfabrics: New York, Springer-Verlag, p. 195–204.

Siedlecka, A., 1972, Length-slow chalcedony and relicts of sulphates; evidences of evaporitic environments in the Upper Carboniferous and Permian beds of Bear Island, Svalbard: Journal of Sedimentary Petrology, v. 42, no. 4, p. 812–816, DOI:10.1306/74D7263A-2B21-11D7-8648000102C1865D.

Smith, M.E., 2007, The stratigraphy and geochronology of the Green River Formation, Western U.S: Madison, University of Wisconsin-Madison, Ph.D. dissertation, 318 p.

Smith, M.E., Carroll, A.R., and Singer, B.S., 2008, Synoptic reconstruction of a major ancient lake system: Eocene Green River Formation, western United States: Geological Society of America Bulletin, v. 120, no. 1-2, p. 54–84, DOI:10.1130/B26073.1.

Swart, P.K., Burns, S.J., and Leder, J.J., 1991, Fractionation of the stable isotopes of oxygen and carbon in carbon dioxide during the reaction of calcite with phosphoric acid as a function of temperature and technique: Chemical Geology—Isotope Geoscience section, v. 86, no. 2, p. 89–96, DOI:10.1016/0168-9622(91)90055-2.

Sweet, D.E, and Soreghan, G.S., 2012, Late Paleozoic tectonics and paleogeography of the ancestral Front Range—Structural, stratigraphic, and sedimentologic evidence from the Fountain Formation (Manitou Springs, Colorado): Geological Society of America Bulletin, v. 122, no. 3/4, p. 575–594, DOI:10.1130/B26554.1.

Tada, R., and Siever, R., 1989, Pressure solution during diagenesis: Annual Review of Earth and Planetary Sciences, v. 17, no. 1, p. 89–118, DOI:10.1146/annurev.ea.17.050189. 000513.

Tänavsuu-Milkeviciene, K., and Frederick Sarg, J., 2012, Evolution of an organic-rich lake basin; stratigraphy, climate and tectonics; Piceance Creek basin, Eocene Green River Formation: Sedimentology, v. 59, no. 6, p. 1735–1768, DOI:10.1111/j.1365-3091.2012.01324.x.

Tänavsuu-Milkeviciene, K., Sarg, J.F., and Bartov, Y., 2017, Depositional cycles and sequences in an organic-rich lake basin—Eocene Green River Formation, Lake Uinta, Colorado and Utah, USA: Journal of Sedimentary Research, v. 87, no. 3, p. 210–229: Online, http://archives.datapages.com/data/sepm/journals/087/087003/210-i1527-1404-87-3-210.htm.

Trurnit, P., 1968, Pressure solution phenomena in detrital rocks: Sedimentary Geology, v. 2, no. 2, p. 89–114, DOI:10.1016/0037-0738(68)90030-4.

Tucker, M.E., and Wright, V.P., 1990, Carbonate sedimentology: Oxford, Blackwell Scientific Publications, 482 p.

Tuttle, M.L., and Goldhaber, M.B., 1993, Sedimentary sulfur geochemistry of the Paleogene Green River Formation, western USA—implications for interpreting depositional and diagenetic processes in saline alkaline lakes: Geochimica et Cosmochimica Acta, v. 57, no. 13, p. 3023–3039, DOI:10.1016/0016-7037(93)90291-4.

Tweto, O., 1975, Laramide (late Cretaceous-early Tertiary) orogeny in the southern Rocky Mountains: Geological Society of America Memoir 144, p. 1–44, DOI:10.1130/MEM144-p1.

Ulmer-Scholle, D.S., Scholle, P.A., and Brady, P.V., 1993, Silicification of evaporites in Permian (Guadalupian) back-reef carbonates of the Delaware Basin, West Texas and New Mexico: Journal of Sedimentary Research, v. 63, no. 5, p. 955–965.

Vanden Berg, M.D., Morgan C.D., Chidsey, T.C., and Nielsen, P., 2013, The Uteland Butte Member of the Eocene Green River Formation—an emerging unconventional carbonate tight oil play in the Uinta Basin, Utah [abs.]: AAPG Eastern Section annual Meeting, Pittsburgh, Pennsylvania, September 6–10.

Vanden Berg, M.D., Wood, R.E., Carney, S.M, and Morgan C.D., 2014, Geological characterization of the Uteland Butte member of the Eocene Green River Formation—an emerging unconventional carbonate tight oil play in the Uinta Basin, Utah [abs.]: Rocky Mountain Section AAPG Annual Meeting, Denver, Colorado.

Veizer, J., 1983, Chemical diagenesis of carbonates—theory and application of trace element technique, *in* Arthur, M.A., Anderson, T.F., Kaplan, I.R., Veizer, J., and Land, L.S., editors, Stable isotopes in sedimentary geology: SEPM Short course, v. 10 p. 4.1–4.22: Online, http://archives.datapages.com/data/sepm_sp/SC10/Chemical_Diagenesis.htm.

Walters, L.J., Claypool, G.E., and Choquette, P.W., 1972, Reaction rates and $\delta^{18}O$ variation for the carbonate-phosphoric acid preparation method: Geochimica et Cosmochimica Acta, v. 36, no. 2, p. 129–140, DOI:10.1016/0016-7037(72)90002-6.

Warren, J.K., 2006, Evaporites—sediments, resources, and hydrocarbons: New York, Springer Berlin Heidelberg, 1035 p.

Warren, J., 2000, Dolomite–occurrence, evolution and economically important associations: Earth-Science Reviews, v. 52, no. 1 , p. 1–81, DOI:10.1016/S0012-8252(00)00022-2.

Weber, J.N., 1964, Trace element composition of dolostones and dolomites and its bearing on the dolomite problem: Geochimica et Cosmochimica Acta, v. 28, no. 10-11, p. 1817–1832, DOI:10.1016/0016-7037(64)90023-7.

Whitehead, H.C., and Feth, J.H., 1961, Recent chemical analyses of waters from several closed-basin lakes and their tributaries in the western United States: Geological Society of America Bulletin, v. 72, no. 9, p. 1421–1425, DOI:10.1130/0016-7606(1961)72[1421:RCAOWF]2.0.CO;2.

Williamson, C.R., and Picard, M.D., 1974, Petrology of carbonate rocks of the Green River Formation (Eocene): Journal of Sedimentary Research, v. 44, no. 3, p. 738–759: Online, http://archives.datapages.com/data/sepm/journals/v42-46/data/044/044003/0738.htm.

Woody, R.E., Gregg, J.M., and Koederitz, L.F., 1996, Effect of texture on petrophysical properties of dolomite—evidence from the Cambrian-Ordovician of southeastern Missouri: Association of Petroleum Geologist Bulletin, v. 80, no. 1, p. 119–131: Online, http://archives.datapages.com/data/bulletns/1994-96/data/pg/0080/0001/0100/0119.htm.

Zachos, J., Pagani, M., Sloan, L., Thomas, E., and Billups, K., 2001, Trends, rhythms, and aberrations in global climate 65 Ma to present: Science, v. 292, no. 5517, p. 686–693, DOI:10.1126/science.1059412.

APPENDIX A

Measured Outcrop Sections

LEGEND

LITHOLOGY

- Cherty Dolostone
- Argillaceous Dolostone
- Interbedded Dolostone and Shale
- Dolomitic Limestone
- Argillaceous Limestone
- Interbedded Limestone and Shale
- Calcareous Shale
- Clastic Limestone
- Calcareous Siltstone
- Siltstone
- Sandstone
- Sample

BIOCLASTS

- Ostracods
- Pelecypods
- Gastropods
- Shell fragments
- Charophites
- Fish Bones
- Algae

STRUCTURES

- Planar Parallel
- Planar no Parallel
- Irregular
- Curved Parallel
- Wavy Parallel
- Wavy Discontinous
- Peloids
- Ooids
- Oncoids
- Nodule

Willow Creek Canyon (WCC)

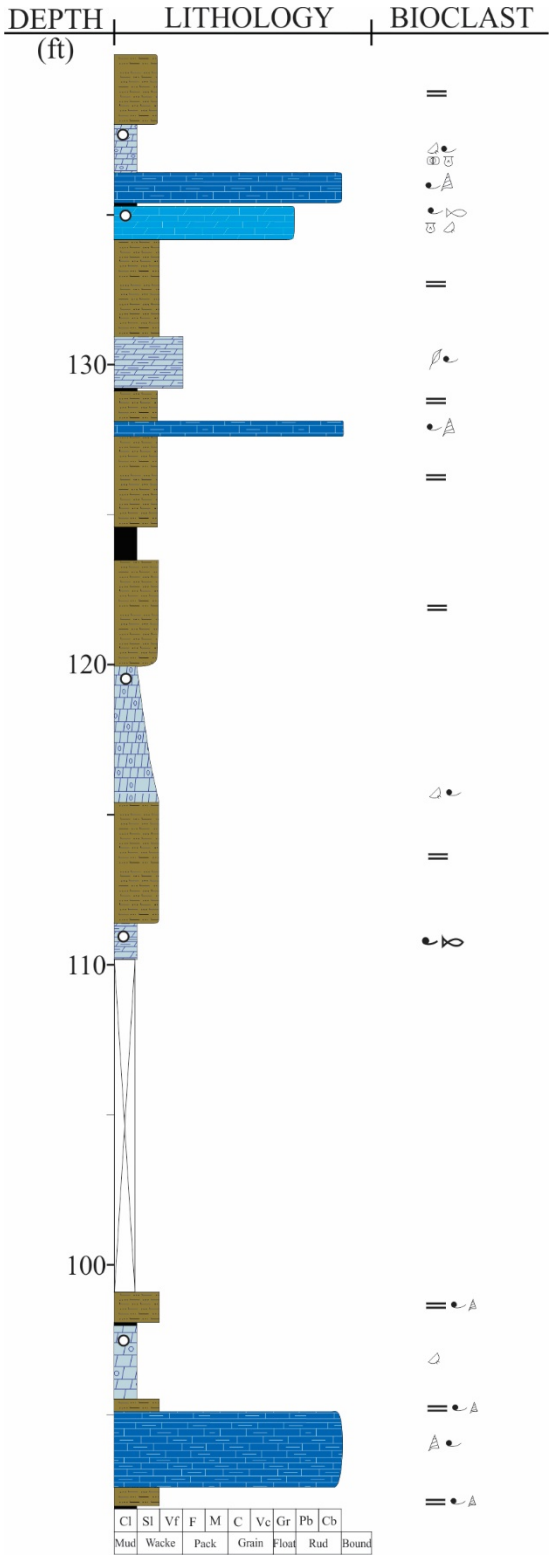

Nine Mile Canyon (NMC)

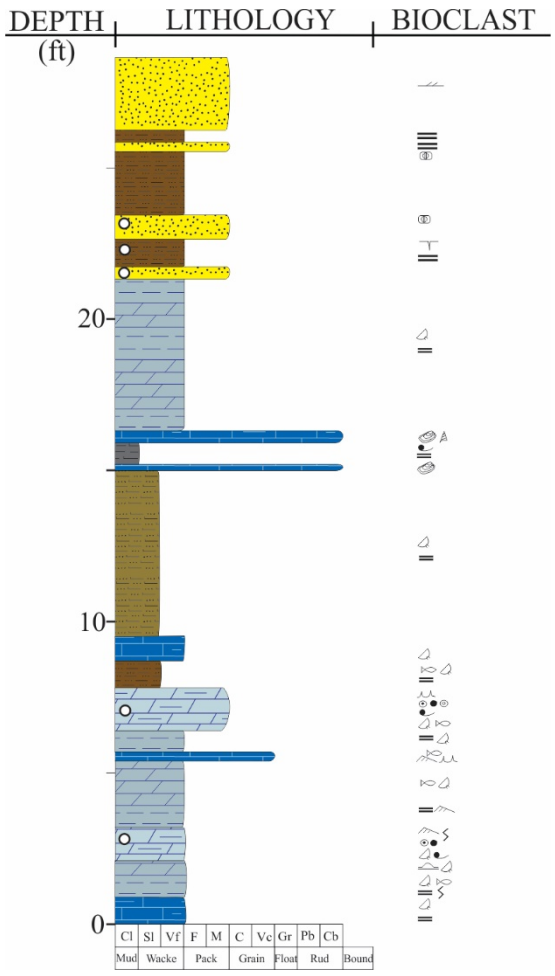

APPENDIX B

Core Descriptions

See appendix 1 for lithology and symbol descriptions.

Well: 14-1-46, code: BBC 14-1

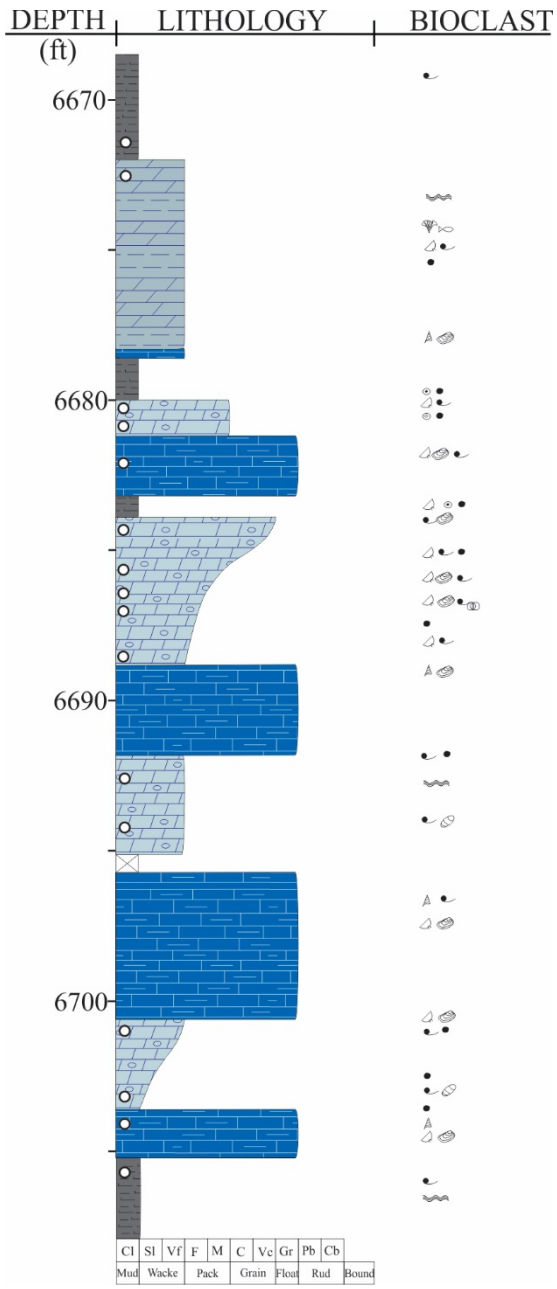

Well: 14-3-45, code: BBC 14-3

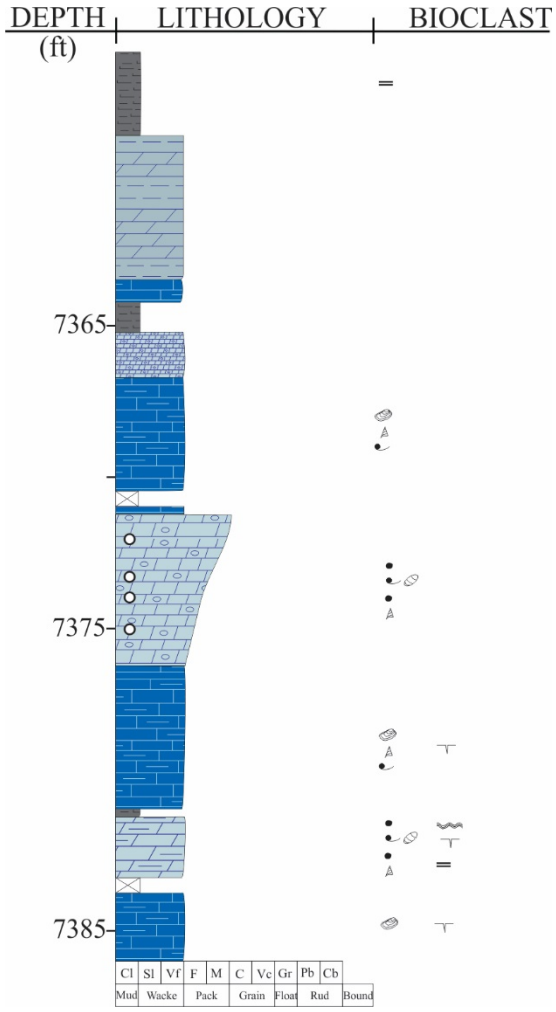

Well: Nickerson 6-28-3-2W, code: N 6-28

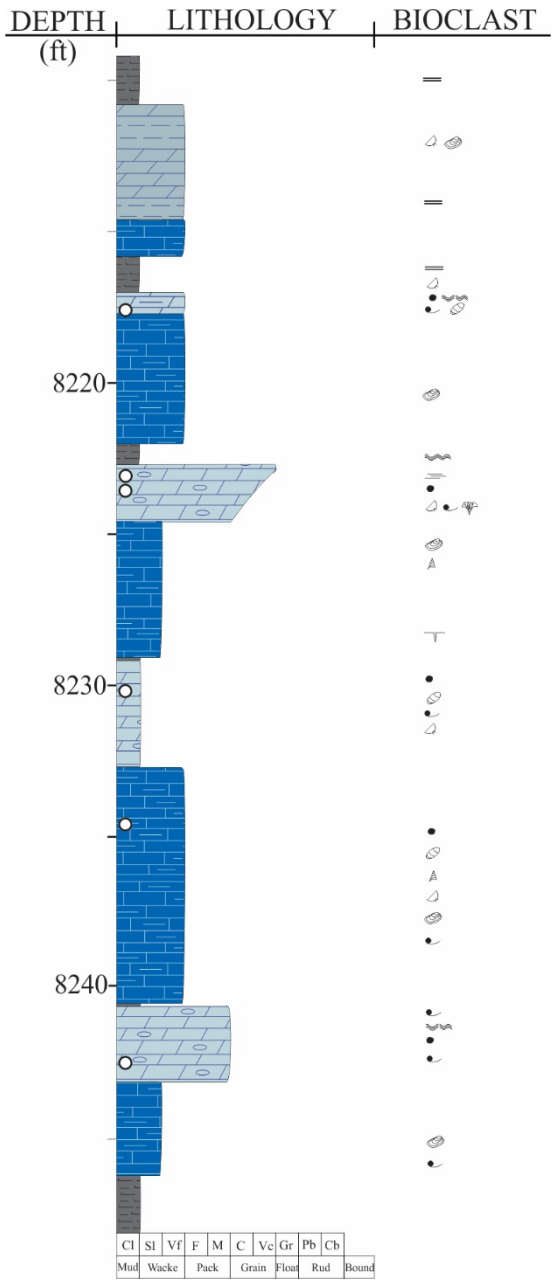

Well: Ute Tribal 15-13-4-3W, code: UT 15-13

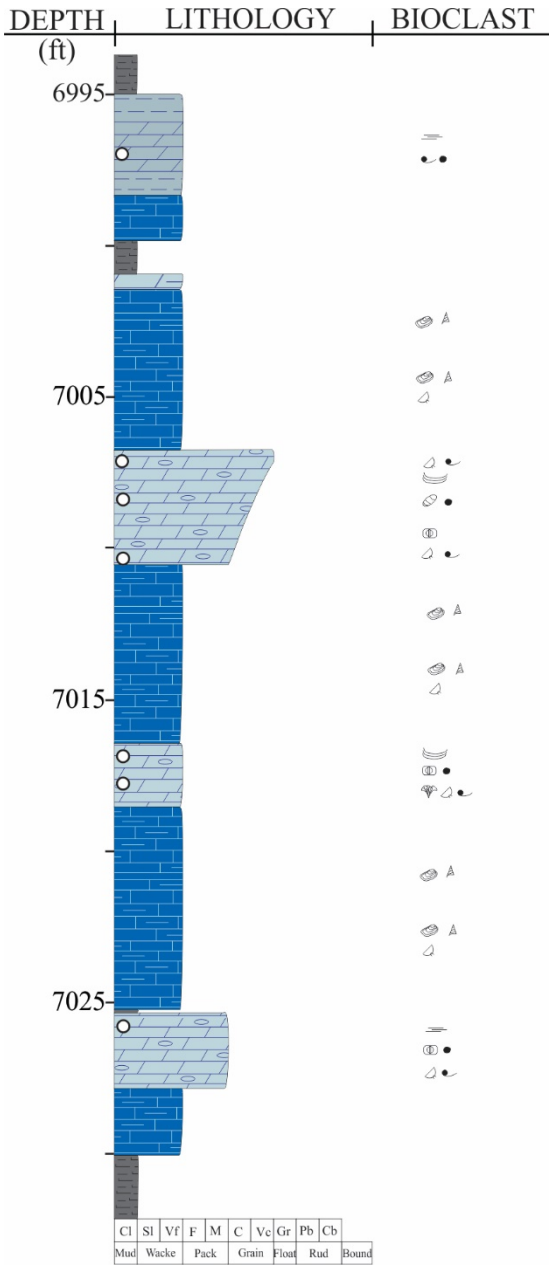

Well: Petes Wash 13-06 GR, code: PW 13-06

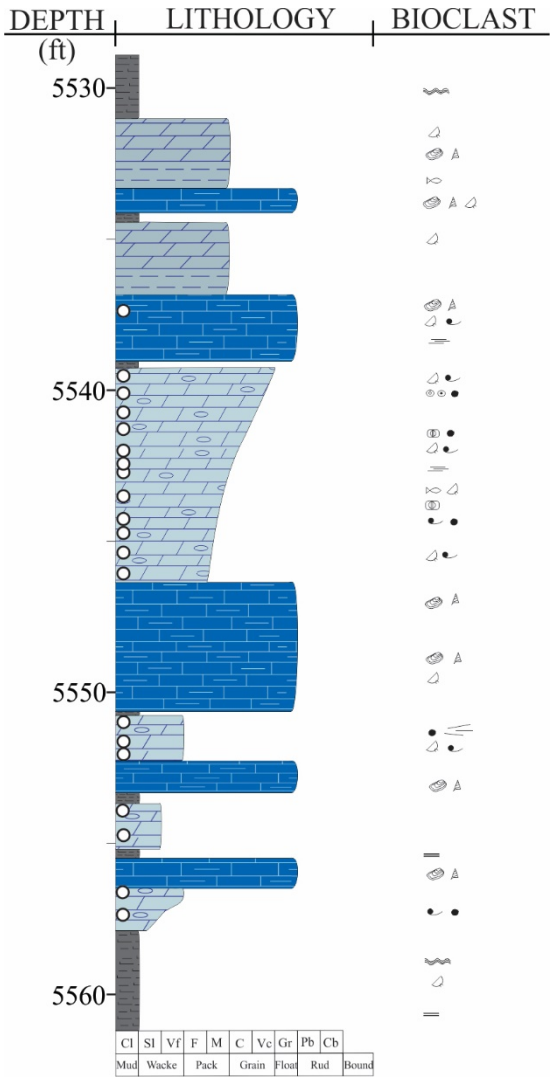

Well: West Desert Spring 11-20-10-17, code: DS 11-20

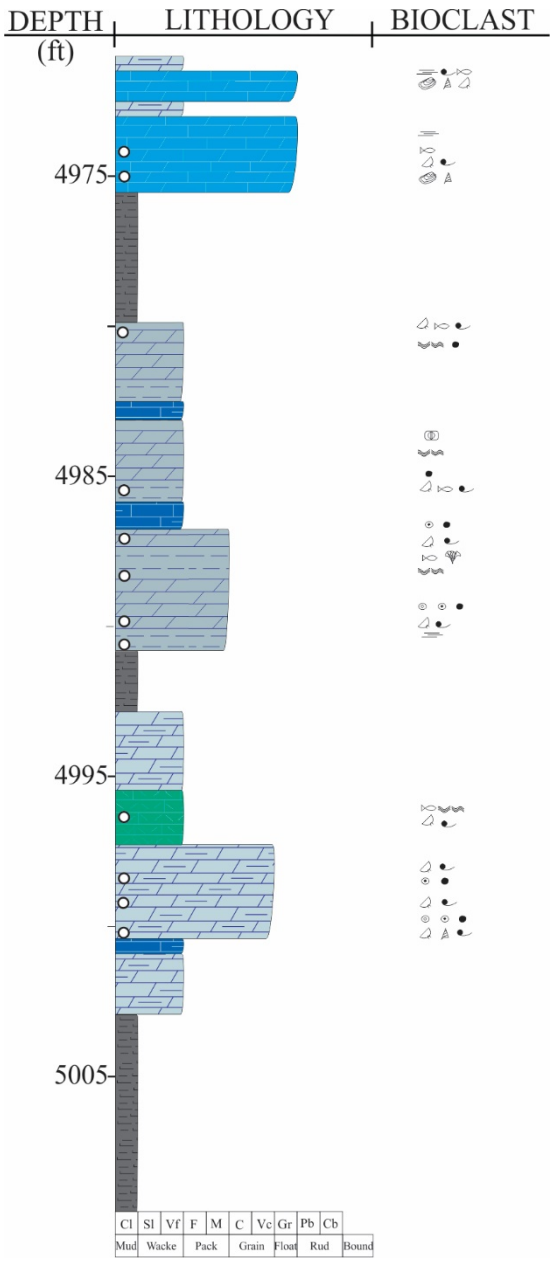

Well: Island Unit 16, code: IU 16

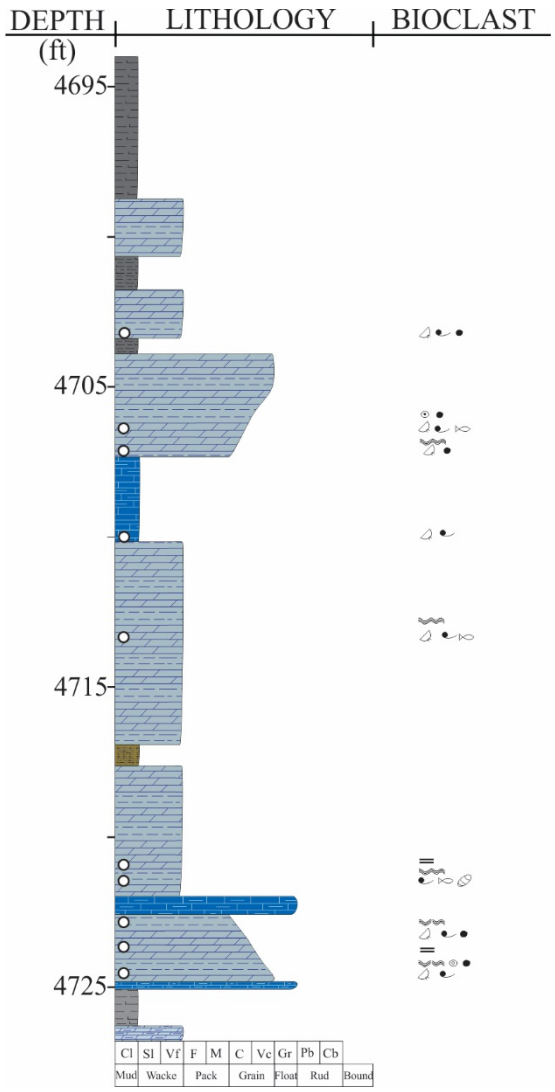

APPENDIX C

Thin section descriptions

Codes used for thin descriptions:

ROCK TYPE

D	Dolomitized (>75% Dol)
M	Mudstone
W	Wackestone
P	Packstone
G	Grainstone
F	Floatstone
R	Rudstone
d	Dolomitic (<75% Dol)
S	Silty
SS	Siltstone
Mud	Mudstone
A	Arenaceous
SSt	Sandstone
Ar	Argillaceous
C	Calcareous
Sh	Shale
CL	Claystone

MINERALOGY

Cal	Calcite
FCal	Ferroan Calcite
Dol	Dolomite
Sil	Silica
Pyr	Pyrite
Gyp	Gypsum

BIOCLASTS

O	Ostracods
P	Pelecypods
G	Gastropods
SF	Shell fragments
FS	Fish scales
CH	Charophyte
FB	Fish Bones (Undefined)
AM	Alga Mats
MAB	Most abundant Bioclast

CARBONATE GRAINS (CG)

RF	Rock fragments
On	Oncoids
Oo	Ooids
Pel	Peloids
Cor	Corticoids
MAA	Most Abundant CG

NON CARBONATE GRAINS (NCG)

Qz	Quartz
Cla	Clay
Sil	Silt
San	Sand
VF	Very Fine
F	Fine
M	Medium
C	Coarse
VC	Very coarse

FABRIC

MS	Matrix Supported
GS	Grain Supported
Ratio	MS/GS

SORTING

MS	Moderately sorted
WS	Well sorted
PS	Poorly sorted
VWS	Very well sorted

ROUNDING

S	Subrounded
R	Rounded
SA	Subangular
A	Angular

STRATIFICATION

I	Irregular stratification
M	Massive (lack)
PP	Plana Parallel
PW	Parallel wavy
WD	Wavy discontinuous
CP	Curved Parallel
SL	Structureless
WN	Wavy non parallel
PNP	Planar non parallel
PD	Planar discontinuous

LAYER THICKNESS

TNL	Thinly laminated
TCL	Thickly laminated
VTB	Very thinly bedded
TB	Thinly bedded

GRADATION

A	Agradational
CU	Coarsening upward
FU	Fining upward

				MINERALOGY							BIOCLASTS										CABONATE GRAINS							NCG					FABRIC			STRATIFICATION					
Well/Outcrop	Sample	Depth	Rock Type	Cal	FCal	Dol	Sil	Pyr	Gyp	Ox	O	P	G	SF	FS	FB	CH	AM	%	MAB	RF	On	Oo	Pel	Cor	%	MACG	Cla	Sil	San	Qz	NCG%	MS	GS	Ratio	Sor	Rou	Bedding	LT	Bio	A	CU	FU
BBC 14-1	7	6672.80	Sh	10	0	0	10	0	1	0	0	0	0	1	0	0	0	0	1	SF	0	0	0	0	0	0	0	1	C	0	1	4	1	0	80/20	WS	S	PP	VBT	0	1	0	0
BBC 14-1	8	6675.30	D-W	5	1	65	20	4	0	5	1	0	0	1	0	1	0	1	5	SF	0	0	0	1	0	25	Pel	0	M	0	1	5	1	0	80/20	WS	S	PP-W	VBT	0	0	1	0
BBC 14-1	9	6680.10	D-P	5	3	75	10	2	0	5	1	0	0	1	0	0	0	0	5	SF	0	1	0	1	0	25	Pel	0	C	VF	1	5	0	1	30/70	WS	S	PNP	VBT	0	1	0	0
BBC 14-1	10	6680.35	D-P	1	3	80	15	1	0	0	1	0	0	1	0	0	0	0	5	SF	0	0	1	1	0	15	Pel	0	M	0	1	3	1	0	50/50	MS	S	M	VBT	0	1	0	0
BBC 14-1	11	6683.15	F	74	1	5	20	0	0	0	1	1	0	1	0	0	0	0	40	P	0	0	0	0	0	0	0	0	M	0	1	10	1	0	60/40	PS	SA	I	VBT	0	1	0	0
BBC 14-1	12	6683.95	d-G	2	40	50	8	0	0	0	1	0	0	1	0	0	0	0	3	SF	1	1	0	1	1	30	Pel	0	0	0	1	0	0	1	30/70	-	-	M	VBT	0	1	0	0
BBC 14-1	13	6684.90	D-P	2	3	80	10	1	0	4	1	0	0	1	0	0	0	0	15	SF	1	0	0	1	0	25	Pel	0	F	0	1	1	0	1	40/60	-	-	M	VBT	0	1	0	0
BBC 14-1	14	6685.40	D-W	3	5	77	10	5	0	0	1	1	0	1	0	0	0	0	10	SF	0	0	0	1	0	3	Pel	0	M	0	0	3	1	0	80/20	-	-	M	VBT	0	1	0	0
BBC 14-1	15	6686.80	D-W	5	3	80	10	2	0	0	1	1	0	1	0	0	0	0	15	SF	0	0	0	1	0	20	Pel	0	M	0	0	5	1	0	70/30	-	-	I	VBT	1	1	0	0
BBC 14-1	16	6688.35	D-P	3	1	89	5	1	0	1	1	0	0	1	0	0	0	0	5	SF	0	0	0	1	0	3	Pel	0	M	0	1	1	1	0	90/10	-	-	M	VBT	0	1	0	0
BBC 14-1	17	6692.60	C-D-M	30	0	60	4	3	0	3	0	0	0	1	0	0	0	0	1	SF	0	0	0	1	0	30	Pel	0	F	0	1	3	1	0	50/50	PS	SA	PP-W	TCL	0	1	0	0
BBC 14-1	18	6693.50	D-M	1	0	95	3	1	0	0	0	0	0	1	0	0	1	0	1	SF	0	0	0	0	0	0	0	0	M	0	1	2	1	0	95/5	WS	R	M	VTB	0	1	0	0
BBC 14-1	19	6696.10	F-R	90	5	3	2	0	0	0	1	1	1	1	0	0	0	0	45	G	0	0	0	0	0	0	0	0	M	0	1	7	1	0	50/50	MS	S	M	VTB	0	1	0	0
BBC 14-1	20	6701.40	D-W	5	3	85	5	1	0	1	1	1	0	1	0	0	0	0	10	SF	0	0	0	1	0	15	Pel	0	M	0	1	7	1	0	80/20	WS	S	CP	VTB	1	1	0	0
BBC 14-1	21	6703.10	D-M	0	0	79	20	1	0	0	0	0	0	1	0	0	1	0	1	SF	0	0	0	1	0	1	Pel	0	M	0	1	2	1	0	99/1	WS	R	M	VTB	0	1	0	0
BBC 14-1	22	6703.75	F	4	0	0	95	1	0	0	0	0	0	0	0	0	0	0	30	P	0	0	0	1	0	0	0	0	M	0	1	5	1	0	50/50	MS	S	M	VTB	0	1	0	0
BBC 14-1	23	6704.50	F	90	1	0	8	1	0	0	1	1	0	1	0	0	0	0	30	P	0	0	0	0	0	0	0	0	M	0	1	5	1	0	50/50	MS	S	M	VTB	0	1	0	0
BBC 14-1	24	6705.30	Sh	70	0	0	20	1	0	0	0	0	0	1	0	0	0	0	50	SF	0	0	0	0	0	0	0	0	F	0	1	10	0	1	30/70	PS	A	PW	VTB	0	1	0	0
BBC 14-3	26	7372.35	D-W	5	0	70	20	5	0	0	1	0	0	1	0	0	0	0	10	SF	0	0	0	1	0	2	Pel	0	F	0	0	1	1	0	75/25	-	-	M	VTB	0	1	0	0
BBC 14-3	27	7373.65	D-W	6	1	70	20	3	0	0	1	0	0	1	0	0	1	0	10	SF	0	0	0	1	0	1	Pel	0	F	0	0	1	1	0	60/30	-	-	M	VTB	0	1	0	0
BBC 14-3	28	7374.05	d-W	10	5	30	50	3	0	2	1	0	0	1	0	0	1	0	15	O	0	0	0	1	0	2	Pel	1	F	0	0	1	1	0	70/30	-	-	WD	VTB	0	1	0	0
BBC 14-3	29	7375.00	D-P	5	2	70	20	3	0	0	1	0	0	1	0	0	1	0	15	SF	0	0	0	1	0	20	Pel	1	F	0	0	1	1	0	70/30	-	-	M	VTB	0	1	0	0
N 6-28	4	8217.60	D-W	1	0	90	7	2	0	0	0	0	0	1	0	0	1	0	0	0	0	0	0	1	0	30	Pel	1	M	0	1	5	1	0	80/20	-	-	WD	VTB	1	0	0	1
N 6-28	5	8223.20	D-W	40	0	40	15	5	0	0	1	0	0	1	0	0	0	0	1	SF	0	0	0	1	0	20	Pel	0	0	0	0	0	1	0	90/10	-	-	M	VTB	0	1	0	0
N 6-28	6	8223.70	D-W	15	0	70	10	5	0	0	1	0	0	1	0	0	0	1	3	O	0	0	0	1	0	5	Pel	1	M	0	0	3	1	0	80/20	-	-	SL	VTB	1	1	0	0
N 6-28	7	8230.20	D-M	1	0	80	18	1	0	0	1	0	0	1	0	0	1	0	1	O	0	0	0	1	0	20	Pel	1	M	0	0	1	1	0	95/5	-	-	M	VTB	0	1	0	0
N 6-28	8	8234.60	W	90	0	8	1	1	0	0	1	1	1	1	0	0	1	0	15	O	0	0	0	1	0	0	0	0	M	0	0	10	1	0	80/20	-	-	M	VTB	0	1	0	0
N 6-28	9	8242.50	D-P	3	0	75	20	2	0	0	0	0	0	1	0	0	0	0	5	SF	0	0	0	1	0	50	Pel	1	M	0	1	2	1	0	50/50	WS	R	WD	VTB	0	1	0	0
UT 15-13	8	6996.40	D-W	5	0	85	9	1	0	0	0	0	0	1	0	0	0	0	1	SF	0	0	0	1	0	20	Pel	1	M	0	1	10	1	0	70/30	WS	S	PD	TCL	0	1	0	0
UT 15-13	9	7006.50	D-G	0	0	80	18	2	0	0	1	0	0	1	0	0	0	0	5	SF	1	1	0	1	0	40	Pel	0	C	0	1	7	1	0	55/45	-	-	CP	TCL	0	1	0	0
UT 15-13	10	7007.80	D-M	1	0	90	8	1	0	0	0	0	0	0	0	0	1	0	1	CH	0	0	0	1	0	1	Pel	1	F	0	0	1	1	0	95/5	-	-	M	VTB	1	1	0	0
UT 15-13	11	7009.90	D-W	1	0	80	18	1	0	0	1	0	0	1	0	0	0	0	1	SF	0	0	0	1	0	10	Pel	1	F	0	1	5	1	0	80/20	-	-	M	VTB	1	1	0	0
UT 15-13	12	7016.40	D-W	2	0	80	10	8	0	0	1	0	0	1	0	0	0	0	20	O	0	0	0	1	0	10	Pel	1	M	0	0	2	1	0	60/40	-	-	PW	VTB	0	1	0	0
UT 15-13	13	7017.40	D-W	5	0	80	13	2	0	0	1	0	0	1	0	0	0	0	1	7	O	0	0	0	1	0	5	Pel	1	F	0	0	1	1	0	90/10	-	-	CP	VTB	1	1	0	0
UT 15-13	14	7025.20	D-P	3	0	85	10	2	0	0	1	0	0	1	0	0	0	0	5	SF	0	0	0	1	0	15	Pel	0	0	0	0	0	1	0	70/30	-	-	SL	VTB	1	1	0	0
PW 13-06	6	5537.30	F	70	5	5	15	0	0	0	1	1	1	1	0	0	0	0	40	O	0	0	0	0	0	0	0	0	C	VF	1	8	0	1	50/51	WS	S	SL	VTB	0	1	0	0
PW 13-06	7	5539.50	C-D-G	20	0	55	25	0	0	0	1	0	0	1	0	0	0	0	5	O	1	1	1	1	0	50	Oo	0	0	0	0	0	0	1	30/70	-	-	SL	VTB	0	1	0	0
PW 13-06	8	5541.90	D-W	3	0	55	40	2	0	0	1	0	0	1	0	0	0	0	5	SF	0	0	0	1	0	10	Pel	1	F	0	1	2	1	0	80/20	-	-	SL	VTB	0	1	0	0
PW 13-06	9	5543.50	D-W	5	0	50	40	4	0	1	1	0	0	1	0	1	0	0	5	O	0	0	0	1	0	5	Pel	0	F	0	0	1	1	0	95/5	-	-	SL	VTB	1	1	0	0
PW 13-06	10	5544.30	D-M	3	0	90	5	2	0	0	0	0	0	1	0	0	0	0	1	SF	0	0	0	1	0	1	Pel	1	0	0	0	1	1	0	100	-	-	SL	VTB	1	1	0	0
PW 13-06	11	5545.30	D-P	5	0	75	15	5	0	0	1	0	0	1	0	0	0	0	5	SF	0	0	0	1	0	50	Pel	1	0	0	0	1	1	0	80/20	-	-	SL	VTB	1	1	0	0
PW 13-06	12	5552.30	D-W	5	0	75	15	5	0	0	1	0	0	1	0	0	0	0	5	SF	0	0	0	1	0	10	Pel	1	M	0	0	2	1	0	70/30	-	-	I	VTB	0	1	0	0
PW 13-06	13	5557.40	D-W	0	0	80	15	5	0	0	0	0	0	1	0	0	0	0	1	SF	0	0	0	1	0	2	Pel	1	M	0	1	15	1	0	95/5	MS	S	M	VTB	1	1	0	0
DS 11-20	4	4980.10	C-D-W	20	0	70	8	2	0	0	1	0	0	1	0	1	0	0	30	SF	0	0	0	1	0	5	Pel	1	M	0	1	15	0	0	50/50	MS	S	WD	TCL	1	1	0	0
DS 11-20	5	4985.50	C-D-W	25	0	60	10	5	0	0	1	0	0	1	0	1	0	0	15	SF	0	0	0	1	0	5	Pel	1	M	0	1	10	1	0	70/30	WS	S	WD	TCL	1	1	0	0
DS 11-20	6	4986.50	C-D-P	20	0	70	8	2	0	0	1	0	0	1	0	1	0	1	10	SF	1	1	0	1	0	15	Pel	1	M	0	1	3	1	0	70/30	WS	S	WP	TCL	1	1	0	0
DS 11-20	7	4987.90	C-D-W	20	0	75	4	1	0	0	1	0	0	1	0	1	0	1	15	SF	0	0	0	1	0	15	Pel	1	M	0	1	3	1	0	80/30	WS	S	PNP	TCL	1	1	0	0
DS 11-20	8	4989.50	C-D-P	25	0	60	14	1	0	0	1	0	0	1	0	0	0	0	3	SF	0	1	1	1	0	20	Oo	1	M	0	1	3	1	0	70/30	WS	S	WD	VTB	0	1	0	0
DS 11-20	9	4990.45	C-D-P	40	0	55	4	1	0	0	1	0	0	1	0	0	0	0	5	SF	0	1	1	1	0	25	Oo	1	F	0	1	1	0	1	50/50	-	-	SL	VTB	0	1	0	0
DS 11-20	10	4996.35	Ar-d-W	30	0	40	10	10	0	0	1	0	0	1	0	1	0	0	5	SF	0	0	0	0	0	0	0	1	M	0	1	15	1	0	50/50	WS	S	WD	VTB	0	1	0	0
DS 11-20	11	4998.50	d-G	10	30	50	5	5	0	0	1	0	0	1	0	0	0	0	15	O	0	1	0	1	0	60	On	0	0	0	0	0	0	1	20/80	-	-	M	VTB	0	1	0	0
DS 11-20	12	4999.35	D-G	10	25	55	5	5	0	0	1	0	0	1	0	0	0	0	15	O	1	1	1	1	0	60	Oo	0	0	0	0	0	0	1	40/60	-	-	M	VTB	0	1	0	0
DS 11-20	13	5000.35	d-G	20	20	50	5	5	0	0	1	0	1	1	0	0	0	0	14	O	1	1	1	1	0	60	Oo	0	0	0	0	0	0	1	40/60	-	-	M	VTB	0	1	0	0

				MINERALOGY							BIOCLASTS										CABONATE GRAINS							NCG					FABRIC					STRATIFICATION					
Well/Outcrop	Sample	Depth	Rock Type	Cal	FCal	Dol	Sil	Pyr	Gyp	Ox	O	P	G	SF	FS	FB	CH	AM	%	MAB	RF	On	Oo	Pel	Cor	%	MACG	Cla	Sil	San	Qz	NCG%	MS	GS	Ratio	Sor	Rou	Bedding	LT	Bio	A	CU	FU
UI 16	2	4705.40	D-W	5	0	70	20	4	0	1	1	0	0	1	0	0	0	0	1	O	0	0	0	1	0	15	Pel	1	0	0	0	0	1	0	90/10	-	-	M	VTB	1	1	0	0
UI 16	3	4706.30	d-G	60	2	30	5	1	1	1	1	0	0	1	0	1	0	0	40	SF	1	1	0	1	0	30	Pel	0	F	0	1	5	0	1	30/70	-	-	WP	VTB	0	1	0	0
UI 16	4	4707.00	D-P	5	2	70	20	3	0	0	1	0	0	0	0	0	0	0	7	O	0	0	0	1	0	40	Pel	1	M	0	0	5	1	0	90/10	-	-	WP	VTB	0	1	0	0
UI 16	5	4710.00	M	75	1	10	10	4	0	0	1	0	0	1	0	0	0	0	2	SF	0	0	0	0	0	0	0	1	M	0	1	7	1	0	95/5	WS	R	M	VTB	0	1	0	0
UI 16	6	4713.20	S-CL	20	0	0	10	10	0	2	1	0	0	1	0	1	0	0	10	SF	0	0	0	0	0	0	0	1	F	0	1	5	1	0	70/30	WS	R	WP	VTB	0	1	0	0
UI 16	7	4720.80	D-W	5	0	80	10	5	0	0	0	0	0	1	0	1	0	0	2	SF	0	0	0	1	0	15	Pel	1	M	0	1	10	1	0	80/20	MS	S	PP	TNL	0	0	1	0
UI 16	8	4721.25	C-D-W	15	0	75	8	2	0	0	0	0	0	1	0	1	1	0	10	SF	0	0	0	1	0	10	Pel	1	F	0	1	5	1	0	60/40	WS	R	WP	VTB	0	1	0	0
UI 16	9	4722.50	C-D-P	15	0	80	3	2	0	0	1	0	0	1	0	0	0	0	10	SF	0	0	0	1	0	25	Pel	1	F	0	1	5	1	0	55/45	WS	R	WD	TNL	0	1	0	0
UI 16	10	4723.30	D-W	5	0	83	10	2	0	0	1	0	0	1	0	0	0	0	5	SF	0	0	0	1	0	5	Pel	1	F	0	1	3	1	0	80/20	WS	S	PP	VTB	0	1	0	0
UI 16	11	4724.20	C-D-G	40	0	53	5	2	0	0	1	0	0	1	0	0	0	0	1	O	0	0	1	1	0	60	Pel	1	0	0	0	0	0	1	40/60	-	-	WD	TCL	0	0	1	0
WCC	1	-	C-D-M	1	24	65	5	2	0	3	1	0	0	1	0	1	0	0	5	SF	0	1	0	0	0	1	On	1	M	0	1	1	1	0	70/30	-	-	SL	VTB	1	1	0	0
WCC	2	-	d-G	45	0	50	4	1	0	0	1	0	0	1	0	0	0	0	20	O	1	1	0	1	0	50	On	0	F	0	0	1	0	1	10/90	-	-	SL	VBT	0	1	0	0
WCC	3	-	D-M	5	0	90	3	2	0	0	1	0	0	1	0	0	0	0	5	SF	0	0	0	0	0	0	0	1	F	0	1	3	1	0	90/10	-	-	SL	VBT	1	1	0	0
WCC	4	-	D-M	5	0	90	3	1	0	2	0	0	0	1	0	1	0	0	1	FB	0	0	0	0	0	0	0	1	F	0	1	3	1	0	90/10	WS	R	SL	VBT	1	1	0	0
WCC	5	-	D-M	3	0	90	3	1	0	3	1	0	0	1	0	0	0	0	2	SF	0	0	0	0	0	0	0	1	F	0	1	3	1	0	90/10	WS	S	SL	VBT	1	1	0	0
WCC	6	-	d-F	82	0	15	0	2	0	1	1	1	0	1	0	1	0	0	15	SF	0	0	0	0	0	0	0	1	F	0	1	3	1	0	60/40	-	-	SL	VBT	0	1	0	0
WCC	7	-	D-M	5	0	60	30	5	0	0	1	0	0	1	0	0	0	0	5	SF	0	0	0	0	0	0	0	1	F	0	1	3	1	0	80/20	WS	R	WD	VBT	1	1	0	0
WCC	8	-	F	80	0	0	15	5	0	0	1	1	1	1	0	1	0	0	60	G	0	0	0	0	0	0	0	1	F	0	1	5	0	1	10/90	-	-	SL	VBT	0	1	0	0
NMC	3	-	d-SSt	10	0	45	40	5	0	0	0	0	0	0	0	0	0	0	0	0	1	0	0	0	0	0	0	1	C	F	1	60	1	0	60/40	VWS	R	SL	VTB	0	1	0	0
NMC	41	-	C-SSt	2	28	5	60	0	0	5	0	0	0	0	0	0	0	0	0	0	1	0	0	0	0	0	0	1	C	F	1	80	1	0	50/50	WS	S	SL	VTB	0	1	0	0
NMC	42	-	C-SSt	1	24	5	65	0	0	5	0	0	0	0	0	0	0	0	0	0	1	0	0	0	0	0	0	1	C	F	1	80	1	0	50/50	WS	S	SL	VTB	0	1	0	0
NMC	43	-	C-SSt	1	19	5	70	0	0	5	0	0	0	0	0	0	0	0	0	0	1	0	0	0	0	0	0	1	C	F	1	80	1	0	50/50	WS	S	SL	VTB	0	1	0	0
NMC	44	-	C-SSt	1	3	10	80	1	0	5	0	0	0	0	0	0	0	0	0	0	1	0	0	0	0	0	0	1	C	F	1	60	1	0	50/50	WS	S	SL	VTB	0	1	0	0
NMC	45	-	C-SSt	1	0	40	50	4	0	5	0	0	0	0	0	0	0	0	0	0	0	0	0	0	0	0	0	1	C	VF	1	50	1	0	70/30	PS	R	SL	VTB	0	1	0	0
NMC	2	-	C-D-P	25	2	60	10	3	0	0	1	0	0	1	0	0	0	1	20	O	0	1	1	1	0	40	Pel	1	C	0	1	10	1	0	40/60	MS	SA	WN	VTB	0	1	0	0
NMC	1	-	C-D-P	15	0	79	5	1	0	0	1	0	0	1	0	0	0	0	20	O	0	1	0	1	0	60	On	1	C	0	1	5	0	1	20/80	MS	S	PW	VTB	0	1	0	0

APPENDIX D

Energy dispersive X-ray spectroscopy from SEM

			Atomic %							
Well	**Sample**	**Spot**	**O**	**Mg**	**Al**	**Si**	**S**	**Cl**	**K**	**Ca**
N 6-28	7	6-28-7_ 1	71.8	10.5		1.0				16.7
N 6-28	7	6-28-7_ 10	65.4	12.9		3.3				18.3
N 6-28	7	6-28-7_ 11	66.9	12.3		2.6				18.1
N 6-28	7	6-28-7_ 2	71.7	10.7		1.3				16.2
N 6-28	7	6-28-7_ 3	71.8	10.8		1.1				16.2
N 6-28	7	6-28-7_ 4	67.4	12.7		2.3				17.6
N 6-28	7	6-28-7_ 5	66.8	13.3		2.1				17.7
N 6-28	7	6-28-7_ 6	66.9	12.6		2.0				18.4
N 6-28	7	6-28-7_ 7	66.7	13.7		2.0				17.6
N 6-28	7	6-28-7_ 8	66.7	12.5		2.7				18.1
N 6-28	7	6-28-7_ 9	68.0	11.4		3.5				17.1
N 6-28	7	6-28-9_ 1	66.3	9.2	1.5	3.3	0.2	3.4	0.4	15.4
N 6-28	7	6-28-9_ 2	57.1	15.1	0.4	2.8	0.1	2.7	0.1	21.4
N 6-28	7	6-28-9_ 3	63.5	14.3		1.5		1.5		18.9
N 6-28	7	6-28-9_ 4	61.4	13.8		1.5		2.0		21.2
N 6-28	7	6-28-9_ 5	63.1	13.7		1.5		2.3		19.2
N 6-28	7	6-28-9_ 6	64.8	5.2		19.3		1.4		9.3
N 6-28	7	6-28-9_ 7	59.3	11.0		12.1		2.0		15.5
N 6-28	7	6-28-9_ 8	59.0	14.4		4.2		2.4		19.7
N 6-28	7	6-28-9_ 9	61.1	7.0		17.3		2.0		12.4
UT 15-13	13	15-13-13_ 1		39.4						60.2
UT 15-13	13	15-13-13_ 2		40.6						59.1
UT 15-13	13	15-13-13_ 3		43.0						57.0
UT 15-13	13	15-13-13_ 5		38.8						61.2
UT 15-13	13	15-13-13_ 6		39.8						60.2
UT 15-13	13	15-13-13_ 7		39.3						60.6
UT 15-13	13	15-13-13_ 8		39.1						60.8
UT 15-13	13	15-13-13_ 9		38.9						61.1
UT 15-13	14	15-13-14_ 1	65.8			34.2				
UT 15-13	14	15-13-14_ 10		44.0						56.0
UT 15-13	14	15-13-14_ 11		41.1						57.7
UT 15-13	14	15-13-14_ 12		42.3						57.0
UT 15-13	14	15-13-14_ 13		43.1						56.9
UT 15-13	14	15-13-14_ 14		45.6						54.4
UT 15-13	14	15-13-14_ 15		43.4						56.1
UT 15-13	14	15-13-14_ 16		44.1						55.9
UT 15-13	14	15-13-14_ 17		44.1						55.9
UT 15-13	14	15-13-14_ 18		42.1						57.8
UT 15-13	14	15-13-14_ 19		43.4						56.3
UT 15-13	14	15-13-14_ 2		43.6						56.4
UT 15-13	14	15-13-14_ 20		43.0						56.5
UT 15-13	14	15-13-14_ 21		42.5						57.2

Well	Sample	Spot	O	Mg	Al	Si	S	Cl	K	Ca
UT 15-13	14	15-13-14_ 4		43.6						56.2
UT 15-13	14	15-13-14_ 5		43.6						56.2
UT 15-13	14	15-13-14_ 6		43.8						56.2
UT 15-13	14	15-13-14_ 7		41.4						58.3
UT 15-13	14	15-13-14_ 8		41.8						57.2
UT 15-13	14	15-13-14_ 9		42.6						56.5
PW 13-06	7	13-06-07_ 1		41.1						58.7
PW 13-06	7	13-06-07_ 2		38.8						61.1
PW 13-06	7	13-06-07_ 3		44.4						55.5
PW 13-06	7	13-06-07_ 4		37.9						62.0
PW 13-06	7	13-06-07_ 5		42.5						57.3
PW 13-06	7	13-06-07_ 6		43.7						56.1
PW 13-06	7	13-06-07_ 7		44.4						55.5
PW 13-06	8	13-06-08_C_ 21		39.6						59.7
PW 13-06	8	13-06-08_C_ 15		45.7						53.5
PW 13-06	8	13-06-08_C_ 14		46.5						52.7
PW 13-06	8	13-06-08_C_ 20		41.6						57.7
PW 13-06	8	13-06-08_C_ 9		45.5						53.9
PW 13-06	8	13-06-08_C_ 13		42.8						56.7
PW 13-06	8	13-06-08_C_ 18		43.8						55.8
PW 13-06	8	13-06-08_C_ 19		40.5						59.1
PW 13-06	8	13-06-08_C_ 8		40.3						59.3
PW 13-06	8	13-06-08_C_ 17		45.7						54.0
PW 13-06	8	13-06-08_C_ 4		47.7						52.0
PW 13-06	8	13-06-08_C_ 5		43.7						56.0
PW 13-06	8	13-06-08_C_ 11		44.8						55.0
PW 13-06	8	13-06-08_C_ 10		42.0						57.9
PW 13-06	8	13-06-08_ 6	69.0	6.5		12.3	0.2	1.3		10.7
PW 13-06	8	13-06-08_ 7	70.7	10.3		1.3	0.1	1.0		16.4
PW 13-06	8	13-06-08_ 12		44.2						55.7
PW 13-06	8	13-06-08_ 8	69.0	11.7		0.9	0.1	0.8		17.5
PW 13-06	8	13-06-08_C_ 7		39.7						60.2
PW 13-06	8	13-06-08_C_ 6		39.8						60.2
PW 13-06	8	13-06-08_C_ 26		41.8						58.2
PW 13-06	8	13-06-08_C_ 25		43.4						56.6
PW 13-06	8	13-06-08_C_ 24		38.1						61.9
PW 13-06	8	13-06-08_C_ 22		41.6						58.4
PW 13-06	8	13-06-08_C_ 16		43.9						56.1
PW 13-06	8	13-06-08_C_ 1		40.7						59.3
PW 13-06	8	13-06-08_C_ 3	64.9			35.1				
PW 13-06	8	13-06-08_C_ 2	63.5		0.1	32.6		2.6		
PW 13-06	8	13-06-08_ 9	65.8	3.2		23.5	0.2	0.8		6.5
PW 13-06	8	13-06-08_ 4	68.1	12.6		0.4		0.9		17.9
PW 13-06	8	13-06-08_ 3	61.9	4.3	6.0	13.0		0.9	5.3	8.2
PW 13-06	8	13-06-08_ 2	63.0	3.5	6.2	13.6		0.9		6.9
PW 13-06	8	13-06-08_ 12	67.2	4.2		18.9	0.2	0.9		8.7
PW 13-06	8	13-06-08_ 11	65.8	3.6		23.3	0.1	0.8		6.4
PW 13-06	8	13-06-08_ 10	65.6	3.4		23.1	0.2	0.9		6.8
PW 13-06	8	13-06-08_ 1	61.7	3.0	7.4	15.5		0.8		4.8
PW 13-06	11	13-06-11_ 1		37.6						61.6

Well	Sample	Spot	O	Mg	Al	Si	S	Cl	K	Ca
PW 13-06	11	13-06-11_ 10		39.2						60.6
PW 13-06	11	13-06-11_ 2		38.3						61.4
PW 13-06	11	13-06-11_ 3		39.8						59.6
PW 13-06	11	13-06-11_ 4		36.7						61.6
PW 13-06	11	13-06-11_ 5		40.7						59.1
PW 13-06	11	13-06-11_ 6		36.5						63.5
PW 13-06	11	13-06-11_ 7		35.1						64.7
PW 13-06	11	13-06-11_ 8		42.2						57.4
PW 13-06	11	13-06-11_ 9		36.7						61.9
PW 13-06	12	13-06-12_ 1		43.2						56.8
PW 13-06	12	13-06-12_ 10		41.7						57.8
PW 13-06	12	13-06-12_ 11		41.7						58.3
PW 13-06	12	13-06-12_ 2		39.5						60.0
PW 13-06	12	13-06-12_ 3		41.2						58.8
PW 13-06	12	13-06-12_ 4		39.3						59.9
PW 13-06	12	13-06-12_ 5		43.2						56.8
PW 13-06	12	13-06-12_ 6		45.4						54.2
PW 13-06	12	13-06-12_ 7		43.4						56.6
PW 13-06	12	13-06-12_ 8		41.4						58.3
PW 13-06	12	13-06-12_ 9		42.4						57.3

APPENDIX E

XRD data from different labs

				%CaCO3		
Well	**Sample**	**Depth**	**Lithology**	**IU**	**U of A**	**WMU**
BBC 14-1	2	6657.8	D		55.2	
BBC 14-1	4	6665.5	D		53.4	
BBC 14-1	8	6675.3	D		55.5	
BBC 14-1	12	6684.0	PZ1			53.8
BBC 14-1	12B	6684.5	PZ1			52.1
BBC 14-1	13	6684.9	PZ1			53.7
BBC 14-1	14	6685.4	PZ1		55.2	53.9
BBC 14-1	14A	6686.1	PZ1			54.6
BBC 14-1	14B	6686.5	PZ1			53.7
BBC 14-1	15	6686.8	PZ1		55.5	53.8
BBC 14-1	14A	6687.2	PZ1			53.6
BBC 14-1	15B	6687.6	PZ1			54.2
BBC 14-1	16	6688.4	PZ1			54.3
BBC 14-1	16A	6692.1	PZ1'			52.7
BBC 14-1	17	6692.6	PZ1'		54.2	52.3
BBC 14-1	18	6693.5	PZ1'			51.3
BBC 14-1	18A	6694.1	PZ1'			51.8
BBC 14-1	18B	6694.9	PZ1'			55.2
BBC 14-1	19	6700.9	PZ2		53.3	53.8
BBC 14-1	20	6701.4	PZ2		54.8	53.2
BBC 14-1	20A	6702.3	PZ2			53.8
BBC 14-1	21	6703.1	PZ2		53.7	51.7
BBC 14-3	26	7372.4	PZ1		55.3	53.6
BBC 14-3	27	7373.7	PZ1			53.9
BBC 14-3	28	7374.1	PZ1			53.6
BBC 14-3	29	7375.0	PZ1			53.9
BBC 14-3	30	7375.9	PZ1			54.4
BBC 14-3	31	7376.8	PZ1			54.9
BBC 14-3	32	7382.0	PZ1'			52.9
BBC 14-3	33	7382.7	PZ1'			52.1
BBC 14-3	34	7383.7	PZ1'			53.1
N 6-28	1	8199.3	D	55.2	52.7	
N 6-28	2	8203.6	D		53.7	
N 6-28	3	8205.6	D		52.1	
N 6-28	4	8217.6	D	55.8	53.3	
N 6-28	5	8223.2	PZ1		52.3	
N 6-28	6	8223.7	PZ1	54.9	53.8	
N 6-28	7	8230.2	PZ1'	51.8	52.6	
N 6-28	9	8242.5	PZ2	54.9	54.6	
N 6-28	10	8248.9	D		55.5	
N 6-28	12	8267.4	D		51.0	
N 6-28	13	8270.3	D		54.7	

Well	Sample	Depth	Lithology	IU	U of A	WMU
UT 15-13	15-13-5	6982.2	D		53.7	
UT 15-13	15-13-6	6983.9	D		54.7	
UT 15-13	15-13-7	6989.0	D		53.7	
UT 15-13	15-13-9	7006.5	PZ1		52.3	
UT 15-13	15-13-10	7007.8	PZ1		53.9	
UT 15-13	15-13-11B	7009.9	PZ1	55.5	55.5	
UT 15-13	15-13-12	7016.4	PZ1'		57.5	
UT 15-13	15-13-13	7017.4	PZ1'	55.2	55.6	
UT 15-13	15-13-14	7025.2	PZ2	52.7	52.3	
PW 13-06	13-06-1	5524.2	D		55.0	
PW 13-06	13-06-2	5524.7	D		55.5	
PW 13-06	13-06-3	5527.3	D		52.6	
PW 13-06	13-06-6	5539.5	PZ1		51.6	50.4
PW 13-06	13-06-6A	5540.1	PZ1			49.7
PW 13-06	13-06-6B	5540.7	PZ1		51.8	50.5
PW 13-06	13-06-6C	5541.3	PZ1			51.9
PW 13-06	13-06-7	5541.9	PZ1	52.7	51.1	49.6
PW 13-06	13-06-7A	5542.4	PZ1		53.1	53.4
PW 13-06	13-06-7B	5542.7	PZ1			52.9
PW 13-06	13-06-8	5543.5	PZ1	53.3	54.2	52.9
PW 13-06	13-06-9	5544.3	PZ1			52.9
PW 13-06	13-06-9A	5544.7	PZ1		54.9	53.1
PW 13-06	13-06-10	5545.3	PZ1	55.5	53.1	54.0
PW 13-06	13-06-10A	5546.1	PZ1		56.0	54.4
PW 13-06	13-06-10B	5551.0	PZ1'		55.7	53.5
PW 13-06	13-06-10C	5551.6	PZ1'		55.5	53.2
PW 13-06	13-06-11	5552.2	PZ1'	55.2	54.6	52.9
PW 13-06	13-06-11A	5553.9	PZ2		53.9	53.2
PW 13-06	13-06-11B	5554.7	PZ2		53.4	52.1
PW 13-06	13-06-11C	5556.6	PZ3			55.1
PW 13-06	13-06-12	5557.4	PZ2	54.3	55.7	51.8
PW 13-06	13-06-13	5563.3	D		55.0	
PW 13-06	13-06-14	5565.9	L		53.9	
PW 13-06	13-06-15	5580.8	D		50.3	
PW 13-06	13-06-16	5595.4	D		54.2	
PW 13-06	13-06-17	5596.0	D		54.2	
PW 13-06	13-06-18	5603.4	L		53.1	
PW 13-06	13-06-19	5607.8	D		54.9	
DS 11-20	11-20-1	4972.5	D		56.2	
DS 11-20	11-20-2	4974.5	L		54.0	
DS 11-20	11-20-4	4980.1	PZ1		56.0	
DS 11-20	11-20-5	4985.5	PZ1'		55.5	
DS 11-20	11-20-8	4989.5	PZ2		52.2	
DS 11-20	11-20-9	4990.5	PZ2		57.7	
I 16	16-2	4705.4	D		55.5	
I 16	16-3	4706.3	PZ1	57.0	58.2	
I 16	16-4	4707.0	PZ1		55.2	
I 16	16-7	4720.8	PZ1'		54.9	
I 16	16-8	4721.3	PZ1'		57.1	

Well	Sample	Depth	Lithology	IU	U of A	WMU
I 16	16-10	4723.3	PZ2		56.5	
I 16	16-11	4724.2	PZ2		55.0	

Note: IU = Indiana University, U of A = University of Alberta, WMU = Western Michigan University

APPENDIX F

EMPA - Electron microprobe analysis

		Concentration (WT %)						
SAMPLE	**Point**	**Fe**	**Mn**	**Mg**	**Ca**	**Sr**	**C**	**O**
13-06-11 t1A	1	0.06	0.00	11.46	23.41	0.10	12.71	50.78
13-06-11 t1A	2	0.52	0.00	10.89	23.90	0.07	12.66	50.61
13-06-11 t1A	3	0.49	0.00	11.12	23.71	0.09	12.72	50.82
13-06-11 t1A	4	0.51	0.02	11.18	23.72	0.08	12.76	51.00
13-06-11 t1A	5	0.10	0.00	10.86	24.55	0.08	12.76	50.98
13-06-11 t1A	6	0.56	0.04	11.11	23.87	0.08	12.78	51.08
13-06-11 t1A	7	0.37	0.00	11.42	23.71	0.08	12.84	51.31
13-06-11 t1A	8	0.55	0.00	10.93	24.25	0.08	12.80	51.15
13-06-11 t1A	9	0.35	0.00	6.22	31.01	0.10	12.46	49.77
13-06-11 t1A	10	0.52	0.00	11.51	23.71	0.07	12.92	51.63
13-06-11 t1A	11	0.14	0.00	10.91	24.85	0.12	12.89	51.49
13-06-11 t2	1	0.26	0.07	10.76	24.22	0.10	12.66	50.59
13-06-11 t2	2	0.61	0.00	10.62	24.24	0.06	12.65	50.56
13-06-11 t2	3	0.31	0.00	11.45	23.57	0.09	12.80	51.15
13-06-11 t2	4	0.18	0.00	10.97	24.33	0.09	12.77	51.02
13-06-11 t2	5	0.37	0.03	11.28	23.83	0.08	12.81	51.20
13-06-11 t2	6	0.34	0.00	11.00	24.31	0.07	12.80	51.17
13-06-11 t2	7	0.73	0.00	10.54	24.62	0.09	12.76	50.99
13-06-11 t2	8	0.59	0.00	10.77	24.48	0.07	12.79	51.13
13-06-11 t2	9	0.05	0.02	12.75	22.48	0.00	13.05	52.15
13-06-11 t3	1	0.41	0.00	11.11	23.66	0.07	12.68	50.67
13-06-11 t3	2	0.40	0.00	11.08	23.80	0.04	12.70	50.75
13-06-11 t3	3	0.51	0.00	10.99	23.93	0.07	12.72	50.85
13-06-11 t3	4	0.55	0.02	11.02	23.90	0.07	12.74	50.93
13-06-11 t3	5	0.29	0.00	10.80	24.49	0.10	12.75	50.96
13-06-11 t3	6	0.06	0.00	11.08	24.30	0.10	12.79	51.10
13-06-11 t3	7	0.37	0.00	11.35	23.92	0.07	12.87	51.42
13-06-11 t3	8	0.43	0.00	11.10	24.31	0.08	12.88	51.46
13-06-11 t3	9	0.52	0.04	11.11	24.20	0.09	12.88	51.46
13-06-11 t4	1	0.40	0.00	11.06	23.70	0.07	12.66	50.61
13-06-11 t4	2	0.44	0.00	11.14	23.58	0.07	12.68	50.66
13-06-11 t4	3	0.43	0.00	11.16	23.58	0.12	12.69	50.71
13-06-11 t4	4	0.49	0.00	11.00	23.79	0.07	12.68	50.67
13-06-11 t4	5	0.53	0.00	11.48	23.35	0.05	12.79	51.11
13-06-11 t4	6	0.33	0.00	10.78	24.47	0.09	12.74	50.92
13-06-11 t4	7	0.24	0.00	11.18	24.04	0.10	12.80	51.14
13-06-11 t4	8	1.36	0.00	10.26	24.46	0.05	12.70	50.75
13-06-11 t4	9	0.74	0.00	10.51	24.69	0.08	12.76	51.01
13-06-11 t4	10	0.68	0.00	11.03	24.15	0.06	12.84	51.33
13-06-11 t5	2	0.95	0.05	10.78	23.79	0.04	12.68	50.66
13-06-11 t5	3	0.35	0.03	10.66	24.49	0.10	12.70	50.77
13-06-11 t5	4	0.48	0.02	10.72	24.33	0.10	12.71	50.78

SAMPLE	Point	Fe	Mn	Mg	Ca	Sr	C	O
13-06-11 t5	5	0.30	0.02	11.16	23.94	0.09	12.77	51.05
13-06-11 t5	6	0.38	0.02	10.77	24.46	0.10	12.75	50.97
13-06-11 t5	7	0.39	0.03	10.83	24.38	0.10	12.76	51.00
13-06-11 t5	8	0.13	0.00	10.95	24.44	0.14	12.78	51.08
13-06-11 t5	9	0.17	0.00	11.06	24.29	0.13	12.80	51.15
13-06-11 t5	10	0.14	0.03	11.35	24.06	0.07	12.87	51.42
13-06-11 t5	11	0.48	0.00	10.92	24.41	0.08	12.83	51.25
13-06-11 t5	12	0.40	0.00	11.40	23.86	0.08	12.88	51.47
13-06-11 t5	13	0.16	0.00	3.78	34.75	0.13	12.33	49.29
13-06-8 t1	1	0.06	0.04	11.74	23.03	0.10	12.74	50.89
13-06-8 t1	2	0.09	0.04	12.02	22.68	0.09	12.77	51.05
13-06-8 t1	3	0.07	0.06	11.83	22.92	0.11	12.76	50.99
13-06-8 t1	4	0.06	0.04	11.58	23.33	0.10	12.75	50.97
13-06-8 t1	5	0.10	0.00	11.95	22.85	0.08	12.79	51.10
13-06-8 t1	6	0.08	0.04	11.77	23.11	0.09	12.78	51.07
13-06-8 t1	7	0.08	0.03	12.08	22.69	0.08	12.80	51.17
13-06-8 t1	8	0.09	0.06	12.02	22.73	0.11	12.80	51.15
13-06-8 t1	9	0.09	0.04	12.26	22.43	0.10	12.82	51.24
13-06-8 t1	10	0.06	0.05	11.71	23.29	0.12	12.81	51.18
13-06-8 t1	11	0.10	0.05	12.49	22.20	0.11	12.87	51.44
13-06-8 t1	12	0.09	0.03	11.81	23.22	0.09	12.83	51.28
13-06-8 t1	13	0.10	0.04	11.93	23.06	0.10	12.85	51.35
13-06-8 t1	14	0.07	0.04	12.00	23.00	0.09	12.86	51.39
13-06-8 t1	15	0.05	0.03	11.76	23.37	0.09	12.85	51.34
13-06-8 t1	16	0.08	0.06	11.99	23.02	0.11	12.87	51.43
13-06-8 t1	17	0.12	0.03	11.91	23.17	0.09	12.87	51.43
13-06-8 t1	18	0.12	0.03	12.01	23.16	0.10	12.92	51.64
13-06-8 t2	1	0.09	0.05	12.00	22.65	0.11	12.76	50.99
13-06-8 t2	2	0.08	0.03	11.92	22.78	0.12	12.75	50.97
13-06-8 t2	3	0.06	0.04	11.83	22.91	0.14	12.75	50.96
13-06-8 t2	4	0.08	0.04	11.74	23.06	0.10	12.75	50.95
13-06-8 t2	5	0.09	0.03	12.26	22.41	0.11	12.82	51.22
13-06-8 t2	6	0.07	0.05	11.76	23.13	0.10	12.78	51.09
13-06-8 t2	7	0.05	0.05	12.13	22.67	0.10	12.82	51.24
13-06-8 t2	8	0.12	0.03	11.97	22.91	0.08	12.82	51.25
13-06-8 t2	9	0.06	0.03	11.73	23.29	0.10	12.81	51.19
13-06-8 t2	10	0.06	0.06	11.65	23.40	0.10	12.81	51.19
13-06-8 t2	11	0.09	0.04	11.79	23.22	0.08	12.82	51.25
13-06-8 t2	12	0.11	0.03	12.02	22.87	0.11	12.84	51.32
13-06-8 t2	13	0.10	0.06	12.13	22.76	0.12	12.87	51.42
13-06-8 t2	14	0.09	0.04	12.63	22.12	0.13	12.92	51.62
13-06-8 t2	16	0.10	0.06	12.13	22.81	0.11	12.88	51.48
13-06-8 t2	17	0.05	0.05	11.70	23.56	0.13	12.88	51.48
13-06-8 t2	18	0.10	0.03	12.09	23.01	0.11	12.92	51.62
13-06-8 t2	19	0.09	0.04	12.16	22.94	0.09	12.93	51.65
13-06-8 t2	20	0.06	0.04	11.88	23.59	0.10	12.97	51.85
13-06-8 t3	1	0.07	0.03	12.57	21.83	0.13	12.79	51.12
13-06-8 t3	2	0.07	0.04	11.90	22.79	0.12	12.75	50.95
13-06-8 t3	3	0.06	0.06	11.76	23.01	0.09	12.75	50.94
13-06-8 t3	4	0.10	0.04	12.25	22.44	0.10	12.83	51.25

SAMPLE	Point	Fe	Mn	Mg	Ca	Sr	C	O
13-06-8 t3	5	0.12	0.02	12.52	22.13	0.10	12.86	51.41
13-06-8 t3	6	0.08	0.04	12.04	22.93	0.09	12.86	51.39
13-06-8 t3	7	0.11	0.03	12.29	22.59	0.11	12.89	51.49
13-06-8 t3	8	0.10	0.05	11.90	23.33	0.11	12.92	51.62
13-06-8 t3	9	0.07	0.04	12.32	22.81	0.08	12.96	51.79
13-06-8 t4	1	0.07	0.05	12.15	22.42	0.10	12.76	51.00
13-06-8 t4	2	0.08	0.05	12.44	22.10	0.11	12.81	51.19
13-06-8 t4	3	0.09	0.06	11.80	23.14	0.09	12.81	51.20
13-06-8 t4	4	0.34	0.05	11.89	22.84	0.09	12.82	51.22
13-06-8 t4	5	0.07	0.04	11.72	23.30	0.14	12.81	51.21
13-06-8 t4	6	0.07	0.00	12.80	21.90	0.15	12.92	51.64
13-06-8 t4	7	0.10	0.03	11.84	23.26	0.10	12.86	51.39
13-06-8 t4	8	0.07	0.03	12.17	22.90	0.11	12.91	51.60
13-06-8 t4	9	0.09	0.00	12.35	22.73	0.08	12.94	51.72
13-06-8 t5	1	0.14	0.07	12.19	22.34	0.06	12.77	51.04
13-06-8 t5	2	0.05	0.06	11.82	23.07	0.13	12.80	51.13
13-06-8 t5	3	0.25	0.03	12.20	22.59	0.11	12.87	51.44
13-06-8 t5	4	0.09	0.04	12.11	23.20	0.10	12.98	51.87
15-13-14 t1	1	0.04	0.00	12.41	22.11	0.10	12.78	51.07
15-13-14 t1	2	0.10	0.00	12.37	22.18	0.10	12.79	51.13
15-13-14 t1	3	0.11	0.00	12.20	22.41	0.09	12.78	51.08
15-13-14 t1	4	0.23	0.04	12.12	22.41	0.08	12.77	51.04
15-13-14 t1	5	0.08	0.00	12.35	22.42	0.09	12.85	51.35
15-13-14 t1	6	0.08	0.00	12.52	22.38	0.09	12.93	51.65
15-13-14 t1	7	0.08	0.00	12.55	22.62	0.12	13.01	52.01
15-13-14 t2	1	0.05	0.00	12.46	22.16	0.09	12.82	51.24
15-13-14 t2	2	0.11	0.00	12.30	22.34	0.08	12.81	51.19
15-13-14 t2	3	0.02	0.00	12.57	22.03	0.10	12.83	51.29
15-13-14 t2	4	0.05	0.00	12.70	21.86	0.10	12.85	51.35
15-13-14 t2	5	0.04	0.00	12.21	22.57	0.09	12.82	51.23
15-13-14 t2	6	0.05	0.00	12.49	22.16	0.13	12.84	51.31
15-13-14 t2	7	0.00	0.00	11.48	23.89	0.00	12.84	51.30
15-13-14 t2	8	0.09	0.00	12.47	22.49	0.11	12.94	51.70
15-13-14 t3	2	0.11	0.00	12.27	22.31	0.07	12.78	51.07
15-13-14 t3	3	0.05	0.00	12.43	22.11	0.10	12.79	51.13
15-13-14 t3	4	0.04	0.03	12.03	22.67	0.11	12.77	51.03
15-13-14 t3	5	0.07	0.00	12.32	22.37	0.08	12.82	51.23
15-13-14 t3	6	0.08	0.00	12.37	22.32	0.09	12.84	51.29
15-13-14 t3	7	0.10	0.00	12.15	22.67	0.06	12.83	51.25
15-13-14 t3	8	0.04	0.00	12.28	22.58	0.09	12.85	51.37
15-13-14 t3	9	0.11	0.00	12.22	22.64	0.12	12.86	51.39
15-13-14 t3	10	0.17	0.00	12.28	22.54	0.06	12.87	51.44
15-13-14 t3	11	0.03	0.00	12.35	22.82	0.04	12.95	51.76
15-13-14 t3	12	0.16	0.04	12.48	22.47	0.07	12.95	51.77
15-13-14 t4	1	0.05	0.00	12.31	22.47	0.11	12.84	51.31
15-13-14 t4	2	0.19	0.00	12.34	22.32	0.10	12.84	51.31
15-13-14 t4	3	0.46	0.00	12.27	22.19	0.10	12.83	51.27
15-13-14 t4	4	0.00	0.00	12.58	22.39	0.10	12.94	51.71
15-13-14 t4	5	0.10	0.00	12.42	22.59	0.09	12.94	51.72
15-13-14 t4	6	0.09	0.00	12.44	22.72	0.07	12.99	51.90

SAMPLE	Point	Fe	Mn	Mg	Ca	Sr	C	O
15-13-14 t5	1	0.10	0.00	12.15	22.49	0.07	12.77	51.04
15-13-14 t5	2	0.10	0.00	12.33	22.38	0.07	12.83	51.27
15-13-14 t5	3	0.18	0.00	12.13	22.60	0.09	12.81	51.21
15-13-14 t5	4	0.05	0.00	12.45	22.37	0.09	12.88	51.46
15-13-14 t5	5	0.26	0.00	12.01	22.91	0.08	12.87	51.41
15-13-14 t5	6	0.09	0.00	12.33	22.60	0.08	12.90	51.54
15-13-14 t5	7	0.04	0.00	12.33	22.80	0.08	12.95	51.74
15-13-14 t5	8	0.08	0.00	12.53	22.65	0.06	13.01	51.99
6-28-7 t1	1	0.00	0.03	12.26	22.36	0.07	12.77	51.05
6-28-7 t1	2	0.11	0.00	12.26	22.30	0.07	12.77	51.05
6-28-7 t1	3	0.00	0.00	12.18	22.52	0.07	12.78	51.06
6-28-7 t1	4	0.00	0.00	12.05	22.68	0.09	12.77	51.02
6-28-7 t1	5	0.03	0.00	12.36	22.27	0.05	12.79	51.13
6-28-7 t1	6	0.00	0.00	12.10	22.68	0.06	12.78	51.08
6-28-7 t1	7	0.13	0.00	11.94	22.78	0.11	12.77	51.03
6-28-7 t1	8	0.06	0.00	11.96	22.83	0.09	12.78	51.06
6-28-7 t1	9	0.07	0.00	12.13	22.56	0.12	12.79	51.11
6-28-7 t1	10	0.06	0.00	12.02	22.77	0.08	12.79	51.10
6-28-7 t1	11	0.09	0.00	12.10	22.66	0.07	12.80	51.14
6-28-7 t1	12	0.00	0.00	12.23	22.56	0.06	12.81	51.21
6-28-7 t1	13	0.04	0.00	12.01	22.83	0.07	12.79	51.13
6-28-7 t1	14	0.03	0.00	12.31	22.48	0.04	12.83	51.28
6-28-7 t1	15	0.05	0.00	12.37	22.39	0.07	12.84	51.33
6-28-7 t1	16	0.08	0.00	12.05	22.83	0.07	12.82	51.25
6-28-7 t1	17	0.04	0.00	12.09	22.80	0.09	12.83	51.27
6-28-7 t1	18	0.03	0.00	12.19	22.71	0.09	12.85	51.34
6-28-7 t1	20	0.11	0.00	12.19	22.71	0.06	12.86	51.39
6-28-7 t1	21	0.00	0.00	12.23	22.78	0.05	12.88	51.47
6-28-7 t1	22	0.08	0.00	12.21	22.74	0.05	12.88	51.46
6-28-7 t1	23	0.04	0.00	12.44	22.48	0.05	12.90	51.55
6-28-7 t1	24	0.04	0.00	12.24	23.01	0.06	12.96	51.80
6-28-7 t2	1	0.04	0.00	12.24	22.37	0.06	12.77	51.03
6-28-7 t2	2	0.08	0.00	12.11	22.50	0.08	12.76	50.99
6-28-7 t2	3	0.12	0.00	11.26	23.68	0.06	12.69	50.73
6-28-7 t2	4	0.02	0.00	12.00	22.72	0.07	12.76	50.98
6-28-7 t2	5	0.06	0.00	12.15	22.53	0.06	12.77	51.05
6-28-7 t2	6	0.00	0.00	12.24	22.47	0.07	12.79	51.12
6-28-7 t2	7	0.00	0.00	12.29	22.47	0.04	12.81	51.20
6-28-7 t2	8	0.05	0.00	12.05	22.74	0.06	12.79	51.11
6-28-7 t2	9	0.09	0.00	12.16	22.61	0.05	12.81	51.19
6-28-7 t2	10	0.05	0.00	12.18	22.62	0.06	12.82	51.21
6-28-7 t2	11	0.02	0.00	12.45	22.31	0.03	12.85	51.34
6-28-7 t2	12	0.00	0.00	12.12	22.76	0.10	12.82	51.24
6-28-7 t2	13	0.00	0.00	12.21	22.74	0.08	12.86	51.40
6-28-7 t2	14	0.09	0.00	12.16	22.76	0.07	12.86	51.40
6-28-7 t2	15	0.04	0.00	12.40	22.60	0.06	12.92	51.63
6-28-7 t2	16	0.03	0.02	12.25	22.80	0.06	12.91	51.58
6-28-7 t2	17	0.00	0.00	12.13	23.06	0.08	12.92	51.62
6-28-7 t2	18	0.11	0.00	12.27	22.84	0.07	12.94	51.72
6-28-7 t2	19	0.00	0.00	12.08	23.18	0.09	12.93	51.68

SAMPLE	Point	Fe	Mn	Mg	Ca	Sr	C	O
6-28-7 t2	20	0.21	0.00	11.93	23.36	0.06	12.95	51.74
6-28-7 t3	1	0.15	0.00	12.02	22.65	0.05	12.77	51.02
6-28-7 t3	2	0.02	0.00	12.31	22.34	0.08	12.79	51.12
6-28-7 t3	3	0.03	0.00	12.09	22.66	0.06	12.78	51.07
6-28-7 t3	4	0.07	0.00	12.09	22.63	0.06	12.78	51.07
6-28-7 t3	5	0.13	0.00	12.06	22.62	0.09	12.78	51.06
6-28-7 t3	6	0.05	0.00	12.25	22.42	0.07	12.80	51.14
6-28-7 t3	7	0.05	0.00	12.24	22.48	0.07	12.80	51.16
6-28-7 t3	8	0.03	0.00	12.33	22.39	0.03	12.81	51.20
6-28-7 t3	9	0.03	0.00	12.13	22.66	0.04	12.80	51.15
6-28-7 t3	10	0.03	0.00	12.25	22.53	0.05	12.82	51.23
6-28-7 t3	11	0.11	0.00	12.13	22.60	0.11	12.81	51.17
6-28-7 t3	12	0.07	0.00	12.13	22.67	0.06	12.81	51.19
6-28-7 t3	13	0.06	0.00	12.23	22.53	0.09	12.82	51.22
6-28-7 t3	14	0.07	0.00	12.20	22.59	0.07	12.83	51.26
6-28-7 t3	15	0.02	0.02	12.11	22.76	0.06	12.82	51.25
6-28-7 t3	16	0.03	0.00	12.16	22.81	0.07	12.86	51.39
6-28-7 t3	17	0.30	0.03	11.66	23.28	0.07	12.82	51.21
6-28-7 t3	18	0.04	0.00	12.29	22.62	0.10	12.88	51.45
6-28-7 t3	19	0.09	0.00	12.27	22.65	0.06	12.88	51.47
6-28-7 t3	21	0.14	0.00	12.29	22.63	0.07	12.89	51.53
6-28-7 t3	22	0.00	0.00	12.01	23.21	0.10	12.90	51.57
6-28-7 t3	23	0.06	0.00	12.26	22.99	0.05	12.97	51.82
6-28-7 t3	24	0.37	0.00	11.94	23.30	0.04	12.97	51.82
6-28-7 t4	1	0.00	0.00	12.39	22.20	0.09	12.79	51.09
6-28-7 t4	2	0.04	0.00	12.09	22.60	0.06	12.77	51.02
6-28-7 t4	3	0.11	0.00	11.95	22.81	0.05	12.77	51.05
6-28-7 t4	4	0.07	0.00	12.13	22.59	0.08	12.79	51.11
6-28-7 t4	5	0.16	0.00	11.86	22.91	0.08	12.77	51.05
6-28-7 t4	6	0.07	0.00	12.28	22.43	0.06	12.81	51.20
6-28-7 t4	7	0.14	0.00	12.22	22.47	0.10	12.82	51.23
6-28-7 t4	8	0.10	0.00	12.25	22.52	0.05	12.83	51.27
6-28-7 t4	9	0.00	0.00	12.40	22.41	0.07	12.85	51.36
6-28-7 t4	10	0.05	0.03	12.09	22.77	0.09	12.83	51.27
6-28-7 t4	11	0.04	0.00	12.25	22.62	0.07	12.85	51.35
6-28-7 t4	12	0.04	0.02	12.29	22.57	0.04	12.86	51.38
6-28-7 t4	13	0.11	0.00	12.13	22.78	0.07	12.85	51.36
6-28-7 t4	14	0.08	0.02	12.19	22.71	0.08	12.86	51.39
6-28-7 t4	15	0.00	0.00	12.38	22.55	0.06	12.88	51.49
6-28-7 t4	16	0.06	0.00	12.20	22.75	0.07	12.87	51.43
6-28-7 t4	17	0.03	0.00	12.27	22.76	0.12	12.91	51.58
6-28-7 t4	18	0.05	0.00	12.36	22.69	0.08	12.92	51.65
6-28-7 t4	19	0.00	0.00	12.13	23.04	0.10	12.91	51.60
6-28-7 t4	20	0.21	0.00	12.36	22.58	0.09	12.93	51.68
6-28-7 t4	21	0.10	0.00	12.20	23.08	0.07	12.98	51.87
6-28-7 t4	22	0.06	0.02	12.60	22.57	0.05	13.02	52.02
6-28-7 t5	1	0.05	0.00	12.07	22.62	0.04	12.76	50.99
6-28-7 t5	2	0.03	0.00	12.26	22.42	0.06	12.79	51.13
6-28-7 t5	3	0.06	0.00	12.14	22.56	0.08	12.78	51.09
6-28-7 t5	4	0.03	0.00	12.26	22.48	0.06	12.81	51.20

SAMPLE	Point	Fe	Mn	Mg	Ca	Sr	C	O
6-28-7 t5	5	0.05	0.00	12.20	22.57	0.08	12.82	51.21
6-28-7 t5	6	0.12	0.00	11.93	22.92	0.05	12.80	51.14
6-28-7 t5	7	0.05	0.00	12.24	22.57	0.08	12.83	51.27
6-28-7 t5	8	0.16	0.00	12.02	22.82	0.00	12.81	51.21
6-28-7 t5	9	0.00	0.00	12.27	22.61	0.08	12.85	51.35
6-28-7 t5	10	0.09	0.00	12.13	22.80	0.05	12.85	51.36
6-28-7 t5	11	0.03	0.00	12.22	22.75	0.06	12.87	51.44
6-28-7 t5	12	0.03	0.00	12.11	22.93	0.07	12.87	51.44
6-28-7 t5	13	0.00	0.00	12.24	22.78	0.07	12.89	51.50
6-28-7 t5	14	0.03	0.00	12.17	22.89	0.07	12.89	51.50
6-28-7 t5	15	0.03	0.00	11.98	23.16	0.08	12.88	51.46
6-28-7 t5	16	0.13	0.00	12.13	22.87	0.09	12.89	51.51
6-28-7 t5	17	0.04	0.00	12.27	22.79	0.06	12.91	51.59
6-28-7 t5	18	0.04	0.00	12.21	22.89	0.06	12.91	51.59
6-28-7 t5	20	0.05	0.00	12.35	22.73	0.08	12.94	51.71
6-28-7 t5	21	0.07	0.00	12.35	22.80	0.06	12.96	51.79
6-28-7 t5	22	0.04	0.00	12.07	23.35	0.06	12.98	51.87

APPENDIX G

ICP-MS analyses

				Concentration (ppm)									
W/O	Sample	Litho	Depth	Ca	Mg	Na	Al	Si	Fe	Mn	Zn	Sr	Pb
BBC-14-1	4	D	6665.5	248675	149442	931.8	693.4	3451.7	5149.6	399.6	5.2	833.2	0.8
BBC-14-1	14	PZ1	6685.4	225617	120877	955.7	777.3	3089.6	4748.1	308.6	12.8	608.5	1.9
BBC-14-1	17	PZ1'	6692.6	244420	126593	873.3	755.8	3467.8	3924.9	326.2	6.7	803.9	1.7
BBC-14-1	19	L	6696.1	372918	15518	425	951	2675	4271	705	17.3	1662	2.69
BBC-14-1	21	PZ2	6703.1	267000	140463	942.2	522.4	2597.5	1848.3	236.3	4.7	811.4	0.8
BBC-14-3	26	PZ1	7372.4	263715	141876	1273.1	243.7	1850.0	2359.4	209.5	2.6	1292.4	0.5
N 6-28	1	D	8199.3	208594	107159	1065.5	1334.8	2885.7	17164.6	207.1	29.6	1012.4	2.5
N 6-28	2	D	8203.6	214855	108400	914.0	621.2	2636.0	7671.4	243.5	10.4	916.8	0.6
N 6-28	3	D	8205.6	254435	130130	741.4	714.2	2678.1	12020.6	352.6	8.3	893.6	1.5
N 6-28	4	D	8217.6	244175	122682	954.0	1029.2	2386.0	7492.0	417.4	27.3	813.8	2.7
N 6-28	6	PZ1	8223.7	252341	137474	1293.9	150.5	1582.8	3205.8	224.4	6.6	1454.9	0.5
N 6-28	7	PZ1'	8230.2	269703	141954	962.5	264.6	1751.3	2224.1	116.1	3.5	892.6	0.6
N 6-28	9	PZ2	8242.5	278704	135641	1042.6	353.6	1683.1	3713.8	423.6	4.7	960.3	0.5
N 6-28	10	D	8248.9	282808	120591	820.3	480.4	1604.9	7606.9	272.8	5.3	1101.1	0.9
N 6-28	13	D	8270.3	254046	136813	1409.5	244.6	1500.7	2255.5	163.2	3.2	1280.7	0.3
UT 15-13	1	L	6945.9	353004	11190	623	1264	2115	12397	929	34.8	1135	8.98
UT 15-13	5	D	6982.2	221106	112451	1161.3	2044.1	2362.7	12491.5	258.6	37.7	848.2	5.1
UT 15-13	7	D	6989.0	268080	148742	1065.7	200.3	1964.1	13188.6	684.5	6.9	1039.9	0.7
UT 15-13	9	PZ1	7006.5	232123	149330	1094.3	181.7	2199.3	4354.4	202.8	7.2	1412.3	2.2
UT 15-13	10	PZ1	7007.8	255347	161219	922.5	159.7	1693.4	2990.9	142.8	3.0	1456.6	0.7
UT 15-13	11B	PZ2	7009.9	253364	129550	988.4	139.3	1462.7	2054.7	245.1	3.4	1200.8	0.3
UT 15-13	14	PZ2	7025.2	232868	147531	1025.4	874.4	8855.6	3092.5	160.1	6.0	1164.7	0.9
PW 13-06	1	D	5524.2	269433	101397	935.1	344.3	1540.2	4600.1	225.3	4.0	935.0	1.6
PW 13-06	2	D	5524.7	277323	115555	1028.8	476.6	2012.0	4545.6	221.9	6.8	1483.2	0.6
PW 13-06	3	D	5527.3	276877	130559	808.1	142.2	1694.0	5340.8	234.9	4.2	905.9	0.3
PW 13-06	4	L	5528.3	407091	6315	384	407	1227	11547	709	13.4	1765	2.11
PW 13-06	6	PZ1	5539.5	282515	164765	822.0	44.2	2159.1	1429.8	91.1	1.3	1846.2	1.4
PW 13-06	6B	PZ1	5540.7	245014	161206	2098.7	119.8	1718.3	1669.5	241.8	7.7	1991.5	0.8
PW 13-06	7B	PZ1	5542.7	264659	146416	1274.0	113.0	1985.0	1439.0	299.8	6.3	1722.1	0.6
PW 13-06	8	PZ1	5543.5	261192	132692	787.6	94.2	2236.8	3932.4	469.9	2.9	1368.8	1.7
PW 13-06	9	PZ1	5544.3	248924	131320	755.4	88.6	1863.8	1626.1	271.5	4.1	1204.2	0.7
PW 13-06	10B	PZ1'	5551.0	246686	132581	1184.6	1020.0	2426.3	5077.2	254.0	8.9	1161.6	1.6
PW 13-06	11	PZ1'	5552.2	246342	134757	982.1	857.1	2162.5	5715.4	203.2	6.8	1011.2	1.2
PW 13-06	11B	PZ2	5554.7	236416	124624	1061.2	670.7	2080.4	3197.3	158.0	4.4	846.0	0.7
PW 13-06	14	L	5565.9	370285	6392	654	1291	2050	10833	654	22.4	1500	5.34
PW 13-06	17	D	5596.0	250691	150098	792.8	98.0	1214.8	2831.3	169.3	3.7	1034.6	0.6
PW 13-06	18	L	5604.0	312560	16660	1168	2456	3131	5129	364	19.5	1237	5.46
PW 13-06	19	D	5607.8	233885	129379	1074.3	267.2	2337.2	3696.5	245.1	2.9	892.3	0.6

W/O	Sample	Litho	Depth	Ca	Mg	Na	Al	Si	Fe	Mn	Zn	Sr	Pb
DS 11-20	2	L	4974.5	381082	8069	1338	824	2002	4851	451	6.34	1159	2.77
DS 11-20	4	PZ1	4980.1	215128	106155	1942.4	1520.6	3328.7	8627.6	282.7	18.0	785.6	3.7
DS 11-20	5	PZ1'	4985.5	234295	107464	1421.2	1440.7	7746.7	7353.1	244.2	76.4	969.8	2.6
UI 16	5	L	4710.0	343576	17018	1090	1371	2488	4162	265	15.2	977	3.78
UI 16	7	PZ1'	4720.8	238937	116240	1507.8	796.6	2271.8	8757.7	208.7	18.3	916.4	3.7
NMC	4	D	-	243544	136852	1310.1	814.0	3299.8	7302.2	495.0	10.0	896.9	1.8
NMC	5	D	-	237415	115591	1122.3	1463.0	3815.5	8262.6	680.5	16.3	787.0	3.0
		Detection limit		10	0.5	0.7	0.1		7	0.02	0.05	0.01	0.02

Note: L = limestone, D = dolomite, PZ = pay zone (dolomite).

APPENDIX H

Isotopic data

Well	Sample	Depth	$\delta^{13}C$ (VPDB)	$\delta^{18}O$ (VPDB)	%Cal	%Dol
BBC 14-1	14-1-2	6657.75	-0.2	-2.8	22.3	77.7
BBC 14-1	14-1-4	6665.5	1.5	-1.5	1.2	98.8
BBC 14-1	14-1-8	6675.3	-1.1	-5.1	15.6	84.4
BBC 14-1	14-1-14	6685.4	-3.3	-2.7	7.0	93.0
BBC 14-1	14-1-17	6692.6	-3.3	-2.4	0.0	100.0
BBC 14-1	14-1-19	6696.1	-1.2	-8.3	99.2	0.8
BBC 14-1	14-1-20	6701.4	1.2	-2.7	16.2	83.8
BBC 14-1	14-1-21	6703.1	1.9	-0.7	1.4	98.6
N 6-28	6-28-1	8199.3	1.4	-0.8	0.0	100.0
N 6-28	6-28-2	8203.6	5.2	-0.1	10.0	90.0
N 6-28	6-28-3	8205.6	6.4	-2.0	0.0	100.0
N 6-28	6-28-4	8217.6	4.1	-1.9	0.0	100.0
N 6-28	6-28-5	8223.2	0.3	-2.1	13.4	86.6
N 6-28	6-28-6	8223.7	2.4	0.9	6.8	93.2
N 6-28	6-28-7	8230.2	5.2	-0.3	0.0	100.0
N 6-28	6-28-8	8234.6	1.3	-7.3	94.7	5.3
N 6-28	6-28-9	8242.5	3.7	-2.1	2.8	97.2
N 6-28	6-28-10	8248.9	2.7	-4.0	7.1	92.9
N 6-28	6-28-11	8256	2.3	-4.9	21.9	78.1
N 6-28	6-28-12	8267.4	3.0	-7.3	21.0	79.0
N 6-28	6-28-13	8270.3	-0.3	-1.3	4.4	95.6
UT 15-13	15-13-1	6945.9	0.1	-7.2	90.4	9.6
UT 15-13	15-13-5	6982.2	2.9	0.1	0.0	100.0
UT 15-13	15-13-6	6983.9	2.0	-2.8	22.4	77.6
UT 15-13	15-13-7	6989	3.5	-2.1	4.0	96.0
UT 15-13	15-13-9	7006.5	4.8	0.0	0.0	100.0
UT 15-13	15-13-10	7007.8	2.1	-1.6	0.0	100.0
UT 15-13	15-13-11A	7009.9	2.9	-7.3	0.0	100.0
UT 15-13	15-13-11B	7009.9	3.9	-2.6	6.1	93.9
UT 15-13	15-13-12	7016.4	4.7	-4.6	14.9	85.1
UT 15-13	15-13-13	7017.4	4.7	-4.8	12.6	87.4
UT 15-13	15-13-14	7025.2	6.0	-1.3	0.0	100.0
PW 13-06	13-06-1	5524.2	2.5	0.5	8.2	91.8
PW 13-06	13-06-2	5524.7	2.3	-4.7	7.3	92.7
PW 13-06	13-06-3	5527.3	3.4	1.1	2.0	98.0
PW 13-06	13-06-5	5537.3	0.4	-6.5	100.0	0.0
PW 13-06	13-06-6	5539.5	4.3	-1.5	1.6	98.4
PW 13-06	13-06-6B	5540.7	3.7	-0.4	0.0	100.0
PW 13-06	13-06-7	5541.9	4.3	-2.6	0.0	100.0
PW 13-06	13-06-7B	5542.7	3.7	-0.7	0.0	100.0
PW 13-06	13-06-8	5543.5	3.5	-2.8	0.0	100.0
PW 13-06	13-06-9	5544.3	2.7	-2.2	0.0	100.0
PW 13-06	13-06-10	5545.3	3.3	-4.3	15.5	84.5

Well	Sample	Depth	$\delta^{13}C$ (VPDB)	$\delta^{18}O$ (VPDB)	%Cal	%Dol
PW 13-06	13-06-10A	5546.1	3.5	-3.3	12.9	87.1
PW 13-06	13-06-10B	5551	2.2	-6.2	6.3	93.7
PW 13-06	13-06-11A	5553.9	1.1	-5.4	68.3	31.7
PW 13-06	13-06-11B	5554.7	1.0	-4.8	0.9	99.1
PW 13-06	13-06-11C	5556.6	1.2	-2.9	48.6	51.4
PW 13-06	13-06-12	5557.4	1.9	-6.0	0.0	100.0
PW 13-06	13-06-13	5563.3	1.1	-4.1	20.2	79.8
PW 13-06	13-06-14	5565.9	-0.9	-9.6	98.4	1.6
PW 13-06	13-06-15	5580.8	-0.9	-6.5	40.1	59.9
PW 13-06	13-06-16	5595.4	-0.5	-1.5	0.0	100.0
PW 13-06	13-06-17	5596	2.9	-2.2	0.0	100.0
PW 13-06	13-06-18	5603.4	0.1	-6.1	98.2	1.8
PW 13-06	13-06-19	5607.8	2.5	-1.4	3.4	96.6
DS 11-20	11-20-1	4972.5	-3.0	-3.8	36.7	63.3
DS 11-20	11-20-2	4974.5	-0.7	-5.3	98.5	1.5
DS 11-20	11-20-4	4980.1	-2.0	-0.8	3.5	96.5
DS 11-20	11-20-5	4985.5	-1.0	-2.4	9.5	90.5
DS 11-20	11-20-8	4989.5	-0.1	-4.8	97.5	2.5
DS 11-20	11-20-9	4990.45	-1.1	-3.5	31.9	68.1
I 16	16-1	4701.3	-0.8	0.5	0.0	100.0
I 16	16-2	4705.4	3.1	-4.0	13.3	86.7
I 16	16-3	4706.3	0.9	-5.6	30.5	69.5
I 16	16-4	4707	-1.3	-4.4	13.1	86.9
I 16	16-7	4720.8	-0.9	0.1	4.3	95.7
I 16	16-8	4721.25	0.5	-3.0	28.0	72.0
I 16	16-10	4723.3	0.2	-3.6	14.1	85.9
I 16	16-11	4724.2	-1.0	-2.0	35.7	64.3
I 16	16-19	4735.8	-2.1	-4.6	4.6	95.4

Precision and accuracy as 1σ of (n=10) lab standards are (i) 0.2 for $\delta^{13}C$ and (ii) 0.2 for $\delta^{18}O$.